Investigation of DC and RF biased gridded ion thruster plume phenomena

Lui Txai Calvoso Habl

INSTITUT POLYTECHNIQUE DE PARIS

NNT : 2022IPPAX039

Thèse de doctorat

Investigation of DC and RF biased gridded ion thruster plume phenomena

Thèse de doctorat de l'Institut Polytechnique de Paris
préparée à l'École Polytechnique

École doctorale n°626 École doctorale de l'Institut Polytechnique de Paris (EDIPP)
Spécialité de doctorat : Optique, Laser et Plasma

Thèse présentée et soutenue à Palaiseau, le 20/05/2022, par

LUI TXAI CALVOSO HABL

Composition du Jury :

Erik Johnson Directeur de Recherche, CNRS, LPICM, École Polytechnique	Président
Laurent Garrigues Directeur de Recherche, CNRS, LAPLACE, Univ. Toulouse III	Rapporteur
Aaron Knoll Senior Lecturer, Imperial College London	Rapporteur
Sedina Tsikata Chargée de Recherche, CNRS, ICARE	Examinateur
Victor Desangles Ingénieur de Recherche, DPHY, ONERA	Examinateur
Pascal Chabert Directeur de Recherche, CNRS, LPP, École Polytechnique	Directeur de thèse
Trevor Lafleur Principal Engineer, ThrustMe	Co-directeur de thèse
Dmytro Rafalskyi CTO, ThrustMe	Co-directeur de thèse

All models are wrong, but some are useful.
George Box

RESUMÉ

Ces dernières années, deux technologies prometteuses ont émergé pour améliorer les performances et diminuer le coût des systèmes de propulsion utilisant des propulseurs ioniques à grille ; la polarisation RF des grilles d'accélération ionique et l'utilisation de l'iode. Ces techniques peuvent représenter une avancée technologique significative ; cependant, lors de l'utilisation de l'un ou l'autre, les processus physiques de la génération de plasma et en particulier sur le panache de plasma en aval sont complexes, ce qui a des implications importantes sur les performances du sisteme. L'objectif principal de ce travail était d'élucider la physique du panache de plasma et de vérifier les influences sur le fonctionnement des propulseurs lors de l'utilisation de ces technologies par une approche numérique et expérimentale.

Un modèle particle-in-cell bidimensionnel dédié du panache a été développé pour étudier la technique de polarisation RF de la grille. Le modèle a utilisé différentes techniques uniques pour modéliser correctement le problème, comme une condition aux limites capacitive et un modèle analytique de l'injection d'électrons pulsés. Deux études différentes ont été menées à l'aide du code : premièrement, une comparaison directe entre un panache typique utilisant l'accélération CC avec un cas nominal de panache utilisant la polarisation de la grille RF ; et deuxièmement, une étude paramétrique du panache RF faisant varier trois paramètres différents. Cette étude numérique a permis une détermination du comportement de plusieurs phénomènes, l'élargissement des travaux numériques antérieurs, et une comparaison réussie avec les résultats expérimentaux passés.

Un prototype utilisant la polarisation de grille RF a également été étudié expérimentalement, qui a fonctionné aux valeurs les plus élevées d'énergie et de fréquence d'accélération à ce jour. L'étude expérimentale s'est concentrée sur trois aspects principaux : démontrer que le panache était bien neutralisé par le faisceau d'électrons pulsé, vérifier que le faisceau d'ions était correctement accéléré et enfin étudier la puissance consommée par le processus d'accélération. Ces aspects ont été étudiés en faisant varier deux paramètres, l'amplitude du signal d'accélération et la fréquence du signal. Les résultats ont démontré que le comportement du faisceau suivait de près de le comportement attendu, montrant un panache bien neutralisé avec des performances acceptables et fournissant les premières données de référence disponibles pour ce type de propulseur. Les expériences ont également montré un excellent accord avec les prédictions numériques et

théoriques, ce qui a confirmé à la fois l'exactitude du modèle développé ici et des travaux antérieurs, et constitue une avancée importante vers le développement d'un prototype de vol.

Pour l'iode, les caractéristiques du panache et les performances du propulseur ont été mesurées et comparées au xénon, montrant des caractéristiques uniques et, dans plusieurs cas, meilleures. Un nouvel instrument, composé d'un groupe automatisé de sondes planaires, a également été développé. Cet instrument a été utilisé pour générer des profils bidimensionnels du faisceau d'ions, permettant une estimation expérimentale de la divergence du panache lors de l'utilisation de l'un ou l'autre gaz. Afin d'améliorer la qualité des expériences et d'augmenter la base de connaissances sur les plasmas d'iode, l'émission d'électrons secondaires des ions d'iode bombardant plusieurs matériaux a été mesuré pour la première fois. Au cours de ces travaux, le propulseur testé a été lancé à bord d'une mission spatiale, ce qui a permis une comparaison des résultats au sol et en vol avec un excellent accord obtenu.

ABSTRACT

In recent years, two promising technologies emerged to improve the performance and decrease the cost of propulsion systems using gridded ion thrusters; RF biasing of ion acceleration grids and the use of iodine as a propellant. These techniques may represent a significant technological step forward; however, when using either of them, the physical processes in the plasma generation and especially on the downstream plasma plume are intricate, having significant implications on the device's performance. The main goal of this work was to elucidate the physics of the plasma plume and verify the influences on the operation of the thrusters when using these technologies through a numerical and experimental approach.

A dedicated two-dimensional particle-in-cell model of the plume was developed to study the RF grid biasing technique. The model employed different unique techniques to properly model the problem, such as a capacitive boundary condition and an analytical model of the pulsed electron injection. Two different studies were conducted using the code: first, a direct comparison between a typical plume using DC acceleration with a nominal case of the plume using RF grid biasing; and second, a parametric study of the RF plume varying three different parameters. This numerical study allowed a determination of the behavior of several phenomena, the expansion of previous numerical work, and a successful comparison with past experimental results.

A prototype using RF grid biasing was also investigated experimentally, which was operated at the highest values of acceleration energy and frequency to date. The experimental study focused on three main aspects: demonstrating that the plume was well-neutralized by the pulsed electron beam, verifying that the ion beam was correctly accelerated, and, lastly, studying the power consumed by the acceleration process. These aspects were studied while two parameters were varied, the acceleration signal amplitude and the signal frequency. The results have demonstrated that the behavior of the beam followed the expected behavior closely, showing a well-neutralized plume with acceptable performance and providing initial benchmark data available for this type of thruster. The experiments also showed an excellent agreement with the numerical and theoretical predictions, which confirmed both the correctness of the model developed here, and previous works, and being an important advancement towards developing a flight prototype.

For iodine, the characteristics of the plume and the thruster performance were measured and compared to xenon, showing unique and, in several cases, better characteristics. A new instrument, consisting of an automated array of planar probes, was also developed. This instrument was used to generate two-dimensional profiles of the ion beam, allowing an experimental estimation of the plume divergence when using either propellant. To improve the quality of experiments and increase the knowledge base on iodine plasmas, the secondary electron emission yield of iodine ions bombarding several materials was measured for the first time. During this work, the thruster tested was launched onboard a space mission, which permitted a comparison of ground and flight results with excellent agreement obtained.

ACKNOWLEDGEMENTS

É clichê, porém não teria como ser diferente: em primeiro lugar eu gostaria de agradecer minha mãe, meu pai, meus irmãos, e o resto da minha família pelo amor e suporte incondicional para minha mudança para a França, desenvolvimento do meu trabalho e escrita da minha tese. Sem esse imenso apoio esse passo não teria sido possível. Em especial gostaria de agradecer à minha namorada e companheira de vida, Bia, que me apoiou, motivou e me relembrou todos os dias da alegria e importância de persistir e completar esse longo trabalho.

Pursuing a PhD was not an easy task and it was a path of continuous learning and adaptation. Although the end result was not what I had in mind at first, it was much better and more rewarding than I could have imagined. During these last three years, I received essential support from all of those around me, and it would have been almost impossible to complete this work without their help. I would like to highlight the great receptivity and kindness with which the ThrustMe and LPP teams welcomed me, a foreigner coming from far away who was still discovering what it was like to do research in France.

First, I would like to thank my academic supervisor Pascal Chabert, who was extremely open from the start and gave me all the support I needed throughout this journey. I would also like to really thank my co-supervisor, Trevor Lafleur; your guidance, conversations, and availability made me really grow as a researcher and taught me to always seek understanding physics in the most accurate and imaginative way possible. In the same way I would like to thank my other co-supervisor, Dmytro Rafalskyi; the daily interaction in the lab and discussions taught me to think about physics in a practical way and not to be afraid to solve the problems necessary to produce good results and thus do research that matters to everyone. I am also grateful to Ane Aanesland for all the discussions, support and for trusting my work from the start. I want to say thanks to the whole team from ThrustMe for all the amazing daily work and personal interactions, including Plamen Proynov, Elena Zorzoli Rossi, Javier Martínez-Martínez, Antoine Poyet, Thomas Baret, Antoine Boré, Olena Rafalska, Giulio Coral, Fernanda Cyrne, Prachi Jain, and Sabrina Livadiotti. Your availability and help during all my struggles with experiments and coding was really invaluable. Furthermore, I also want to thank the LPP team for all the meetings and technical discussions, including Anne Bourdon, Alejandro

Alvarez Laguna, and all my fellow current and past PhD students, including Thomas Charoy, Antoine Tavant, Romain Lucken, Federico Petronio, Benjamin Esteves, Tarek Ben Slimane, and Louis Reboul. Thank you all for your receptivity, kindness, and help with the bureaucracy; I would not be able to deal with it without all your help. I also highlight the enormous importance that the Universidade de Brasília and my former professors had for my training and preparation. In particular, I am grateful to my former supervisor and friend, Paolo Gessini, who first introduced me to plasma physics and electric propulsion, and continuously encouraged me to pursue a high-quality research career. I would also like to thank professor Ivan Ferreira, my master's supervisor, who left us so soon. He certainly inspired a whole generation of young physicists in Brasília and his memory will stay with us forever, always encouraging us to be curious and *to boldly go where no one has gone before.*

I would like to thank the Association Nationale de la Recherche et de la Technologie (ANRT) in collaboration with ThrustMe and LPP for funding this PhD through the CIFRE contract number 2019/0409; I thank European Space Agency for supporting the in-orbit demonstration through the TURBO project, ARTES C&G programme, contract number 4000131883/20/NL/MM/can; and I thank the Centre National d'Etudes Spatiales for supporting part of this work through the INODIN grant, R&T action R-S19/PF-0002-108-92. I thank the Cité Universitaire Internationale de Paris and more specifically the Maison du Brésil, for welcoming me to Paris and providing a high-quality and fairly priced accommodation during more than half of my PhD studies.

Finally, I would like to thank all the amazing developers working on open-source projects that were fundamental for this thesis. In particular, I thank all the contributors from the Python, NumPy, SciPy, Pandas, Matplotlib, and Hypre projects. Following these examples, I hope one day Science will be completely free and open for all people on the planet.

TABLE OF CONTENTS

CHAPTER 1

INTRODUCTION

The central objective of this research effort is to further understand the physical phenomena taking place in the plasma plume generated by novel gridded ion thrusters using either radio-frequency grid biasing, or DC biasing with iodine as a working gas. In this chapter, we explore the background knowledge involved in the development of the work, such as basic plasma processes, the concepts behind plasma-based space propulsion, and the most important aspects of the physics of plume expansion. At the end of the chapter, an outline of the thesis and description of the main objectives of this work are described.

1.1 Basic plasma physics

1.1.1 Definition, natural occurrences and applications

In a general definition, a *plasma* consists of a group of particles similar to a gas in which its constituent particles are partially or completely ionized. A plasma is generally composed of different species such as free electrons and charged or neutral heavy species such as atoms, molecules, and macroscopic particles. Two important aspects differ between a plasma and a typical gas [1]: the first is that long-range electromagnetic fields generated by plasma particles and external sources have an important influence on the behavior of the macroscopic and microscopic phenomena of the plasma, generating collective behavior; the second is that it must be *quasi-neutral*, i.e. the resulting net charge of the plasma is close to zero.

In a typical neutral gas, if gravity is neglected, macroscopic perturbations and forces are transmitted to its particles via collisions, and most low-intensity fields do not affect the trajectory of particles. On the other hand, the charged particles in a plasma react to any resulting electromagnetic field at its current location. In this way, in general, for non-relativistic situations, the trajectory of a given charged particle inside a plasma can be computed using Newton's second law and the Lorentz force as

$$m\frac{d\mathbf{v}}{dt} = q(\mathbf{E} + \mathbf{v} \times \mathbf{B}) + \mathbf{F_c} \tag{1.1}$$

where m is the mass of the particle, $\mathbf{v}$ is its velocity, q its charge, $\mathbf{E}$ and $\mathbf{B}$ are the resulting electric and magnetic at the location of the particle respectively, and $\mathbf{F_c}$ is a

force due to collisions. The electric and magnetic fields inside a plasma, in turn, can be determined using the classical set of Maxwell's equations given by

$$\nabla \cdot \mathbf{E} = \frac{\rho}{\varepsilon_0} \tag{1.2}$$

$$\nabla \times \mathbf{E} = -\frac{\partial \mathbf{B}}{\partial t} \tag{1.3}$$

$$\nabla \cdot \mathbf{B} = 0 \tag{1.4}$$

$$\nabla \times \mathbf{B} = \mu_0 \left(\mathbf{J} + \varepsilon_0 \frac{\partial \mathbf{E}}{\partial t} \right) \tag{1.5}$$

where ε_0 and μ_0 are the vacuum permittivity and permeability respectively, and, ρ and $\mathbf{J}$ are the charge density and current density at a given location in space. In the electrostatic case, $\mathbf{E}$ becomes conservative and can be written in the form $\mathbf{E} = -\nabla\phi$ where ϕ is a scalar electric potential field; with this, equation 1.2 can be calculated as

$$\nabla^2 \phi = -\frac{\rho}{\varepsilon_0}. \tag{1.6}$$

which is called Poisson's equation.

Considering that a plasma is composed of many charged species, the charge density ρ can be calculated as

$$\rho = \sum_k q_k n_k \tag{1.7}$$

where q_k and n_k is the charge and number density (given in particles per cubic meter) of the k-th species, respectively. For the simplest case where there are only two species, electrons (e) and positive singly-charged ions (i), the charge density is simply given by

$$\rho = e(n_i - n_e) \tag{1.8}$$

where e is the elementary charge in coulombs. In this way, in a quasi-neutral plasma $n_i \approx n_e$. It is important to note, however, that the difference in magnitude of n_i and n_e is often not negligible, both in space and time, at some locations, and it is responsible for important effects taking place within the plasma body, such as sheaths, waves, and instabilities among others [1].

As in a typical gas, the most generic description of a species in a plasma is usually achieved using distribution functions of the particles which may vary in space, time, and velocity-space [2]. This way, a given distribution function $f = f(\mathbf{x}, \mathbf{v}, t)$ provides the density of particles at each location of phase space, at a given time t. If one has available the distribution functions of a system, they can be used to derive several statistical quantities. One example is the particle number density of a species k which is defined as

$$n_k(\mathbf{x}, t) = \int_v f_k(\mathbf{x}, \mathbf{v}, t) d^3 v. \tag{1.9}$$

In this context, one of the simplest (and relatively accurate in many situations) ways to describe a particle population is to assume it has a constant particle density in space,

$n_{0,k}$, and it is in thermal equilibrium. When this is assumed, f_k does not have a spatial dependency anymore and it can be described by what is called a Maxwell velocity distribution in the form

$$f_k(\mathbf{v},t) = n_{0,k}\left(\frac{m}{2\pi k_B T_k}\right)^{\frac{3}{2}} \exp\left(-\frac{|\mathbf{v}|^2}{2k_B T_k}\right) \tag{1.10}$$

where k_B is the Boltzmann constant and T_k is defined as the temperature of the species k. This distribution is very common in different plasma physics phenomena and has the form of a Gaussian probability distribution with a standard deviation of $\sqrt{k_B T/m}$. In this way, the temperature is connected to the spread in the velocity distribution of particles and is directly related to the average energy $\langle E\rangle$ of the system as $\langle E\rangle = \frac{3}{2}k_B T$. One of the most common situations in plasma physics, and which is often going to be the case in the present work, is to have an electron temperature, T_e, which is much higher than the ion temperature, T_i, due to the much lower mass of electrons. Despite being often accurate, this temperature definition is not appropriate for several plasma physics situations where a specific particle population is non-Maxwellian. In these cases, specific statistical definitions are used which may better fit the phenomena being studied [3].

One of the most fundamental effects of a plasma that illustrates its collective nature, is its ability to shield the potential of a body placed inside a plasma, and is called Debye shielding. Whenever a body that has a given potential different from the bulk plasma potential is placed inside the discharge, the particles rearrange themselves to block the potential effectively making the electric field generated by the body decay much faster than in free space. For a plasma with only electrons and cold positive ions, it can be considered that ions behave as a static positive charge background and that electrons, being more mobile, respond to the change in the potential configuration and shield the internal potential distribution. Considering this case, it is possible to compute a characteristic length of the potential decay after the shielding has taken place. Assuming a one dimensional case and that $n_i = n_0$ and $n_e = n_e(x)$, equations 1.6 and 1.8 can be expressed as

$$\frac{d^2\phi}{dx^2} = -\frac{e}{\varepsilon_0}(n_0 - n_e(x)). \tag{1.11}$$

If one considers that the electron population is Maxwellian and that the electron inertia is negligible, the electron density can be estimated using the so-called Boltzmann relation as

$$n_e(x) = n_0 \exp\left(\frac{\phi(x)}{T_e}\right) \tag{1.12}$$

where T_e is the electron temperature in eV and it is considered that the plasma has a density n_0 far away from the point analyzed. In this way, equation 1.11 can be solved to yield a solution of the form $\phi(x) = \phi(x=0)\exp(-|x|/\lambda_D)$, where λ_D is called the Debye length and is defined as

$$\lambda_D \equiv \sqrt{\frac{\varepsilon_0 T_e}{n_0 e}} \tag{1.13}$$

The Debye length is a widely used parameter in plasma physics to characterize spatial processes and qualify its degree of quasi-neutrality. If one considers a given plasma characteristic length l, to guarantee quasi-neutrality one must have $\lambda_D \ll l$. This is because if a charged region is present inside the plasma, this disturbance will only be shielded (and thus guaranteeing a uniform potential) if there is enough space compared to λ_D.

For a plasma to exist there must be a set of processes to produce its charged species. Typically these reactions, which are responsible for sustaining the discharge, take place within the plasma itself and are a consequence of collisional processes between the different species of the system. Numerous collisional reactions might depend on the working gas chemistry and the operational conditions of the discharge [4]. In a typical low-temperature plasma, some of the most common types of reactions during the discharge include electron ionization ($e^- + A \longrightarrow 2\,e^- + A^+$), charge exchange ($A^+ + B \longrightarrow A + B^+$), among others. There are numerous other elastic and inelastic collisional processes that take place during a discharge and are of great importance to understand the evolution of a plasma system, however, the major part of them are greatly dependent on the chemical and physical properties of the particles and must be analyzed in the context of a specific system.

Despite typically not being acknowledged by the general public, plasmas are widely present in numerous situations in natural phenomena and technology – a phrase often found in specialized and popular literature is that "99% of the observable universe is in a plasma state" [5]. In nature, common examples include electric discharges such as lightning bolts [6]; planetary magnetospheres and atmospheric layers such as the ionosphere [7]; stars, the sun, and solar winds [5, 8]; and the interstellar and intergalactic media [9]. In technology, artificially produced plasmas include fusion energy research plasmas such as in Tokamaks and other types of reactors [10]; electric arcs used for welding and in plasma torches [11]; manufacturing processes such as reactive-ion etching and vapor deposition used in specialized industries, notably in the manufacturing of semiconductors [12]; and finally in plasma-based space propulsion, where plasma is used to generate charged particles that are accelerated by electromagnetic fields producing thrust to move a satellite [13, 14].

The different types of discharge found in nature and technological applications share some common aspects, however, in each case, the range of operational parameters vary considerably requiring a specific theoretical approach for each case. Plasma discharges can be classified using different aspects which can greatly modify their behavior, including particle temperature and density; the presence of a magnetic field and whether the species are magnetized or not; the presence of particle beams; and the specific particle distribution shapes. One common way to visualize the large range of discharge conditions is a density-temperature diagram as shown in fig 1.1. In the upper right direction, for extreme values of both density and temperature, these are the typical conditions for natural and artificial nuclear fusion plasmas. On the other hand in the lower left end of the diagram, it is possible to see what is typically called "low-temperature plasmas" including discharges used in plasma medicine, general industrial processing, and also

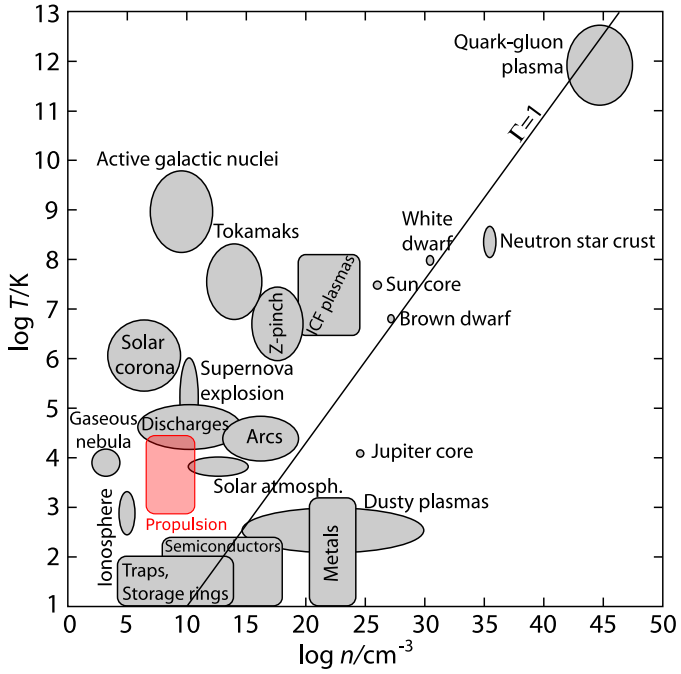

Figure 1.1: Diagram showing the different plasma regimes as a function of temperature and particle density (adapted from Ref. [15]).

the ones found in common plasma-based space thrusters. In the present work, the main focus will be on low-temperature plasmas, in the region marked by the red rectangle on the diagram, since this is usually what is found in plasma propulsion.

1.1.2 Plasma modeling

Because plasmas are a complex media and can exist in many different conditions, distinct theoretical approaches are developed to model their behavior, each of which is a better fit for different circumstances. The first approach consists of directly analyzing the trajectory of charged (and neutral) particles immersed in a given electromagnetic field. This model is called "particle orbit theory" and despite not providing a complete macroscopic description of the plasma, gives important insight into the dynamics of individual particles and aids in the understanding of different processes. The core of this theory is the analysis of the equation of motion 1.1 under different field configurations.

As in a gas, theoretically, it is possible to describe any plasma using only the equations of motion of each individual particle plus the set of electromagnetic equations. However, apart from very simple cases, this would require enormous computational power, and so to circumvent this issue plasmas are typically analyzed statistically. This way, the second theoretical approach is called "kinetic theory" and consists of modeling the spatial and temporal evolution of the particle distribution functions for each species present in a plasma and their interactions. If one considers the distribution function $f_k(\mathbf{x}, \mathbf{v}, t)$ for a

species k, its generalized evolution is described by a kinetic differential equation called the Boltzmann equation [2] in the form

$$\frac{\partial f_k}{\partial t} + \mathbf{v} \cdot \nabla f_k + \frac{\mathbf{F}}{m} \cdot \frac{\partial f_k}{\partial \mathbf{v}} = \left(\frac{\delta f_k}{\delta t} \right)_{\text{coll}} \tag{1.14}$$

where $\mathbf{F}$ is a force field and the right-hand side term is called the collision term and describes the change in the evolution of f_k due to collisions between the same and different species. Typical collision models include the Krook model, the Boltzmann collision integral and the Fokker-Plank collision term [2]. A common simplification of equation 1.14 is called the Vlasov equation and is derived by considering that the collisional term is zero and that $\mathbf{F} = \mathbf{F}_{ext} + \mathbf{F}_{int}$, where $\mathbf{F}_{ext}$ is any external force (including electromagnetic forces) and $\mathbf{F}_{int}$ is the electromagnetic force generated by the particle population within the plasma. The internal force is calculated using Maxwell's equations while assuming that $\rho_k = q_k \int_v f_k d^3v$ and $\mathbf{J} = q_k \int_v \mathbf{v} f_k d^3v$, which are the macroscopic average charge density and current at a given location. The variable $\mathbf{F}_{int}$ is said to be the force due to the smoothed electromagnetic fields, since average values are used for ρ and $\mathbf{J}$. The Boltzmann and Vlasov equations are two of the most fundamental equations in plasma physics and can be directly applied to analyze several important problems including instabilities and oscillations among others [16]. However, as they are non-linear and the function f_k can have great complexity, these equations are typically hard to be treated and not commonly applied directly, but serve as the foundation to derive several simplified and averaged models that describe different phenomena with relatively high accuracy.

To obtain a model which is more easily treatable, it is assumed that a set of macroscopic parameters that represent certain local characteristics of the distribution function may be derived by taking *moments* of the Boltzmann equation through an averaging process. In this model, called "two-fluid" or "many-fluid" theory, information of the specific shape of the distribution function is lost, and the system is represented by macroscopic parameters related by a set of transport equations. If one is representing a system using this model, the specific distribution function cannot be recovered and it is only known that the *most probable* local distribution must be somewhat close to a Maxwell-Boltzmann distribution. To derive this model, it is necessary to define that for any physical property $\Lambda(\mathbf{x}, \mathbf{v}, t)$ its average is given by

$$\langle \Lambda \rangle (\mathbf{x}, \mathbf{v}, t) = \frac{1}{n_k(\mathbf{x}, t)} \int_v \Lambda(\mathbf{x}, \mathbf{v}, t) f_k(\mathbf{x}, \mathbf{v}, t) d^3v \tag{1.15}$$

where n_k is given by equation 1.9. To obtain the moments, the Boltzmann equation is multiplied by Λ and its average is calculated while considering $\Lambda = m$, $\Lambda = m\mathbf{v}$ or

$\Lambda = \frac{1}{2}mv^2$. The typical three equations of the multi-fluid model are then derived as

$$\frac{\partial n}{\partial t} + \nabla \cdot (n\mathbf{u}) = S \tag{1.16}$$

$$nm\frac{d\mathbf{u}}{dt} + \nabla \cdot \mathbf{P} - n\langle \mathbf{F} \rangle = \mathbf{S}' \tag{1.17}$$

$$\frac{3}{2}\frac{dp}{dt} + \frac{3}{2}p\nabla \cdot \mathbf{u} + (\mathbf{P} \cdot \nabla) \cdot \mathbf{u} + \nabla \cdot \mathbf{q} = \mathbf{S}'' \tag{1.18}$$

where $\frac{d}{dt} = \frac{\partial}{\partial t} + (\mathbf{u} \cdot \nabla)$ is the total derivative, $\mathbf{u} = \langle \mathbf{v} \rangle$, $\mathbf{P} = mn\langle \mathbf{cc} \rangle$ is the kinetic pressure tensor, $\mathbf{c} = \mathbf{v} - \mathbf{u}$ is the random velocity component, p is the diagonal value of the pressure tensor, $\mathbf{q}$ is the heat flux vector, and S, $\mathbf{S}'$ and $\mathbf{S}''$ are collision terms. Equations 1.16, 1.17 and 1.18 are denoted as the continuity, momentum and energy equation respectively. This formulation is equivalent to the Navier-Stokes equation for a generic fluid, however here $\mathbf{F}$ is typically generated by electromagnetic forces arising from the charge density and current density of the system, and the collision terms, apart from affecting the dynamics of the system, also account for a sink and source of particles through chemical or collisional processes. A typical simplification when using this model on several plasma phenomena is to consider that the plasma has only two species (electrons and singly-charged ions), that it is collisionless, and that it is locally isotropic[17]. In this simplified case, referred to as the two-fluid model, since the distribution is isotropic, the energy equation may be ignored and a state equation may be used to make the system self-consistent, in the form of equation 1.22, or in the polytropic form $p = Cn^\gamma$.

When the random velocity $\mathbf{c}$ is isotropic or the pressure tensor contains only diagonal elements, the tensor $\mathbf{P}$ can be written as $\nabla \cdot \mathbf{P} = \nabla p$ where p is the scalar kinetic pressure [17]. The pressure p is defined as the trace of the tensor P divided by three and can be represented as

$$p = \frac{1}{3}nm\langle c_x^2 + c_y^2 + c_z^2 \rangle = \frac{1}{3}nm\langle c^2 \rangle \tag{1.19}$$

At this point is important as well to define the concept of absolute temperature in a plasma or gas. Thermodynamically, the definition of temperature is that there is a temperature T_j, where $j = x, y, z$, for each spatial direction that is associated with the mean thermal energy in the form $T_j = \frac{m}{k_B}\langle c_j^2 \rangle$, where k_B is the Boltzmann constant. When the particle distribution is isotropic, $c^2/3 = c_x^2 = c_y^2 = c_z^2$ the temperature in every direction becomes the same, and the total temperature is represented in the form

$$T = \frac{m}{3k_B}\langle c^2 \rangle \tag{1.20}$$

Defining the average thermal energy as $\langle E \rangle = \frac{1}{2}m\langle c^2 \rangle$, the internal energy of a gas or plasma in the isotropic case may be represented as

$$\langle E \rangle = \frac{3}{2}k_B T \tag{1.21}$$

The same result may also be obtained in the anisotropic case if one considers that the temperature T represents actually an average of the temperatures in the three directions, $T = \frac{1}{3}(T_x + T_y + T_z)$. Equation 1.21 is also obtained using this approach, but in this case, it would represent the average thermal energy in the three spatial directions.

Because the isotropic Maxwellian distribution in the form of equation 1.10 is so commonly found in different discharges, it is useful to calculate a number of quantities that can be used when making different theoretical approximations. In this case, the scalar pressure equation 1.19 and the temperature equation 1.20 can be combined and written as

$$p = nk_BT \tag{1.22}$$

which is known as the ideal gas state equation. Because the velocity distribution is isotropic, it is possible to find a speed distribution $g(v)$ that gives the probability of a particle having a given speed magnitude $v = |\mathbf{v}|$. This can be calculating by representing the velocity in polar coordinates and integrating the velocity distribution function over all possible angles in the form $g(v) = \int_0^{2\pi} \int_0^{\pi} v^2 f(v) \sin\theta d\theta d\phi$, yielding

$$g(v) = 4\pi n_0 \left(\frac{m}{2\pi k_B T}\right)^{\frac{3}{2}} v^2 \exp\left(-\frac{v^2}{2k_BT}\right) \tag{1.23}$$

which is known as the Maxwell speed distribution. Using equation 1.15 but with the distribution $g(v)$, one can calculate the mean particle speed for a given species as

$$\bar{v} = \sqrt{\frac{8k_BT}{\pi m}} \tag{1.24}$$

For this case, it is also possible to find the mean flux $\Gamma = nv$ of particles crossing an arbitrary plane within the plasma. This can be found by integrating the average of Γ in the velocity distribution function, but considering only positive velocity values in one of the coordinates giving

$$\Gamma_m = \frac{1}{4} n\bar{v} \tag{1.25}$$

1.1.3 Sheaths

One fundamental aspect in the modeling of plasma behavior is to understand the regions where an interface between the plasma and a material boundary exists. Commonly in this region, the assumptions made for modeling the bulk region of the plasma are no longer valid, and the quasi-neutrality condition is usually not fulfilled. This interaction region, where particles are lost and which may introduce different discontinuities, is typically called a plasma sheath.

The boundaries introduce a spatial discontinuity inside the plasma body. Typically these boundaries are either of a conducting or dielectric material. Whenever the boundary is conductive, this means that the electric potential is uniform across the boundary and that the potential at this boundary can be set by an external circuit. On the other

hand, when the boundary is a dielectric, this implies that there can be local charge accumulation and that this body is typically floating within the plasma with its potential being controlled both by the charge flux and external electromagnetic fields.

An interface case was shown when considering the effect of the Debye shielding which resulted in the relation for the Debye length with equation 1.13. In that case, a body with a given fixed potential ϕ was inserted into the plasma and it was assumed that the ion population was distributed constantly over space and was not perturbed by the body. Furthermore, the calculation required that that $\phi \ll T_e$ and that the species were always Maxwellian and isotropic.

In a second approach it is possible to assume an interface between the plasma and a body with a given potential $\phi_b < 0$ and in this case the density and velocity of ions vary in the sheath region. To model this case, it is assumed that ions are cold ($T_i \approx 0$) and the bulk plasma potential is close to zero $\phi_p \approx 0$. Taking the continuity fluid equation 1.16 and the momentum fluid equation 1.17 in one dimension, while considering that all quantities do not vary in time, neglecting collisions, and noting that $\langle \mathbf{F} \rangle = -e\frac{d\phi(x)}{dx}$, it is possible to write

$$n_i(x)u_i(x) = K \tag{1.26}$$

$$\frac{1}{2}mu_i^2(x) + e\phi(x) = K' \tag{1.27}$$

where K and K' are constants. It is considered that the interface is located at $x = 0$, that the sheath region starts at $x = l$ and that for $x > l$ the plasma has the properties of the bulk plasma with $n_i \approx n_e$ and $\phi(x) = 0$. In this way, it is possible to determine the constants as $K = n_0u_0$ and $K' = \frac{1}{2}mu_0^2$ where n_0 and u_0 are the ion density and velocity at $x = l$ respectively. With this, it is possible to calculate the ion density profile inside the sheath as

$$n_i(x) = n_0\left(1 - \frac{2e\phi(x)}{mu_0^2}\right)^{-\frac{1}{2}} \tag{1.28}$$

Using the Poisson equation 1.6, the Boltzmann relation 1.12 and equation 1.28, it is possible to get a differential equation that gives the potential profile within the sheath in the form

$$\frac{d^2\phi(x)}{dx^2} = \frac{n_0e}{\varepsilon_0}\left[\exp\left(\frac{\phi(x)}{T_e}\right) - \left(1 - \frac{2e\phi(x)}{mu_0^2}\right)^{-\frac{1}{2}}\right] \tag{1.29}$$

This equation is non-linear and its solution is not trivial. To analyze it, one can make a Taylor expansion of the right-hand side of the equation and ignore the higher-order terms, which yields an equation in the form $\frac{d^2\phi}{dx^2} = \phi/C^2$, where $C = \lambda_D\left(1 - \frac{eT_e}{m_iu_0^2}\right)^{-1/2}$. The solution to this equation is in the form $\phi(x) = \phi(0)\exp(-x/C)$, and since it is expected that the potential ϕ increases monotonically from $x = 0$ to l, C must be positive and real. In this way, to fulfill this requirement the ion velocity at the edge of the sheath must be such that $u_0^2 > eT_e/m$, which is known as the Bohm criterion. With this, a minimum ion

speed is defined as

$$u_B = \sqrt{\frac{eT_e}{m}} \tag{1.30}$$

which is called the Bohm speed and is equal to the ion-acoustic velocity[18]. On the other hand, for the bulk region of the plasma, the ion velocity must always be $u < u_B$ to maintain charge balance[4]. In this way, since in the model all ions are initially at rest, there must be a region with a weak electric field that accelerates the ions from zero to u_B when they get to the edge of the sheath. This region, called the pre-sheath, has an extension considerably larger than sheath and has a potential drop of $\Delta\phi = T_e/2$ to accelerate the ions[4]. At the boundary between the pre-sheath and the sheath, ions transition from a subsonic ($u_i < u_B$) to a supersonic ($u_i > u_B$) regime in an effect close to a shockwave in a gas, and after that, the quasi-neutrality condition is no longer fulfilled at the supersonic regime. Since the ion speed must be $u_i \approx u_B$ at the sheath edge, where the plasma density is still $n_i \approx n_0$, and the flux is conserved through the sheath, the ion flux impinging the wall is

$$\Gamma_w = n_0 u_B. \tag{1.31}$$

Another type of interface is when a floating body is inserted into the plasma. In this case, the body absorbs particles and charges up to a potential in which it ensures that an equal current of ions and electrons reaches the body at steady-state. In this way, to compute the potential of the floating wall, it is necessary that $\Gamma_i = \Gamma_e$ at the wall. Since there is a sheath between the body and the plasma, the ion flux is calculated with equation 1.31, while the electron flux is calculated using the Boltzmann relation and equation 1.25

$$\Gamma_e = \frac{1}{4} n_0 \bar{v} \exp\left(\frac{\phi_w}{n_0}\right) \tag{1.32}$$

where ϕ_w is the potential of the wall. Solving the equation, the potential at the boundary can be estimated as

$$\phi_w = -T_e \ln\left(\frac{m_i}{2\pi m_e}\right) \tag{1.33}$$

This value is typically called the floating potential and is negative relative to the bulk plasma potential.

A different situation may arise when the potential drop within the sheath between the bulk plasma and the body's wall is much larger than T_e. In this case, the electron density in the sheath goes to zero and there is only ion acceleration in that region. In this case, it is possible to consider that the mass and momentum conservation equations are reduced to $n_i(x)u_i(x) = \Gamma_i$ and $\frac{1}{2}mu_i^2 + e\phi(x) = 0$. Using equation 1.6, one can solve the differential equation analytically to obtain

$$J_i = \frac{4}{9}\varepsilon_0 \sqrt{\frac{2e}{m}} \frac{\Delta\phi^{3/2}}{l^2} \tag{1.34}$$

where $J_i = e\Gamma_i$ is the ion current density, and $\Delta\phi$ is the potential drop between the sheath edge and the wall. Equation 1.34 is known as the Child-Langmuir law [19] and

gives the maximum current density that can cross a gap of size l with a potential drop $\Delta\phi$, with particles starting at rest. This current limitation is due to the space charge created by the particles themselves, and whenever a larger current enters the domain, the space charge creates an electric field which is sufficient to repel back a portion of the particles and reduce the current back towards the Child-Langmuir limit. Equation 1.34 may be applied to many situations other than a high-voltage sheath, whenever a current of particles is crossing a gap with a given applied voltage. For the case of the sheath, it is possible to estimate the gap size l if it is considered that the current density is given by $J_i = eu_B n_0$. Using the Child-Langmuir law and the ion current density at the sheath edge, the gap can be estimated as

$$l = \frac{\sqrt{2}}{3}\lambda_D \left(\frac{2\Delta\phi}{T_e}\right)^{\frac{3}{4}} \tag{1.35}$$

where λ_D is the Debye length at the sheath's edge. One important observation is that the size of a high-voltage sheath is considerably larger than a typical sheath, that is of the order of one or several Debye lengths [4], and scales up as the sheath potential drop is increased.

Yet another relevant case is when the voltage applied at a boundary varies in time, particularly at radio-frequencies. This case is common in radio-frequency (RF) discharges such as capacitively coupled plasmas (CCP) and may lead to different effects depending on the frequency of the voltage when compared to the ion and electron plasma frequencies [18].

1.1.4 Collisions and chemistry

Collisional processes are an important piece in understanding the dynamics of plasma discharges. Collisions have two major effects in plasmas: the first is the chemical reactions with the gain or loss of particles of different species altering the composition of the discharge; and the second is the alteration of the velocity magnitude and direction of particles through elastic and inelastic collisions, resulting in the modification of the particle distribution functions as collision processes take place. Collisions may happen between particles of the same or different species, and the probability of a specific collision event taking place in a given interval of time depends on a number of factors, including the species densities, and relative velocity of particles among other factors.

In a simple one-dimensional approximation, it is possible to quantify the number of particle collision events happening in the case of a particle beam with constant velocity v crossing a population of static particles of the same species. In this way, consider a flux of particles $\Gamma_0 = n_0 v$ coming from $x < 0$ that enters a region at $x \geq 0$ with static particles distributed randomly with a density n_t. With this, if one considers that the particles are removed from the beam once they suffer a collision, it is possible to estimate a flux $\Gamma(x)$ that interacted with the static particles as x increases. Considering a thin slice of the filled region of thickness dx, the number of particles per unit area is $n_t dx$. The ratio of the area of the slice which is covered by particles can be calculated as $n_t dx\sigma$, where σ is

the cross-section area of one particle. Because the incident particles that collide are lost, it is possible to conclude that the difference in flux magnitude after crossing the thin slice is $\Delta\Gamma = -n_t dx\sigma\Gamma$. Writing this equation in the differential form $d\Gamma/dx = -n_t\sigma\Gamma$ and solving yields $\Gamma(x) = \Gamma_0 e^{-\frac{x}{\lambda}}$, where

$$\lambda = \frac{1}{n_t\sigma} \tag{1.36}$$

is called the mean free path and gives the average distance that a particle will travel before suffering a collision. Another way of interpreting the result is to rewrite the solution of $\Gamma(x)$ to provide an estimation of collision probability as x increases, in the form

$$p(x) = 1 - e^{-\frac{x}{\lambda}} \tag{1.37}$$

such that λ is the distance that gives a 63% chance for a particle to suffer a collision.

Since the flux velocity is fixed at u_0 it is possible to calculate as well the mean time that it takes for a particle to collide, which is simply $\tau_c = \lambda/v$. With this the collision frequency can be written as

$$\nu = \frac{1}{\tau_c} = n_t v\sigma \tag{1.38}$$

which gives the average number of collisions that a particle undergoes per second. Another parameter which is commonly used when analyzing collisional processes is called the rate constant, and is defined as

$$K = \sigma v \tag{1.39}$$

This simplified model is known as a hard-sphere collisional model and may be reasonable as a first approach to study collisions between low energy neutral atoms since they do not have large scale interactions and their cross-section is close to their atomic radius, with $\sigma \approx \pi a^2$, where a is the diameter of the atom. On the other hand, when the species involved in the collision event are charged or the energies are relatively large this picture changes, and it is necessary to consider the electromagnetic and quantum mechanical interactions taking place during the event. In this case, the scattering cross-section σ is not constant anymore and starts to depend on different parameters, especially the energy or relative velocity between the particles. Some relevant examples of reactions involving charged and neutral species which cannot be approximated with the hard-sphere model are ionization, excitation and elastic scattering.

Despite the existence of different theoretical approximations for the collision cross-sections [4], commonly in experimental and numerical situations where a higher degree of fidelity is required, experimental cross-section curves are used. For different commonly used working gases, databases such as LXCat [20] make the cross-section data available as curves of $\sigma = \sigma(E)$ as a function of the particle energy for different types of atomic and molecular reactions. To derive other collision parameters from non-trivial cross-section curves dependent on the particle velocities, typically an averaging procedure over the distribution functions is used. Considering two species, with distribution functions $f_0(v_0)$

and $f_1(v_1)$, one can obtain the average rate constant as

$$K = \langle \sigma(v_r) v_r \rangle = \frac{1}{n_0 n_1} \int_v \sigma(v_r) v_r f_0(v_0) f_1(v_1) d^3 v_0 d^3 v_1 \tag{1.40}$$

where $v_r = |\mathbf{v}_0 - \mathbf{v}_1|$. One common approximation that corresponds to numerous real situations, is to assume that the projectile species is much more energetic than the target species, such that $v_r \approx v_0 = v$, reducing the average to $K = \langle \sigma(v) v \rangle = \int_v \sigma(v) v f(v) d^3 v$. Because the species involved in collisional processes commonly tend towards a Maxwellian distribution as a consequence of the scattering, it is also common to assume that $f(v)$ is Maxwellian and isotropic. If this is the case, the rate constant can be calculated for a given particle temperature defined by the distribution.

1.2 Electric propulsion

1.2.1 The need for plasma-based propulsion

The main purpose of space vehicles, such as spacecraft and rockets, is to be able to move into and through outer space. To create this movement, it is necessary to employ a type of *propulsion system*, which is a device that creates thrust (or force) through conservation of momentum. The vast majority of propulsion system concepts are based on the acceleration and exhaust of a mass flow rate $\dot{m}$ of *propellant* given in kg/s, which generates a counteracting force with a magnitude of roughly $\mathbf{F} = -\dot{m}\mathbf{u}_e$, where $\mathbf{u}_e$ is the average flow velocity of the exhaust. Notable exceptions to this working principle are solar sails [21], which uses the solar wind pressure to generate thrust, and laser propulsion [22], which uses the radiation pressure generated by a laser beam – however, the focus here is on so-called *reaction engines* which are the systems that must carry their own mass reservoir and accelerate this mass to generate the required impulse.

If it is considered that the vehicle which has a propulsion system is in vacuum, and there are no forces acting on its body, it is possible to estimate the change in velocity due to the exhaust of a given amount of mass. Considering that the initial mass of the vehicle is m_0 and its final mass is m_1, the change in velocity is

$$\Delta V = -u_e \ln \frac{m_0}{m_1} \tag{1.41}$$

where u_e is the mean exhaust velocity of the mass. Equation 1.41 is known as the Tsiolkovsky rocket equation and despite its simplicity it is widely used in space mission estimations with a high level of accuracy. If the total propellant mass carried by the vehicle is defined as $m_p = m_0 - m_1$, the ratio of propellant mass to initial mass can be calculated as

$$\frac{m_p}{m_0} = 1 - \exp\left(-\frac{\Delta V}{u_e}\right) \tag{1.42}$$

From equation 1.42, it is possible to observe that the amount of propellant needed to perform a given change in ΔV, decreases exponentially with the magnitude of the exhaust

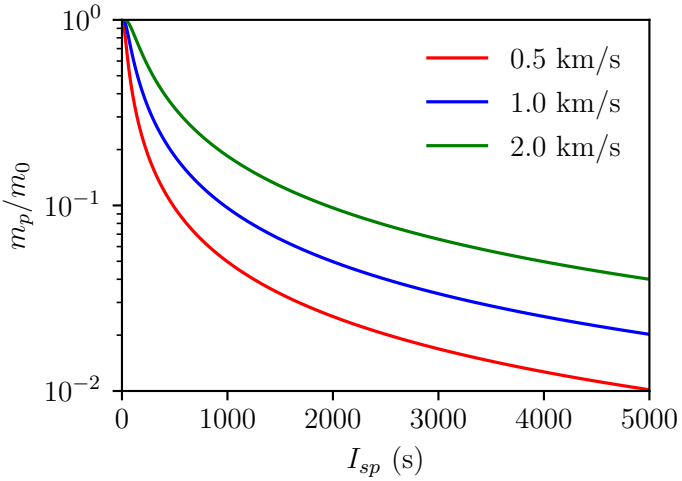

Figure 1.2: Propellant mass ratio, m_p/m_0, as a function of the specific impulse, I_{sp}, for three different values of ΔV.

velocity u_e. This implies that one of the objectives when designing a propulsion system, apart from maximizing the thrust, is to maximize its exhaust velocity to improve the mass efficiency of the mission. For historical reasons [23], a factor that is commonly used to indicate the mean exhaust velocity of a propulsion system and quantify its performance is called *specific impulse* which is given in units of seconds and is defined as

$$I_{sp} = \frac{u_e}{g_0} = \frac{T}{\dot{m} g_0} \tag{1.43}$$

where $g_0 = 9.806\,\mathrm{m/s}$ is the standard gravitational acceleration, and

$$T = |\mathbf{F}| = \dot{m} u_e \tag{1.44}$$

is the thrust. Figure 1.2 shows the plot of the propellant mass ratio given by equation 1.42 for three different values of ΔV that are typical for space missions [14, 24]. It is possible to see that for $\Delta V \approx 1.0\,\mathrm{km/s}$, the propellant mass ratio starts to be a considerable fraction $> 10\,\%$ for values of specific impulse smaller than $1000\,\mathrm{s}$.

There are numerous different concepts of propulsion systems used in space, and they can be understood and classified in distinct manners. Nevertheless, there are two factors that are essential to understanding their working principle. The first one is the *energy source* used for the propellant acceleration, which has three main types: (1) chemical energy, which consists of using the energy stored in the chemical bonds of the propellant(s); (2) solar energy, where the energy used is collected from solar radiation using solar cells; (3) nuclear energy, where the energy comes from an onboard nuclear reactor. The second aspect is the *acceleration method*, which can be: (1) thermal acceleration, when gas is accelerated by being heated and expanded through an appropriate nozzle; and (2) electric acceleration where the mass is accelerated by electrostatic or electromagnetic

fields. Despite existing devices using many of these combinations, the two most common types are chemical thermal propulsion and solar electric propulsion. The power required from any of the energy sources to accelerate a mass flow rate $\dot{m}$ to an exhaust velocity u_e, generating a given thrust T, is

$$P_j = \frac{1}{2}\dot{m}u_e^2 = \frac{g_0}{2}TI_{sp} \tag{1.45}$$

where P_j is commonly called the jet power [24].

Chemical thermal thrusters are the oldest and most used concept in the propulsion of launch vehicles and spacecraft. The central idea of this concept is the combustion of a reactive propellant in a controlled manner inside a chamber, heating up the combustion products and other gases, which then exit the device through a nozzle, creating an opposing thrust. This raw concept, of a device being propelled by a controlled and continuous combustion, initially appeared around 200-300 BC in China together with the invention of gun powder and fireworks and continued to be used over the next few centuries for many applications, namely weaponry [25]. However, the first efforts to study this type of propulsion to be used on space travel appeared at the beginning of the 20th century with important pioneers such as Konstantin Tsiolkovsky, Robert Goddard, and Hermann Oberth among others [25]. The first object to reach space, crossing the Karman line[1], was the German rocket and missile V-2 in 1944, led by the scientist Wernher von Braun [26]. Even today, chemical propulsion continues to be widely used and is the only one to successfully provide the necessary propulsion capabilities to launch objects into space because of its ability to provide high levels of thrust when compared to other concepts. The main reason for being able to provide this level of thrust can be seen with equation 1.45. In a chemical thermal thruster, the jet power is provided by the propellant itself, so the power generated is coupled to the mass flow rate as $P_j = \eta\dot{m}\bar{E}$, where $\bar{E}$ is the energy generated by the reaction per kilogram of propellant in $\mathrm{J\,kg^{-1}}$, and η is an efficiency. Using this definition and equation 1.45, the theoretical maximum specific impulse of a chemical rocket, ignoring all gas and pressure losses, and using $\eta = 1$, can be written as

$$I_{sp,max} = \frac{1}{g_0}\sqrt{2\bar{E}} \tag{1.46}$$

With present-day technology, the most energetic chemical reaction that can be reliably used in a chemical propulsion system is the combustion of H_2 and O_2, where the energy generated per mass of propellant can be estimated for the stoichiometric combustion as $\bar{E} \approx 1.3 \times 10^7\,\mathrm{J\,kg^{-1}}$ [24]. In this way, the maximum possible specific impulse provided by present devices is roughly $I_{sp,max} \approx 520\,\mathrm{s}$, meaning that for example, the propellant ratio for this type of propulsion will always be larger than 30% for $\Delta V > 2\,\mathrm{km/s}$. The thrust generated by these devices can also be estimated as $T = \dot{m}\sqrt{2\eta\bar{E}}$, meaning that for a given reaction and a given efficiency, the thrust generated is actually proportional to the mass flow rate of propellant. Despite having a limited specific impulse, this characteristic makes the scaling of chemical thrusters straightforward, and in fact devices of this type

[1]Defined as the limit between the atmosphere and space, at 100 km.

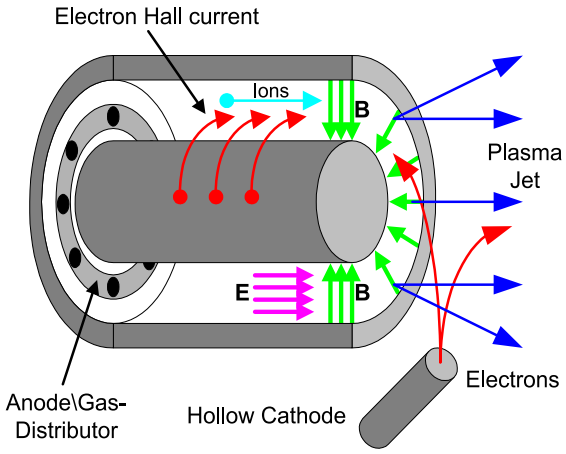

Figure 1.3: Schematic of a Hall effect thruster (adapted from Ref. [31]).

have thrust values ranging from 1 N up to 10 MN [24] making it suitable for applications on launch vehicles and spacecraft.

One of the biggest limitations of chemical thrusters is the theoretical ceiling of the specific impulse, which does not allow a significant reduction in the amount of propellant required to perform a given mission independent of the system's optimization. Solar electric propulsion on the other hand is based on the generation of thrust through the acceleration of massive charged particles (such as atoms, molecules, or droplets) by electrostatic or electromagnetic fields, making the power input and the mass flow rate decoupled which allows the specific impulse to be limited only by the amount of available power and the device's hardware. Real devices can reach specific impulse levels above 5000 s, however, their main drawback is that they typically produce much lower thrust levels ($T < 1$ N) making the maneuvers considerably longer when compared with chemical thrusters. These devices were also first idealized at the beginning of the 20th century by different pioneers such as Robert Goddard and Ernst Stuhlinger[27] but were only first tested on a real mission in 1964 onboard the SERT-I spacecraft [28]. Nowadays, there are more than 2000 satellites using electric propulsion systems for different maneuvers including orbit changes, drag compensation, deep space trajectories, and station keeping among others [29, 30].

There are numerous electric propulsion concepts [13], however, the two most successful and widespread are: Gridded Ion Thrusters (GIT) and Hall Effect Thrusters (HET). Hall effect thrusters are based on the acceleration of ions generated by a plasma discharge in a $\mathbf{E} \times \mathbf{B}$ configuration. A general schematic of a HET is displayed in figure 1.3. The discharge chamber of the thruster has an annular geometry, at the bottom of the chamber the propellant gas gets injected and there is an anode that gets biased to a given voltage forming an axial electric field. A radial magnetic field $\mathbf{B}$ is applied close to the exit surface of the annular chamber, and together with the electric field generated by the anode, a cross-field configuration is established. An external electron source, typically a hollow cathode, inject electrons close to the exit surface of the chamber – these electrons

are attracted by the anode and get trapped at the cross-field forming an azimuthal Hall current. This current ionizes the propellant gas which gets accelerated outwards by the axial electric field. The radial magnetic field is carefully selected such that the electrons are magnetized so that their Larmor radius is smaller than the dimensions of the chamber's channel, and ions are not magnetized and so the deflection of their trajectory due to the magnetic field is minimized. Part of the current provided by the electron source also goes outwards within the ion beam to maintain charge balance of the thruster. Because they generally have a higher thrust-to-power ratio, actual HET devices can usually generate considerably higher levels of thrust compared with the GIT or other concepts such as the FEEP, in the range of 1–500 mN, and I_{sp} in the range 500–2500 s [14]. Hall effect thrusters are widely used for many different missions due to their capability of generating high thrust levels for an electric propulsion device thus decreasing the time of maneuvers while preserving a low propellant ratio [29]. Recently, between the years of 2019 and 2021, SpaceX launched more than 2000 satellites using HETs for their Starlink constellation, which makes the HET the most used EP thruster until today [30].

Gridded ion thrusters, similarly to HETs, are also devices that generate thrust via the acceleration of ions generated by a plasma. However, in the case of GITs, the ions are accelerated through a set of grids biased with a high-voltage potential. Gridded ion thrusters are one of the central subjects in this work, so their characteristics and modeling will be discussed in the next section. Nonetheless, compared to HETs, GITs are able to generate a considerably higher specific impulse, above 3000 s, however their thrust-to-power ratio is generally lower. This makes GITs fit for other types of mission when compared to either the FEEP or HET, being typically more preferred for longer missions that have continuous thrust profiles, where the propellant ratio is a critical aspect such as in deep space probes like the Hayabusa spacecraft [32] or very-low earth orbit drag compensation for scientific missions such as the GOCE [33].

1.2.2 Gridded ion thrusters

The modern concept of gridded ion thrusters or sources appeared in the late 1950s for applications both in propulsion and industrial material processing [34]. Notably, the concept was developed by Harold Kaufman at NASA where he developed a variation that is today called the Kaufman-type GIT [35].

The general architecture of a GIT is shown in figure 1.4 and consists mainly of three different parts (labeled A, B, and C in the figure). The first (A) is the plasma generation section, which consists of a chamber where gas is injected and a plasma generation process is used to ionize the gas and maintain a discharge within the cavity. Different plasma generation methods are used with different advantages, the main ones being electron bombardment [36], electron cyclotron resonance (ECR) [37], and inductively coupled plasmas (ICP) [38]. The electron bombardment method consists of using an internal electron source, typically a hollow cathode, to generate a DC discharge between the cathode and an internal anode. Commonly a cusped magnetic field is applied between the two electrodes to decrease the electron mobility between them and enhance the

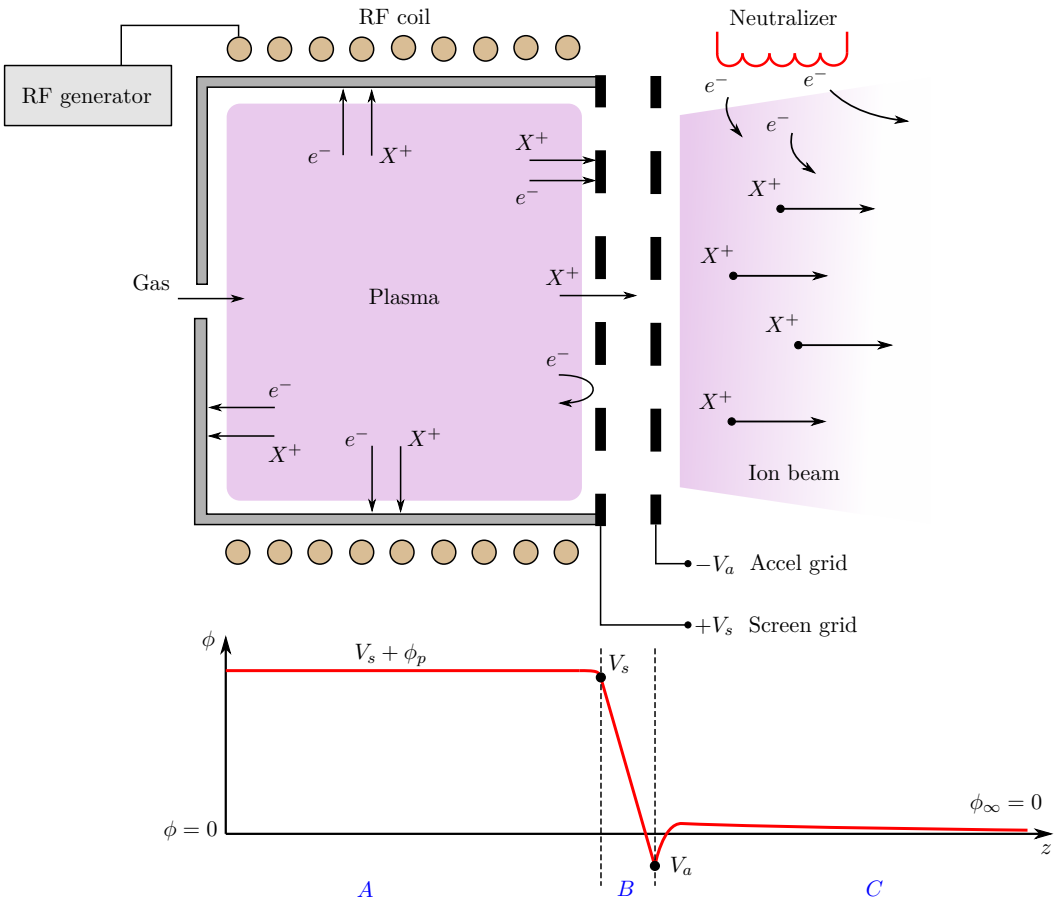

Figure 1.4: Schematic of the cross-sectional view of a radio-frequency gridded ion thruster and a qualitative profile of the electric potential in the axial direction.

ionization of the gas. Thrusters using this method are also called generically ring-cusp fields and this is one of the most traditional methods of plasma generation; there are numerous examples of successful missions using this type of ionization such as the Deep Space 1 probe [39], and the Dawn spacecraft [40]. The ECR method consists of applying a static magnetic field in conjunction with a microwave antenna to excite electrons in their cyclotron resonance frequency which in turn heats them and maintains ionization. Notable successful examples of systems using ECR are the thrusters used in the Hayabusa 1 and 2 missions [32, 41]. Lastly, the ICP consists of a discharge based on the inductive heating of electrons through the application of an RF field through a coil. In this discharge, the electric field generated by the varying axial magnetic field generates an oscillating azimuthal electron current which heats the plasma and sustains ionization by collisions and other effects [4, 42]. Despite a major part of the subsequent discussion being valid for any type of GIT, the text will focus mostly on ICP devices, since this was the plasma generation technique used throughout the work.

The second part (B) of a GIT, is the acceleration section. As shown in the figure, the plasma chamber is interrupted by a set of two or more grids; the first one which immediately touches the plasma is denoted the *screen grid*, the second is the *accel grid* and the third (if any) is the *de-accel grid* [14]. The screen grid is biased to a high positive potential, V_s, in the 0.5–4 kV range, so that the plasma potential reference is the screen grid and its potential is slightly higher than V_s relative to ground, i.e. $V_s + \phi_p$. The accel grid is biased to a slightly negative potential, V_a, in the -100–0 V range and the de-accel is left close to ground potential. At steady-state, plasma inside the cavity generates a steady flux of ions and electrons through the sheath to all walls of the chamber and the screen grid surface. Because of the strongly negative potential drop between the screen and the accel grids, as shown in the potential profile in the figure, only ions pass through the grid orifices while electrons are reflected back. The ions are then accelerated and leave the grid set at roughly the energy of the potential drop, $E_i \approx e(V_s + \phi_p - V_a)$ for a two-grid set, where it was considered that the ions start at rest inside the plasma. Since the electric potential goes to zero at infinity, and considering that $\phi_p \ll V_s$, the kinetic energy of ions leaving the system is approximately $E_i \approx eV_s$ and their speed is estimated as

$$u_i = \sqrt{\frac{2eV_s}{m_i}} \tag{1.47}$$

Despite the assumptions, this estimation finds good correspondence with real data since the magnitude of V_s is much higher than other potential energies of the system [14].

The contribution of thermal neutral particles to the overall thrust of a GIT is typically negligible. In this way, the thrust of a GIT can be estimated as $T = \alpha \dot{m}_i u_i$, where $\dot{m}_i$ is the mass flow of ions leaving the grid set, and α is a correction factor. Using equation 1.47 and noting that for singly-charged ions $\dot{m}_i = \frac{m_i}{e} I_b$, where I_b is the total ion current, the thrust can be written as

$$T = \alpha_c I_b \sqrt{\frac{2m_i V_s}{e}} \tag{1.48}$$

The factor α_c is commonly decomposed as a product of two different factors, γ which is a function of the beam divergence, and β which depends on the composition of the beam.

The third section of a GIT (C) is the plasma plume, which consists of the thruster's plasma exhaust. Since the thruster is continuously accelerating positive charges away from the spacecraft, the system must provide an equal current of negative charges so that the current-free condition is kept and the spacecraft is not charged [43]. This is done using an additional electron source, which is called the *neutralizer* or *cathode*. Furthermore, this neutralizer must provide the electron current in close proximity to the ion beam exit surface in order to maintain local quasi-neutrality and avoid space charge accumulation which could lead to beam stalling [44]. In this way, the plume is composed of several species, the energetic ion beam originating from the grids being the most important, thermalized electrons, and a population of slow ions that are created by downstream ionization and charge exchange [45]. In this context, the main reason to bias the accel grid negatively is to decrease the flux of electrons generated by the neutralizer going back to the thruster, called a backflow current. Since any upstream electrons entering an

accel grid orifice would immediately be accelerated by a strong electric field generated by the screen grid, any backflow current can generate a considerable power loss of the order of $P_e \approx I_{e,b}V_s$, where $I_{e,b}$ is the backflow current.

The ion beam leaving the thruster is not completely collimated and has a finite divergence which is quantified by the divergence half-angle θ_d and defined as $\cos\theta_d = \frac{I_a}{I_b}$, where I_a is the axial ion current crossing a given downstream surface that intersects the beam [14]. In this way, the angle θ_d quantifies the thrust loss due to particle trajectories that are not parallel to the thruster axis and its correction factor is

$$\gamma = \cos\theta_d \tag{1.49}$$

The thrust is also impacted by the presence of ion species that have a different mass to m_i and charge to e. Considering that all ion species are approximately monoenergetic, it is possible to show that the thrust is the sum of the contributions from each ion species n, as $T = \sum_n I_n\sqrt{2m_nV_s/q_n}$. Defining $Z_n = q_n/e$, $k_n = m_n/m_i$, and $\zeta_n = I_n/I_b$, the correction factor β can be written as

$$\beta = \sum_n \zeta_n\sqrt{\frac{k_n}{Z_n}}. \tag{1.50}$$

In this case, the value of m_i is assumed to be one of the dominant ion species and that this species has a single charge as this is the most common case.

Using equation 1.43 and the estimation of thrust from equation 1.48, the specific impulse of a GIT is estimated as

$$I_{sp} = \frac{\eta_m\gamma\beta}{g_0\beta'}u_i \tag{1.51}$$

where $\beta' = \sum_n \zeta_n\frac{k_n}{Z_n}$ and

$$\eta_m = \frac{\dot{m}_i}{\dot{m}} = \frac{I_b m_i}{e\dot{m}}\beta' \tag{1.52}$$

is called the *mass utilization efficiency* and computes the ratio of mass flow rate that is really used for acceleration compared to the total input mass flow rate. The power consumed to generate the ion beam does not correspond directly to the jet power computed in equation 1.45 since it is considered that only the ions contribute to the power consumption which can be computed as $\frac{1}{2}\dot{m}_i u_i^2$, that can be rewritten as

$$P_b = I_b V_s \tag{1.53}$$

Considering that the jet power is the power actually used to propel the spacecraft, a *beam efficiency* can be defined as

$$\eta_a = \frac{P_j}{P_b} = \eta_m\frac{\gamma^2\beta^2}{\beta'} \tag{1.54}$$

which computes the part of the beam power converted into beam kinetic power.

For an RF GIT, the plasma generation cavity is typically made of a dielectric material so that the fields can penetrate the chamber and the RF power is mostly transmitted to the plasma to sustain the discharge. During steady-state, it is necessary that an equal current of electrons and ions leaves the plasma through the sheath at every point of the dielectric wall so that there is no charge accumulation and that the voltage at a given point on the wall does not change over time. At the screen grid on the other hand there is a current imbalance, only ions can leave at the grid orifices, so there is a higher electron current to the screen grid surface to maintain charge balance. Since, at steady-state, the density of ions and electrons is not changing over time inside the plasma, the current of ions and electrons leaving the plasma must be the same, i.e. $\sum_n I_{e,n} = \sum_n I_{i,n}$. Considering that the subscript w refers to the current going to the walls and s going to the screen grid, current balance can be written as

$$I_{e,w} + I_{e,s} = I_{i,w} + I_{i,s} + I_b \tag{1.55}$$

$$I_{e,s} - I_{i,s} = I_b \tag{1.56}$$

which implies that the current measured at the screen grid power supply, $I_s = I_{e,s} - I_{i,s}$, is approximately equal to the total ion beam current. This estimation is widely used in experimental measurements since it gives a straightforward method to have an accurate quantification of the ion beam current.

Because the potentials at the screen grid and the accel grid are fixed and there are only ions flowing between them, there is a limit to the current that can be emitted by the thruster given by the Child-Langmuir law, in equation 1.34. Considering a single ion species, that the ions leave through an area $A_g = \eta_t A$ where A is the total area of the grid and η_t is called the grid transparency, the space-charge limited ion current flowing through the grids is

$$I_{\max} = \frac{4}{9}\varepsilon_0 \eta_t A \sqrt{\frac{2e}{m_i}} \frac{(V_s - V_a)^{3/2}}{L_{\text{eff}}^2} \tag{1.57}$$

where $L_{\text{eff}} = \sqrt{(t_s + L_g)^2 + r_s^2}$ is an effective gap, where t_s is the screen grid thickness, L_g is the grid gap and r_s is the radius of the screen grid orifices [14]. Therefore, using equation 1.48, the limit of the thrust density of a GIT with a single species ion beam is

$$\frac{T_{\max}}{A} = \frac{8}{9}\alpha_c \varepsilon_0 \eta_t \frac{V_s^{1/2}(V_s - V_a)^{3/2}}{L_{\text{eff}}^2} \tag{1.58}$$

It is worth noting that the thrust limit depends primarily on the maximum screen grid voltage attainable in the system and the geometry of the grids. However, both increasing the maximum screen grid voltage and decreasing L_{eff} after a given limit can pose important engineering problems due to the appearance of spurious electrical discharges, decrease of lifetime, and other phenomena [14]. Therefore, the engineering limitation of the operational range directly poses a ceiling for the performance obtained for these systems. The thrust density limitation of GITs typically implies that for high power systems, it is necessary to increase the total exit area of the propulsion system

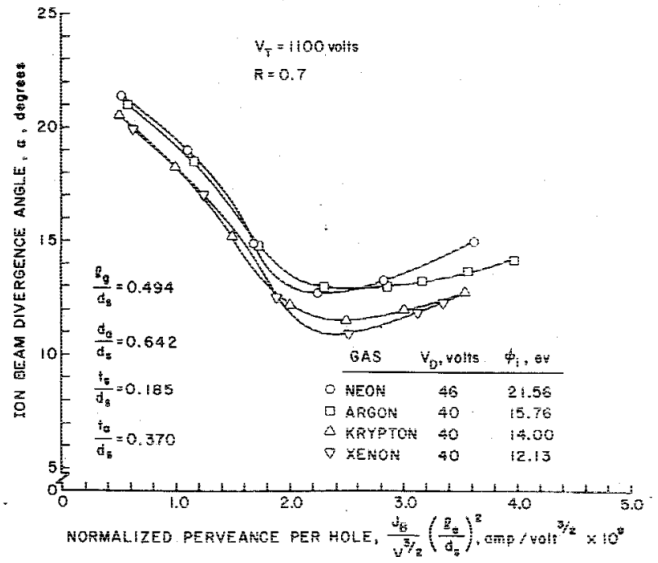

Figure 1.5: Ion beam divergence as a function of normalized perveance for different propellant gases (source: [48]).

as it was typically seen on early high-power prototypes [46]. Nowadays, technology advancements are allowing the construction of more compact high-power thrusters with more extreme operational ranges [47].

One of the fundamental aspects of the performance of a GIT is the correct geometrical design of its grid set. The format of the impact of the grid on several parameters of the system including its transparency η_t, the maximum attainable thrust, and especially the ion optics [14]. The potential field formed by the grid biases works as a set of lenses that focus the ions in an analogous manner to typical optical lenses. The design of a grid set is a complex problem and involves the use of specialized computational tools for the optimization of its geometry to a specific operating condition [49]. Aspects such as the modification of the bias values and the magnitude of the ion space charge between the grids, directly affect the ion trajectories and may increase their divergence or cause sputtering of the grids, decreasing the system's lifetime. The divergence of the ions for a specific grid set is mostly dependent on a quantity called the *perveance* [48] which is defined as

$$p_d = \frac{I_b}{V_T^{3/2}} \tag{1.59}$$

where I_b is the ion beam current and $V_T = V_s - V_a$. This quantity in fact is directly related to the Child-Langmuir law (eq. 1.34) and a maximum perveance is defined as

$$p_{d,max} = \frac{4}{9}\varepsilon_0\sqrt{\frac{2e}{m_i}}\frac{\eta_t A}{L_{\text{eff}}^2} \tag{1.60}$$

This value corresponds to the point where the ion space charge starts to be important

and deflects their trajectories. Figure 1.5 shows the measurement of ion beam divergence as a function of the normalized perveance, $p_d(L_{\text{eff}}^2/\eta_t A)$, for different propellants gases, made by Aston *et al.* [48]. In this case, the maximum normalized perveance is the smallest for xenon which is roughly $3.77 \times 10^{-9}\,\text{A/V}^{3/2}$, so it is important to note that the measurements were done below this value. The beam divergence curve generally follows the shape shown in the figure. First, there is an optimal perveance point at which the ions are focused and the value of the beam divergence is the smallest. Below this point is a regime called *under-perveance*, where the orifice sheath is pushed further inside the plasma in a concave shape and the ions may be accelerated in cross-over trajectories possibly hitting the accel grid; while above the optimal perveance, the regime is called *over-perveance* and causes the sheath to be flattened, accelerating ions directly towards the accel grid [14]. Therefore, to improve the grid set lifetime and increase the thrust generated by the system it is necessary to operate the system close to the optimal perveance point.

Another important aspect to consider when designing a GIT is the type of electron source used for the plume neutralization. These devices have typically a great complexity and are not very robust against air contamination or mechanical stress, serving as a potential life-limiting component. The three most used types of neutralizers are thermionic hot filaments [50], hollow cathodes [51], and plasma cathodes [52]. Thermionic filaments are one of the most traditional electron sources in physics and engineering since the late 19th century [53], and consist of a thin filament that is submitted to a high current that heats it to temperature levels where it can start to emit electrons thermionically, usually between 2000 to 3000 K. The thermionic emission can be estimated using Richardson's law, which has the form $I \propto T^2 \exp\left(-\frac{W}{k_B T}\right)$, where T is the filament's temperature, and W is the material's work function. Therefore, to improve emission, materials with low work functions are favored, one of the most typical being tungsten. Filament neutralizers are typically able to provide enough electron current with relatively low power consumption, however, their lifetime can be short due to material evaporation at high temperature, ion bombardment, and other mechanisms, with a usual lifetime up to 1000 h [50]. The hollow cathode is the most common type of neutralizer used in GITs and HETs and consists of a cylindrical device that contains a coaxial insert made of a material of low work function and a set of electrodes used to sustain a discharge inside the system with gas that is injected at one of the system's ends. This discharge is used to heat the insert via ion bombardment, which starts to emit electrons. The plasma creates as well a *plasma bridge* connecting the inner discharge to the beam, facilitating the transport of electrons to neutralize the plume. Literature reports that hollow cathodes have been proved to be capable of operating for up to 30 352 h [54], making them fit for demanding missions such as for deep space maneuvering. However, these systems are complex, require several additional power systems, and the insert materials used are susceptible to atmospheric poisoning making their handling more complicated than other cathodes [14]. Lastly, plasma cathodes are devices that have a cavity where typically an RF discharge is created and an additional inner electrode is used to increase the ion collection area and produce an excess of electrons which are then transmitted to the

plume through a plasma bridge. Plasma cathodes were tested using different types of discharges [55–57], and one of these systems, using microwave ECR heating, was operated during the Hayabusa mission [58].

1.2.3 RF grid biasing

Because of the complexity and additional power consumption of neutralization devices, several concepts to eliminate its need on GIT propulsion systems were researched over the last few years [59]. These neutralizer-free concepts can be divided into two types, the first is based on the acceleration of positive and negative ions by two different aligned sources [60], and the second is based on the co-extraction of positive and negative particles from the same plasma source through radio-frequency biasing of the grid set. The latter can be realized with either electronegative plasmas which emit negative and positive ions [61], or typical electropositive plasmas generating a beam of positive ions and electrons [62]. Between these concepts, the RF co-extraction of ions and electrons is one of the most promising, requiring limited modification for a typical GIT, using the same propellants, and presenting promising preliminary performance results [62–65].

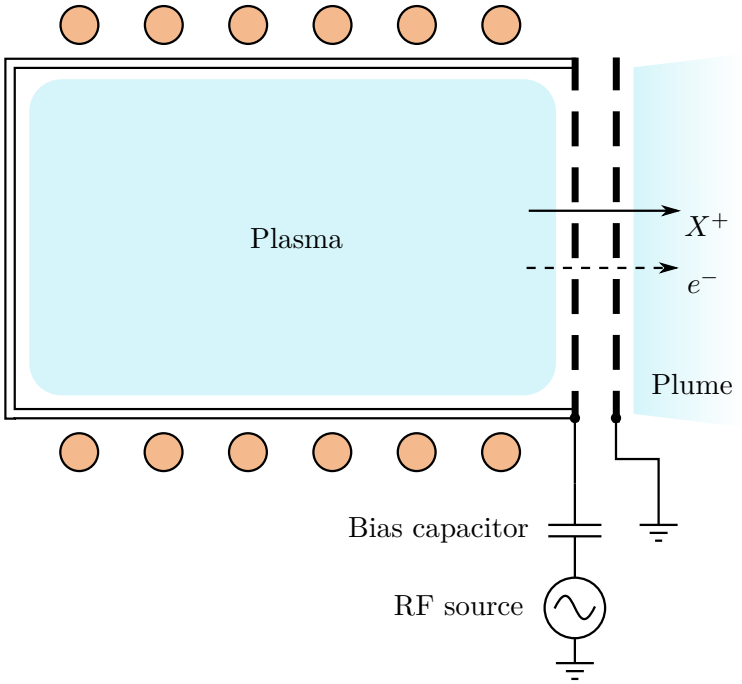

Figure 1.6: Schematics of a GIT with RF grid biasing.

Figure 1.6 shows the basic architecture of the co-extraction of ions and electrons using RF grid biasing. The discharge is generated with a given plasma production method, the most common being an ICP discharge. Instead of using a constant bias, a high-voltage RF signal is applied to the screen grid through a so-called *bias capacitor*, while the accel grid is connected to ground. The currents of ions and electrons to each grid are modeled

similarly to an asymmetric capacitively coupled plasma (CCP). Because the effective area of each grid seen by the plasma is different, a DC bias forms at the bias capacitor so as to ensure equal currents of ions and electrons at each grid [4, 66]. Because this DC bias is formed, the resulting voltage waveform applied to the screen grid is similar to a shifted sinusoidal curve. If the frequency of the signal is high enough, ions are accelerated almost continuously by the DC bias and whenever the voltage gets close to zero electrons can escape in a pulse. Therefore, instead of an external current, the ion beam in this case is neutralized by a pulsed electron current originating from the thruster itself.

The RF biasing technique was studied in several experimental works [62–65, 67], and a theoretical model for the estimation of the self-bias and the modeling of the particle currents for RF biased grids was proposed by Lafleur and Rafalskyi [66] with successful validation by simulation investigations. This model is described below for reference during the present work. At steady-state, it is considered that the time-averaged currents of ions and electrons at the screen grid must be equal and can be written in the form

$$I_i^s = en_0 u_B A_i^s \tag{1.61}$$

$$I_e^s = \frac{1}{4} en_0 \bar{v}_e A_e^s \exp\left(-\frac{\phi_{sh}}{T_e}\right) \tag{1.62}$$

where n_0 is the bulk plasma density inside the discharge chamber, A_i^s and A_e^s are the screen grid areas seen by the ions and electrons respectively[2], and ϕ_{sh} is the potential drop of the sheath. The ion current going to the accel grid is due mostly due to charge-exchange ions formed in the plume, $I_i^a = \alpha I_b$ where α is the rate of slow ions formed for a given ion total ion current, and the electron current is given by

$$I_e^a = \frac{1}{4T} en_0 \bar{v}_e A_e^a \int_0^T \exp\left(-\frac{\phi_u(t) - V_a}{T_e}\right) dt \tag{1.63}$$

where the V_a is the potential at the accel grid, A_e^a is the accel grid area seen by the electrons, $T = 2\pi/\omega$, $\phi_u(t)$ is the potential at the bulk upstream plasma and is estimated as $\phi_u(t) = \phi_{sh} + V_{sb} + V_{RF} \sin \omega t$, where V_{RF} is the amplitude of the RF bias outputted from the power supply. These equations can be solved for the self-bias voltage, giving

$$V_{sb} = T_e \left\{ \ln\left[I_0\left(\frac{V_{RF}}{T_e}\right)\right] - \ln\left[\frac{\alpha \eta_t A_e^s}{(1-\eta_t) A_e^a}\right]\right\} \tag{1.64}$$

where I_0 is the modified Bessel function of the first kind and η_t is the grid transparency. Despite being non-trivial, the strongest dependence of V_{sb} is on V_{RF}, and for $V_{RF} \gg T_e$, the self-bias voltage is reduced to $V_{sb} \approx V_{RF}$. Previous experimental results show that $V_{sb} \approx 0.8 V_{RF}$ for RF amplitudes between 0 and 350 V [62].

For the ions to be effectively undisturbed during their trajectory between the grids, the signal period must be much faster than their transit time across the grid gap length. For ions starting at rest and neglecting the effect of their space charge between the grids,

[2] See ref. [66] for further details on the estimation of A_i^s, A_e^s and A_e^a.

this transit time is given by $\tau = \sqrt{2L_{\text{eff}}^2 m_i / 2V_{sb}}$, and so the frequency must satisfy the condition

$$f \gg \frac{1}{L_{\text{eff}}} \sqrt{\frac{eV_{sb}}{2m_i}} \tag{1.65}$$

If this conditions is satisfied, and if it is assumed that $\phi_{sh} \ll V_{sb} + V_{RF}$, the ion leaves the grid set at an average energy given by $\langle E_i \rangle = e \langle \phi_u \rangle \approx eV_{sb}$, with an average speed

$$u_i = \sqrt{\frac{2eV_{sb}}{m_i}} \tag{1.66}$$

If the frequency requirements are met, the ion beam current leaving the thruster is approximately the same as in the case of a typical DC, given by

$$I_b = en_0 u_B \eta_t A \tag{1.67}$$

where A is the total area of the grid. The electron current emitted by the thruster can be estimated considering that, at every instant of the RF cycle, their density can be estimated using the Boltzmann relation. This way, the time-averaged electron current escaping the grids is

$$I_e = \frac{1}{4T} en_0 \bar{v}_e \eta_t A \int_0^T g(t) dt \tag{1.68}$$

where $g(t) = \exp\left(-\frac{\phi_u(t) - \phi_a^h(t)}{T_e}\right)$ for $\phi_u(t) - \phi_a^h(t) > 0$ and $g(t) = 1$ otherwise. The $\phi_a^h(t)$ is the potential at the center of the accel grid orifice and is a superposition of several components. If $V_a = 0$, the central potential can be expressed as $\phi_a^h(t) = \phi_s(t) + \phi_{sc}(t) + \phi_d(t)$, where ϕ_s is the potential contribution due to the penetration of the screen grid potential, ϕ_{sc} is the ion space charge contribution and ϕ_d is the penetration of the downstream plume potential. The precise determination of these contributions is not trivial and requires a full solution of the problem, however estimations can be done using a method similar to that used in DC thrusters [14].

Despite being a promising concept, potentially eliminating the need for an additional electron source, the RF grid biasing technique still requires further study for a more precise understanding of several mechanisms taking place during its operation. The RF signal and pulsed electron current injected into the plume create a global oscillatory dynamic to the system which leads to phenomena not easily modeled by theory. Its dynamical behavior makes computational simulations much more challenging as well, requiring typically fully kinetic approaches, special boundary conditions, and a high computational cost. In this context, simulations performed up to now [66, 68] had to be limited to one grid orifice of the system, which did not allow the study of the interaction of the acceleration and the downstream plasma expansion or a complete picture of the modeling of the acceleration of the particles. Furthermore, previous experimental work [62, 65] already verified several phenomena which are not present in typical DC thrusters, such as strong energy anisotropy in the electron population in the plume, higher plume potentials, between others, all of which are not predicted by theory. Therefore, to advance this

concept to a fully functional system that can be eventually tested in space, it is necessary to further develop the modeling of the thruster through numerical and experimental work so that the negative impact of the additional operational characteristics found in this type of thruster can be minimized and its performance optimized.

1.2.4 Iodine as a propellant

Another aspect of GIT propulsion systems that can be the subject of important optimization is the type of propellant used. Propellant gases must meet a number of criteria in terms of performance, storage and cost to be considered feasible for a propulsion system:

1. *Performance*: its main aspect is the characteristics, in terms of mass and charge, of the dominant ion population that is accelerated during the operation. Observing equations 1.48 and 1.47, it is possible to see that $T \propto \sqrt{m_i}$ and $I_{sp} \propto 1/\sqrt{m_i}$. Since GITs typically generate high levels of specific impulse due to their voltage operational range, historically designers have preferred to maximize m_i, decreasing the I_{sp} to maximize the thrust [69]. Another important characteristic is the amount of energy required for ionization of a neutral propellant particle. In this sense, it is important to analyze the ionization energy, E_{iz}, and the cross sections of the atoms or molecules of the propellant and also, in the case of molecules, its structural complexity, since this may lead to energy losses due to vibrational modes or dissociation processes [42, 70].

2. *Storage and filling conditions*: gases typically need to be stored in high-pressure tanks that can be massive, voluminous, and may require additional high-pressure piping for flow management [71]. Therefore, propellants that can be stored under low-pressure conditions are desired for the overall propulsion system design and to facilitate its handling during the filling process.

3. *Reactivity*: certain propellants might present several types of chemical reactions with the materials in direct contact with it in the propulsion system or with other spacecraft components. Therefore, inert propellants require less engineering effort in this aspect. In contrast, this chemical compatibility must be accounted with reactive propellants to guarantee a safe operation of the propulsion system and avoid damaging the spacecraft.

4. *Cost*: the requirement to increase the performance of a given propulsion system, maximizing its I_{sp}, is driven primarily by the financial limitations of the mission. A decrease in the required propellant for a mission or the ability to increase the amount of propellant available (potentially increasing the mission lifetime) has a direct impact on the mission cost due to factors such as launch cost. Therefore, an increase in the propellant cost might in fact decrease the "financial performance" of the propulsion system, since a worse but cheaper propulsion system might be more advantageous from a high-level project view [72].

The most used propellant in GITs and other thrusters such as HETs is xenon [14]. Xenon is one of the heaviest elements in the periodic table ($m_i \approx 131.29\,\mathrm{u}$), it is stable as an inert atomic gas, and has relatively low ionization energy ($E_{iz} \approx 12.13\,\mathrm{eV}$) [73]. On the other hand, xenon is considerably expensive (2500 €/kg for propulsion grade [69]), and its storage usually must be done at high pressures (100 to 500 bar). Apart from requiring a pressure vessel, the high-pressure storage of xenon increases the risk during ground handling which can increase the operational cost of the propulsion system. Furthermore, the cost of xenon is continuously increasing over the years due to higher demand from other industries, such as the medical and semiconductor industries, and a lower level of stock availability [74].

Because of the drawbacks of xenon, several alternatives were researched and proposed over the years. Recently, this research gained further traction due to the appearance of a large number of new satellite and constellation missions using electric propulsion, thus requiring cheaper and more abundant propellants to be feasible. In this context, one the alternative propellants being used is krypton, which is being employed by the Starlink constellation for example, and is cheaper (225 €/kg for propulsion grade [69]) but lighter ($m_i \approx 83.79\,\mathrm{u}$) than xenon. In parallel, in recent years several studies have been dedicated to the use of iodine as a propellant which shows promising results to address several of the problems with xenon. At room temperature iodine is stable as a solid crystal with a melting point at 113.7 °C, and as a gas, it is stable as a diatomic molecule (I_2). Iodine has an atomic mass close to xenon ($m_i \approx 126.90\,\mathrm{u}$), lower ionization energy ($E_{iz} \approx 10.45\,\mathrm{eV}$ for I and $E_{iz} \approx 9.41\,\mathrm{eV}$ for I_2), and lower cost (50 €/kg [69]). Because iodine is solid at room conditions, its storage density ($4.9\,\mathrm{g/cm^3}$) is roughly three times higher than xenon ($1.6\,\mathrm{g/cm^3}$) at 80 bar and the system's storage tank can be simplified without the need for high-pressure capabilities, decreasing the dry mass, volume, and cost. Furthermore, since iodine gas is molecular, during a discharge there is a rate of production of molecular ions (I_2^+) which has double the mass of single ions ($m_i \approx 253\,\mathrm{u}$) which can lead to an increase in thrust as shown in equation 1.50.

Despite its advantages, iodine has a strong reactivity and non-trivial chemistry, especially when in the plasma state. Due to the growing interest in iodine plasmas, several works have been performed over the last few years including experimental investigations [75, 76], global modeling [70, 77], and numerical simulations [75, 78] to elucidate these dynamics. However, despite these efforts, there are still a number of aspects of iodine plasma not available in the literature, such as several physical properties, collision cross-sections, and surface chemistry characterization among others.

1.3 Plasma plumes

A plasma plume is a jet of plasma that is typically an exhaust from a natural or artificial process expanding in free space. This plume can have different characteristics, such as the presence, or not, of magnetic fields or particle beams, and they display complex physical behavior that is often not solvable by a purely analytical approach. Examples of plasma plumes are found in many different situations of physics and engineering, some cases

are solar wind interaction with astronomical bodies [79], ion beams used for material science [80, 81], mass spectrometry [82], plasma jets for medical applications [83], and the exhaust of electric propulsion systems. In the context of electric propulsion, the study of plasma plumes has great importance in many areas, including the mitigation of the damage caused by its interaction with other parts of the spacecraft, control of the neutralization process to guarantee the correct operation of the system and to protect against possible backflow of energetic particles that may damage the propulsion system. In some special cases, the plume may also be used for other purposes such as a jet to thrust other bodies for applications such as the de-orbiting of space debris [84].

One of the main goals of the present work is to further study phenomena taking place in a GIT plume. Therefore the focus in this section will be on plumes in conditions similar to those found in typical thrusters, with plasmas consisting of hot electrons, with $T_e = 1\,\text{eV}$ to $10\,\text{eV}$, and fast cold ions, with $T_i \approx 300\,\text{K}$ and supersonic drift velocities $u_i \geq u_B$ in the direction of the exhaust.

1.3.1 Free plasma expansion

The most basic problem to understand the evolution of a plume in space is the free expansion of a plasma body with no ion drift velocity. Since a plume consists of a jet of plasma moving directionally away from an origin, if one follows a perpendicular "slice" of the particles as they move with a given drift velocity, often their behavior in the radial direction will resemble what is observed in the temporal evolution of a group of particles expanding freely from a given initial condition – especially if the ion drift velocity is much higher than their thermal velocity. In the literature, the study of freely expanding plasmas appears mainly in the context of pulsed laser plasmas used for fusion and material science research [85]. In this application, short laser pulses are used to ionize and heat a small region of material creating a concentrated plasma bunch that expands outwards on a nanosecond time scale. Although the conditions found in these experiments are not the same as what is found in propulsion plumes, nonetheless, their modeling and some of the effects observed can be relevant to the present case.

The modeling of free expansion is often limited to a one-dimensional analysis and several assumptions are made to simplify the analytical solution of the problem. The model presented, for example, by Crow *et al.* [86] and later extended in other works [79, 87], assumes an initial condition such that the ion density $n_i(x) = n_0$ for $x < 0$ and $n_i(x) = 0$ otherwise, and with temperature $T_i \approx 0$. Electrons are assumed to be collisionless, with a temperature T_e and always in thermal equilibrium such that they follow the Boltzmann relation (eq. 1.12). Using the two-fluid plasma model shown in section 1.1.2, it is possible to obtain the set of equations for this problem as

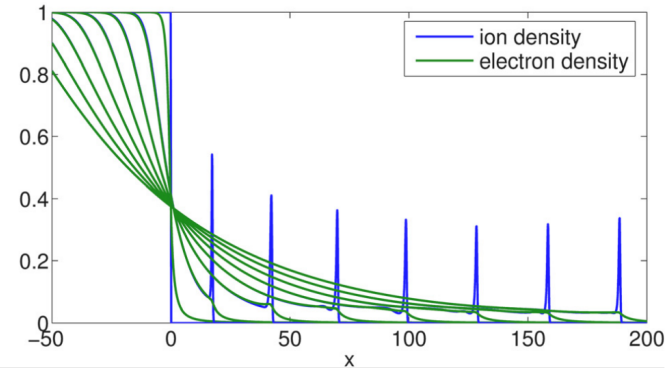

Figure 1.7: Profile of ion and electron density for a 1D free expanding plasma. The different curves show the profiles for different moments in time. (source: [88]).

$$\frac{\partial u_i}{\partial t} + u_i \frac{\partial u_i}{\partial x} = -\frac{e}{m_i}\frac{d\phi}{dx} \tag{1.69}$$

$$\frac{\partial n_i}{\partial t} + \frac{\partial}{\partial x}(n_i u_i) = 0 \tag{1.70}$$

$$n_e = n_0 \exp\left(\frac{\phi}{T_e}\right) \tag{1.71}$$

$$\frac{d^2\phi}{dx^2} = \frac{e}{\varepsilon_0}(n_i - n_e) \tag{1.72}$$

An example of the solution reproduced from ref. [88], is shown in figure 1.7 displaying a series of characteristics typical for this type of expansion. Initially, as shown in figure 1.8, due to the different ion and electron density at the edge of the plasma a positive electric field appears. This electric field accelerates ions towards the positive direction of x forming an *ion front* which propagates to the right. As time evolves, the line dividing the region of static ions and the population that is being accelerated moves to the left and is called the *rarefaction wave*. In this case, the wave travels at the ion sound speed, $u_B = \sqrt{eT_e/m_i}$ [79]. Between the rarefaction wave and the ion front, ions are continuously accelerated due to a decrease of the electron density close to the plasma edge which pushes ions outwards, and the presence of an electron cloud outside of the plasma which pulls the ions at their front by what is called an *ambipolar field*.

As explained by Allen and Perego [88] and shown in figure 1.7, for certain initial ion spatial distributions a ion density spike may be formed in the ion front. It is shown that the peak is a result of the slope of the ion density going n_0 to zero at $t = 0$. As shown in figure 1.8, when there is a slope, the electric field peak is behind the ion front, causing an accumulation of ions at the edge of the expansion as the system evolves in a process called wave breaking [89]. In the present simplified case, there is a discontinuity of n_i at $x = 0$ therefore no ion peak should exist. Nevertheless, due to limitations in the numerical mesh and accuracy of the method used to solve the system of equations the

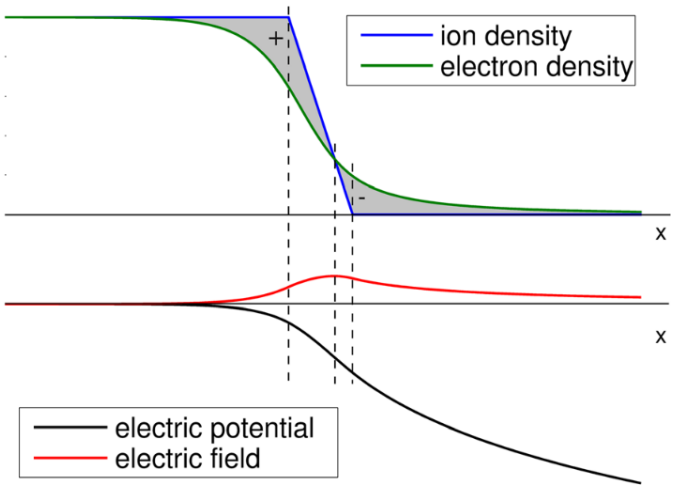

Figure 1.8: Profile of density, potential and electric field for a free expanding plasma (source: [88]).

peak may appear due to an "artificial" density slope. In applications and more realistic analyzes, however, it is more probable to have smoother transitions in the ion density thus facilitating the appearance of ion density peaks at the front.

Despite providing insight into the free expansion mechanics, the present model is not adequate enough to explain many phenomena due to its assumptions, namely of electrons in thermal equilibrium always following a Maxwellian distribution and the absence of collisions [87]. In real expansion cases, during the ion acceleration process, the distribution of electrons may continuously change due to the energy transfer process from electrons to the ion population and the cooling of the electrons. On the other hand, whenever the collisional processes in the electron population are important and cannot be ignored, the expansion ceases to be dominated only by the ambipolar fields and behave similarly to a typical gas expansion. In these cases, when these effects are important, it is typically necessary to adopt a fully kinetic analytical or numerical approach to model the plume.

1.3.2 Ambipolar plasma plume

Different thruster concepts, such as the ECR thruster, use the ion acceleration caused by the plasma expansion as their main mechanism to generate thrust [90]. These so-called "expanding-plasma thrusters" shown schematically in figure 1.9, consist typically of a cylindrical discharge chamber with an open-end where an RF plasma is generated. The open end allows the plasma to flow out of the chamber and expand into vacuum. The expansion of the thruster's plume is dominated by the ambipolar fields that transfer energy from the hot electron population to the ion flow in a similar manner to what was described in the simplified one-dimensional case. However here, in contrast, at steady-state, the problem is not time-dependent and the expansion has only a spatial

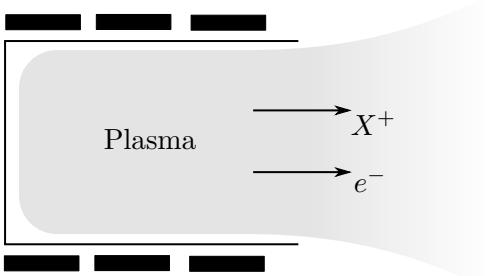

Figure 1.9: Schematic of a generic expanding-plasma thruster.

dependency and the fields and acceleration are a consequence of the pressure and potential gradients at different spatial positions. Here the expansion is as well intrinsically a two (or three)-dimensional problem, in which the expansion characteristics have a direct impact on the performance of the thruster.

The modeling of this type of plume is typically done using a fluid model approach in a similar way to the one-dimensional case and solving it through a numerical approach or techniques such as the self-similar method [91]. In the simplest case, a so-called "spherical expansion" is assumed, where the flux decays as $nu \propto 1/r^2$, with a relative successful agreement with experimental data [92]. To provide a closure for the equations, many different fluid models, including this one, use the assumption of isothermal electrons, thus adopting the Boltzmann relation. However, this assumption entails that electrons have an infinite amount of energy so that ions are accelerated to velocity values that diverge and go to infinity. For small, truncated domains, this effect might not create any issues, however, in the case of a thruster's plume, it is important to determine the final energy of ions and properly model the expansion of the plume at far distances so that the behavior and performance of the system can be predicted. The proper modeling of the electron cooling mechanisms has been the focus of numerous works over the past few years [93, 94]. One solution, given by Merino and Ahedo [95], is to assume a polytropic law in the form

$$\frac{T_e}{T_0} = \left(\frac{n_e}{n_0}\right)^{\gamma_e - 1} \tag{1.73}$$

where γ_e is the polytropic coefficient, and T_0 and n_0 are respectively the electron temperature and density at the thruster's exit. Using this law, the fluid model can be solved to yield a plume potential drop of $\phi_p = -T_0 \frac{\gamma_e}{\gamma_e - 1}$ and thus a maximum ion energy of $E_{i,f} = T_0 \left(\frac{1}{2} + \frac{\gamma_e}{\gamma_e - 1}\right)$. Despite providing a good estimation of the terminal ion energy, the polytropic law introduces the parameter γ_e which needs to be experimentally determined and can be sensitive to changes in the operational conditions. A model later proposed by Lafleur *et al.* [94] solves the dependence on γ_e by analyzing the current free condition on the expansion. In their model, the plume potential drop and final ion energy

is written as

$$\phi_p = -\frac{T_0}{2}\ln\left(\frac{m_i}{2\pi m_e}\right) \tag{1.74}$$

$$E_{i,f} = \frac{T_0}{2}\left[1 + \ln\left(\frac{m_i}{2\pi m_e}\right)\right] \tag{1.75}$$

This way, this model permits as well the estimation of the polytropic coefficient as $\gamma_e = C/(C-2)$, where $C = \ln\left(\frac{m_i}{2\pi m_e}\right)$. This estimation for xenon is around $\gamma_e \approx 1.23$, which agrees well with what is measured in experiments [94]. As can be seen from equation 1.75, the total ion acceleration is directly proportional to the electron temperature of the upstream plasma. Therefore, in this type of thruster, it is generally necessary to maximize the operational electron temperature of the discharge to improve performance.

One critical point in this type of expansion is that, since the ion acceleration occurs in a non-directed fashion along the plume, their typical beam divergence values are considerably higher when compared to other thrusters where the majority of ions are accelerated axially and leave the thruster close to the nominal velocity. As for other systems, the thrust in this case is estimated as $T = \cos\theta_d \dot{m}_i u_i$, where θ_d is the divergence angle of the plume. This angle can be estimated as $\cos\theta_d \approx \sqrt{2T_0/E_{i,f}}$ [94], in this way, the divergence dependence is largely on the mass of the ions used and the electron temperature of the plume. Using equation 1.75 for xenon we have, $\theta_d \approx 53.94°$ which corresponds to a 41.2 % loss of thrust. To decrease the divergence, a commonly adopted strategy is to use a system called a "magnetic nozzle", which consists of a divergent magnetic field configuration generated by a set of magnets installed around the exit of the thruster [95–97]. The principle of the magnetic nozzle is to act as a guide to the plasma flow, allowing it to expand along the field lines, focusing the expansion forward and reducing beam divergence before the plasma detaches from the magnetic field.

1.3.3 Hypersonic plasma plumes

The plume generated by an ion thruster is similar to an ambipolar plume in some sense. However, their key difference is that in the GIT case, the ions do not enter the plume close to their sonic speed, u_B, but at a much higher energy, determined especially by the screen grid potential. Using equation 1.47 for the exhaust ion speed, it is possible to define an ion Mach number as

$$M = \frac{u_i}{u_B} = \sqrt{\frac{2V_s}{T_e}} \tag{1.76}$$

Screen grid voltages in the range of 1 kV to 2 kV and an electron temperature of 5 eV give Mach numbers in the range of 20 to 28. Therefore, the plumes generated by gridded ion thrusters are commonly considered as *hypersonic* [98]. In this case, the radial and axial ambipolar fields created by the electron expansion have much less impact on the trajectory of ions, and the energy transferred from the electron population to the ions is much smaller than the initial ion energy. In contrast with ambipolar plumes, because the

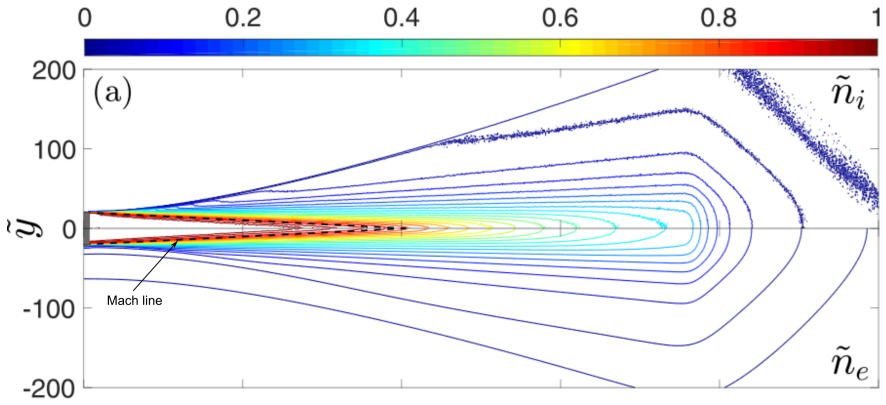

Figure 1.10: Contour plot of a typical hypersonic plume simulation showing normalized values of ion (top) and electron (bottom) densities (adapted from Ref. [100]).

thrust, in this case, is mainly dependent on the ion acceleration taking place at the grid set, it is typically more desired to operate at lower electron temperatures in the plume since radial ambipolar fields may increase the beam divergence [99].

Figure 1.10 shows the contour plot of a typical hypersonic expansion from the simulation work by Wang and Hu [100]. Different aspects may be noted from the structure of the plume. The first is the presence of a triangular region, called the *Mach cone*, marked with a dashed line in the figure. This cone defines the boundary of a rarefaction wave traveling radially in the direction of the axis starting at the boundary of the beam when the beam exits the thruster. Because the ions are cold and hypersonic, their thermal expansion in the radial direction is considerably slower than their axial displacement (by a factor M). Therefore, along the plume, the radial expansion resembles what is seen in the 1D free plasma expansion described in section 1.3.1 [99]. Hu and Wang [99] show that there is a very good correlation between radial expansion using a hybrid 2D simulation of a plume and the 1D semi-infinite expansion modeled by Mora [101]. Within the Mach cone, the ion beam is unperturbed and outside the ions are dragged by ambipolar fields created by the electron population. The half-angle of the Mach cone (also called the Mach angle), between the dashed line and the axis of the plume, can be estimated by considering that the rarefaction wave travels at the sonic speed in the radial direction. In this way, if all ions are moving downstream at u_i, this angle is

$$\tan\theta_M = \frac{1}{M} \tag{1.77}$$

and its length is $l_M = MR$, where R is the radius of the beam exit. Despite the unique plasma dynamics, the hypersonic plume expansion close to its injection region has similar features to a supersonic gas flow expansion [102]. Specifically, in the region just downstream of the Mach cone, the structure is similar to a Prandtl-Meyer expansion fan. However, closer to the radial boundaries, there is the formation of ambipolar fields which accelerate the ion front outwards while cooling electrons and creating the non-straight

divergence pattern seen in the figure. The value of the final radial ion velocity of the front is computed to be $u_{i,y}/u_B \approx 7$ to 8 depending mostly on $\sqrt{m_i/m_e}$ [99]. In the axial direction, the influence of the expansion is less pronounced and ions are accelerated mostly due to the plume potential drop from the exit region to zero. Using the same approach from Lafleur *et al.* [94] it is possible to estimate the plume potential for the hypersonic case. However here, instead of having ions injected at their acoustic speed, they are injected at $u_i \approx \sqrt{2eV_s/m_i}$. In this case the plume potential drop can be estimated as $\phi_p \approx -\frac{T_e}{2} \ln\left(\frac{m_i}{4\pi m_e}\frac{T_e}{V_s}\right)$. For xenon, $V_s = 1\,\text{kV}$ and $T_e = 5\,\text{eV}$, the maximum potential is $|\phi_p| \approx 11.3\,\text{V}$, which is roughly what is expected in real GIT plumes [91]. Numerical investigations have shown as well that due to the electron cooling process at the edge of the plume, their velocity distribution functions start to present an important anisotropy and drift components at these locations [103]. This aspect can be incompatible with typical assumptions made in theoretical models that treat the electron population using, for example, the Boltzmann relation.

One of the most important characteristics of a plume is its divergence due to its direct impact on the thrust value. In the hypersonic case, it is possible to note that the divergence has two main components: the acceleration process and the plasma expansion. The acceleration component was described in section 1.2.2 and consists of the angular distribution of the ions caused by the grid optics as they leave the thruster. The second component is due to the plasma expansion caused by the electron population present in the plume, both injected by the neutralizer and produced in the plume by chemical processes. Therefore, even if we consider an ideal thruster grid set that injects ions exactly in the same direction, the electron ambipolar fields cause the beam to spread downstream. It is noted, for example, that the beam shown in figure 1.10 does not have an initial angular spread as it is injected and nevertheless presents a non-negligible divergence. However, because of conservation of momentum only the divergence produced during the acceleration process impacts on the thrust generated by the system, since downstream of the grids, no further thrust can be transferred to the system in the absence of any magnetic fields. Nevertheless, despite the divergence generated downstream by the expansion process not directly impacting system performance, it can still increase plume-spacecraft interactions and other similar phenomena.

The complete modeling of the hypersonic plume expansion has been the focus of many different research efforts over the years. One of the first models to appear was proposed by Parks and Katz [104] and consists of a fluid model using a self-similar solution. This model describes the expansion of an isothermal gaussian beam, such that at every axial position one has

$$n_i(r) = \frac{n_0}{h(t)^2} \exp\left(-\frac{r^2}{2R^2 h(t)^2}\right) \tag{1.78}$$

where R is the initial width of the beam, $h(t)$ is a function that describes the radial plasma expansion in time, and the time can be transformed to axial position by considering a constant axial ion velocity, $t = z/u_z$. It is shown that h can be determined by solving

$$\frac{dh}{dt} = \frac{u_B}{R}\sqrt{2\ln h} \tag{1.79}$$

and its solution can be approximated as $h(t) \approx 1 + 0.6524\tau + 0.0552\tau^2 - 0.0008\tau^3$, where $\tau = \sqrt{2}\frac{u_B}{R}t$ [14]. It is interesting to note that the result obtained in equation 1.79 is similar to the 1D isothermal expansion of a gaussian plasma profile given by Mora [105], apart from the differences due to the use of cylindrical and Cartesian coordinates. Ignoring the higher order terms of h and making a simple approximation for the divergence angle as $\tan\theta_d \approx \frac{h(t)-h(0)}{u_z t}$, it is possible to see that $\tan\theta_d \sim \sqrt{T_e/V_s}$, showing, as expected, that the expansion divergence grows with the electron temperature and decreases with the energy of the ions. Over the years, several other analytical formulations were proposed including fluid [98, 106, 107], kinetic [93, 99, 100] and hybrid [100, 108] models. As in the case of the ambipolar expansion, one of the biggest challenges addressed by these models is also the process of electron cooling, which is still the subject of active research. Due to the complexity of the problem, currently, the analysis of the plume expansion is commonly done through a numerical approach using methods such as particle-in-cell (PIC), hybrid-PIC, and other methods for solving partial differential equations.

1.3.4 Neutralization and chemistry

Because the GIT exhaust consists only of a beam of high-energy ions, it is necessary to provide an electron flux so that current balance is kept and the plume remains quasi-neutral at every location. This electron current is provided by a neutralizer, and the characteristics of the electron population, such as its temperature, and thus the plume expansion, are dependent on the characteristics of the external source used. Peralez-Díaz *et al.* [109] describe the process of beam formation and neutralization through a series of hybrid-PIC simulations of the grid and near-plume regions. The authors show, for example, that the current of electrons emitted and their trajectories are sensitive to the positioning of the neutralizer but, as long as there is enough current to the main beam, the ion trajectories are not affected by this positioning or the asymmetric location of injection of electrons. Another important aspect of the neutralization is the formation of the plasma sheaths at the interface between the plume and the external grid. This sheath together with the natural plume potential drop towards infinity traps a certain electron population within the plume guaranteeing that the plume remains quasi-neutral. This sheath is also affected by the negative bias that is usually applied to the accel grid that increases the potential well between the plume and the accel grid and prevents an excessive current being drawn from the neutralizer [14]. The neutralizer typically sits at a negative but higher potential than the accel grid, so that electron extraction is facilitated but electrons are not attracted to the thruster.

Considering the ion beam, the electrons injected from the neutralizer and the remaining neutral population that escapes from the thruster, a series of collisional reactions typically take place within the plume during expansion. However, because the neutral particles leave the thruster at their thermal speed, their density in the plume can be significantly higher than ions and electrons, and thus the collisional processes between charged and neutral particles are typically much more dominant than reactions between charged species. To provide a comparison, it is possible to estimate the ratio of neutral to ion density at the exit of the thruster. Considering a mass utilization efficiency η_m, the neutral gas

mass flow rate in the exhaust is approximately $\dot{m}_g = (1-\eta_m)\dot{m} = \frac{1}{4}mA_g n_g\sqrt{8eT_g/\pi m}$, while the ion mass flow rate is $\dot{m}_i = \eta_m\dot{m} = mA_i n_i\sqrt{2eE_i/m}$. In this way, the density ratio at the thruster's exit is roughly

$$\frac{n_g}{n_i} = \frac{1-\eta_m}{\eta_m}\sqrt{4\pi\frac{E_i}{T_g}} \tag{1.80}$$

where T_g is the neutral gas temperature in electronvolt, and $A_i \approx A_g$ was assumed. For $T_g = 300\,\mathrm{K} \approx 0.025\,\mathrm{eV}$, $E_i = 1\,\mathrm{kV}$ and $\eta_m = 0.5$, this ratio is $n_g/n_i \approx 708.97$. In this context, two of the most important effects of the reactions between charged and neutral particles are the thermalization due to elastic and inelastic collisions and the formation of a low-energy ion population, which change the neutralization process and may flow back to the spacecraft or damage the thruster due to their backstreaming current that gets accelerated by the accel grid sheath [45]. Often common sense is that the neutralization process consists of the actual recombination of ions and electrons when they leave the thruster. However, because of the particles' low density, the recombination reaction has a large mean free path when compared to the scale of the plume, and thus most of the energetic population remain charged, but quasi-neutral, when propagating downstream [45].

For the formation of slow ions, the two most important reactions, in this case, are ion charge exchange (CEX) and electron-neutral ionization. It is possible to roughly estimate the production of slow ions in the plume as $\dot{n}_{i,slow} \approx n_i n_g K_{\mathrm{cex}} + n_e n_g K_{\mathrm{iz}}$, where n_g is the neutral density, n_e is the electron density, n_i is the fast ion density, and K_{cex} and K_{iz} are the rate constants of the ionization and charge exchange reactions respectively. Assuming quasi-neutrality ($n_e \approx n_i$) and that the ion density is given by $n_i = J_b/eu_i$, it is possible to re-write the equation as $\dot{n}_{i,slow} \approx \frac{n_g J_b}{eu_i}(K_{\mathrm{cex}} + K_{\mathrm{iz}})$. If fast ions are considered mono-energetic, it is possible to write $K_{\mathrm{cex}} \approx \sigma_{\mathrm{cex}}u_i$, where the cross section σ_{cex} is mainly a function of the ion energy, E_i, and can be approximated for xenon as

$$\sigma_{\mathrm{cex,Xe}}(E_i) \approx 10^{-20}(97.51 - 6.15\ln E_i) \tag{1.81}$$

from the data of Miller *et al.* [110]. A fit of the ionization rate constant for xenon is given by Goebel and Katz [14] for the range 0.1 eV to 10 eV. From the simple model derived, it is possible to see that this is the case when $\sigma_{\mathrm{cex}}(E_i)u_i(E_i) > K_{\mathrm{iz}}(T_e)$. Using the estimations of rate constants, figure 1.11 shows the plot of the minimum temperature, T_e^*, at which the ionization becomes more important than the charge exchange for different values of ion energy. Despite being relatively simple, this estimation shows that for the electron temperatures generally found in GIT plumes ($T_e < 5\,\mathrm{eV}$), the dominant process for ion production is always charge exchange. If it is considered that all slow ions produced until a certain distance l_s from the exit surface go back to the thruster, it is possible to make a rough estimation of the backstreaming current as

$$I_{\mathrm{back}} \approx \frac{I_b l_s n_g}{u_i}(K_{\mathrm{iz}} + \sigma_{\mathrm{cex}}u_i) \tag{1.82}$$

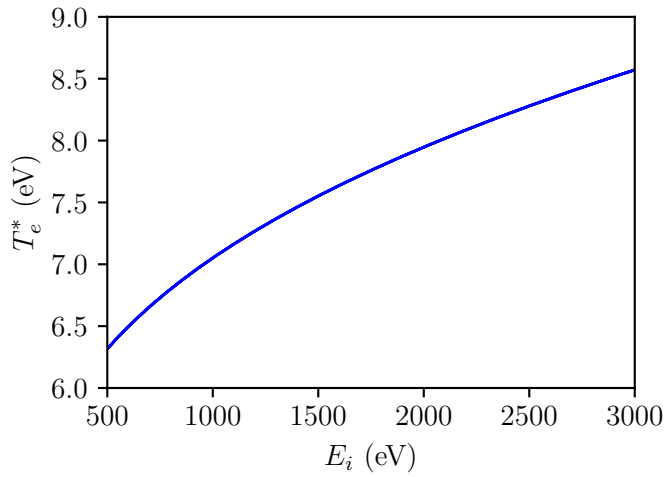

Figure 1.11: Estimation for xenon of the minimum electron temperature, T_e^*, at which ionization becomes more dominant than charge exchange for the production of slow ions.

For $T_e = 5\,\text{eV}$, $n_g = 10^{18}\,\text{m}^{-3}$, $E_i = 1000\,\text{eV}$, and $l_s = 1\,\text{cm}$, the backflow current is estimated as $I_{\text{back}} \approx 0.008 I_b$.

Several other collisional processes may take place during the plume expansion. One example is excitation and de-excitation, and recombination that lead to the emission of photons in the visible or near-visible spectrum. These reactions are used for plasma diagnostics using spectroscopic techniques [111]. Apart from this, when using more complex propellants such as iodine, many reactions taking place in the plume are still not well understood, and their modeling and diagnostics require more intricate techniques.

1.4 Objectives and outline of the thesis

The central objective of this work is to investigate the characteristics of the plasma plume of a gridded ion thruster when using RF grid biasing or iodine as a propellant. Both of these modifications to traditional thrusters can bring important advantages on a system level, however, they entail as well different physical and chemical processes in the plume which are not well understood and have a direct impact on the performance of the thruster. In this way, to turn these innovations into feasible technologies, it is imperative not only to elucidate their behavior as a complete system but also specifically of their plasma exhaust which is more complex to characterize due to its dependence on environmental conditions, interaction with other bodies and non-trivial modeling. To make this characterization possible, one of the main tools in this study will the comparison of the behavior of the thrusters using these technologies and the typical DC xenon thruster. This investigation is done using two different approaches, numerical simulations, and experimental investigations. In this way, despite not offering a complete description of all processes, this study sheds light on the key differences to expect when

adopting these new techniques.

After this introductory part, the thesis starts with a chapter on the description of the numerical modeling of the DC and RF GIT plume. This chapter shows the development process of a fully-kinetic 2D particle-in-cell code which is used to simulate the plasma expansion. The code implements different features such as collisions and reactions with a neutral flow, and a capacitive boundary condition used to guarantee the current free condition without inserting artifacts into the model as it is usually done in other plume simulation codes. Starting from the RF grid biasing theory presented in section 1.2.2, the chapter then presents a particle injection model that replicates the pulsed electron current found when using RF biasing. After that, a code validation procedure is presented showing the comparison of the code results with a 1D benchmark and other 2D plume results. Lastly, the results of the DC and RF plume expansions are presented, including the analysis of spatial profiles, distribution functions, and the dependence of several parameters of the RF biasing.

The next chapter describes the general experimental setup used during this work for the experiments with the DC xenon thruster, the DC iodine thruster, and the RF xenon thruster. First, the details of the thrusters and the vacuum facility are presented. Next, the description of the standard plasma diagnostic systems used during the experiments are shown including their mechanical construction and theory. The last part of this chapter describes the design and construction of a new automated probe array that was used during the work to characterize the plume divergence and shape for the DC thruster, and compare results for iodine and xenon.

After that, there is the first chapter showing the results of the experimental investigation and describing the measurement, for the first time, of the secondary electron emission (SEE) of iodine ions impinging several different materials. Although this part not being directly related to the properties of the iodine plume, the measurement of the SEE is fundamental for the corrections of the experimental data collected in the next chapter and important for many other iodine plasma studies. This effort has shown itself to be important during this work because of the lack of fundamental data available in the literature on iodine and its plasmas. This lack of basic information is one of the critical points for iodine plasma research, making its progress considerably slower than other fields. Therefore, this dedicated effort had the objective of improving the general knowledge base on iodine for this and future studies.

Then, the next chapter shows the experimental results of a DC thruster using xenon and iodine and the comparison between both propellants. The chapter starts with the general characterization of the plume, with measurement of parameters such as plasma potential, ion energy, and background plasma density. After that, a characterization of the plume divergence is presented using the automated probe system presented previously and a study on the general performance of the thruster using both propellants is shown. Since the iodine thruster used for this work has been recently tested in space, this chapter also presents a comparison of the experimental results obtained on the ground and in space, verifying the quality and validity of data obtained in these two situations.

The following chapter shows the results of the experimental investigation of the RF

thruster using xenon. In the first part, a brief review of the previous experimental results available in the literature is presented. Next, the thruster electrical measurements and analysis of the RF plume experiments is shown. The comparison with the simulations conducted previously and the DC thruster is also presented.

In the last two chapters, conclusions and the prospects for future work are presented, together with a list of publications resulting from this work is shown.

CHAPTER 2

SIMULATION OF PLASMA PLUME IN DC AND RF GRID BIASING MODES

This chapter describes a numerical study using a PIC code of the plume generated by a GIT using either DC or RF biasing. Here, the main goal is to show the key differences between the plume expansion in both cases and how parameters of the RF biasing method affect the plume characteristics. Furthermore, another important goal is to connect this study to previous simulation and experimental works on RF grid biasing, helping to complement these works and to elucidate missing aspects of the system modeling.

2.1 Overview

The numerical study of plasma plume expansion, and other types of plasmas, is typically done using one of three different methods: fluid-based simulations, kinetic simulations or hybrid simulations. The fluid-based case consists of modeling the plasma using a many-fluid set of equations and their solution using a discretized method for the solution of partial differential equations, e.g. the finite element method. This modeling has the advantage of typically having a lower computational cost due to the representation of the system's parameters as averaged macroscopic variables, but its applicability is limited when the system has characteristics such as strong gradients or important anisotropic species velocity distribution functions. The kinetic method, on the other hand, aims for the direct simulation of the particle distribution functions using discretized procedures, mainly the particle-in-cell method. The information level and fidelity achievable with kinetic simulations is typically higher than in the fluid case, however it has a considerably higher computational cost, limiting its application in several problems, e.g. with large computational domains. Hybrid modeling tries to decrease the computational cost of the kinetic method by considering one or more species as a fluid, while other species are still simulated kinetically. Despite offering speed improvements over the kinetic case, the hybrid method can only be applied when it is known from a problem that one of the species has a less complex behavior than the other species.

Because of the important density gradients and non-Maxwellian behavior present in plasma expansion, plasma plumes are usually simulated using either kinetic or hybrid methods. The main difference, in this case, is that, for hybrid methods applied to this type

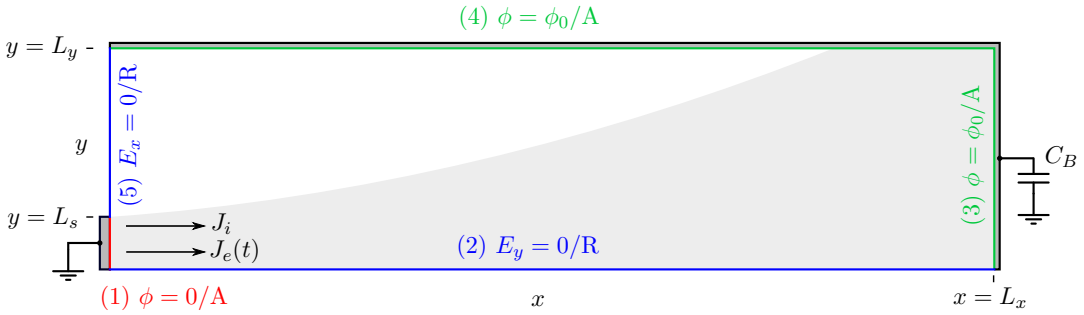

Figure 2.1: Schematic of the simulation domain. Field boundaries 2 and 5 (blue) are of Neumann type, 1 (red) is of Dirichlet type with $\phi = 0$, and 3 and 4 (green) are of Dirichlet type with their potential determined from the external capacitive circuit. Particles are absorbed on A and undergo specular reflection on R. J_i and J_e are the injected ion and electron current densities respectively (adapted from Ref. [112]).

of problem, electrons are often considered an isothermal, massless fluid with an isotropic distribution and density following the Boltzmann relation, while ions are simulated kinetically. Wang and Hu [100] present a comparison of these methods for simulating a hypersonic plume. For a typical DC plume, both the hybrid and kinetic models present acceptable results, reproducing the main features of the expansion. However, because of the assumptions on the electron population, this type of hybrid model fails to model the complex electron cooling processes taking place during the expansion and generates non-physical results when considering effects such as the magnitude of the ambipolar acceleration of ions. Furthermore, the authors note that, during the kinetic simulation, a strong electron anisotropy was observed, specially close to the edges of the beam, a factor that is also not reproduced by the hybrid simulation. It is important to note, however, that some of the problems attributed to the hybrid model could, in principle, be circumvented by dropping the assumptions about the electron population and simulating it as a physical fluid – however, this approach could increase the computational cost, making it less attractive.

The code developed in the present work is used for the simulation of two different plumes: a DC case, similar to previous numerical plume studies, where a continuous electron current is provided to replicate the behavior of a neutralizer; and an RF case, where electrons escape to the plume in bursts when the voltage drop between the grids collapses allowing electrons to leave the upstream thruster plasma source. Because the RF plume simulation is an inherently dynamical problem, with oscillating electrons

that are accelerated and de-accelerated during their propagation within the plume, the assumptions made for hybrid models of massless isotropic electrons are incompatible for this study. Therefore, a fully kinetic approach was adopted here with the development of a PIC code used for the simulations.

Figure 2.1 shows an overview of the simulation domain used for this study. It consists of a 2D Cartesian domain, similar to domains used in previous simulation works [100, 113], where a current of ions and electrons is injected through a boundary (1) and the flow is allowed to expand downstream. Boundaries 2 and 5 are symmetry axes and act as mirrors of the domain in the x and y directions so that every ion or electron that crosses these boundaries are effectively reflected and the scalar potential field is symmetric in its perpendicular direction. The charged particles inside the domain create their own potential field distribution, which is solved using a set of field boundary conditions that are applied to all boundaries of the domain. At the boundary where the particles are injected (1), the potential is fixed at zero; at the boundaries 2 and 5 the perpendicular electric field is zero; and boundaries 3 and 4 act as a metallic wall connected to ground through a capacitor C_B which is charged through the currents flowing to it. This capacitive connection ensures the current-free condition without adding artificial boundary conditions, and mimics the behavior of a floating ion source within a vacuum chamber connected to its surroundings through a capacitive connection or a thruster in space with a certain capacitive with respective to infinity. The choice for the Cartesian domain over a cylindrical one was done to decrease the development complexity and because it was shown in previous works [113] that there is no important difference in the plume expansion in both systems of coordinates.

2.2 Particle-in-cell method

2.2.1 General description

The particle-in-cell method is a discrete statistical method to simulate the temporal evolution of a distribution function. This method utilizes the concept of macro-particles to sample the distribution function in phase space and integrate their trajectory to obtain a new statistical estimation of the distribution function at each time step. On a physical perspective, each macro-particle represents a group of N_p real particles that are assumed to be located inside a given small volume $\Delta\mathbf{x}\Delta\mathbf{v}$ at $\mathbf{x}, \mathbf{v}$ in phase space and evolve together to another phase-space location $\mathbf{x}', \mathbf{v}'$ after a given time t. The parameter N_p is called the macro-particle weight. The movement of the n-th particle (used as a synonym for a macro-particle in this chapter) is obtained from the integration of its equation of motion

$$m_n \frac{d\mathbf{v}_n}{dt} = \mathbf{F}_n(t) \tag{2.1}$$

where $\mathbf{F}_n(t)$ is the force applied on the particle. In the case of charged particles in a plasma, the electric force for example, can be calculated by the coulomb force generated by each particle p on the particle n plus any external forces, i.e. $\mathbf{F}_e(t) = \mathbf{F}_{\text{ext}} + \frac{q_n}{4\pi\varepsilon_0}\sum_{p\neq n} q_p \frac{\mathbf{x}_n - \mathbf{x}_p}{|\mathbf{x}_n - \mathbf{x}_p|^3}$. Despite being precise, the direct force calculation has an elevated

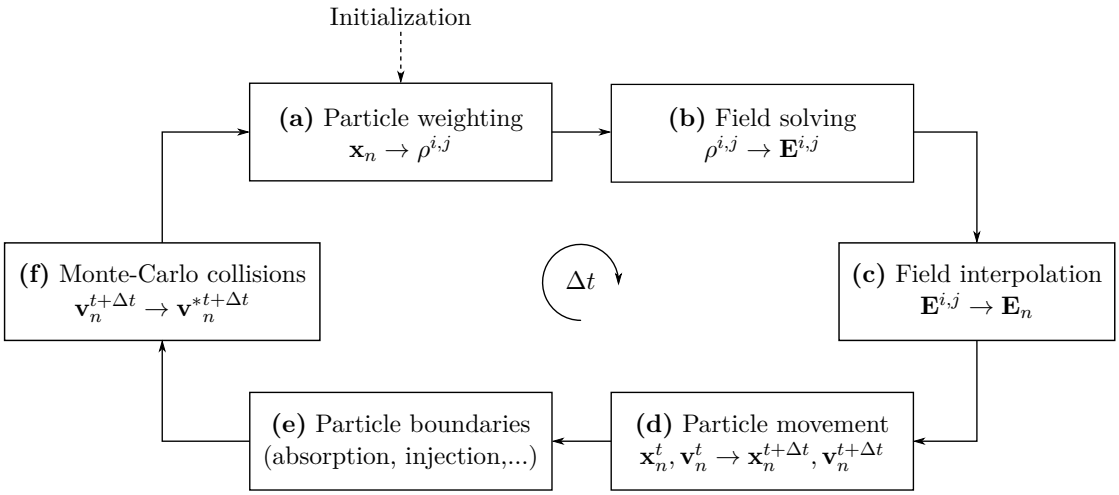

Figure 2.2: Schematic of the particle-in-cell simulation algorithm.

computational cost (scaling with $O(n^2)$) and is unfeasible for the simulation of a big number of particles – computations using this type of formulation are usually called particle-particle simulations and enter into the realm of N-body problems [114]. Therefore, to decrease the time complexity to roughly $O(n)$, in the PIC method particles are placed within a spatial *mesh* that is used to compute the field generated by the particles at each node of the mesh. To estimate $\mathbf{F}_n$, the resulting field is then interpolated at the location $\mathbf{x}_n$.

The simulation code developed for this work uses a standard PIC calculation loop [115] which is shown in figure 2.2 and which will be described throughout this section. The main purpose of this algorithm is to determine the forces and effects acting on each particle so that they can be moved iteratively through the domain. The code developed for this work simulates a two-species plasma, positive ions and electrons, in a 2D rectangular spatial mesh and assumes that particles interact only through electrostatic forces. Therefore, the force felt by a particle can be written as $\mathbf{F}_n(t) = q_n\mathbf{E}(\mathbf{x}_n, t)$, where $\mathbf{E}$ is the electric field in the domain. Because no magnetic fields are considered, the electric field anywhere in the domain can be represented as $\mathbf{E} = -\nabla\phi$, where ϕ is the electric potential field. Using this representation, and equations 1.6 and 1.8, the potential field can be obtained by solving Poisson's equation

$$\nabla^2\phi = -\frac{e}{\varepsilon_0}(n_i - n_e) \tag{2.2}$$

where $n_i = n_i(\mathbf{x}, t)$ and $n_e = n_e(\mathbf{x}, t)$ are the ion and electron number densities respectively. The solution of eq. 2.2 over a spatial mesh is widely known, however it requires the knowledge of the particle densities at every mesh node i, j. The values of the particle densities are obtained through a procedure called *weighting* (step a), in the form

$$n^{i,j} = \frac{N_p}{A_{i,j}} \sum_n S(\mathbf{x}_n - \mathbf{x}_{i,j}) \tag{2.3}$$

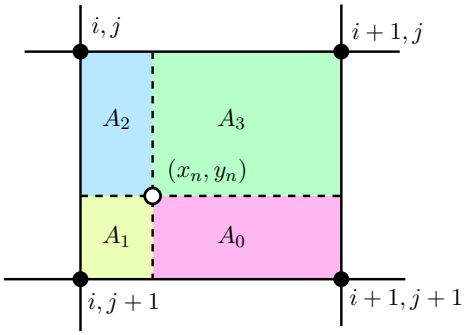

Figure 2.3: Weighting schematic of a particle at (x_n, y_n) inside the spatial mesh.

where $A_{i,j}$ is the area of the cell and $0 \leq S(\mathbf{x}) \leq 1$ is called the weight function, and gives the contribution of each particle to a given node based on its location. Equation 2.3 is in fact an approximation of the ensemble average over the particle distribution function (given in eq. 1.9), and therefore the average of any property Λ of the particle population can be estimated at a mesh node

$$\langle \Lambda \rangle^{i,j} = \frac{1}{n^{i,j}} \sum_n \Lambda_n S(\mathbf{x}_n - \mathbf{x}_{i,j}) \tag{2.4}$$

The function S can have different forms, however the most common and the one used here is called "cloud-in-cell" which has a similar form to a bilinear interpolation. In this scheme, if the particle is inside a given cell between i, j and $i+1, j+1$ as shown in figure 2.3, the value of S at each one of the surrounding nodes is given by the ratio of the opposite area to the total area of the cell [115],

$$S_{i,j} = \frac{A_0}{A} = \frac{(x_{i+1,j+1} - x_n)(y_{i+1,j+1} - y_n)}{\Delta x_i \Delta y_j} \tag{2.5}$$

$$S_{i+1,j} = \frac{A_1}{A} = \frac{(x_n - x_{i,j})(y_{i+1,j+1} - y_n)}{\Delta x_i \Delta y_j} \tag{2.6}$$

$$S_{i+1,j+1} = \frac{A_2}{A} = \frac{(x_n - x_{i,j})(y_n - y_{i,j})}{\Delta x_i \Delta y_j} \tag{2.7}$$

$$S_{i,j+1} = \frac{A_3}{A} = \frac{(x_{i+1,j+1} - x_n)(y_n - y_{i,j})}{\Delta x_i \Delta y_j} \tag{2.8}$$

where $S_{i,j} = S(\mathbf{x}_n - \mathbf{x}_{i,j})$, $\Delta x_i = x_{i+1,j} - x_{i,j}$ and $\Delta y_j = y_{i,j+1} - y_{i,j}$. With the values of the particle densities at the mesh nodes, equation 2.2 can be solved using a finite-difference method. Using a central difference scheme with a 5-point stencil [116], the equation is discretized as

$$\frac{\phi_{i+1,j}\Delta x_{i-1} - \phi_{i,j}(\Delta x_i + \Delta x_{i-1}) + \phi_{i-1,j}\Delta x_i}{\frac{1}{2}\Delta x_{i-1}\Delta x_i(\Delta x_i + \Delta x_{i-1})} + \frac{\phi_{i,j+1}\Delta y_{j-1} - \phi_{i,j}(\Delta y_j + \Delta y_{j-1}) + \phi_{i,j-1}\Delta y_j}{\frac{1}{2}\Delta y_{j-1}\Delta y_j(\Delta y_j + \Delta y_{j-1})} = \frac{\rho^{i,j}}{\varepsilon_0} \tag{2.9}$$

where $\rho^{i,j} = e(n_i^{i,j} - n_e^{i,j})$. As mentioned before, two types of boundary conditions are used to solve Poisson's equation, Dirichlet and Neumann. In the first type, the potential at the boundary is fixed at a given value V_b. Considering that the boundary is at $i-1, j$, equation 2.9 becomes

$$\frac{\phi_{i+1,j}\Delta x_{i-1} - \phi_{i,j}(\Delta x_i + \Delta x_{i-1})}{\frac{1}{2}\Delta x_{i-1}\Delta x_i(\Delta x_i + \Delta x_{i-1})} + \cdots = \frac{\rho^{i,j}}{\varepsilon_0} - \frac{V_b}{\frac{1}{2}\Delta x_{i-1}(\Delta x_i + \Delta x_{i-1})} \tag{2.10}$$

In the second type, the derivative of the potential in the direction of the boundary is set to zero. If the boundary is in the x-direction at i, j ($\partial\phi/\partial x = 0$), it is necessary to set $\phi_{i+1,j} = \phi_{i-1,j}$, where $i-1, j$ is a ghost cell outside of the mesh. Assuming that $\Delta x_{i-1} = \Delta x_i$, equation 2.9 for the Neumann boundary becomes

$$\frac{2\phi_{i+1,j} - 2\phi_{i,j}}{\Delta x_i^2} + \cdots = \frac{\rho^{i,j}}{\varepsilon_0} \tag{2.11}$$

Using equations 2.9, 2.10 and 2.11 over the mesh, a linear system, $A\Phi = b$ where $\Phi = [\phi_{0,0} \quad \phi_{1,0} \quad \cdots \quad]^T$, is assembled and solved using an appropriate computational method (step b).

Once the electric potential has been obtained at the mesh nodes, the electric field is calculated through $\mathbf{E} = -\nabla\phi$. This equation can be discretized as

$$\mathbf{E}^{i,j} = \frac{\phi_{i-1,j} - \phi_{i+1,j}}{\Delta x_i + \Delta x_{i-1}}\mathbf{i} + \frac{\phi_{i,j-1} - \phi_{i,j+1}}{\Delta y_j + \Delta y_{j-1}}\mathbf{j} \tag{2.12}$$

where $\mathbf{i}$ and $\mathbf{j}$ are unit vectors in the x and y-directions respectively. A bilinear interpolation is then used to find the electric field at the location of every particle n (step c),

$$\mathbf{E}_n = S_{i,j}\mathbf{E}^{i,j} + S_{i+1,j}\mathbf{E}^{i+1,j} + S_{i+1,j+1}\mathbf{E}^{i+1,j+1} + S_{i,j+1}\mathbf{E}^{i,j+1} \tag{2.13}$$

where S is defined in equations 2.5 to 2.8. Using the electric field values, the particle equations of motion 2.1 are integrated (step d) using the standard *leapfrog method* [117]. The velocity equation is discretized as $\frac{\mathbf{v}_n^{t+\Delta t} - \mathbf{v}_n^t}{\Delta t} = \frac{q_n}{m_n}\mathbf{E}_n$, while the position equation, $\frac{d\mathbf{x}_n}{dt} = \mathbf{v}_n$, is integrated using the average velocity $\mathbf{v}_n^{t+\Delta t/2} = \frac{\mathbf{v}_n^t + \mathbf{v}_n^{t+\Delta t}}{2}$. The final equations used to integrate the movement of the particles are

$$\mathbf{v}_n^{t+\Delta t/2} = \mathbf{v}_n^t + \frac{\Delta t}{2}\frac{q_n}{m_n}\mathbf{E}_n \tag{2.14}$$

$$\mathbf{x}_n^{t+\Delta t} = \mathbf{x}_n^t + \mathbf{v}_n^{t+\Delta t/2}\Delta t \tag{2.15}$$

The use of the half-step velocity value is the main difference compared with the traditional Euler integrator, and makes the leapfrog method symplectic (i.e. conserves the energy of the system) and time-reversible [118].

After particle movement, their interactions with the domain boundaries are treated (step e). The present simulation uses three different types of particle boundaries: (1) absorption, (2) specular reflection and (3) injection. In absorption (1), once a particle

crosses the boundary and its position is currently outside of the domain limits, the particle is removed from the simulation. This is the typical boundary condition for metallic and dielectric boundaries and during the simulation the absorption event may be used to compute the particle current entering the surface. Specular reflection (2) is used here for symmetry planes, i.e. a particle leaving the domain represents as well one entering it with an opposite normal velocity. During a specular reflection, the change in the velocity vector is represented as

$$\mathbf{v}_n' = \mathbf{v}_n - 2(\mathbf{v_n} \cdot \hat{\mathbf{n}})\hat{\mathbf{n}} \tag{2.16}$$

where $\hat{\mathbf{n}}$ is the normalized normal vector of the boundary surface. For a boundary in the x-direction, the velocity component in y is conserved, $v_y' = v_y$, and the x component changes sign, $v_x' = -v_x$. The particle only undergoes specular reflection once it has crossed the boundary, so to continue its simulation it is necessary to move it back to the domain. This can be done by mirroring the position of the particle relative to the boundary [117]. Again, for a boundary in the x-direction, if x_b is the location of the boundary, the new mirrored particle position is

$$x' = 2x_b - x. \tag{2.17}$$

Particle injection (3) follows the Maxwellian flux injection procedure described by Cartwright *et al.* [119]. For a given particle flux $\dot{m}(t)$, the number of particles injected, N_{inj}, at every time step is

$$N_{\text{inj}} = \frac{\dot{m}(t)}{m}\frac{\Delta t}{N_p} \tag{2.18}$$

where m is the mass of a real particle. All particles injected are assumed to come from a Maxwellian distribution with a temperature T_0 and to be accelerated by a given amount Δv_{drift}. The magnitude of the perpendicular injection velocity is given by

$$v_{\text{inj}} = v_{\text{th}}\sqrt{-2\ln R_1} + v_{\text{drift}} \tag{2.19}$$

where $v_{\text{th}} = \sqrt{eT_0/m}$ is the mean thermal velocity and R_1 is a uniform random number in the range $(0, 1]$. The velocity components parallel to the injection boundary are sampled from a normal distribution with standard deviation $\sigma = v_{\text{th}}$ and mean $\mu = 0$. The position of the injected particle is sampled from a uniform random distribution along the boundary length. To ensure a continuous particle flux, a small displacement is added (or subtracted) to the initial particle position in the direction perpendicular to the boundary,

$$\Delta L = \Delta t R_2 v_{\text{inj}} \tag{2.20}$$

where R_2 is another uniform random number. This ensures that there is no particle accumulation close to the injection boundary at every time step which would lead to a bunched particle current.

The last phase of the PIC loop is the simulation of particle collisions (step f) using the Monte-Carlo collision algorithm [120]. For this, a neutral gas density field is obtained at the beginning of the simulation and used to calculate the probability of collisions

between charged particles and the neutral species. This probability is estimated from experimental collision cross section data that is interpolated during the simulation. Whenever a given collision event happens, different effects may take place including the change of the particle velocity due to scattering, and the addition or removal of particles. This procedure will be further discussed in a subsequent section.

For the PIC simulation to be stable and a good statistical representation of the real system, several numerical criteria must be fulfilled [114, 121]. The first is known as the CFL (Courant-Friedrichs-Lewy) condition, which is a widely used convergence criterion in physics, and in this case can be written as

$$\frac{\Delta x}{\Delta t} > v \tag{2.21}$$

where Δx is the width or height of a spatial cell, Δt is the time step of the simulation and v is the speed of a particle. In the context of PIC simulations, this guarantees that a particle will not travel a path which is larger than a cell during one time step. Since electrons are the fastest particles due to their significantly lower mass, typically v is assumed to be the mean speed of electrons. The second and third criteria state the need for resolving different plasma phenomena, such as Debye shielding and sheaths, and are defined as

$$\Delta x \lesssim \lambda_D \tag{2.22}$$

$$\omega_p \Delta t \lesssim 0.2 \tag{2.23}$$

where ω_p is the plasma frequency.

2.2.2 Current injection model

To simulate the expansion of DC and RF plumes, a correct model of the current injected at every time step is required. In the DC case, this modeling is straightforward, with the ion current given by

$$I_i = eAn_0 v_{\text{drift}} \tag{2.24}$$

where n_0 is the plasma density inside the thruster discharge, and its initial drift velocity is given by $v_{\text{drift}} = \sqrt{2eE_i/m_i}$, where E_i is the mean energy obtained during acceleration. Electrons are injected with no drift velocity, and with a current magnitude that guarantees quasi-neutrality at the injection boundary, i.e. $\frac{I_e}{v_e} = \frac{I_i}{v_i}$. Considering that the electrons are injected as a maxwellian flux and that their velocity is given by equation 1.24, the injected electron current is

$$I_{e,DC} = I_i \sqrt{\frac{m_i}{4\pi m_e} \frac{T_e}{E_i}}. \tag{2.25}$$

In the RF case, the injected current may be estimated from the theoretical work presented in section 1.2.3. First, it is assumed that frequency requirement from equation 1.65 is met. In this way, the ion current can still be estimated by equation 2.24, and its drift energy is approximately given by $E_i \approx eV_{sb}$. For the electrons, if we consider

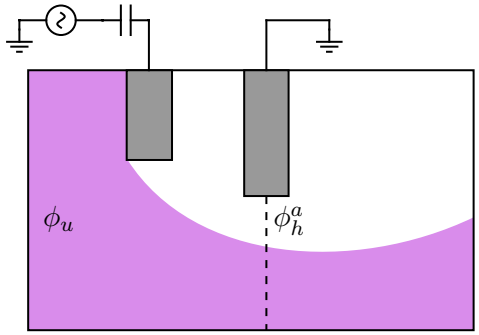

Figure 2.4: Grid geometry considered for the current injection model. ϕ_u is the upstream plasma potential and ϕ_h^a is the potential across the accel grid hole.

that the upstream plasma is quasi-neutral and that they follow a Maxwellian distribution (obeying the Boltzmann relation), the electron current leaving the source can be estimated as

$$I_e(t) = I_i \sqrt{\frac{m_i}{2\pi m_e}} \exp\left(-\frac{\Delta\phi(t)}{T_e}\right), \tag{2.26}$$

where $\Delta\phi(t) = \phi_u(t) - \phi_h^a(t)$, $\phi_u(t)$ is the upstream plasma potential and $\phi_h^a(t)$ is the central potential of the accel grid hole as shown in figure 2.4. For a first approximation it is assumed that $\phi_h^a(t) \approx 0$ and that the upstream sheath potential drop is much smaller than the screen grid potential, such that

$$\Delta\phi(t) \approx V_{sb} + V_{RF} \sin \omega t \tag{2.27}$$

In practice this equation could already be used to model the current injection, with V_{sb} as the only unknown variable to be determined. There are numerical and theoretical techniques to determine the value of V_{sb} depending on a specific source configuration and geometry, as shown by Lafleur and Rafalskyi [66]. However, to keep the model agnostic to the source and grid geometries, and to be able to study the effect of the extracted electron current, an artificial free parameter α is introduced to control V_{sb}. The parameter is defined as

$$\alpha \equiv \frac{\langle I_e \rangle}{I_i} \tag{2.28}$$

and corresponds to the ratio of the injected time-averaged electron current to the ion current. Using this definition, it is possible to estimate V_{sb} using equations 2.26 and 2.27 and performing a time average on $I_e(t)$ over an RF period

$$\begin{aligned} \langle I_e \rangle &= I_i \sqrt{\frac{m_i}{2\pi m_e}} e^{-\frac{V_{sb}}{T_e}} \frac{1}{2\pi} \int_0^{2\pi} \exp\left(-\frac{V_{RF}}{T_e} \sin\theta\right) d\theta \\ &= I_i \sqrt{\frac{m_i}{2\pi m_e}} e^{-\frac{V_{sb}}{T_e}} I_0\left(\frac{V_{RF}}{T_e}\right) \end{aligned} \tag{2.29}$$

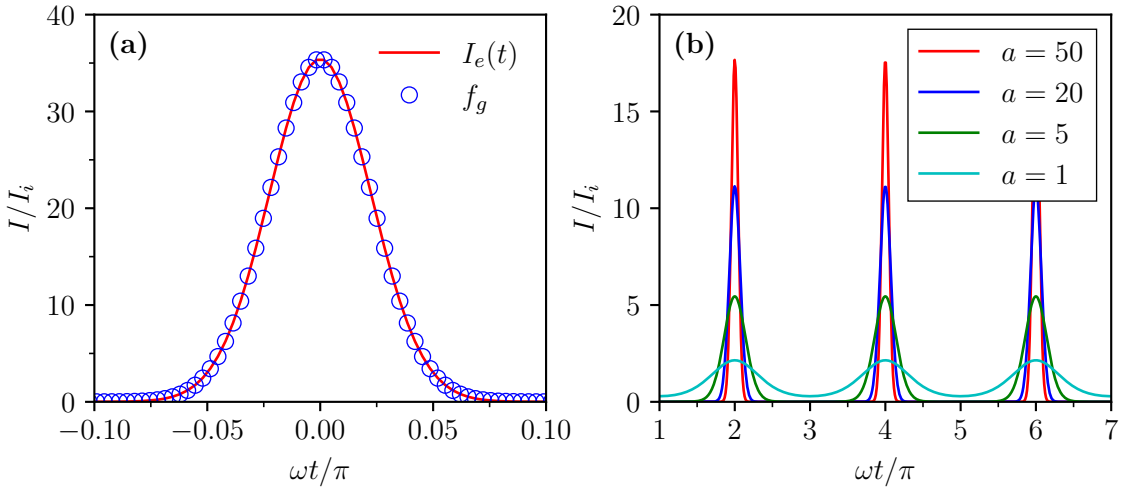

Figure 2.5: (a) Comparison of pulse generated by the electron current equation 2.31, $I_e(t)$, and gaussian curve approximation, f_g, for $V_{RF} = 1\,\text{kV}$, $T_e = 5\,\text{eV}$ and $\alpha = 1$. (b) Electron current, $I_e(t)$, for different values of $a = V_{RF}/T_e$.

where I_0 is the zeroth order modified Bessel function of the first kind. Rearranging equation 2.29, the self-bias voltage is estimated as

$$V_{sb} = T_e \left(\ln \left[I_0 \left(\frac{V_{RF}}{T_e} \right) \right] + \frac{1}{2} \ln \left[\frac{m_i}{2\pi m_e} \right] - \ln \alpha \right). \tag{2.30}$$

Substituting equation 2.30 into equation 2.26, the instantaneous electron current can be rewritten as

$$I_e(t) = \frac{\alpha I_i}{I_0 \left(\frac{V_{RF}}{T_e} \right)} \exp \left(-\frac{V_{RF}}{T_e} \sin \omega t \right) \tag{2.31}$$

Equation 2.31 consists on a train of pulses repeating itself every $2\pi/\omega$ second and with an average magnitude αI_i. It is interesting to note that each pulse has the shape of a gaussian curve which can be seen if a parameter $\tau = \omega t - 3\pi/2$ is defined and substituted in equation 2.31. Using the small angle approximation, the equation becomes

$$I_e(\tau) \approx A \exp \left(-\frac{\tau^2}{2\sigma^2} \right) \tag{2.32}$$

with $A = \frac{\alpha I_i}{I_0(V_{RF}/T_e)} \exp\left(\frac{V_{RF}}{T_e}\right)$, $\sigma = \sqrt{V_{RF}/T_e}$ and $\alpha = 1$. Figure 2.5a shows the comparison between the actual electron current model given by equation 2.31 and the gaussian curve approximation for $V_{RF} = 1\,\text{kV}$ and $T_e = 5\,\text{eV}$. It is possible to see that the current profile closely follows the gaussian approximation. Figure 2.5b shows the current profile for three periods and different values of V_{RF}/T_e. As in the gaussian case, the width of the pulse is controlled by this ratio and as it decreases, the pulses start to overlap and the current profile starts to diverge from the gaussian approximation.

During the simulation of the RF plume, equation 2.31 is used to estimate the approximate number of electrons to be injected at each time step for different values of α, and is used with equation 2.18 to be converted into the number of simulated particles added at boundary 1. Furthermore, in contrast with the DC case, electrons are injected with a positive drift velocity of 50 eV as further discussed in the next sections. This is justified by observations from previous simulation works of the grids [66, 68] which verified that electrons were accelerated during their injection due to the presence of the ion space charge between the grids.

2.2.3 Capacitive boundary condition

An appropriate model of the simulation outer boundaries (3 and 4 in figure 2.1) is not straightforward. Due to current conservation, and because the injected electron current is typically higher than the ion current (eq. 2.25), an large fraction of the injected electrons are not actually completely lost but are reflected downstream and ultimately return to the source. However, many of these electrons may have large scale trajectories before returning to the thruster, so a spatial truncation of the domain with particle absorption may lead to an exaggerated electron current loss, causing non-physical results and instabilities.

In past works, mainly three different kinds of boundary conditions were employed for this type of simulation: (a) Dirichlet type (fixed potential) with particle absorption; (b) Neumann type (zero-electric field) with particle absorption; and (c) Neumann type with partial reflection of electrons. As mentioned, types *a* and *b*, where all particles are absorbed and removed from the simulation, leads to instabilities during steady-state, therefore works using these schemes typically ensure that the simulation is terminated before the ion front arrives at the outer limits of the domain [99, 103]. Type *c*, proposed by Li *et al.* [113], establishes an energy criterion to determine if an electron should be reflected back to the domain or absorbed. This strategy guarantees stability and keeps the current-free condition of the simulation during the transient and steady-state evolution. Despite offering a good alternative for the simulation of DC plumes, this boundary type makes use of time-averaged quantities and assumes that there are no gradients of electric potential at the boundaries, making it unfit for the simulation of the RF plume which has an oscillatory nature. Due to the pulsed electron current injection, fast temporal and spatial variations of the potential field and other plasma quantities are expected, which cannot be modeled using an open-boundary condition.

Because of this, and to decrease uncertainties and avoid the addition of artifacts in the boundary modeling, the solution proposed here is to model the outer boundary as a metallic surface connected to a capacitive circuit, as shown in figure 2.1. In this way, it is guaranteed that the system evolves in a self-consistent manner and, once that equilibrium is reached, the method also ensures that the current-free condition is met. Physically, this model represents the situation where a thruster is electrically floating relative to the vacuum chamber ground or the case where the thruster is operating in space and has a finite capacitance relative to infinity. This boundary condition is similar to a Dirichlet-type BC with particle absorption, however in this case the potential is set by the

external circuit coupled to the the plasma discharge so that the system is self-consistent. To solve the capacitive circuit in conjunction to the fields in the simulation domain, the methodology proposed by Vahedi and DiPeso [122] is used, which consists on a scheme that guarantees that the circuit and the Poisson's equation are solved simultaneously without any iterative method. Here we present the derivation of the expression used to calculate the boundary potential at every time step as proposed by the authors, but the expression is generalized to non-uniform grids, in contrast with the original work that assumes a uniform rectangular grid.

Using superposition, it is possible to decompose the electric potential field inside the domain as

$$\phi = \phi_\rho + \phi_0 \phi_L, \tag{2.33}$$

where ϕ_ρ is the potential calculated for the space charge distribution ρ with the boundary voltage set to $V_b = 0\,\mathrm{V}$, ϕ_L is the potential calculated considering no charges ($\rho = 0$) inside the domain and the boundary voltage at $V_b = 1\,\mathrm{V}$, and ϕ_0 is a scalar coefficient determined by solving the circuit, with a numerical value equivalent to the boundary voltage. To determine ϕ_0, it is first necessary to consider the integral form of Gauss' law near the electrode wall (which the circuit is connected to), which can be written as

$$\varepsilon_0 \oint_S \mathbf{E} \cdot d\mathbf{S} = -\varepsilon_0 \int_V \nabla^2 \phi dV = Q \tag{2.34}$$

where Q is the total charge in the volume. Since the considered volume touches the wall, the charge may be decomposed as

$$Q = \int_V \rho_v dV + \oint_S \sigma_s dS \tag{2.35}$$

where ρ_v is the volume's space charge density and σ_s is the surface charge density on the wall. Using equations 2.34 and 2.35, it is possible to write

$$\oint_S \sigma_s dS = -\int_V \varepsilon_0 \nabla^2 \phi + \rho_v dV \tag{2.36}$$

Considering a small rectangular volume close to the wall, equivalent to one grid cell at i, j, and assuming that all quantities stay constant inside this volume, it is possible to discretize equation 2.36 as

$$\sigma^t_{s,i,j} = -\varepsilon_0 \frac{V_{i,j}}{A_{i,j}} \left[\nabla^2_{i,j} \phi^t + \frac{\rho^t_v}{\varepsilon_0} \right] \tag{2.37}$$

where the superscript t means that the quantity is calculated on the current time step, $V_{i,j}$ is the volume of the cell, $A_{i,j}$ is the area of the electrode's wall in the considered volume, and $\nabla^2_{i,j}$ is the discrete Laplacian operator at i, j given by the LHS of equation 2.9. When evaluating $\nabla^2_{i,j}$, whenever the operand has an index that is outside of the domain, its value and spacing are assumed to be the one of the central cell of the stencil, e.g. if $i-1, j$ is outside the domain, $\phi_{i-1,j} = \phi_{i,j}$ and $\Delta x_{i-1} = \Delta x_i$.

It is possible to calculate the average surface charge density on the whole electrode as

$$\sigma_T^t = \frac{1}{A_T} \sum_{i,j} A_{i,j} \sigma_{s,i,j}^t \tag{2.38}$$

where A_T is the total area of the electrode and the summation is over all the mesh cells touching to the electrode's wall. Equation 2.37 can then be rearranged as

$$\sigma_T^t = -\frac{\varepsilon_0}{A_T} \sum_{i,j} V_{i,j} \left[\nabla_{i,j}^2 \phi^t + \frac{\rho_v^t}{\varepsilon_0} \right] \tag{2.39}$$

Considering the current passing through the external circuit I_c and the convection current I_p caused by plasma particles that hit the wall, the equation for the surface charge density can be written as

$$A_T \frac{d\sigma_T}{dt} = I_c + I_p \tag{2.40}$$

To solve this equation, the capacitive circuit topology shown in figure 2.1 is used. Therefore, the voltage drop across the capacitor can be calculated as $V_c = -\phi_0$ and the circuit current is $I_c = -C_B d\phi_0/dt$. Finally, equation 2.40 can be discretized as

$$\sigma_T^t = \sigma_T^{t-\Delta t} - \frac{C_B}{A_T}(\phi_0^t - \phi_0^{t-\Delta t}) + \frac{Q_p^t}{A_T} \tag{2.41}$$

where Q_p^t is the net particle charge that hits the wall at the time step t. Combining equations 2.39 and 2.41 with the decomposition it is possible to obtain an expression for ϕ_0^t in the form

$$\phi_0^t = \frac{C_B \phi_0^{t-\Delta t} + A_T \sigma_T^{t-\Delta t} + Q_p^t + \sum_{i,j} V_{i,j}(\varepsilon_0 \nabla_{i,j}^2 \phi_\rho^t + \rho_v^t)}{C_B - \sum_{i,j} V_{i,j} \varepsilon_0 \nabla_{i,j}^2 \phi_L} \tag{2.42}$$

Equations 2.41 and 2.42 can be used together at every time step to determine the potential ϕ_0^t at the outer boundaries. The final potential field used to move the particles at the time step t can be obtained from eq. 2.33 in discrete form

$$\phi_{i,j}^t = \phi_{\rho,i,j}^t + \phi_0^t \phi_{L,i,j} \tag{2.43}$$

Note that now in step b of the PIC loop, only the field ϕ_ρ must be solved. The field ϕ_L can be solved just once at the initialization phase of the code, since it depends only on the geometry of the problem. With this, the whole denominator of equation 2.42 can also be solved just once in the simulation, since it contains no time-dependent variables.

2.2.4 Neutral flow and collisions

Collisions and reaction processes play an important role in the expansion of the plume, potentially affecting several aspects of its evolution. Therefore, a numerical model to simulate the collisional processes was added to the PIC calculation loop. The reactions

considered here are only those between charged and neutral particles, since they are the dominant processes taking place in the plume as discussed in section 1.3.4. The simulation of the collisions is based on the Monte-Carlo collision (MCC) algorithm proposed by Vahedi and Surendra [120], using a static neutral gas density field that is calculated at the beginning of the simulation.

The MCC model consists of a probabilistic method to determine if a particle will collide based on random samples. Similarly to equation 1.37, the probability that the n-th particle will suffer *any* collision during a time step Δt is given by

$$P_n = 1 - \exp(-\Delta t v_n \sigma_t(E_n) n_g(\mathbf{x}_n)) \tag{2.44}$$

where v_n is the particle speed, $E_n = \frac{1}{2} m_n v_n^2$ is its kinetic energy, $n_g(\mathbf{x}_n)$ is the density of the target species at its location, and $\sigma_t(E_n) = \sum_i \sigma_i(E_n)$ is called the total collision cross section and it consists of the sum of all collision cross sections σ_i between the particle and the target species. However, the check of P_n for every simulated particle at every time step is very computationally intensive. To get around this issue, a criterion is used to select a subset of particles that will be checked for collisions. For this, a virtual reaction called a "null collision" is introduced, which does not represent any real interaction but has a constant collision frequency with a value higher than the sum of all other collision frequencies,

$$\nu' = \max(n_g(\mathbf{x})) \max(\sigma_t(E) v) \tag{2.45}$$

where $v = \sqrt{2eE/m}$. In this equation, the first term of the RHS calculates the maximum value of the target density field over all the domain, and the second term calculates the maximum total value of the total cross section times the velocity v. The number of particles that suffer a collision, including the null collision, is then $N_{\text{coll}} = P_{\text{null}} N$, where

$$P_{\text{null}} = 1 - \exp(-\nu' \Delta t) \tag{2.46}$$

and N is the number of all particles in the simulation. At each time step, N_{coll} particles are randomly selected from the population and checked for a collision event. For each collision type i and particle n, the collision frequency is calculated as $\nu_i(E_n) = n_g(\mathbf{x}_n)\sigma_i(E_n)v_n$. To determine if a particle will undergo a collision of type j, the following check must be done

$$\frac{1}{\nu'} \sum_{i=0}^{j-1} \nu_i(E_n) < R \leq \frac{1}{\nu'} \sum_{i=0}^{j} \nu_i(E_n) \tag{2.47}$$

where R is a uniform random number in the range of $(0, 1]$. At each time step, just one value for R is drawn for each particle, that is then used to check which collision type is selected for each particle. Note as well that when $j = 0$, the LHS of equation 2.47 returns an empty sum with a value of zero.

All simulations in this work consider xenon as the propellant gas, which makes the simulations more easily comparable to previous numerical and experimental results and avoids overcomplicated chemical processes which are present for other propellant types. With this, three different reactions are considered for the electron population:

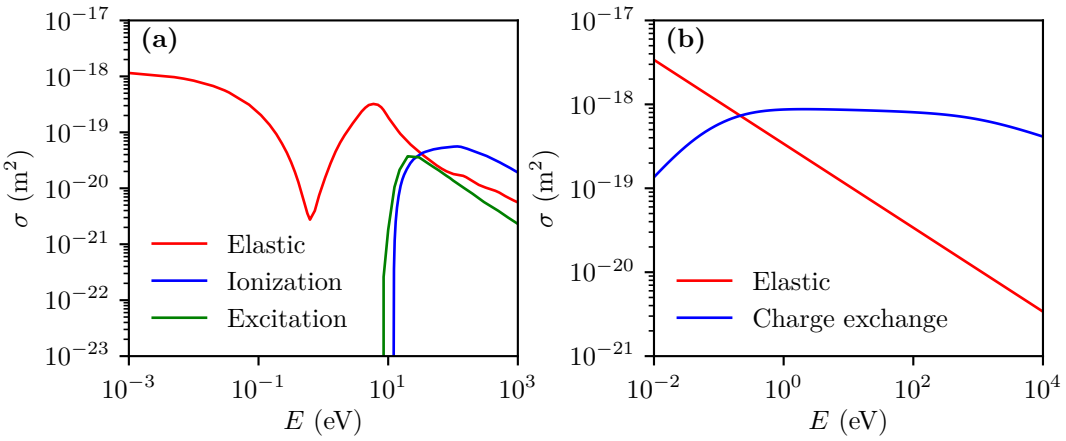

Figure 2.6: Xenon cross-section data for (a) electron-neutral collisions and (b) ion-neutral collisions.

1. Elastic scattering: $e^- + Xe \longrightarrow e^- + Xe$
2. Excitation: $e^- + Xe \longrightarrow e^- + Xe^*$
3. Ionization: $e^- + Xe \longrightarrow 2\,e^- + Xe^+$

While for ions, two reactions are considered:

1. Elastic scattering: $Xe^+ + Xe \longrightarrow Xe^+ + Xe$
2. Charge exchange: $Xe^+ + Xe \longrightarrow Xe + Xe^+$

The experimental cross-sections for all the reactions were obtained from the LXCat website [20]. The data for ionization and electron elastic scattering was obtained from the Biagi v7.1 [123] compilation, for excitation from the Morgan database [124], and ion-neutral collisions from the Phelps database [125]. Figure 2.6 shows the values of the cross-section data for electron-neutral and ion-neutral collisions.

Whenever a given particle undergoes a type of collision, the event needs to be treated differently for every reaction. For this work, it is assumed here that for all electron-neutral collisions, the projectile electron is always scattered isotopically. In this way, after colliding with a target neutral, the new direction of the electron velocity vector is

$$\hat{\mathbf{v}}' = \hat{\mathbf{v}}\cos\chi + \hat{\mathbf{v}} \times \mathbf{i}\frac{\sin\chi\sin\phi}{\sin\theta} + \hat{\mathbf{v}} \times (\mathbf{i} \times \hat{\mathbf{v}})\frac{\sin\chi\cos\phi}{\sin\theta} \tag{2.48}$$

where $\cos\theta = \hat{\mathbf{v}}\cdot\mathbf{i}$, $\phi = 2\pi R$, $\chi = \cos^{-1}\sqrt{1-2R'}$, R and R' are uniform random numbers. The magnitude of the electron velocity vector after the collision is given by

$$v' = \sqrt{\frac{2e(E-\Delta E)}{m_e}} \tag{2.49}$$

where ΔE is an energy loss that depends on the type of collision. For an elastic collision

$$\Delta E_{el} = \frac{2m_e E}{m_i}(1 - \cos\chi) \tag{2.50}$$

For excitation, this energy loss is $\Delta E_{exc} = E_{exc}$, where E_{exc} is the excitation energy threshold (8.32 eV for xenon). For ionization collisions, a new ion and a new electron are added to the simulation at the position of the projectile electron. The electron created is a copy of the projectile and undergoes the same isotropic scattering procedure. To maintain energy conservation, the energy of the projectile electron is first subtracted by the ionization threshold E_{iz} (12.13 eV for xenon). Then, the remaining energy is split equally between the scattered projectile electron and the newly created electron. Thus, the effective energy loss is $\Delta E = (E + E_{iz})/2$ and the final velocity magnitude of both electrons after the collision event is $v = \sqrt{e(E - E_{iz})/m_e}$. The new ion is sampled from a Maxwellian distribution with a temperature T_g, which corresponds to the temperature of the neutral gas.

In contrast with the former case, in ion-neutral collisions it is necessary to perform the collision checks according to the relative velocity between projectile and target particles. Since the target particles are not simulated, a new particle with velocity $\mathbf{v}_N$ is sampled from a maxwellian distribution with a temperature T_g and, before the collision check of eq. 2.47, the projectile velocity is corrected as $\mathbf{v}_R = \mathbf{v}_n - \mathbf{v}_N$. If a elastic collision happens, the ion undergoes isotropic scattering following equation 2.48, but in this case using $\chi = \cos^{-1}\sqrt{1 - R'}$, and a final relative ion velocity

$$v'_R = \sqrt{\frac{2eE\cos^2\chi}{m}} \tag{2.51}$$

After computing the scattering, the final ion velocity is simply reconverted to its former reference as $\mathbf{v}'_n = \mathbf{v}'_R + \mathbf{v}_N$. In the case of charge exchange collisions, since the target particle becomes an ion and the projectile ceases to be simulated, the velocity of the target is simply assigned to the projectile, $\mathbf{v}'_n = \mathbf{v}_N$.

The final piece of information required to simulate the collisions is the neutral density field, $n_g(\mathbf{x})$. For simple simulation cases, where no important gradients are expected in the gas density field, the density can be set to a constant value, $n_g(\mathbf{x}) = n_{g,0} = p/k_B T_g$, where p is the gas pressure. However, for the simulation of the plume, the gas exiting the thruster expands into vacuum and thus a much higher gas density is expected close to the exit plane than in the downstream region. To obtain the gas expansion profile, a particle simulation following the same method as in the PIC case was used. However here, there are no forces acting on the particles, which allows a much faster simulation with only steps d and e of the figure 2.2. This method is similar to a DSMC (Direct Simulation Monte-Carlo) [126], but without considering particle collisions. The mean-free path of the gas for typical values of the neutral flow, $n_g = 10^{18}\,\mathrm{m}^{-3}$ and $T_g = 300\,\mathrm{K}$, is $\lambda \approx 1.7\,\mathrm{m}$, which is much larger than the size of the domain considered here, therefore the flow can be considered effectively collisionless. After the gas simulation, the neutral flow is then weighted using equation 2.3, and the resulting density field is used during

the PIC simulation, with its interpolation at the position of the particles at each time step so that the collision checks can be done. During the neutral gas simulation, the injected mass flow rate is calculated using the value of the mass utilization efficiency, η_m, so that for a given ion current, I_b, it is determined as

$$\dot{m}_g = (1 - \eta_m)\dot{m} = \frac{1 - \eta_m}{\eta_m} \frac{m}{e} I_b \tag{2.52}$$

Since in this case there are no electromagnetic interactions between the particles, the criteria given by equations 2.21, 2.22 and 2.23 no longer need to be fulfilled during the simulation. This allows the simulation to use a longer time step and, since there are no strong gradients expected in the density field, a higher value of the particle weight.

2.3 Development

2.3.1 Code implementation

The PIC simulation code used for this work was implemented using C++11, while the post-processing and data analysis was done using Python 3. Despite using C++, the code organization followed more closely the approach traditionally used with C, focusing more on the handling of the simulation steps through functions rather than a purely object-oriented approach. This was done to decrease the computational overhead of object handling and improve the clarity of several operations. The state of each particle species is represented by a double-precision array of size $6N$, where N is the number of particles, that holds the value of the six components of position and velocity of every particle. Despite being a 2D simulation, to ensure a correct representation of the particle kinetic energy, particularly during the MCC phase, it is necessary to store the velocity information over the three spatial axis, which is called a 2D3V approach [120]. The particle arrays, together with the other data structures holding the simulation state such as the fields, circuit variables, between others, are held by an object of type `simulation` which handles the main calculation loop. The functions used for each of the simulation steps are grouped in classes that contain the required information to process that step. These classes do not contain any simulation state, but they all have a reference to a `configuration` object, which contains the simulation initialization data loaded from a YAML file at the beginning of the run.

During the evolution of the simulation, several diagnostics are registered, including the complete particle state array, potential field, flow fields, energy field, boundary currents, among others. The type and frequency of how each diagnostic is saved is controlled through the configuration file. The diagnostics are all saved using the *Exdir* directory structure proposed by Dragly *et al.* [127]. This data format consists of a hierarchical file structure similar to HDF5, however in this case the datasets are not saved within just one binary file but distributed inside a directory structure with a root that has a `.exdir` extension. In this specification, each dataset is saved inside the directories using Numpy's NPY binary format [128], which can be directly loaded in Python, and attributes and metadata are saved in YAML files. Compared to HDF5 and other binary

formats, Exdir provides the advantages of preventing complete data loss whenever a single dataset is corrupted, not requiring additional libraries for data saving and allowing a native interface with Numpy tools.

To increase the overall performance of the simulations, the code was almost completely parallelized using MPI (Message Passing Interface) through OpenMPI [129]. Because in typical PIC simulations the particles only interact through the fields generated by their own density, the time-evolution of each particle is almost independent making its parallelization trivial. Each MPI process holds an instance of the domain and a separate set of particles which are treated equally. At each time-step, the number of particles to be injected into the simulation is divided equally between the processes and added to their sets, i.e. the electron current injected in the domain of a given process is $I_{e,\mathrm{proc}} = I_e/N_{\mathrm{proc}}$, where N_{proc} is the total number of processes. This way, all steps except step b of figure 2.2 are executed in parallel. The field and circuit solving are performed only at the first process, and to do this, between steps a and b, `MPI_Reduce` is used to reduce the particle density fields and the boundary currents to the main process. After the calculation is finished, `MPI_Bcast` is used to broadcast back the electric field to all processes, so that the calculation loop can proceed. Despite having a limited scalability and a potential performance bottleneck at the field calculation step, this parallelization method offers a considerable improvement since the biggest computational cost of PIC simulations is typically on particle-handling stages. This method was also chosen since it avoids the need for dealing with complex domain decomposition and boundary interfaces so the development process was not overly laborious. Input and output are also handled exclusively at the main process.

The solution of linear systems is a complex field in computer science, and the development and optimization of iterative linear solvers is beyond the scope of this work. Therefore, in step b, the library HYPRE [130] was used to solve the potential field linear system. This library consist of a set of high performance solvers for sparse linear systems, which are designed primarily for massively parallel applications. Despite the parallel optimization, the solvers can also be used in serial applications as in the present case, without considerable performance penalties, and at the same time offering the possibility of future parallelization. The method chosen for the calculations was the SMG (semicoarsening multigrid) solver, since it offered the best performance for the characteristics of the grid used here. The SMG is a finite-difference solver designed for the solution over a rectangular grids of the diffusion equation, $\nabla \cdot (A\nabla f) + Bf = g$, which is reduced to Poisson's equation for $A = 1$ and $B = 0$. This solver requires the number of cells of the grid to be a multiple of two, which was taken into consideration when selecting the simulation conditions.

2.3.2 Benchmarks

To ensure that all modules of the PIC simulation were correctly implemented and that the code produces the desired results, the code was tested with the implementation and replication of the PIC benchmark proposed by Turner *et al.* [121], which consists of a set of 1D simulations of a capacitive discharge using helium as the working gas. This

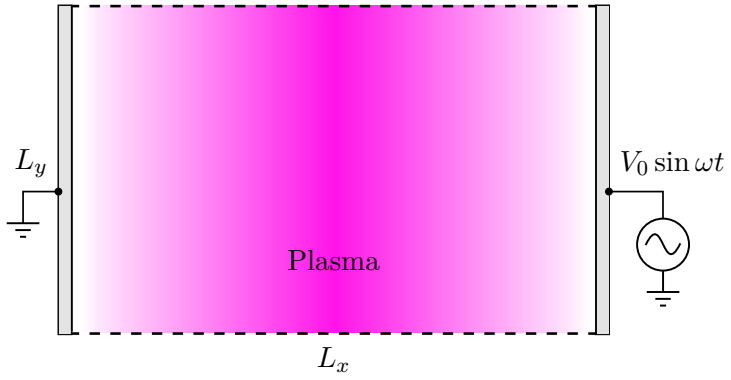

Figure 2.7: Schematics of the capacitive benchmark domain. The LHS and RHS boundaries are Dirichlet-absorbing boundaries and dashed lines represent symmetry boundaries.

benchmark uses a 1D domain with two Dirichlet boundaries, with the LHS boundary set to ground and the RHS boundary biased with a sinusoidal voltage at 13.56 MHz. At the beginning of the simulation, the domain is initialized with a uniform density of ions and electrons, and the discharge evolves self-consistently in time, without the need of an external source of particles. This is possible due to the MCC algorithm, which reproduces the generation of new particles through its reactions, permitting a self-sustainable discharge. The benchmark consists of four different simulation cases with increasing computation time and different values of neutral pressure, initial plasma density, time step, simulation time and grid spacing.

Because the code developed for this work uses two dimensions, it was necessary to adapt the benchmark domain to be represented in a 2D grid. Figure 2.7 shows the modified domain used for the benchmark simulations. As in the 1D case, the lateral boundaries are of the Dirichlet type with the LHS boundary set to zero, and the RHS set by $\phi_0 = V_0 \sin \omega t$. The top and bottom boundaries are set to be Neumann-type reflecting boundaries to act as symmetry planes. This way, because of the symmetry in y, the simulation replicates the 1D case in the x-direction, with no gradients in the y-direction. Because no electric fields are expected in y, only four cells are used in this direction and $L_y = L_x/2$ is assumed. To maintain a statistical equivalence between the benchmarks and the present simulation, the number of particles-per-cell, N_{PPC}, was maintained, so the number of particles simulated in this case was increased as $N_T = (N_x - 1)(N_y - 1)N_{\mathrm{PPC}}$, where N_x and N_y are the number of cells in x and y respectively. Because N_{PPC} and the initial plasma density, n_0, are specified by the benchmark description, it is possible to calculate the particle weight factor as

$$N_p = \frac{n_0 L_x L_y}{(N_x - 1)(N_y - 1)N_{\mathrm{PPC}}} \tag{2.53}$$

The results of the benchmark simulations are shown in figure 2.8. To obtain the 1D field profiles displayed, the values of the 2D density fields were averaged in the y-direction, which also reduced the statistical noise. The plots show the comparisons

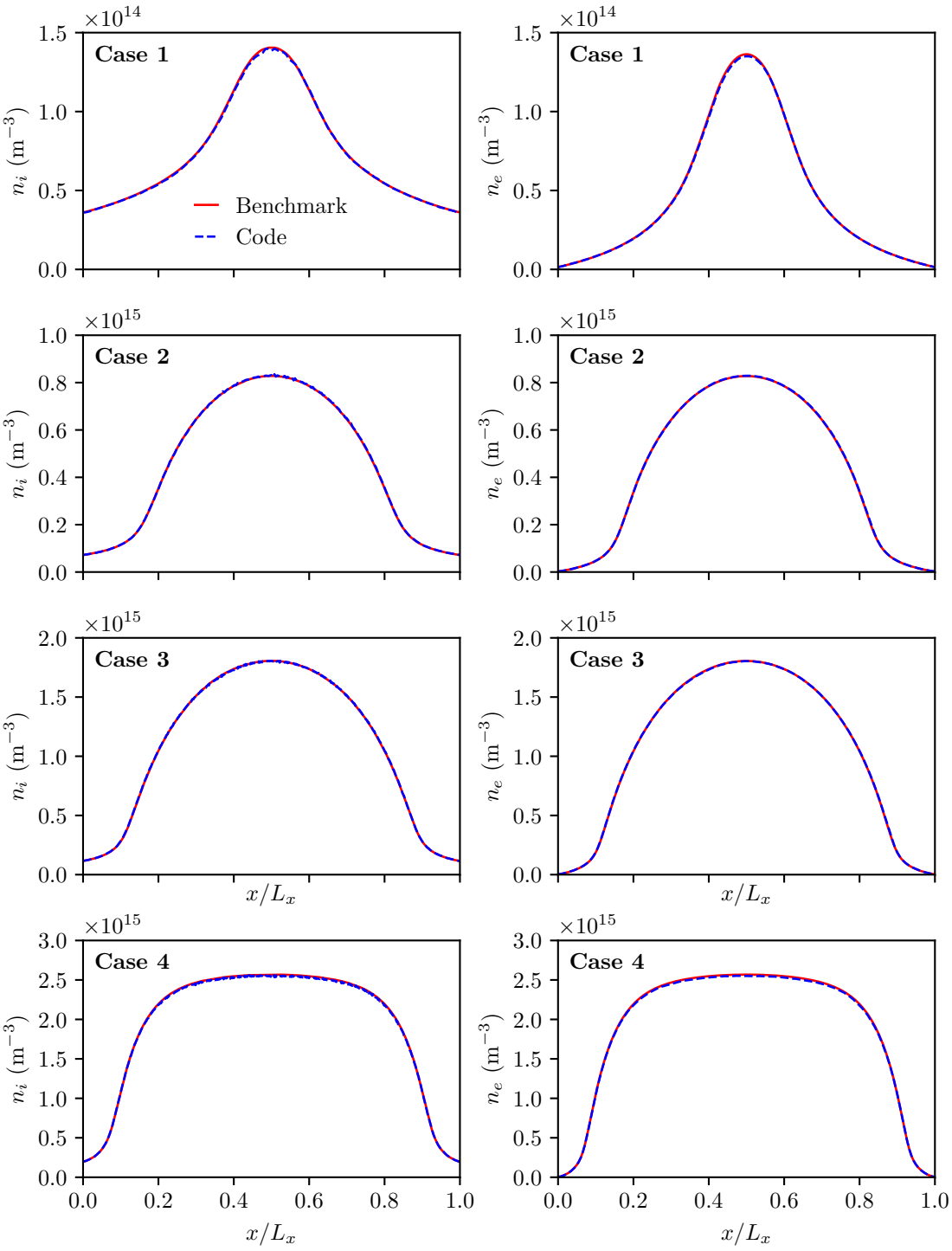

Figure 2.8: Comparison of ion density, n_i, and electron density, n_e, profiles generated by the code and the results from the benchmark.

between the ion and electron density curves provided by the benchmark and results obtained in the present simulation, for the first three cases of the benchmark. It is possible to observe that the simulation results show good agreement with the benchmark for all cases, with almost negligible statistical noise. The first benchmark case is the only one that presents a noticeable difference between the results, this is because the first benchmark has the lowest level of averaging, number of particles and total simulation time, making it more susceptible to statistical fluctuations. It is important to notice that the benchmark simulations are sensitive to almost any difference in the physics of the simulation, therefore any mistake or bug in the PIC calculation steps would be directly noticeable from the final result comparisons. Therefore, the good agreement between the curves is strong evidence that the modules are performing correctly, reproducing the same phenomena in terms of particle movement, field calculations and collisional processes.

2.4 Results

2.4.1 Simulation conditions

The simulation work is divided into two main parts: (1) a comparison of a DC and an RF plume expansion case with the objective of identifying the major differences between both and (2) a parametric study of the RF plume expansion simulation with the variation of different parameters, particularly the excitation frequency f, the current ratio α, and the boundary capacitance C_B. Table 2.1 shows the fixed simulation parameters used for the different simulation cases and table 2.2 shows the parameters which are varied during part 2. The parameter range selected corresponds to values typically found in ion thrusters. However, it is important to note that some of the parameters that are kept fixed during the simulation, such as J_i, E_i and E_e, could have an important impact on the behavior of the system. Therefore, future investigations might be needed to better understand their influence on the expansion.

In part 1, one of the cases in the range shown in table 2.2 is selected as the "nominal case" for comparison with a reference DC plume expansion case. The nominal RF case uses $f = 30\,\mathrm{MHz}$, $\alpha = 3$ and $C_B = 10^{-11}\,\mathrm{F}$. This group of parameters is similar to what was used in previous simulation works [66], which allows a more direct comparison of results, and also satisfies the frequency constraint from equation 1.65 which gives approximately 14.23 MHz in the selected parameter range, assuming $L_{\mathrm{eff}} = 1.35\,\mathrm{mm}$ as in the references [66, 68]. The capacitance used in the nominal case is close to what is found experimentally in laboratory setups with a floating ion source within a vacuum chamber, and also close to the capacitance of a spherical body in space, $C \sim 2\pi\varepsilon_0 D$, with a diameter D of the order of 10 cm. In part 2, 20 different cases are simulated, 10 values of f, 4 values of α, and 5 values of C_B.

The electron injection in the DC plume simulation is done using equation 2.25 and in the RF plume using equation 2.31. As shown in the parameter table, the electrons in the RF cases are injected with an initial drift energy of 50 eV. This is done because, in

Table 2.1: Fixed simulation parameters.

Parameter		Value
Reference Debye length	λ_D (mm)	0.220
Reference electron plasma frequency	$\omega_{p,e}$ (rad/s)	$4.37 \cdot 10^9$
Number of horizontal cells	N_x	512
Number of vertical cells	N_y	128
	$\Delta x/\lambda_D$	1
Horizontal domain length	L_x (mm)	112.42
Normalized horizontal domain length	$L_x/\Delta x$	511
Vertical domain length	L_y (mm)	27.94
Normalized vertical domain length	$L_y/\Delta x$	127
Source exit length	L_s (mm)	$15\lambda_D$
Time step	Δt (s)	$5 \cdot 10^{-12}$
	$\omega_{p,e}\Delta t$	0.022
Simulated time	t_s (µs)	12
Simulated time steps	N_s	$2.4 \cdot 10^6$
Time steps per RF period[1]		6667
Particle weight	N_p	$3.2 \cdot 10^5$
Average particles-per-cell at equilibrium[1]		102.48
Ion energy	E_i (eV)	1000
Initial ion density	n_s (m^{-3})	$6 \cdot 10^{15}$
Ion current density	J_i (A/m^2)	35
Ion mass (Xe)	m_i (kg)	$2.18 \cdot 10^{-25}$
Ion temperature	T_i (K)	300
Initial electron drift energy	E_e (eV)	50
Electron temperature	T_e (eV)	5
Neutral gas mass flow rate	$\dot{m}_g$ (mg/s)	0.15

previous grid simulations [66, 68], it was observed that because of the ion space charge between the grids during the electron emission pulse, the electrons were accelerated and left the grid region with drift energies between 20 and 80 eV. A higher electron energy in the axial direction was also observed in past experiments [65] when quantifying the anisotropy of the electron energy distribution. In the DC case on the other hand, the electrons are injected simply as a Maxwellian flux without any initial drift energy.

The complete domain has approximate dimensions of 11.24 cm by 2.79 cm. The injection length, L_s, is roughly 3.3 mm which is much smaller than the typical ion thruster diameter due to computational reasons. However, this can be viewed as representing plasma extraction from acceleration grids with a single aperture. The numerical grid spacing is the same in both directions and given by $\Delta x = \Delta y = \lambda_D$, which is less than the Debye length found in the downstream plume since the temperature of the electron population is much greater than T_e in the pulsed case (and approximately the same in

[1]For the nominal RF condition.

Table 2.2: Variable simulation parameters.

Parameter		Range
Frequency	f (MHz)	5–55
Electron-to-ion current ratio	α	1–5
Boundary capacitance	C_B (F)	10^{-12}–10^{-8}

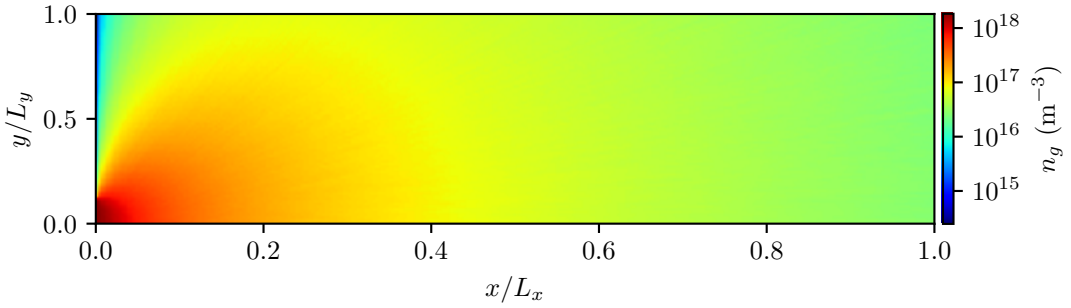

Figure 2.9: Neutral density field, n_g, generated by the simulation. The density is shown on a logarithmic scale.

the DC case), and the plasma density is much lower than that at the source exit which is used to calculate the reference Debye length. The total simulation time of 12 µs is selected for the RF case because it guarantees that every case achieves a good steady-state, with no significant subsequent variations. In the DC case, the simulation of the expansion requires a shorter time to achieve equilibrium, thus the total simulation time used is 6 µs.

Before the plume simulations, the neutral flow used for the collision calculations was simulated using the method described in section 2.2.4. The flow is injected at 300 K and with a mass flow rate of 0.15 mg/s. In this case, the time step used was $\Delta t = 2 \times 10^{-9}$ s, the total simulation time $t_s = 1$ ms, and the particle weight factor $N_p = 10^8$. To improve the statistical quality of the density field used in the MCC phase, the neutral density field was averaged over 5×10^4 time steps before being saved. The resulting density field, used for all plume simulations, is shown in figure 2.9.

2.4.2 DC plume expansion

In this section, the main results of the DC plume expansion simulation will be shown. The focus is to highlight its main features, so that in the next section, the DC and RF expansion characteristics can be compared.

Figure 2.10 shows the ion density and electric potential profile of the DC plume at steady-state. It is possible to observe that the density field follows a typical ambipolar expansion, similar to what is found in previous works that performed analogous simulations [108, 113]. Apart from statistical noise differences, the peak density near the source exit is

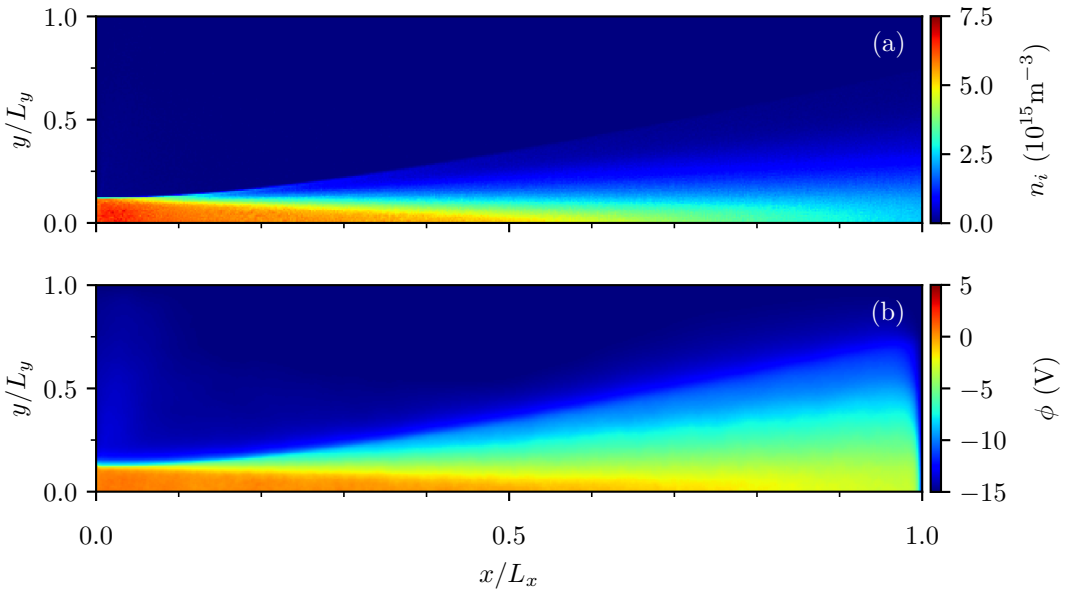

Figure 2.10: Result of the DC plume expansion in steady-state. (a) shows the ion density field, n_i, and (b) shows the electric potential profile.

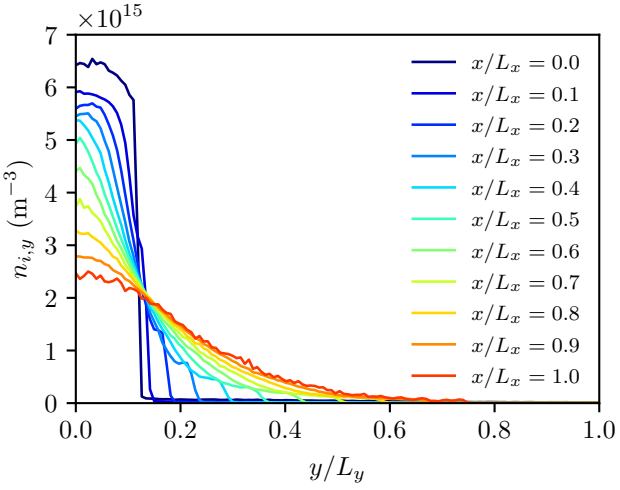

Figure 2.11: Ion density along the y-axis for different values of x.

around $6 \times 10^{15}\,\mathrm{m}^{-3}$ as expected from the injected ion current density and energy defined in table 2.1. As is typically seen in hypersonic plume expansions, it is possible to observe the formation of a Mach cone with a length of roughly $310\lambda_D$. Using the formulation of equation 1.77, this cone would roughly correspond to a Mach number of 19.4, which is

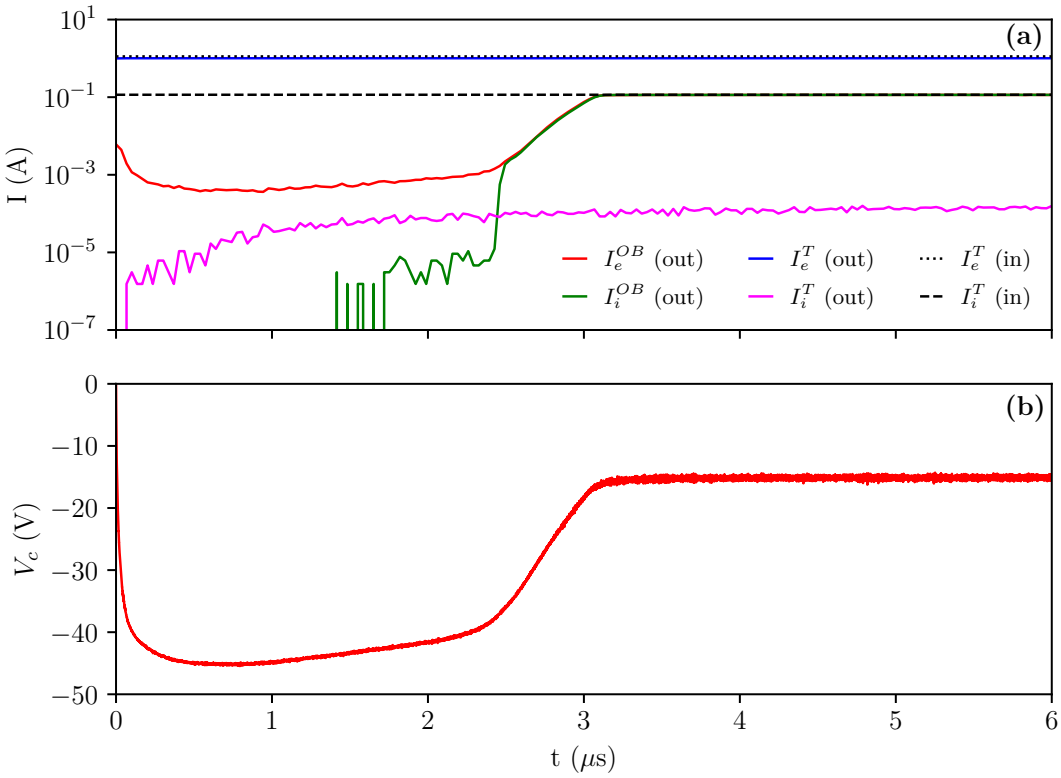

Figure 2.12: Temporal evolution of voltages and currents in the DC plume simulation. (a) shows the ion and electron current entering and leaving the domain through each boundary. Superscript OB refers to the outer boundary and T to the thruster boundary. (b) shows the capacitor voltage, V_c.

close to the injection Mach number, $M = 20$. Figure 2.11 shows the ion density along the y-axis for different values of x. As stated in section 1.3.3, there is an important similarity between these radial profiles and the 1D plasma free expansion models, including the formation of a density peak at the ion front as the plasma propagates outwards. The average electron energy over the complete domain is around $\langle E_e \rangle \approx 6.25\,\text{eV}$. Since there is no significant drift velocity in the electron population, the average temperature can be approximately estimated using equation 1.21, which gives $T_e \approx 4.17\,\text{eV}$. Apart from the approximation errors of using this formulation, this decrement in the temperature, from 5 eV, can be associated with electron cooling mechanisms during the expansion. The potential field is shown in fig. 2.10b, where it can be seen that the peak plume potential in this case is about 1 V close to the exit surface of the thruster. The potential descends monotonically until the outer boundary, which is at the capacitor voltage, where a sheath is formed.

Figure 2.12 shows the temporal evolution of the ion and electron currents entering

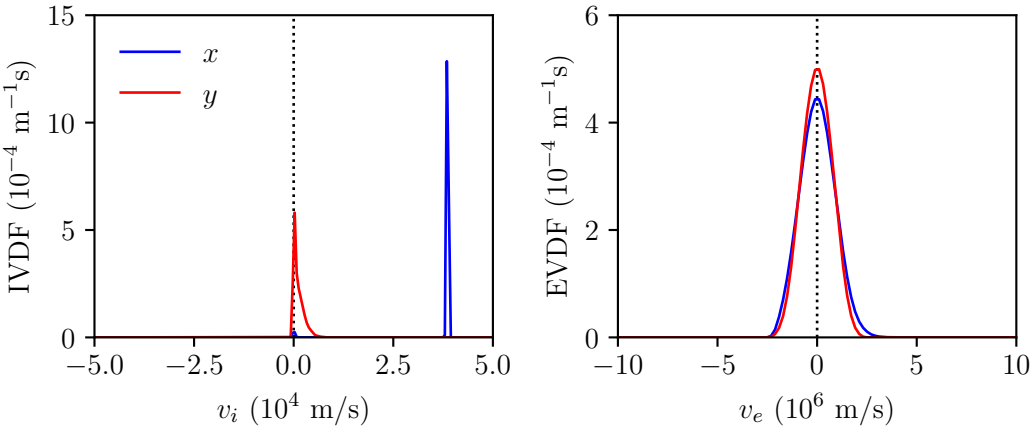

Figure 2.13: Velocity distribution function of ions (left) and electrons (right) over the whole domain, for the DC expansion.

and leaving the domain (a) and the boundary capacitor voltage (b). Observing both plots, it is possible to see that the simulation effectively achieves steady-state at around 3 µs, and after that there is no significant variation in any quantity. During the transient phase, when ions are propagating downstream, it can be seen that only electrons are able to reach the outer boundary due to their higher mobility. As soon as the ion front reaches the outer boundary, the electron current matches the ion current, so that current balance is maintained at the capacitor, as expected. In the first part, the capacitor voltage goes initially to a negative minimum at around −45 V, due to the electron current. When the ion front reaches the outer boundary, the capacitor voltage rises and stabilizes at roughly −15.11 V. Since the capacitor circuit ensures an equal current of ions and electrons at the wall, the voltage is close to the potential of a floating body inside a plasma. Considering an ion current given by $I_i = eA_i n_i \sqrt{2eE_i/m_i}$, where A_i is the effective ion loss area to the walls, and an electron current given by the boltzmann relation (eq. 1.12), the floating wall potential inside the beam can be calculated as

$$\phi_f \approx -T_e \ln \left[\frac{A_e}{A_i} \sqrt{\frac{T_e m_i}{4\pi E_i m_e}} \right] \tag{2.54}$$

Using $A_e \approx A_i$, $T_e \approx 5\,\text{eV}$ and $E_i \approx 1\,\text{kV}$, the floating potential is $\phi_f \approx -11.4\,\text{V}$ – similar to the capacitor voltage in equilibrium. It is also possible to observe that throughout the simulation, a major fraction of the electron population actually returns to thruster boundary, which is necessary to maintain the current-free condition while ensuring local quasi-neutrality. Lastly, it is also possible to observe the slow increase of the backstreaming current due to the slow-ion population formed in the plume; at steady-state, its magnitude is around 0.1 mA, which is the same order of magnitude as the predictions made in section 1.3.4.

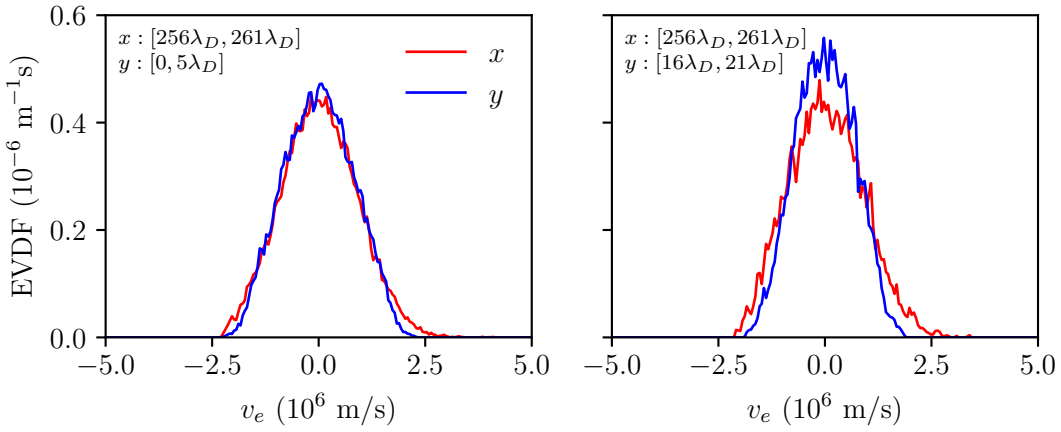

Figure 2.14: Local electron velocity distribution function within a box of size $5\lambda_D \times 5\lambda_D$. The function is calculated for $x = 256\lambda_D$ at $y = 0$ (left), and $y = 16\lambda_D$ (right).

Figure 2.13 shows the velocity distribution function of ions and electrons over the whole domain, in both directions. The ion distribution shows a peak in the x-direction at 38 442.2 m/s, which corresponds to the energetic ion beam propagating downstream at roughly 1 keV. Since the ions are injected with a thermal spread in the y-direction, their distribution in this direction is around zero, and the elongation of the tail towards positive values is due to expansion by the ambipolar fields created by the electron population. It is also possible to see the formation of a short peak in the x-direction close to zero, which corresponds to the population of slow ions created in the plume by CEX and ionization. The electron distribution shows, as expected, that the electron population is approximately Maxwellian in both directions. However, it is possible to see that there is a noticeable anisotropy, with a slightly wider distribution in x. This can be explained by electron cooling that takes place during the expansion with the transfer of energy to ions, which happens namely in the y-direction. This can be seen as well in figure 2.14, where the local electron distribution function is shown for two different locations in the plume. These distribution functions are calculated for a box of size $5\lambda_D \times 5\lambda_D$, with the lower-left corner at $(256\lambda_D, 0)$ in the LHS plot and $(256\lambda_D, 16\lambda_D)$ in the RHS plot. It is possible to observe that the electron distribution at the axis, inside the Mach cone, is essentially isotropic. On the other hand, the second plot, which is closer to the edge of the beam, in a region of radial ambipolar expansion, shows less energetic electrons in the y-direction as in the case of the global distribution function.

2.4.3 RF plume expansion

In this section, the results of the nominal RF simulation are presented and compared with the DC plume expansion, showing the main features and unique phenomena during pulsed neutralization.

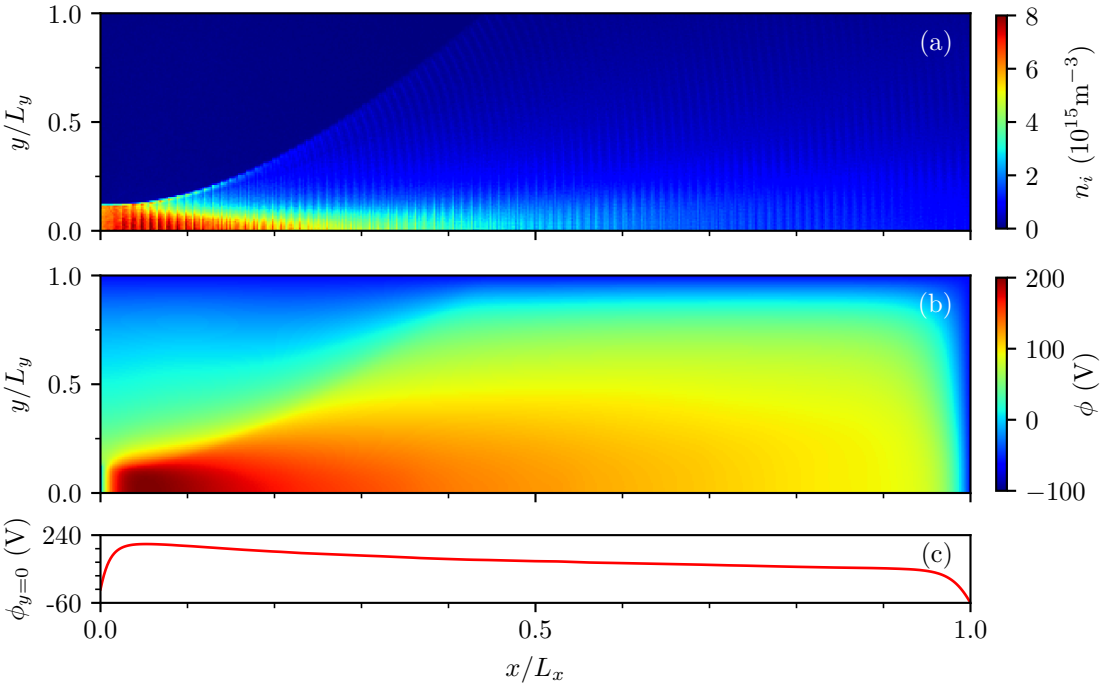

Figure 2.15: Result of the nominal RF plume expansion at steady-state. (a) shows the instantaneous ion density field, n_i, (b) shows the electric potential profile averaged over one RF period and (c) shows the potential field at the axis ($y = 0$) of the plume.

Figure 2.15 shows the instantaneous ion density field and the electric potential field averaged over one RF period. The density field presents a number of unique features when compared to the DC expansion in figure 2.10. Firstly, it is possible to notice the much higher beam divergence, which is a direct consequence of the higher electron temperature in the plume. In this case, the average electron energy in the domain is approximately 46 eV, which increases significantly the magnitude of the transverse ambipolar fields. The higher electron energy is mainly connected to the initial electron drift energy, at which they are injected. Nevertheless, despite the injection drift energy being in the axial direction, electrons are considerably thermalized and heated in the transverse direction due to collisions and electrostatic oscillations. The higher electron temperature also causes a shorter Mach cone, which in this case ends at roughly $128\lambda_D$. In this case, this would suggest a $M \approx 8$, which is consistent with an estimation using equation 1.76 considering ions at 1 keV and electrons with a temperature $T_e \approx (2/3)46\,\text{eV} \approx 31\,\text{eV}$. The second important feature is the formation of wave-like structures that propagate downstream with the same velocity as the ion flow. These structures appear because of the strong oscillations in the potential field close to the thruster's exit during the injection of the electron pulse. During the major part of the RF cycle, only ions are injected into the plume. In this way, there is a continuous accumulation of positive charges close to the thruster's exit that builds up a space-charge region with a potential hill that slightly

slows down incoming injected ions increasing their local density and forming a bunched group. When the electron pulse occurs, the potential drops rapidly and the ions remain grouped as they move downstream. Because the ion thermal energy is much lower than their drift energy, and the low neutral pressure does not favor collisions, these higher density structures remain coherent in the axial direction. On the other hand, because of the high electron mobility, the plume is kept quasi-neutral, especially in the downstream region and the wave structures do not create any significant electric field perturbations. There are as well a number of unique features in the average potential field. Figure 2.15c shows the potential at the axis ($y = 0$) of the plume and it can be noticed that the peak average potential in the domain is around 200 V, which is considerably higher than any DC plume. This is also a direct consequence of the more energetic electrons, which can escape the plume in a larger number, elevating the overall plasma potential. It is important to notice however, that this situation is analogous to the operation of a DC thruster. In DC systems, the accel grid is generally biased to a negative voltage (-50 V to -250 V) so that electrons do not backstream into the thruster. This backstreaming effect can be clearly seen in figure 2.12, where no negative voltage is applied to the injection surface and almost all the electron current drawn from the cathode goes back to the thruster. In the RF case, however, to ensure that electrons are trapped, the plume must acquire a high-enough positive potential to reduce this backstreaming current and guarantee quasi-neutrality. In this way, the grounded accel grid acts effectively as a negatively biased electrode with respect to the plume potential, with the formation of a sheath at the thruster exit, as can be seen in figure 2.15c. The same process was seen as well in previous simulations of the grid system during the RF acceleration process [66, 68]. The plume potential at 30 MHz reported by Lafleur *et al.* [68] is approximately 180 V, which is close to what is observed here for the nominal case, suggesting that the physical processes that trap and control electrons are similar in both models.

Figure 2.16 shows the velocity distribution of ions and electrons over the whole domain and averaged over one RF cycle during steady-state, which can be directly compared to the DC distributions shown in figure 2.13. First, it is possible to observe that, compared to the DC case, the ion high-energy peak is broader and has a slightly lower mean value. The lower mean value is a direct consequence of the higher plume potential that slows down on average the ion flow, while the increase in the peak width can be explained by the continuous potential oscillations that tend to modify the velocity distribution of the initially coherent ion beam. It can also be noticed that the low-energy ion peak is also more prominent which is a consequence of the higher ionization rate due to the hotter electrons. The electron distribution shows a clear non-Maxwellian behavior with a much stronger anisotropy. In this case, electrons are more energetic in the x-direction, due to their initial drift energy and other acceleration mechanisms such as the sheath formed in front of the accel grid due to the accumulation of positive charges. Nevertheless, the distribution in the y-direction also shows a hot tail of electrons. This is due to thermalization caused by electron-neutral collisions and scattering from electrostatic oscillations in the plume. This anisotropic behavior was also observed in previous experiments performed by Rafalskyi and Aanesland [65], where the energy

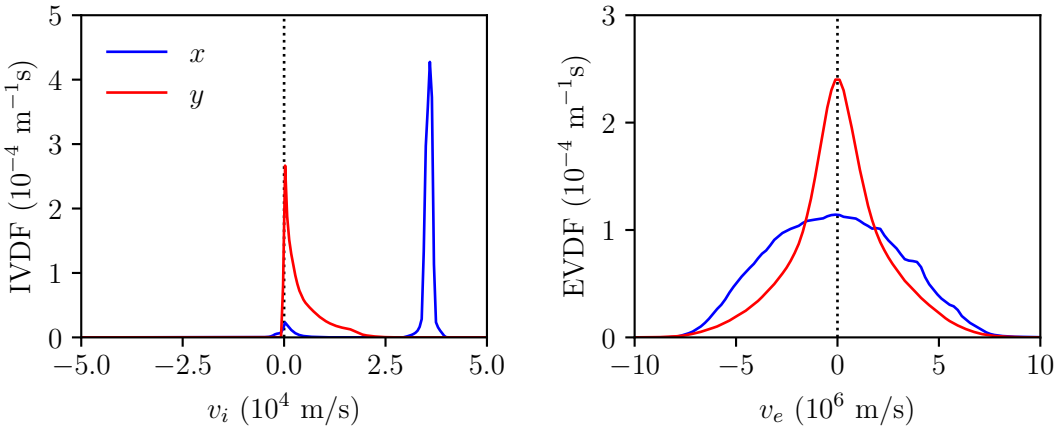

Figure 2.16: Velocity distribution function of ions (left) and electrons (right) over the whole domain, for the nominal RF expansion.

distribution of electrons was measured in the axial and radial directions of the plume.

The temporal evolution of the average currents in the domain and the charging of the capacitor is shown in figure 2.17. First, it is possible to observe that the system achieves steady-state around 6 µs, which is roughly double the DC case. This can be explained by the higher plume potential that, on average, slows down the ions while they are propagating downstream, and the higher production rate of slow particles. The higher number of slow ions can also be seen in the magnitude of the ion backstreaming current, I_i^T, shown in the figure which is roughly ten times higher than in the DC case. This difference is due to the higher electron temperature that increases significantly the electron-impact ionization rate. This can also be seen if one considers the figure 1.11 where, for ions at 1 keV, the temperature required for ionization to become more dominant than CEX is around 7 eV, which is much lower than what is observed in the RF expansion. Therefore, the dominant process for slow ion production in this and the other RF plume simulations done in this work, is typically ionization.

The temporal evolution of the capacitor voltage shown in 2.17b shows a number of unique features as well. First, in this case, the capacitor voltage signal presents continuous rapid variations with an amplitude of approximately 125 V, related to the pulsed electron injection and the plume variations. The overall curve envelope follows a similar trend to the DC case with an initial drop followed by an approach to equilibrium. However, here, the lower limit value is around −700 V which is due to the more energetic electron population. The average trend of the capacitor voltage also shows a considerably longer time to achieve steady state, around 8 µs, which is about 2 µs longer than the equilibrium of the currents. At steady-state, the capacitor has a time-averaged voltage (over one RF cycle) of $\langle V_c \rangle \approx -60.51$ V, which can also be seen in the outer boundary sheath in figure 2.15c. Since the floating potential of a metallic body is strongly dependent on the electron temperature of the plasma, and since the average electron energy is significant

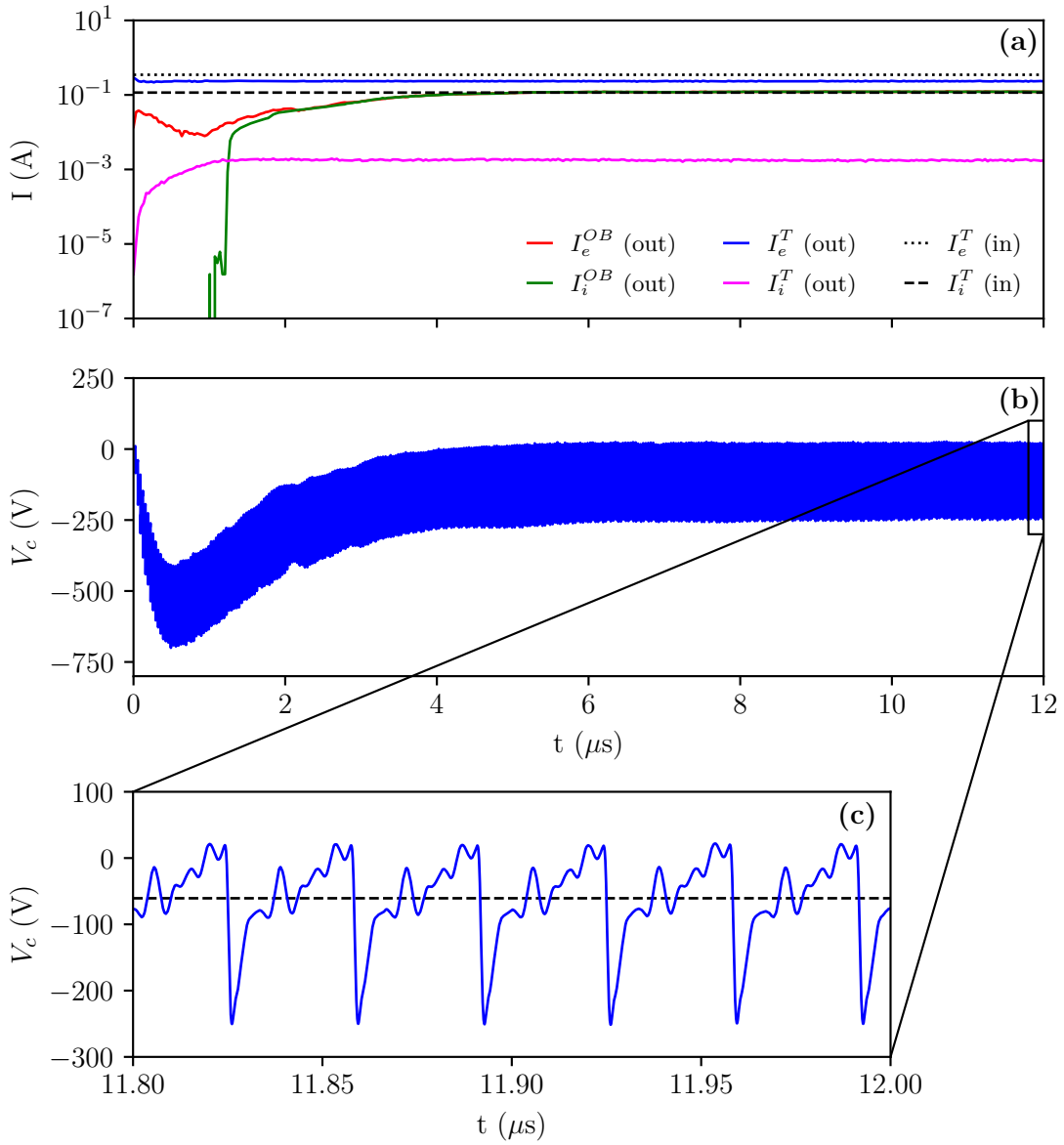

Figure 2.17: Temporal evolution of voltages and currents in the nominal RF plume simulation. (a) shows the average ion and electron current entering and leaving the domain through each boundary. The average is done over one RF cycle. Superscript OB refers to the outer boundary and T to the thruster boundary. (b) shows the capacitor voltage, V_c. (c) shows the detailed view of the voltage capacitor between 11.8 µs and 12 µs, and the dashed line marks the average capacitor voltage at steady-state $\langle V_c \rangle = -60.51\,\mathrm{V}$.

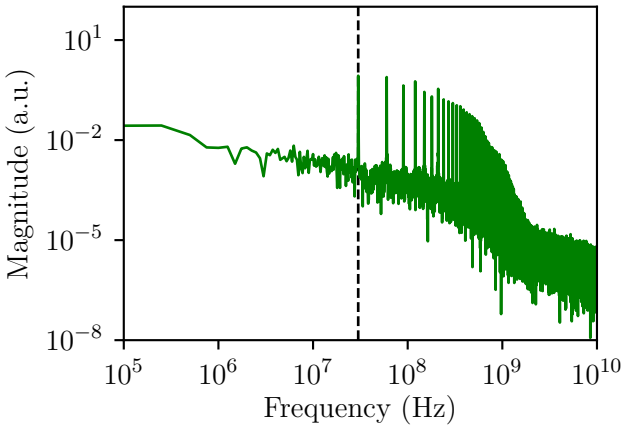

Figure 2.18: Fourier transform of the capacitor voltage signal at steady-state, between 8 and 12 µs. The dashed line shows the position of 30 MHz.

higher in the RF case, the average voltage to ensure equal ion and electron currents over an RF period is expected to have a higher magnitude than the DC case, as is indeed observed. As shown in figure 2.17c, the oscillations of the capacitor voltage present a large negative spike as a consequence of the electron pulsed injection, and a number of shorter spikes related to the back and forth reflection of the electron beam between the injection electrode and the outer boundary. This electron bouncing effect was also observed in previous simulations [66]. Figure 2.18 shows the Fourier transform of the capacitor voltage signal between 8 and 12 µs. The main peak of the spectrum is at 30 MHz, which is the RF injection frequency used in the nominal case, and a number of smaller peaks that correspond to harmonics of this frequency which are located at multiples of the fundamental frequency. These harmonics indicate the presence of secondary electron oscillations within the plume which may be connected to their bouncing between the thruster and the outer boundary sheaths, or the presence of electron waves created by the interaction of subsequent pulses which create different interference patterns, and possibly complex streaming instabilities due to forward and counter-propagating beams. Despite having different origins, these electron beams are also found in low-pressure CPPs [131].

Figure 2.19 shows the detailed view of the ion and electron currents entering and leaving the domain over three RF periods at steady-state. The injected electron current is shown in the first row. It is possible to observe the shape of the electron pulse as given by equation 2.31 repeating itself at the beginning of every RF period. The second row shows the electron current leaving the domain through the injection boundary. It is possible to see that there is an important part of the electrons that are reflected back to the source just after the pulse, which is caused by the formation of a virtual cathode as a consequence of the high magnitude of the current pulse. After the initial reflection, a smaller electron current continues to flow back to the injection plane during the rest of the RF cycle. The average value of the electron backstreaming current is approximately

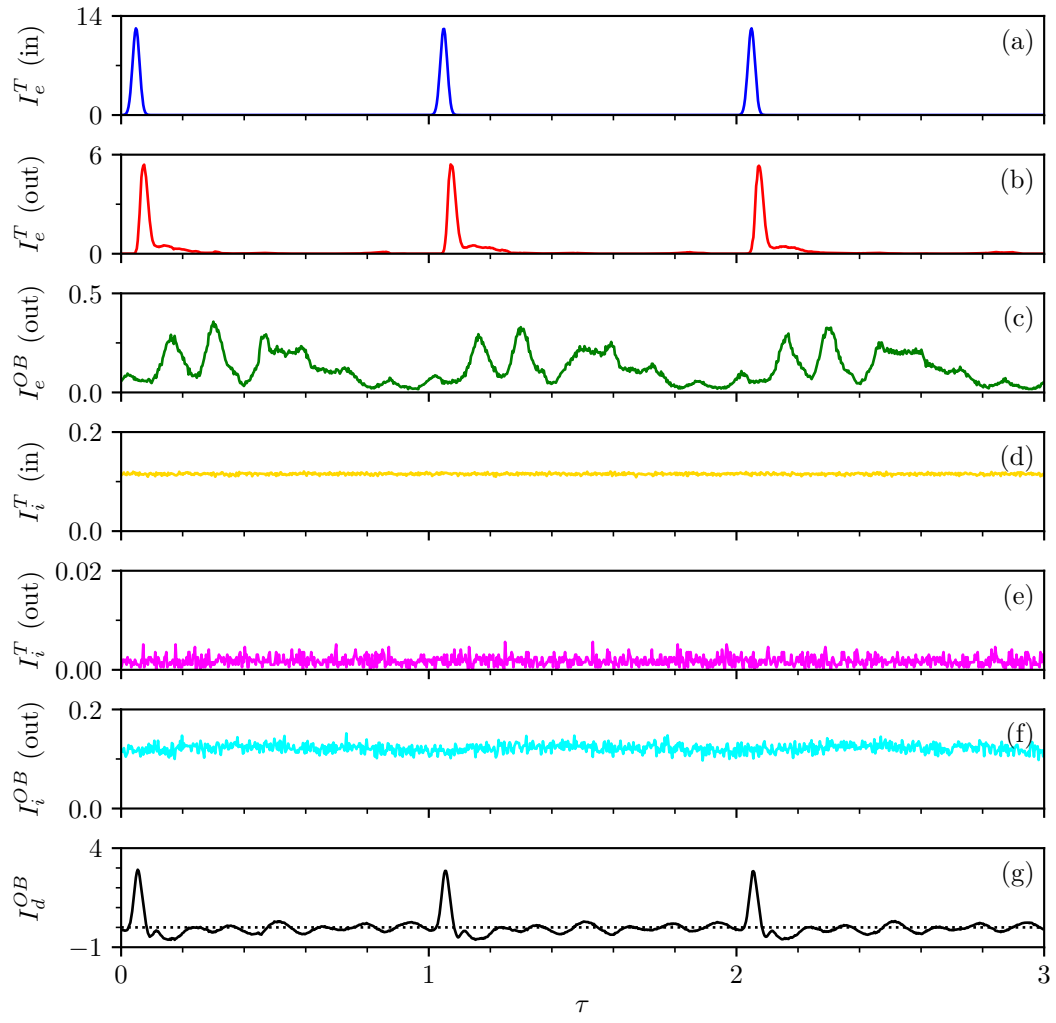

Figure 2.19: Particle currents entering and leaving the domain boundaries over three RF periods. τ is a normalized time given by $\tau = (t - t_0)/T$, where $t_0 = 11.69\,\mu s$. Electron and ion currents are represented by the subscripts e and i respectively. The superscript T represents the currents at the thruster boundary and OB at the outer boundaries. I_d^{OB} is the displacement current at the outer boundary. All currents are expressed in amperes (assuming an out-of-page simulation length of 1 m).

$\langle I_e^T \rangle \approx (\alpha - 1) I_i$, which is necessary to keep the current free condition. The dynamics of the electron reflection during the pulse injection can also be visualized in figure 2.20. This figure shows the density of particles in the x-v_x phase-space for $0 \leq x \leq 20\lambda_D$, during the injection of the first electron pulse of the simulation when only a small ion population is present in the domain. It is possible to see that the pulse starts as a monoenergetic electron beam propagating forward, and when the space charge is high enough, part of

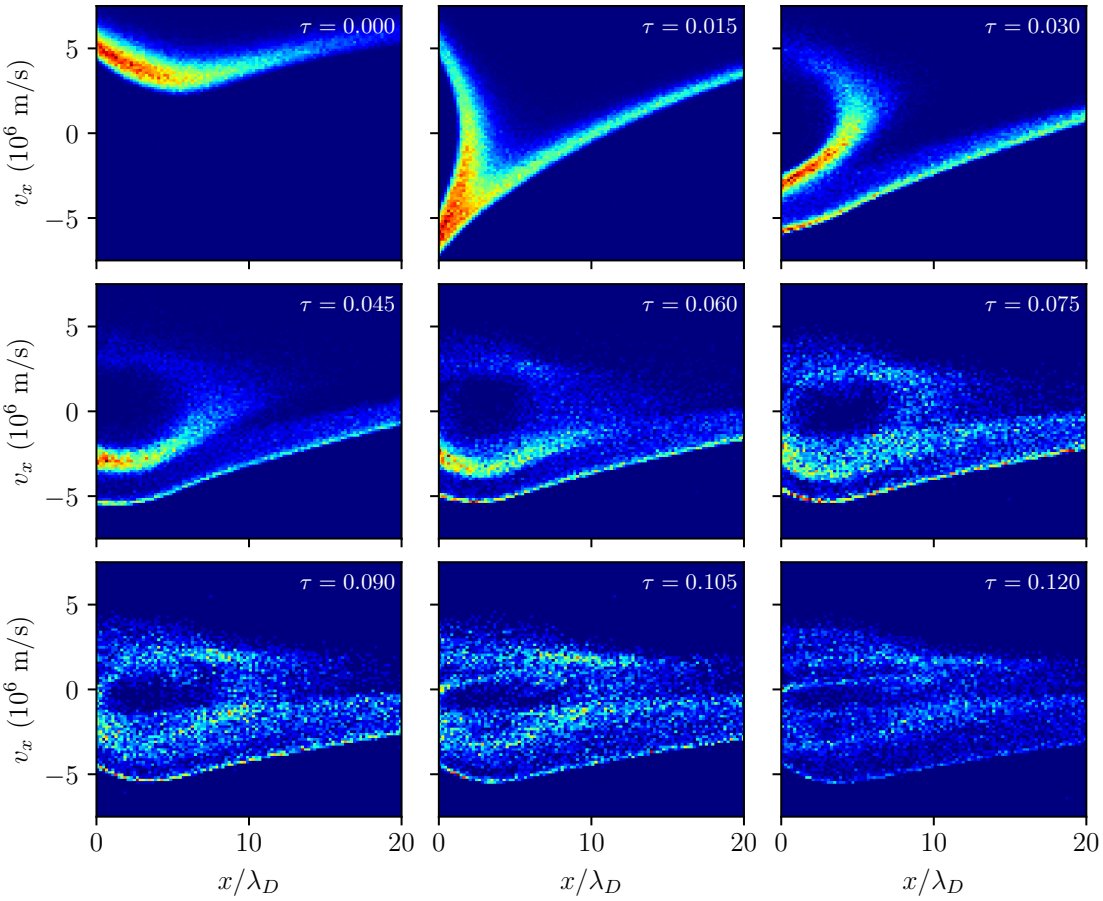

Figure 2.20: Particle density in the x-v_x phase-space during the first RF cycle of the simulation. Here $\tau = (t - t_0)/T$ and $t_0 = 25\,\text{ns}$.

the beam is reflected back to the source with a similar velocity magnitude. After this, part of the electron population continues to propagate downstream towards the outer walls and another part gets trapped in a circulating trajectory in phase-space, close to the exit of the thruster, which ensures the neutralization of the ion population. A similar backstreaming effect was seen in the simulations performed by Lafleur and Rafalskyi [66], including the electron trapping resulting in a circulating electron population at the exit of the thruster. Depending on the energy and the phase location in the RF period of these backstreaming electrons, they may enter directly within the grid set and be further accelerated backwards to the upstream plasma discharge. This beam may disturb the discharge and be an additional factor of undesired power consumption.

The electron current flowing to the outer boundaries, I_e^{OB}, can be visualized in the third row of figure 2.19. The first characteristic that can be seen is that the amplitude of its oscillation is much lower than the injected and reflected currents, with an average magnitude given by $\langle I_e^{OB} \rangle = I_i$. Despite the short and intense electron pulse profile, it is

possible to see that the actual electron current collected at the outer boundaries has a broader profile with several higher frequency short peaks. These peaks are associated with the oscillation of electrons between the potential well at the source exit and the sheath in front of the outer boundary walls, and their higher frequency can be related to the electron transit time. This electron current profile has a very similar shape to what was observed in the experiments done by Dedrick *et al.* [67], where an electrostatic probe was used to measure the time-resolved ion and electron current emitted by an ion thruster using RF grid biasing. This resemblance suggests that the model used here can successfully replicate, at least partially, the dynamics of the electrons within the RF plume and shows that self-induced electrostatic waves are an important aspect of pulsed neutralization.

The next three rows of figure 2.19 (d, e and f) show the ion current entering and leaving the domain. It is possible to observe that their profile is not greatly affected by the potential oscillations in the plume and their magnitude is coherent with what is expected. The only difference compared with the DC case, as already shown in figure 2.17a, is that the production of slow ions is augmented by the higher electron temperature and therefore the backstreaming ion current is also increased. The last row in the figure shows the displacement current, I_d^{OB}, at the capacitor circuit, caused by the potential oscillations in the plume. It is possible to see its magnitude is considerably higher than the actual particle (convection) current reaching the walls, thus having an important contribution on the charging of the boundary capacitor. Since the electron current reaching the outer boundary has a broader profile, the sharp spikes seen in the capacitor voltage signal during steady-state, shown in figure 2.17c, are mainly caused by the displacement current. This shows that the displacement current has an important impact on the dynamics of the system and any modeling of the system's behavior must necessarily take this into consideration.

For the proper neutralization of the ion beam to occur, a number of processes must take place to trap some of the energetic electrons that are propagating downstream in the plume to maintain quasi-neutrality. Figure 2.21 shows the profile of the axial potential field ($y = 0$) during the injection of an electron pulse at steady-state, and can provide a partial visualization of some of these mechanisms. As shown in the first plot, at $\tau = 0$, when the electron pulse occurs, the plume has an excess of ions and the electrons at the leading edge of the pulse are accelerated by this positive potential hill towards the downstream region. However, as already mentioned and shown in figure 2.20, the density of electrons becomes high enough to bring the local potential to a very low value, making the sheath in front of the thruster collapse, and accelerating part of the electrons backwards towards the thruster. This can be seen in the plots for between $\tau = 0.03$ and 0.045. From that moment on, the group of electrons that continues to propagate downstream creates a local negative potential well which further accelerates electrons which are located at its leading edge and decelerates electrons at its trailing edge. This electrostatic wave also accelerates and decelerates part of the thermalized electron population that was already in the downstream region of the plume, increasing its magnitude and creating secondary waves. The group's potential well can be seen at the

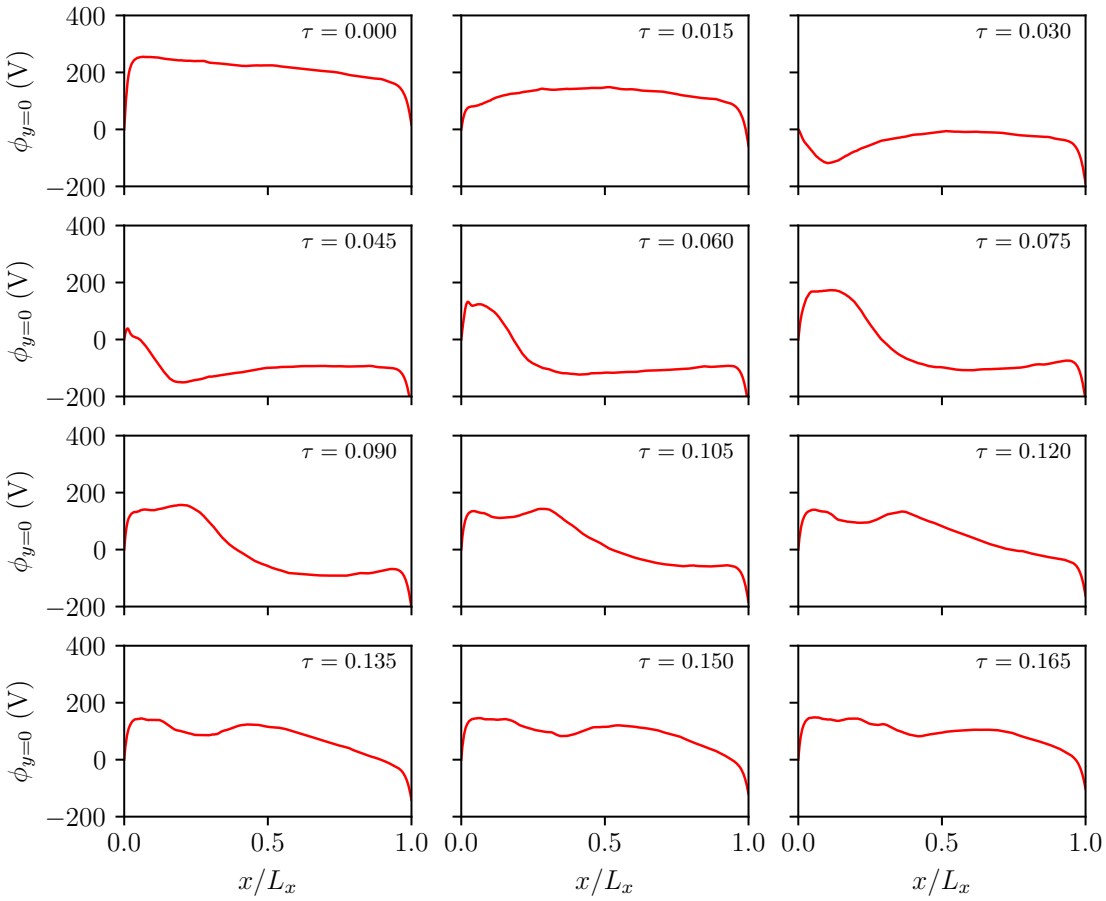

Figure 2.21: Plasma potential on the axis ($y = 0$) during the injection of an electron pulse at steady-state. Here $\tau = (t - t_0)/T$ and $t_0 = 12.0245\,\mu s$.

plots between $\tau = 0.06$ and 0.12. This effect is similar to the working principle of electron wakefield accelerators [132]. In the plots between $\tau = 0.09$ and 0.165, it is possible to see the formation of a secondary potential hill that moves downstream at a lower velocity. This can be associated with the group of electrons that were decelerated or partially trapped in the circular trajectory shown in 2.21, and forms a secondary electron wave that travels downstream, repeating the same acceleration-deceleration pattern. Despite the initial potential collapse, it is possible to see that the system quickly reforms the sheaths after the pulse, approximately 2 ns from the beginning of the injection. This quick reestablishment ensures electrons are trapped with repeated reflections from the potential wells formed.

Figure 2.22 gives another visualization of the potential fluctuations seen in figure 2.21 showing the temporal variation in the value of the axial potential field at two different locations, $x/L_x = 0.05$ and 0.95. The vertical dashed line shows the starting point for the plots in figure 2.21. It is possible to see that at the moment when the pulse occurs

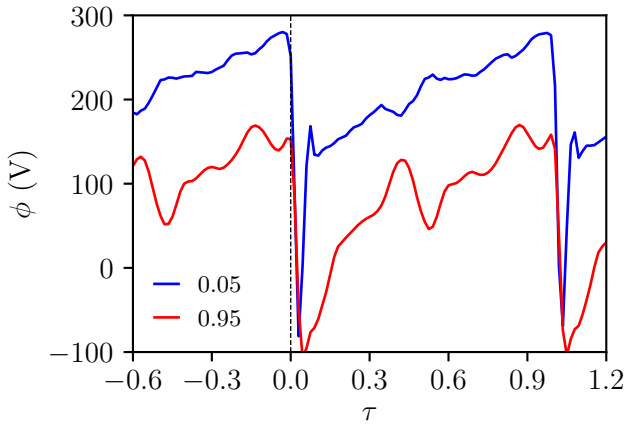

Figure 2.22: Time variation of the plume potential on the axis ($y = 0$) for $x/L_x = 0.05$ and 0.95. The vertical dashed line highlights the starting point of figure 2.21, when $\tau = 0$. $\tau = (t - t_0)/T$ is the normalized time, where $t_0 = 12.0245\,\mu s$.

there is an immediate drop in potential. Interestingly the potential at both locations drop in conjunction, showing that it is not caused by a travelling electron wave but by an electrostatic wave generated by the rapid accumulation of electrons at the RHS of the domain. The negative spike generated by the pulse reaches approximately $-100\,V$. After that, the potential at the thruster's exit goes back to around $150\,V$ and starts to slowly increase in an almost linear fashion as the ions are accumulated through the RF cycle. On the other hand, at the location close to the outer boundary, the response after the spike is more complex, displaying a slower rise after the negative peak and a number of smaller oscillations. This can be seen as a consequence of the number of electron oscillations at the downstream region and the slower accumulation of ions during the RF cycle due to the plume expansion.

The propagation of the electron pulse can also be visualized in figure 2.23. The figure shows the plots of the electron average flow velocity in the x-direction, during the injection of a pulse, for the same time points as figure 2.21. Before the pulse, the electron population over the whole domain is homogeneous and thermalized. When the pulse occurs, it is possible to see the appearance of a dense high-speed electron population close to the exit of the thruster. At the same time, in the downstream region, there is the formation of a high-speed electron cloud composed of pulse electrons and electrons in the plume that are accelerated by the potential well. As expected, in conjunction with the forward-propagating cloud, part of the electrons that are behind this cloud are accelerated backwards and can clearly be seen marked in blue on the plots. Between $\tau = 0.045$ and 0.06 it is also possible to visualize the electron reflection close to the injection surface. Lastly, there is the formation of the secondary electrostatic wave, visualized from $\tau = 0.09$, which also creates the forward and backward acceleration

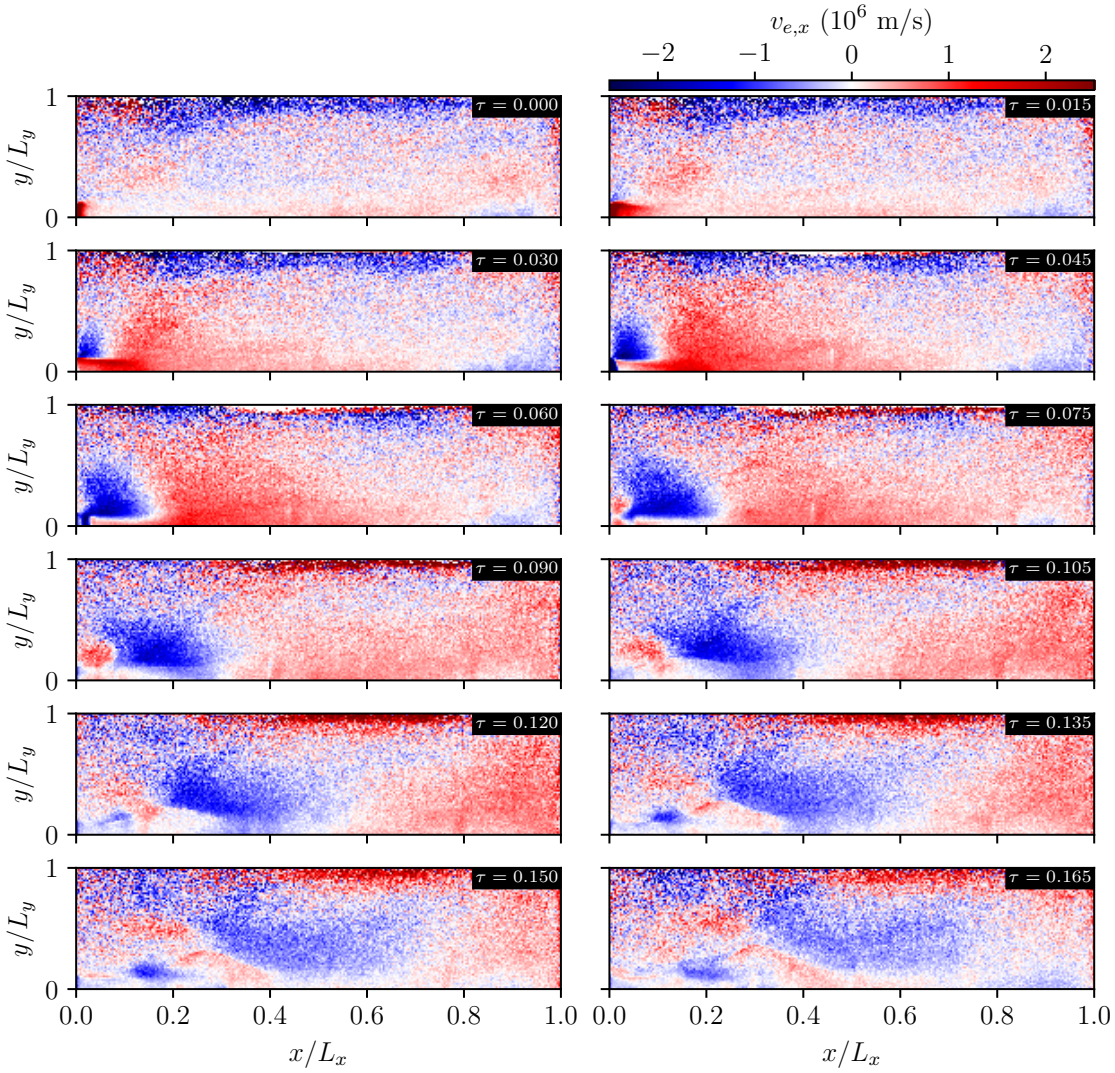

Figure 2.23: Electron average flow velocity field in the x-direction, v_x, during the injection of a pulse at steady-state. $\tau = (t - t_0)/T$ and $t_0 = 12.0245\,\mu s$.

effect. It is interesting to note that the electrostatic wave propagation does not happen exclusively at the region close to the axis, but its effect can be seen over almost the whole domain.

In parallel, another mechanism contributing to electron trapping is that a part of the injected electrons also undergo collisions, which can decrease their energy in the case of inelastic processes or randomize their initially coherent velocity. Due to these two processes, the continuous reflection of electrons at the sheaths and the collisions with the neutral species, the electron beam becomes thermalized within the plume, however maintaining a considerably higher temperature when compared to the DC case.

When the primary and secondary electron waves reach the outer boundary, the fast electrons penetrate the wall creating the first and second current peak observed in 2.19c. At the same time, the strong electrostatic wave seen in 2.21 created by the electron propagation, generates the displacement current peak which further charges the capacitor.

2.4.4 Parametric study

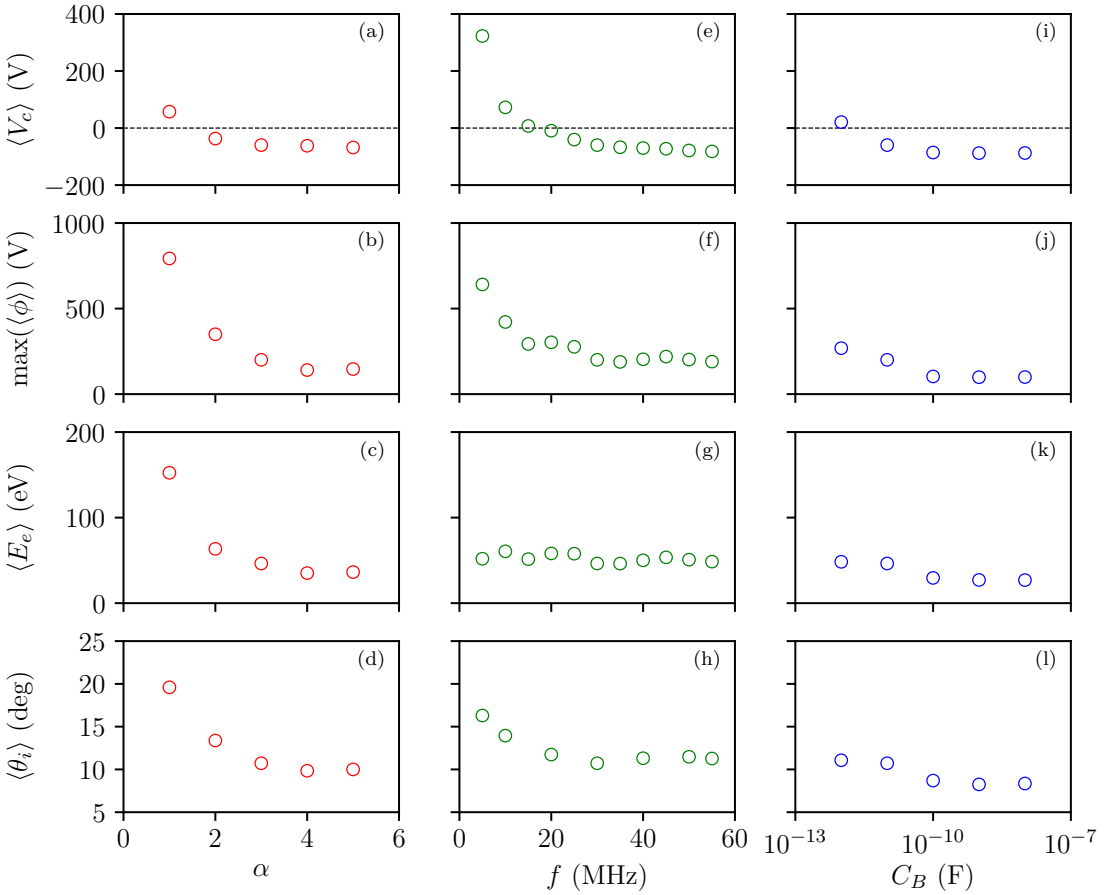

Figure 2.24: Results of average capacitor voltage, $\langle V_c \rangle$, maximum value of the averaged potential field, $\max(\langle \phi \rangle)$, and average electron electron energy, $\langle E_e \rangle$ as a function of the pulse magnitude, α, frequency, f, and boundary capacitor, C_B.

This section shows the results of the parametric study of the RF plume expansion. The influence of the variation of the pulse magnitude, α, frequency, f, and boundary capacitor, C_B, on the main parameters of the expansion is analyzed. For this study, 11 different frequency values, 5 values of α and 5 values of C_B were considered, in the range shown in table 2.2. For each simulation, just one parameter is varied, while the others assume the value used in the nominal case.

Figure 2.24 shows the results of this variation on four different parameters: average capacitor voltage, $\langle V_c \rangle$; maximum value of the average potential field, $\max(\langle \phi \rangle)$; average electron energy, $\langle E_e \rangle$; and the average ion divergence angle, $\langle \theta_i \rangle$. The divergence angle is calculated as $\langle \theta_i \rangle = \langle \cos^{-1}(\mathbf{v} \cdot \mathbf{i}/|\mathbf{v}|) \rangle$, for all ions in the region $x > L_x/2$.

On the first column, on plots *a* to *d*, the results for the variation of the pulse magnitude, α, are shown. It is possible to see that $\langle V_c \rangle$ decreases as the magnitude of the injected electron current increases. For $\alpha \lesssim 3$, the capacitor voltage increases due to a lack of electrons in the plume. All the subsequent plots show the same trend, most probably due to a poor neutralization process taking place. It is interesting to observe that the average electron current magnitude has the strongest impact on $\langle E_e \rangle$ varying from 25 eV up to 150 eV. This can be seen as a consequence of the less pronounced virtual cathode created during the pulse, which in turn produces a weaker electron breaking effect and favors their acceleration at the positive potential hill created by the ions at the source's exit. As the electron energy $\langle E_v \rangle$, increases, analogous to a high electron temperature, the magnitude of the radial ambipolar fields becomes stronger, thus increasing the ion beam divergence, as can be seen in plot *d*. The divergence in this case varies from 10 to 20°. Furthermore, due to the high electron energy and the lack of neutralization, the plume potential increases significantly for $\alpha < 2$, reaching values as high as 900 V. This potential value is close to the injection ion energy and can cause the beam to stall, reflecting ions back to the source and making the discharge unstable. For the present conditions, it was possible to identify that all the major parameters stabilize asymptotically for electron current magnitudes larger than $\alpha \approx 3$. This is similar to what was observed in refs. [66, 68], where the self-consistent value of α was estimated to be roughly 2.5–3, suggesting that this is the required current magnitude to maintain a well-neutralized plume in the RF case, and above this magnitude the amount of electrons in the plume starts to become saturated.

The second column, plots *e* to *h*, shows the influence of the the pulse frequency variation. It is first interesting to note that the average electron energy is not greatly affected by the change in frequency, staying close to 50 eV. Next, in plot *c*, it is possible to visualize the change in the average capacitor value which asymptotically decreases with frequency. For values below 15 MHz, the average capacitor voltage becomes positive and increases rapidly reaching roughly 380 V at 5 MHz. The plume potential shows a similar behavior. These decreasing profiles were also observed in ref. [68], where the potential difference between the plume and the downstream accel grid showed a descending trend as the RF frequency was increased. This behavior is a consequence of the system's capacitive characteristics which makes the plume potential and the boundary voltage proportional to the charges in the domain. As in a typical capacitor, the average net charge over the RF cycle decreases as the frequency is increased, roughly in the form $V \sim 1/f$, with this decreasing the plume and capacitor voltages. Nevertheless, the development of an accurate model for the plume capacitance and its voltage response is not trivial due to its coupling with the sheath capacitances, and non-uniform particle distributions. As f increases to large values, it is expected that the system approaches the behavior of a DC thruster. This means that the value of $\langle V_c \rangle$ tends to the value of a floating body inside

a beam to ensure equal currents of ions and electrons. This floating potential can be estimated using equation 2.54 while assuming $T_e \approx (2/3)50 = 33.3\,\text{eV}$, and $E_i = 1\,\text{keV}$, giving $\phi_f \approx -108\,\text{V}$. Observing figure 2.24c, it is possible to see that indeed this value is close to the asymptote of the average capacitor voltage as f increases. Because the electron energy does not vary significantly in this case, the variation of divergence is also less pronounced here, mainly connected to the average plume potential.

The third column, plots i to l, show the variation of the parameters with the boundary capacitance. Overall, C_B has the least pronounced impact over the plume expansion characteristics of all of the studied parameters. However, it is still possible to observe that the capacitor voltage and the plume potential decreases as the capacitor value is increased. Again this can be explained by the behavior of a capacitive circuit, where an increase on the capacitance also increases its charging time, which decreases the magnitude of the voltage oscillations and the accumulated net charge. The lower influence from C_B on the plume and boundary voltages when compared to α or f, can be explained by the fact that these voltages are dependent on the combined capacitance from both the external circuit and the sheath capacitances. Therefore, when C_B is varied only part of the effective capacitance is altered.

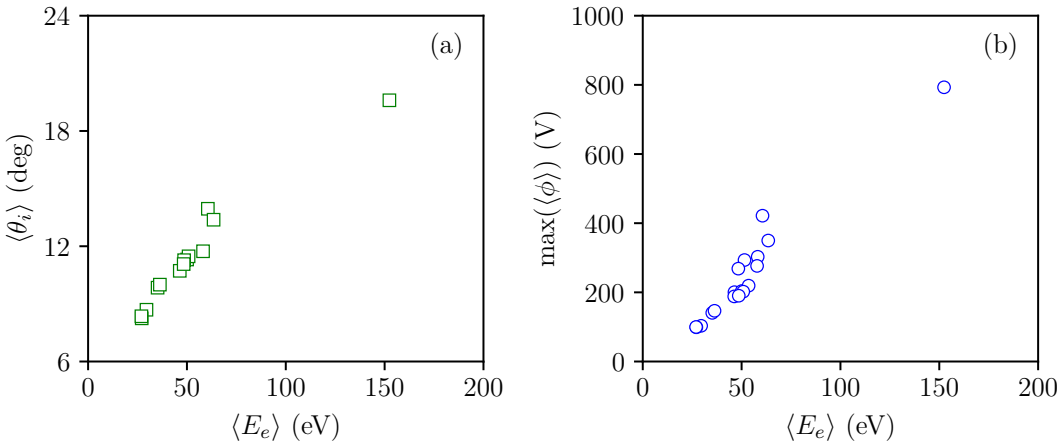

Figure 2.25: Ion beam divergence (a) and maximum average potential (b) as a function of average electron energy.

Figure 2.25 shows the dependence of the ion beam divergence and the maximum average potential on the average electron energy. As expected, the plots show that both parameters have an almost linear dependence on the electron temperature, confirming the behavior predicted in theory.

CHAPTER 3

EXPERIMENTAL APPARATUS

This chapter describes the instruments, facilities, and devices used during the experimental part of this work. In the first part, the three different thrusters (or ion sources) used during the experiments are detailed, including a DC ion thruster operating with xenon, a DC thruster operating with iodine, and an RF thruster which also operates with xenon. Next, the two vacuum facilities where the thrusters are operated and characterized are shown. The third part shows the primary plasma diagnostic systems used to characterize and study the plasma plume in the DC and RF cases. This part includes the description of a new instrument developed during this research which is used to study the divergence of the plume in DC thrusters. The new instrument consists of an automated planar probe array used to scan the ion beam under different circumstances.

3.1 Ion thrusters

In this section, the different thrusters used in the experiments are described. All the systems are based on the same thruster family, called the NPT30, but each model has unique features that allow them to operate over the required conditions in terms of propellant used and acceleration method. The NPT30 consists of a miniaturized propulsion system developed by ThrustMe since 2014, with the main focus on serving as a completely integrated propulsion system for small satellites.

3.1.1 NPT30-Xe

The NPT30-Xe was the first thruster to be developed in this context, and it consists of a 4-cm diameter gridded ion thruster based on an ICP discharge for the production of ions and which uses xenon as the propellant. Figure 3.1 shows the general architecture of the system. The mechanical design of the thruster uses a 2U CubeSat form-factor [133] for higher compatibility with small satellite missions; this effectively consists of two side-by-side cubes of $10\,\text{cm} \times 10\,\text{cm} \times 10\,\text{cm}$. Figure 3.2 shows an external photograph of the assembled system.

As shown in figure 3.1, one of the cubes contains the pressurized xenon tank and flow control valves, labeled the "propellant management system", and the second cube contains all other required thruster subsystems, including the electronics, the thruster,

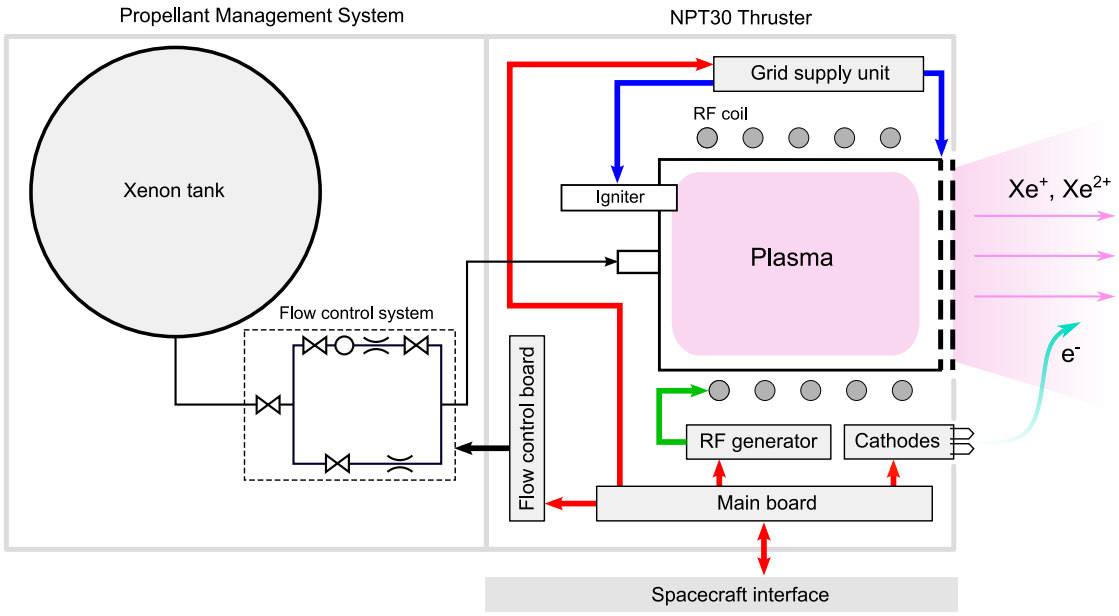

Figure 3.1: Diagram of the NPT30-Xe architecture and subsystems (source: [134]).

and the neutralization system. All electronic boards are controlled by the "main board", which is the actual onboard computer containing the main control algorithm of the thruster and the digital interfaces to the spacecraft or ground setup. The electrical interface between the thruster and the satellite is done through 6 cables, two power connections, and two digital communication pins. The digital communication is done using either a redundant CAN bus or an I^2C interface. The total power consumed by the thruster during operation ranges from roughly 30 W to 65 W.

The propellant valves are controlled by a "flow control board" that sets the required flow rate during operation. The flow coming from the valves is then injected at one of the ends of the plasma chamber. This thruster operates with mass flow rates between 0.01 mg/s to 0.15 mg/s of Xenon (approximately 0.1 sccm to 1.5 sccm) and the tank can hold up to 120 bar and 200 g of propellant. However, because of the complicated handling of loaded high-pressure vessels and the filling procedure, the experiments in the context of this work did not use the propellant storage hardware of the NPT30-Xe. Instead, the propellant was fed from an external gas bottle and controlled by a digital mass flow meter. Therefore, it was not required to have the tank, valves, and flow control boards during the experiment. The mass flow of xenon is controlled using a Bronkhorst FG-201CV mass flow controller, rated to provide from 0.01 sccm to 10 sccm of Xenon with accuracy of 0.5 %. The xenon bottle used was provided by Air Liquide and had a 99.99 % purity.

The inner plasma generation of the thruster is based on an ICP discharge generated by a helicoidal RF antenna placed around the plasma chamber, powered by the "RF generator board". The system is capable of generating from 6 W to 14 W of RF power at the plasma and generating a total ion current ranging from 5 mA to 35 mA.

Figure 3.2: Photo of the NPT30-Xe propulsion system.

The ions generated in the ICP discharge are accelerated by a set of two grids that are controlled by the "grid supply unit". The screen grid can be biased to voltages from 500 V to 1300 V, while the accel grid is biased with values from −50 V to −100 V to prevent electron backstreaming.

The thruster uses two redundant tungsten hot thermionic filaments positioned close to the beam exit for the neutralization of the plume. During operation, the filament is heated up to temperatures close to 2300 K which generates up to 40 mA of electron current. To decrease the plume potential and thus the energy of backstreaming ions, the cathode is generally biased to a voltage of −30 V during operation.

During the experiments, to improve the quality of measurement stability of the system and facilitate the change of operation conditions, several subsystems may be bypassed by external equipment. One of the most important cases is the grid supply unit that is substituted by external high-voltage supplies in several experiments of this work. Whenever this is the case, the power supply used to bias the screen grid is a Heinzinger PNC-1500, and the one used to bias the accel grid is an ETAT 600. During the text, it will be pointed out whenever any subsystem externalization is done.

3.1.2 NPT30-I2

The NPT30-I2 is similar to the xenon version; however, it uses iodine instead of xenon as its propellant. Therefore, most thruster subsystems are similar to the xenon model, with the main significant difference being the propellant storage and flow control system and its form factor. Because iodine can be stored in solid-state with a much higher density than xenon and without the need for a high-pressure vessel, the total volume of the system was considerably reduced, having a version with a 1U form-factor and another one with 1.5U that has an extended propellant tank.

Figure 3.3 shows a 3D section-view of the 1U version of the thruster, which is the one used during the experiments. As shown, the propellant tank, in this case, consists of a rectangular reservoir, which is located inside the same cube of the thruster and attached to the bottom of the plasma chamber. This reservoir is filled with solid iodine, which is sublimated with electrical heaters during operation. To improve thermal conductivity

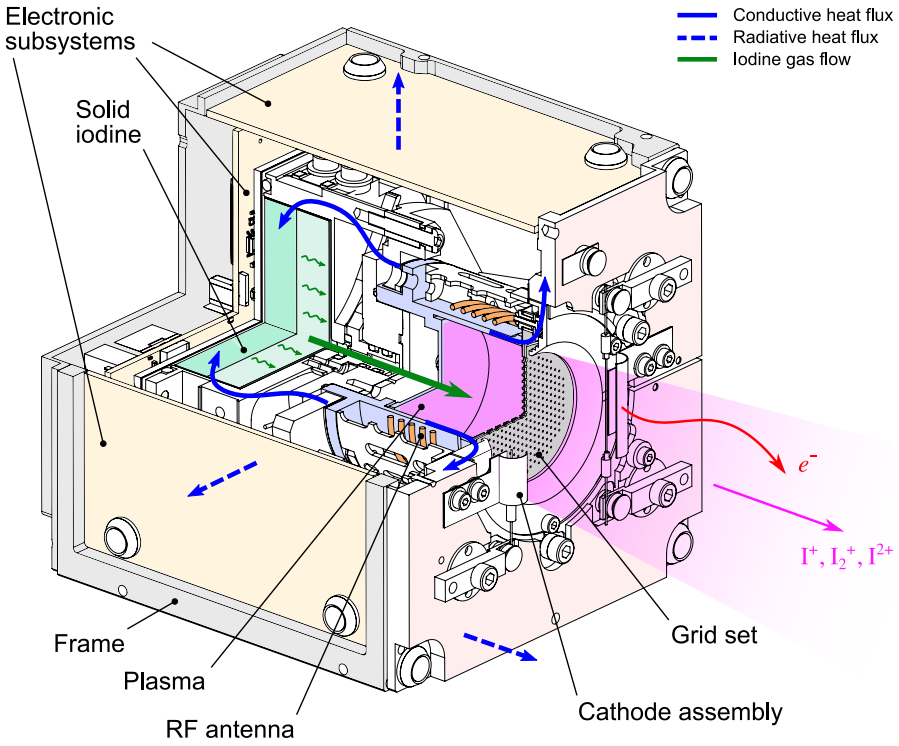

Figure 3.3: Section view of the NPT30-I2 (source: [135]).

and mitigate damaging effects of vibration during launch, which may lead to shattering of the solid propellant, the iodine is loaded as a liquid into a porous ceramic matrix located inside the propellant tank. The matrix is made of porous aluminum oxide and has a 95 % porosity. For sublimation to take place at a sufficient rate to generate the gas flow necessary for operation, the iodine is heated up and kept at a temperature between 80 and 100 °C by the heaters. The mass flow rate is adjusted by controlling the tank temperature and maintaining the specified saturation pressure. The propellant management system is capable of providing a mass flow rate that ranges from 0.04 mg/s to 0.1 mg/s during operation. During operation, the mass flow rate is determined with an empirical model developed and calibrated by ThrustMe's technical team, which can estimate the mass flow rate with an uncertainty of 1 %.

During the heating-up phase, the heaters can consume up to 50 W of power, and it takes around 10 to 15 min to go from an idle state to full operation. However, during operation, the heat generated by the plasma chamber and the other subsystems is recirculated and goes to the propellant tank through the mechanical connections, decreasing the necessary power to maintain the required sublimation temperature of iodine. In this way, in steady-state, the heater consumes less than 1 W.

The use of iodine as a propellant also imposes a number of engineering challenges due to its highly reactive nature. To avoid reactions or corrosion, several inner components in

direct contact with the propellant flow had to be modified to be either made of technical ceramics or, if metallic, coated with a polymeric film. The grid set, which is in direct contact with the iodine flow, is made of molybdenum, a material that is, at the same time, significantly resistant to iodine corrosion and to high-energy ion sputtering [136]. In the propellant storage system, the typical approach to avoid continuous loss of iodine via natural sublimation when the thruster is not working would be the use of an automated valve. However, the design of such a valve, with moving metallic parts resistant to iodine, is not trivial and could considerably increase the risk of failure and the total volume of the system. Therefore, to avoid this propellant loss, the gas connection is designed so that the iodine deposits itself on a connection orifice when the system is cold, blocking any further flow from passing. The leakage of this passive blocking system under vacuum was verified to be less than 0.08 µg/s.

The prediction of the performance in this thruster is similar to what is done in the NPT30-Xe. However, because of the multiplicity of chemical reactions and collisional processes in the ICP discharge and the plasma plume expansion, several assumptions have to typically be made, and the precision of these performance estimations is lower than in the xenon case. One of the objectives of this work is to study several aspects of the plume of the NPT30-I2 so that the models can be adapted to better predict its performance.

3.1.3 NPT30-Xe with RF biasing

The thruster used for the experiments on the RF grid biasing is a modified version of the NPT30-Xe. Because several aspects of the RF biasing technique are still not well understood, most parts of the thruster subsystems were removed and replaced by external equipment so that the number of unknown variables was decreased and the experiment could be more efficiently operated.

Figure 3.4 shows a general electrical schematic of the experimental setup used during the RF biasing experiments. The only electronic subsystem remaining inside the thruster is a part of the RFG subsystem, consisting of the RF matching circuit between the RFG board and the ICP coil. The RFG board is removed from the thruster and positioned outside the chamber to avoid RF interference between itself and the grid RF signal.

To power the grids, an external wave generator, and an E&I 2200L linear power amplifier, capable of generating up to 200 W of RF power, is used. The amplifier is connected to a "grid matching box", which is mechanically attached to the back of the thruster. This box contains the circuitry necessary to match the impedance of the external RF generator and the grid set. This matching circuit contains three capacitors (C_0, C_1 and C_2) and a coil. The value of the capacitors is defined through experimentation to generate the desired resonance profile. The design of the circuit allows an easy replacement of the coil so it can be used to control the value of the resonance frequency to allow the operation of the thruster under different frequency regimes. In this configuration, the setup was capable of generating a sinusoidal frequency of up to roughly 1.2 kV peak-to-peak. During the experiments, the forward and reflected power from the RF generator were measured from the readings of the generator itself – this

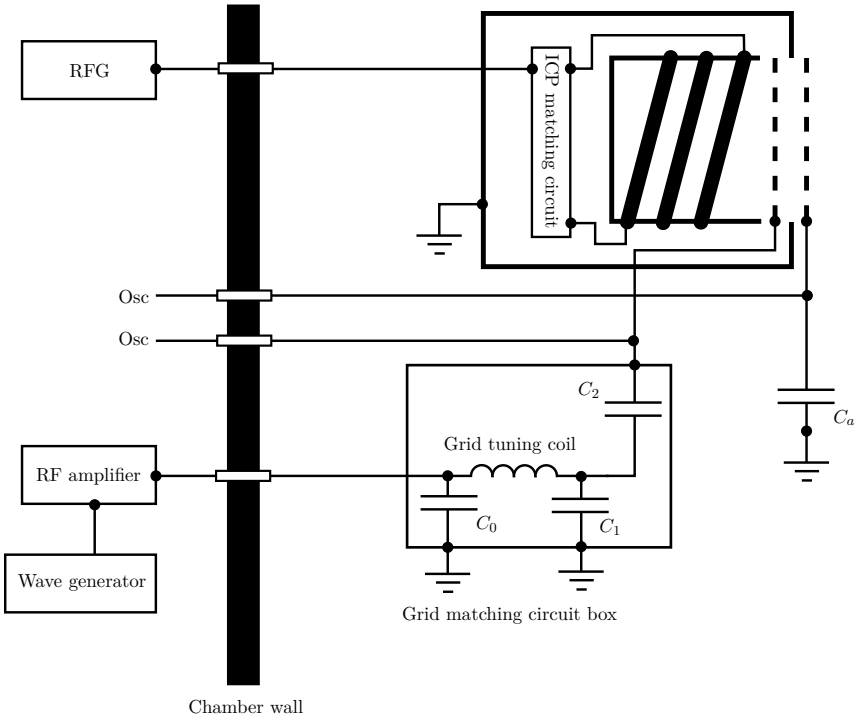

Figure 3.4: General electrical schematic of the thruster used during the RF biasing experiments.

reading has a considerably limited precision and it is used only as a first estimation.

The accel grid is connected to ground through a capacitor, C_a. This configuration allows the accel grid to act as a floating body and ensures, on average, that the grid collects equal ion and electron currents. This configuration is analogous to the simulation setup studied in chapter 2. However, in this case, the reference of the circuit is the surrounding vacuum chamber instead of the accel grid as it was in the simulations.

Ideally, for better replication of space operational conditions, the entire body of the thruster and all its subsystems would have to be electrically floating relative to the chamber. In this case, all subsystems would have to be inside the thruster, and the power would have to be provided by an isolated voltage supply or batteries attached to the module. However, as said, the RF biasing experiments bring several complications, and, due to a limitation on setup and the need to externalize the subsystems, only the accel grid was kept as a floating body in this case.

3.2 Vacuum facilities

All the experimental investigations done in the context of this work were performed in the facilities of ThrustMe's R&D laboratory. The laboratory currently has two vacuum systems capable of operating plasma physics experiments, and either was used depending

on the specific characteristic of the experiment. Figure 3.5 shows an overview photograph of the laboratory with the two chambers.

3.2.1 PEGASES vacuum system

The PEGASES vacuum chamber, shown in the bottom left of figure 3.5, consists of a cylindrical pressure vessel, made of stainless steel, with a diameter of 0.6 m and a length of 0.83 m. The system is equipped with a primary mechanical pump and a turbo-molecular pump. These pumps are capable of a total pumping speed greater than 2500 l/s (for N_2). The base pressure in the chamber, with no experiments running, is always from 10^{-6} mbar to 5×10^{-7} mbar. For all experiments, during operation, the pressure was always kept below 4×10^{-5} mbar. The pressure in the chamber was measured with an absolute pressure transducer MKS Baratron 627B and a Balzers IKR 050 cold cathode gauge.

Between the two vacuum setups, this is the only one prepared for the operation with iodine. For this, a cryogenic trap is installed on the inner surface of the chamber and constantly kept at $-75\,^{\circ}$C during operation by an external industrial chiller. Apart from increasing the general pumping speed capability of the system, this setup favors the deposition of iodine on the surface of the trap while decreasing the iodine flow at the main vacuum pumps, decreasing the risk of damage due to corrosion.

All the experiments of this work involving the operation of the NPT30-I2 and the DC NPT30-Xe were conducted in this vacuum system.

3.2.2 ThrustMe II vacuum system

The ThrustMe II chamber is shown in the top right of figure 3.5. It is a larger system when compared to the PEGASES chamber, consisting of a cylindrical stainless steel vessel with a diameter of 1 m and length of 2 m. The system also contains two smaller sub-chambers with a diameter of 30 cm and length of 50 cm, which are attached to the side of the main vessel through pneumatic gate valves. The complete system uses two primary mechanical pumps and two 3050 l/s turbo-molecular pumps, which add up to a total pumping speed of approximately 6500 l/s. The first primary pump is used to evacuate the main chamber through the turbo-molecular pumps, while the second is used to pump down the sub-chamber so that they can be independently opened and closed without the need to fill the main chamber.

The pressure in the system is measured with two different sensors, a Pfeiffer PBR 260 Pirani/Bayard-Alpert sensor and a Pfeiffer PKR 360 cold cathode gauge. During the experiments, the background pressure of the chamber is maintained below 1×10^{-6} mbar, and during operation of the thruster the pressure always stays below 2×10^{-5} mbar.

This chamber is used for all the experiments with the NPT30-Xe with RF biasing. This is preferred in this case because one of the main aspects that can impact the expansion dynamics of the plume is its capacitive coupling with the grounded surfaces surrounding the thruster, and increasing the distance between the plume and the chamber surfaces effectively increases this capacitance making it more similar to a space environment.

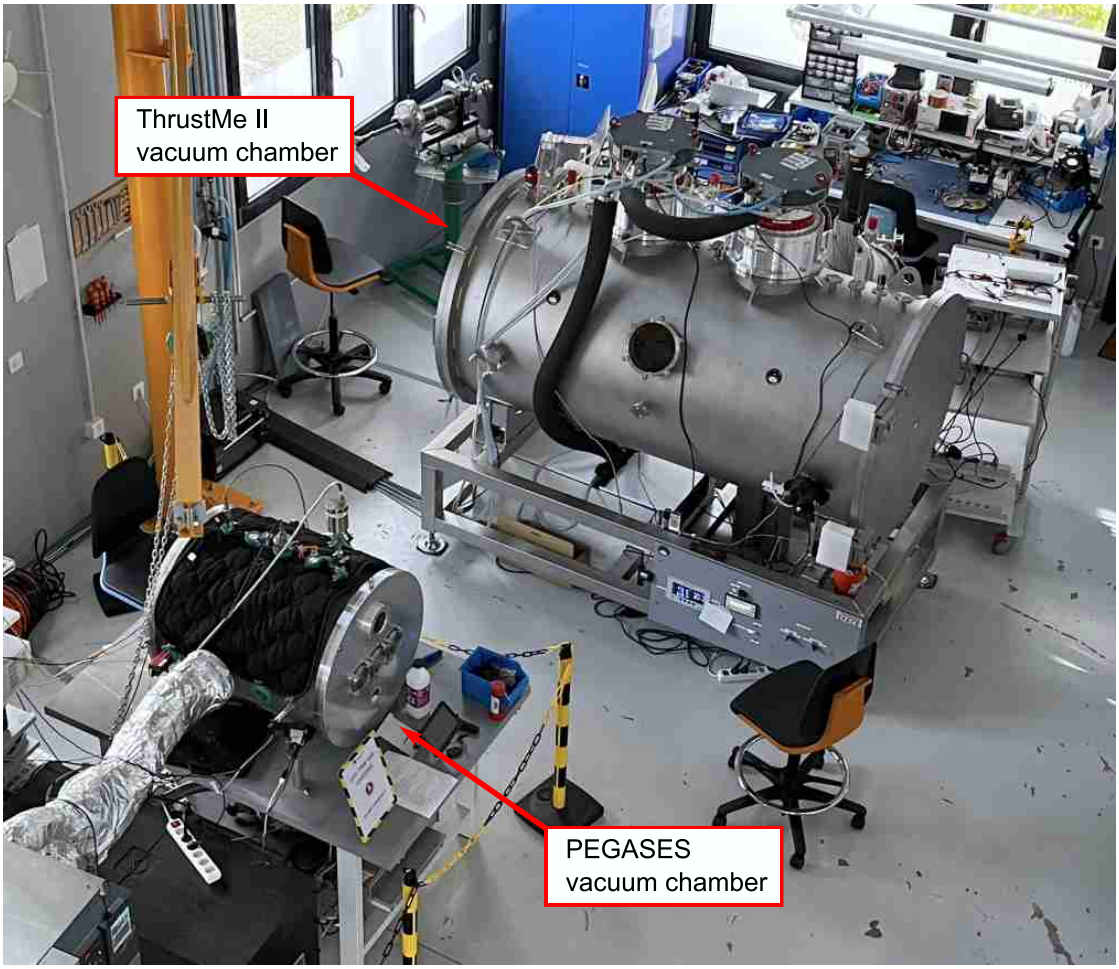

Figure 3.5: Overview of ThrustMe's R&D laboratory showing the two vacuum systems used during this work.

Furthermore, since the neutralization process is a central point when studying this technique, it is important to guarantee that the vast majority of electrons in the plume are indeed coming from the pulsed neutralization. In the case of a smaller chamber, the short-scale interaction between the plasma plume and the grounded surface could lead to a spurious neutralization process with the additional contribution of secondary electron emission from the surfaces and a stronger electrical connection between the ground and the plume. This effect could make one believe that the neutralization quality is higher than it actually is in a space-like environment.

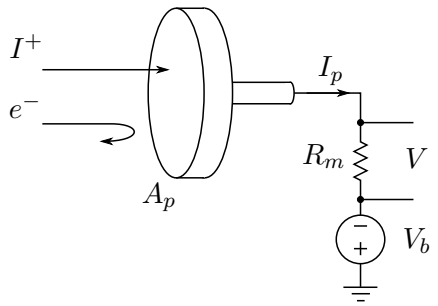

Figure 3.6: Generic schematic of a planar probe.

3.3 Plasma diagnostics

This section describes the plasma and beam diagnostic devices used in different parts of this work. Other instruments used just in specific situations in the experiments are described in the relevant sections during the text.

3.3.1 Planar probe

The planar probe is one of the simplest instruments in plasma physics, and it is generally used to measure the local ion current density of a plasma. It consists of a metallic disk that is biased to a negative potential so that the plasma electrons are repelled, and only the ions are collected. The bias value is selected such that the current collected corresponds to the ion saturation current, which is the point where no electrons are collected in a Langmuir probe [1]. Figure 3.6 shows a general schematic of a planar probe. In this case, I_p is the current passing through the probe, R_m is the measurement resistor, V_b is the bias voltage, and V is the measured voltage.

In an ideal case, the current collected by a planar probe is given by

$$I_p = eA_p n_i v_i \tag{3.1}$$

where A_p is the area of the probe, n_i is the local ion density and v_i is the average velocity perpendicular to the probe surface. In a Maxwellian plasma with no drift in the ion population, this could be rewritten as

$$I_p = eA_p n_s u_B \tag{3.2}$$

where u_B is the Bohm velocity and n_s is the ion density at the edge of the sheath in front of the probe. However, in a real case, different effects might alter the probe's reading. One of the most important is called *sheath expansion*. In this effect, as the magnitude of the negative bias applied to the probe is increased, the thickness of the electrostatic sheath around the probe increases as well. The sheath expands in a three-dimensional shape, increasing its surface area in contact with the bulk plasma. Since the ions that enter the sheath are attracted to the probe due to its negative potential, the larger sheath surface effectively acts as a larger ion collection area for the probe, increasing the measured

current. This results in an ion saturation current that increases with the magnitude of the probe bias. Sheridan [137] studied this phenomenon with a computational approach and proposed a semi-empirical model to correct the measurements for this effect. However, the so-called Sheridan model can only be used for Maxwellian plasmas with no drift, thus not being ideal for the study of ion beams.

Different modifications to the basic planar probe have been proposed to mitigate this effect. One of the most widespread is solutions is called the Faraday probe [138]. In this model, an additional annular electrode, called the guard ring, biased to the same potential as the probe, is placed around the probe disk with a small gap between them. As the sheath expands around both electrodes, only the ions entering at the region close to the disk are collected by the probe, while ions entering with lateral angles are collected by the ring. Another solution is called the Faraday cup [139], and it consists of a metallic housing around the probe, with an orifice that allows ions to pass. Since the probe is enclosed, the sheath only expands inside the housing, maintaining a constant collection area.

Another phenomenon that might affect the measurements is secondary electron emission due to ion impact [4]. For an ion current I_i impacting the probe with an average energy E_i, a secondary electron current is produced with the value of

$$I_{SEE} = I_i \gamma(E_i) \tag{3.3}$$

where γ is the SEE yield, which depends on the material of the probe, the ion species, and the average ion energy and impact angle. The emitted electron current flows away from the probe, and therefore the measured current is higher than the actual ion current. This correction can easily be done for ion species with known SEE yields; however, new propellants such as iodine do not have this data available in the literature. Therefore, to be able to correct the measurements with planar probes and other instruments for the SEE influence when using iodine, it is necessary to measure the values of the SEE yield for iodine impinging on different materials.

3.3.2 Retarding field energy analyzers

The retarding field energy analyzer (RFEA) consists of an electrostatic diagnostic system designed to measure the energy (or velocity) distribution function of a given particle species, typically positive ions. This instrument uses a set of biased grids in front of a sensor, similar to a planar probe, to create an electrostatic potential configuration that filters particles depending on their energy. Hutchinson [111] shows a detailed theoretical description and working principle of RFEAs.

The number of grids and their biases may vary for each specific design. However, in the most basic design, an RFEA has just one grid used to repel the electrons coming from the plasma with a negative bias and a collector electrode used to measure the ion current. In this scheme, the potential of the collector, V_c, is varied, and only ions that have an energy $E_i > eV_c$ can reach the sensor and generate a measurable current. The

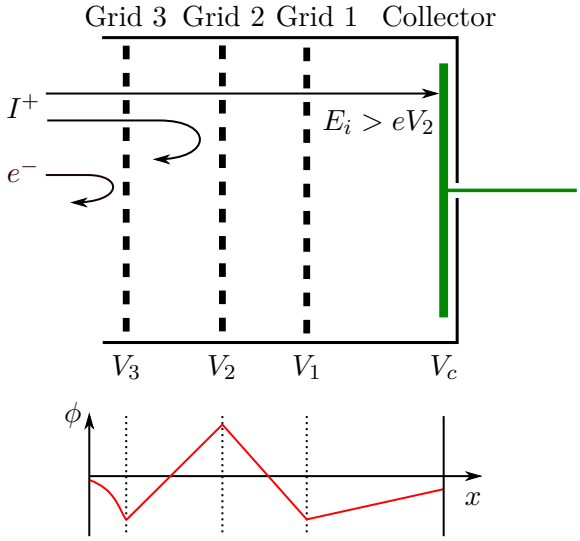

Figure 3.7: General schematic of a four-grid RFEA.

flux of particles reaching the electrode is given by [111]

$$\Gamma(V_c) = \int_{-\infty}^{-\sqrt{2e|V_c|/m}} f_\infty(v_\infty) v_\infty dv_\infty \tag{3.4}$$

where f_∞ is the particle distribution function in the bulk plasma and v_∞ is their velocity in the bulk plasma. Differentiating the equation and using $v_\infty = -\sqrt{2e|V_c|/m}$, one obtains

$$\frac{dI(V_c)}{dV_c} = \frac{e^2 A}{m} f_\infty(v_\infty) \tag{3.5}$$

where $I = eA\Gamma$ is the current reaching the sensor, and A is the collection area. In other words, this means that the distribution function of the collected particles is directly proportional to the derivative of the current measured at the electrode as its voltage is varied. The function $f(v)$ corresponds to the velocity distribution function, given in units of energy or on an energy scale. To obtain the true energy distribution function, $g(E)$, it is necessary multiply the function f by the Jacobian which makes the velocity-to-energy conversion, resulting in

$$g(E) = \frac{1}{\sqrt{2meE}} f\left(\sqrt{\frac{2eE}{m}}\right) = \frac{1}{e^2 A}\sqrt{\frac{m}{2eE}}\frac{dI(E)}{dE} \tag{3.6}$$

However, in an actual device, the one-grid design can present precision problems due to the emission of secondary electrons by the ion impact on the grid. This electron current is attracted to the collector due to its positive potential, causing the net current signal measured to drift from the ion current collected. Generally, to solve this issue, additional grids are used with a potential configuration that does not allow the secondary

electron current to reach the collector. Figure 3.7 shows an example of a configuration typically used. In this configuration, the voltage variation is done at Grid 2, V_2, and the collector is kept at a slightly negative voltage. Grid 1 is kept at a lower potential than the collector, which allows the reflection of secondary electrons emitted at the grids.

Another important aspect when designing a grid-based probe is the space-charge current limitation. Since there is almost exclusively ions inside the probe, the maximum current that can be collected is given by the Child-Langmuir current (eq. 1.34). If the probe is placed in a region where the current density is given by J_i, the spacing between any two grids of the probe must fulfill the requirement

$$l < \left[\frac{4}{9}\varepsilon_0\sqrt{\frac{2e}{m}}\frac{\Delta V^{3/2}}{J_i}\right]^{\frac{1}{2}} \tag{3.7}$$

where ΔV is the voltage difference between the grids where the gap is being analyzed.

For most cases in this work, the Impedans Semion 2500 RFEA was used to measure the ion energy. This instrument consists of a 50 mm diameter, four-grid sensor, designed to measure ion energies up to 2.5 keV. Other similar in-house probes were also used and are described in the relevant sections below.

3.3.3 Emissive probe

An emissive probe consists of an electrostatic probe that emits electrons at its measuring region [140]. This is typically done using a hot thermionic filament, heated by a current, as the probe. This filament is typically placed at the tip of a ceramic tube, which is then positioned in the region of interest in the discharge. An emissive probe can be used in different ways, however here, it is used exclusively in the so-called *floating configuration* for measurement of the local plasma potential.

In this configuration, the filament is heated by an isolated current supply so that any net current emitted or received by the probe charges the system. This way, the measured quantity, in this case, is the potential that the probe obtains as it is placed within the plasma. Figure 3.8 shows the schematic of a floating emissive probe. Here I_h is the heating current, and V is the bias voltage measured relative to ground. When a floating emitting surface is placed inside the plasma, the sheath formed at its vicinity is not the same as a typical floating body. Because the sheath forms a growing potential well towards the plasma, the electrons emitted by the surface are accelerated towards the plasma, decreasing the sheath potential drop. If the emissive probe can provide enough electrons, the current balance is achieved when the sheath drop is almost zero, and the floating potential of the probe coincides with the bulk plasma potential.

However, as the electrons are emitted from the emissive probe, their current creates a space charge distribution, limiting the possible current flowing from the plasma and altering the probe's floating potential at equilibrium. This maximum current happens when the electric field on the surface of the probe is zero. Modeling of the emissive probe in a current limited regime is not trivial. Ye and Takamura [141] provide this derivation

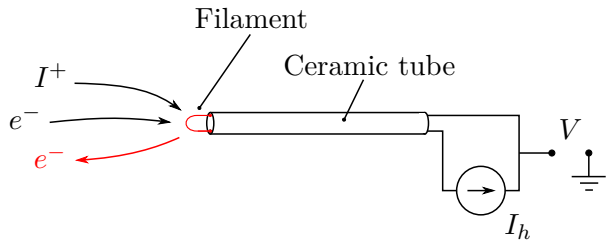

Figure 3.8: Generic schematic of a floating emissive probe.

and showed that the sheath potential drop between the floating potential of the probe, ϕ_f, and the bulk plasma, ϕ_p, can be estimated in the form

$$\phi_f - \phi_p = gT_e \tag{3.8}$$

where T_e is the bulk plasma electron temperature, and g is a function that depends on the ratio of the ion-to-electron mass. The value of the function g varies from 0.95, for hydrogen, to 1.03, for infinitely massive ions. This way, for xenon or iodine, it is reasonable to assume $g \approx 1$. The space charge effect, together with other phenomena, such as the shape of the particle distribution function, makes the measurement error of floating emissive probes to be of the order of $1.5T_e$ to $2T_e$, where T_e is the electron temperature in the plasma [140].

Several mechanical designs have been proposed and studied for the actual construction of the probe tip [142]. The most commonly used are the linear and the hairpin design. In the linear case, a straight filament is held by a ceramic support that fixates the filament at its ends. This technique provides slightly better measurement accuracy but is considerably more complex mechanically. The present work adopts the hairpin design due to its more straightforward design and relatively good accuracy. In this design (represented in figure 3.8), the filament is bent into a loop with its ends entering the orifices of a two-channel ceramic tube. The filament is then connected by friction pressure to the wires that provide the heating current. The main requirement, in this case, is that the loop length must be roughly bigger than $2\lambda_D$ so that the ceramic tube sheath does not interfere with the probe's sheath.

The emissive probe used for this work uses an alumina tube with a length of 8 cm and a diameter of 5 mm. The tube has two channels with a diameter of 1 mm. A tungsten filament with a diameter of 0.15 mm is used for the hot tip, assembled as a loop with a length of 8 mm. To provide the saturation emission, the probe has to be run with a heating current of approximately 3.2 A.

3.3.4 Dipole probe

A dipole probe is an RF diagnostic method proposed by Rafalskyi and Aanesland [143], and used for the estimation of the local electron density. In this method, a miniaturized matched dipole is placed inside the plasma body, and a vector network analyzer (VNA) is used to measure its impedance response as a function of the excitation frequency. Using

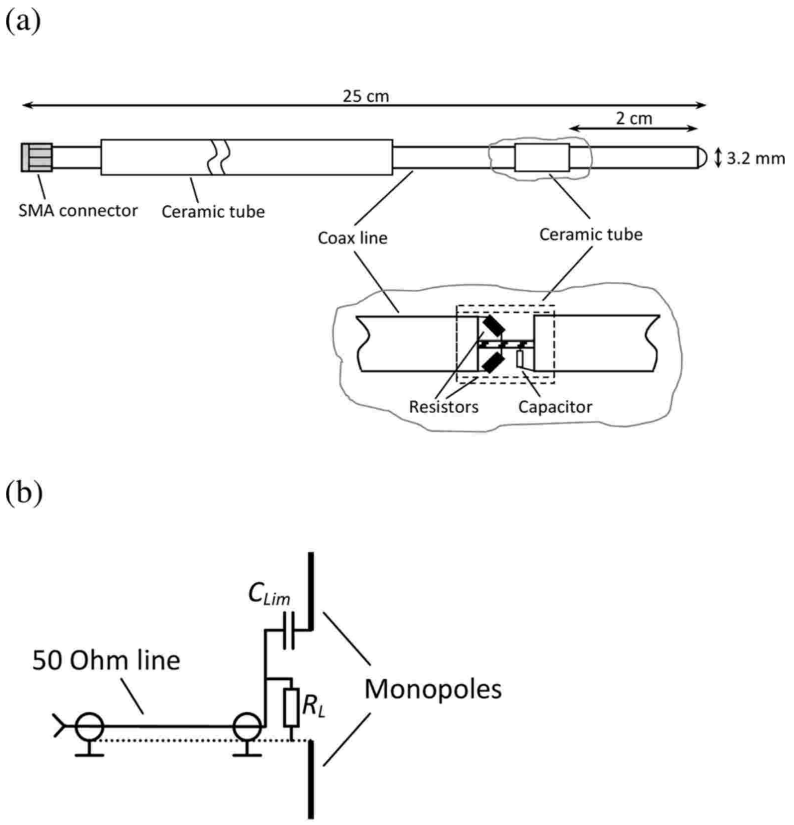

Figure 3.9: Schematic of the dipole probe. (a) shows its assembly and filtering circuit and (b) shows the circuit of the dipole antenna (source: [143]).

the theory developed by Balmain [144], it is demonstrated that the impedance of a short dipole antenna inside a non-magnetized plasma presents a single resonance peak at the plasma frequency, ω_{pe}. With this, the electron density can be estimated as

$$n_e = \frac{m_e \varepsilon_0}{4\pi^2 e^2} f_{pe}^2 \tag{3.9}$$

where $f_{pe} = \omega_{pe}/2\pi$ is the frequency of the resonance peak. It was shown that this method is adequate for plasmas with electron densities ranging from $10^{12}\,\mathrm{m}^{-3}$ to $10^{15}\,\mathrm{m}^{-3}$.

Figure 3.9 shows the general schematic of the matched dipole probe given in ref. [143]. The probe is built from a rigid copper coaxial line with a $50\,\Omega$ characteristic impedance and an SMA connector at one of its ends. To create the dipole, the shroud and the insulator of the line are removed 2.5 cm from the tip of the probe. In this way, the actual antenna poles are the two hollow copper cylinders, the first around it at the tip and the second grounded, attached to the SMA connector. At the location of the gap, two resistors and a capacitor are connected to the poles to create the required circuit shown in figure 3.9b. R_L represents these two resistors that have a value of $100\,\Omega$ each, and

guarantees correct matching. The capacitor C_{Lim} has a value of 47 nF. Furthermore, the grounded end of the dipole is covered by a ceramic tube, ensuring no DC connection to the surrounding discharge.

The dipole probe used in this work is a commercial probe manufactured by ThrustMe. The probe is employed only for measurements of background plasma density outside the plasma plume cone. This is done because this technique is a better fit for low-density measurements and because the probe used is not prepared for an environment with high-energy ions. An mRS miniVNA PRO is used for the impedance measurements.

3.4 Planar probe array

This section describes a new instrument designed in the context of this work, which is primarily used to measure the divergence of the ion beam produced by a DC ion thruster. The instrument consists of an automated planar probe array capable of producing two-dimensional profiles of the ion beam by measuring the ion current density at different positions in the plume. In the context of this work, this instrument is employed to characterize the differences in the iodine and xenon DC ion thrusters in the following chapters.

3.4.1 Instrument design

Mechanical design

Figure 3.10 shows an overview of the instrument's construction and its assembly in the PEGASES vacuum chamber. It consists of a movable metallic arc that holds 15 planar probes to measure the ion beam profile and two additional probes at the ends of the arm to measure the background plasma density. The instrument aims to measure the ion saturation current at each probe while rotating the arm in front of the ion beam. Instead of using the typical uniform distribution of probes found in similar devices, [146, 147], the positioning and the area of the probes follow a gaussian-like distribution to improve the quality of the signal reconstruction based on previously available experimental measurements and theoretical models of plume expansion. This arrangement is described later in this section.

The arm of the instrument has a radius of curvature of 269 mm, with rectangular cross-section of 3 mm × 15 mm. The arc is made of stainless steel to improve the resistance to ion bombardment and iodine corrosion. The arm is moved by two KH4238 stepper motors attached to its ends. Each motor has a maximum static torque of 0.34 Nm and can rotate the structure 180° from the bottom vertical position to the top vertical position with a step size of about 0.1°. The stepper motors are connected to two chamber flanges through metallic adaptors. Two aluminum counterweights, positioned at the arm's ends, are used to reduce the motors' load generated by the structure. Generally, this type of automated scanning device is designed to rotate horizontally so that the actuators' load is reduced. However, the present instrument is designed to move in the vertical direction so that in case of failure of the motors, the sensor arm can fall with

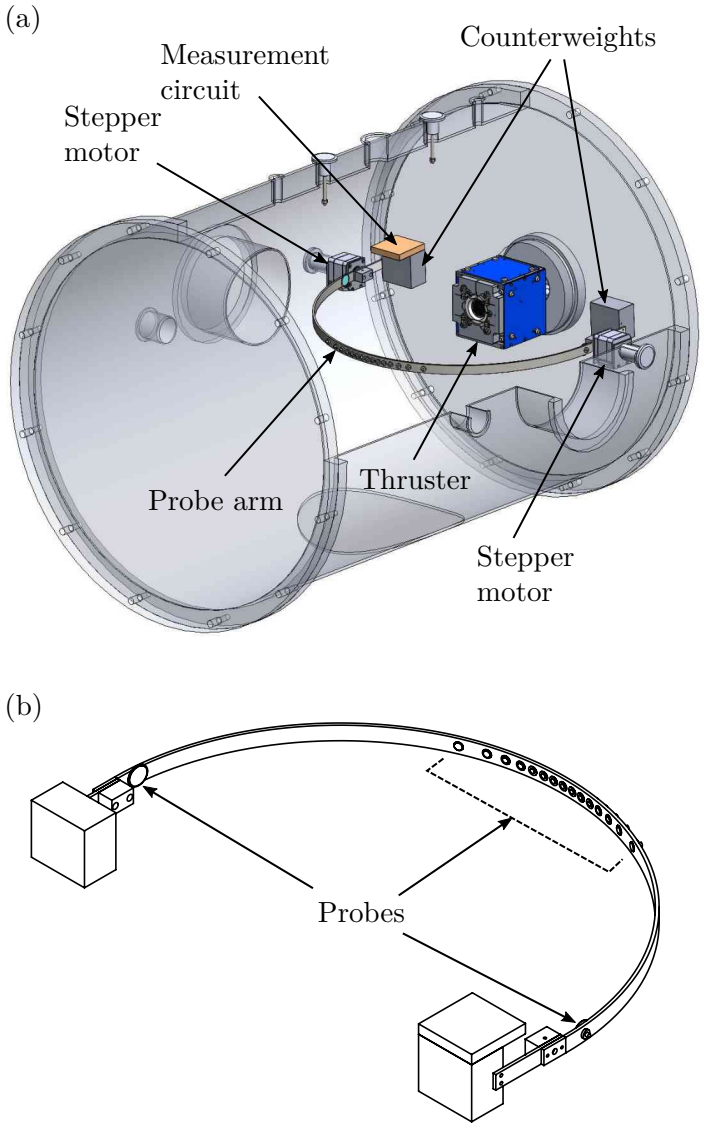

Figure 3.10: (a) Schematic of the planar probe array assembled in the vacuum chamber. (b) Front view of the instrument showing the probe positioning (adapted from Ref. [145]).

gravity, avoiding unnecessary damage due to bombardment by the energetic ions. The measurement circuit, containing the required circuitry to convert the current reading to a voltage signal and perform a pre-filtering of the signal, is placed on top of one of the counterweights. To mitigate the interaction of the background plasma discharge, which can lead to a significant increase in the signal noise level and arcing, the measurement circuit is covered by a copper box that is connected to the chamber ground.

Since the array is used not only for the xenon thruster but also with iodine, it was important to improve its resistance to corrosion due to contact with background iodine gas. Apart from the connectors, the measurement board was covered with a polymeric coating, isolating the tracks and components from contamination. After installing the instrument in the chamber, all electric connectors were covered with disposable adhesive aluminum foil, and a PTFE-based grease was used on the shaft of the motors to isolate its internal mechanism from the iodine atmosphere. To avoid further reactions with oxygen at the end of every operation cycle with iodine, the instrument was removed from the chamber and cleaned with alcohol, and the probe collecting surfaces were polished to remove any deposition or reaction products that may alter their readings. No perceptible degradation of the probes or accumulation of systematic errors was observed during the operation with iodine.

Array arrangement

The size of the probes and their position along the arc can substantially impact the final reconstruction of the beam profile, especially on the signal-to-noise ratio and the shape of the density curve. If the probes have identical areas and are uniformly distributed along the arm, important features with higher "spatial frequency" can be lost because the spatial sampling step is too large. This can have an impact on both the value of the integration of the data and on the reconstruction of the original shape. As described by Theunissen and Gjelstrup [148], when there are a limited number of sensors available, a method similar to mesh-refinement heuristics can be employed to improve the measurement quality by increasing the number of sensors in regions where it is known that the signal is more complex and stronger.

Several criteria may be used to determine the distribution of sensors along the region of interest using the information on the expected signal profile. Some examples are the signal intensity, curvature, gradient, among many others [148]. In the present work, to better resolve the shape of the ion beam peak and increase the sensors in the region with the highest gradient, it is chosen to have a density of sensors along the arc, $\delta_s(\theta)$, proportional to the expected current density. The probe density in this case is simply defined as

$$\delta_s(\theta) = \frac{dN_p}{d\theta} \tag{3.10}$$

where θ is the angular position along the semi-circle and N_p is a variable representing the number sensors between two values of θ.

As already discussed, in the case of ion thrusters, the ion current density profile in the plume roughly follows the shape of a Gaussian function. Therefore, the density here

Table 3.1: Summary of planar probe angular positions, dimensions and connected measurement resistors.

Probe number	Position (°)	Diameter (mm)	R_m (kΩ)
-8	-85	25.5	100
-7	-22.9	7	100
-6	-17.3	6	100
-5	-13.4	5	100
-4	-10.1	5	100
-3	-7.4	4.1	20
-2	-4.8	4.1	20
-1	-2.4	4.1	20
0	0	4.1	20
1	2.4	4.1	20
2	4.8	4.1	20
3	7.4	4.1	20
4	10.1	5	100
5	13.4	5	100
6	17.3	6	100
7	22.9	7	100
8	85	25.5	100

is assumed to approximately follow the shape $n(\theta) \sim a\exp(-\theta^2/2\beta^2)$. Assuming that $\delta_s(\theta) \propto n_i(\theta)$, where n_i is the ion density at a given position, it is possible to determine the number of sensors at a given position by calculating

$$N_p(\theta) = \frac{k}{\beta\sqrt{2}} \int_0^{\theta} \exp\left(-\frac{\theta'^2}{2\beta^2}\right) d\theta' \tag{3.11}$$

where $a = k/\beta\sqrt{2}$ was chosen to ensure the proper normalization and k is a constant. It is important to note that β is an angle that is related to the standard deviation of the curve and thus the divergence of the beam. Evaluating the integral, the number of probes can be then calculated as

$$N_p(\theta) = \frac{k}{2}\mathrm{erf}\left(\frac{\theta}{\sqrt{2}\beta}\right) \tag{3.12}$$

Assuming that at a given position θ_i, $N_p(\theta_i)$ probes are present and that at least one is the i-th probe, it is possible to set $i = N_p$. Solving 3.12 for θ_i while considering that $i = N_T - 1$ at θ_f, where N_T is the total number of probes and θ_f is the final position, gives

$$\frac{\theta_i}{\beta\sqrt{2}} = \mathrm{erf}^{-1}\left(A\frac{i}{N_T - 1}\right) \tag{3.13}$$

where $A = \mathrm{erf}(\theta_f/\beta\sqrt{2})$.

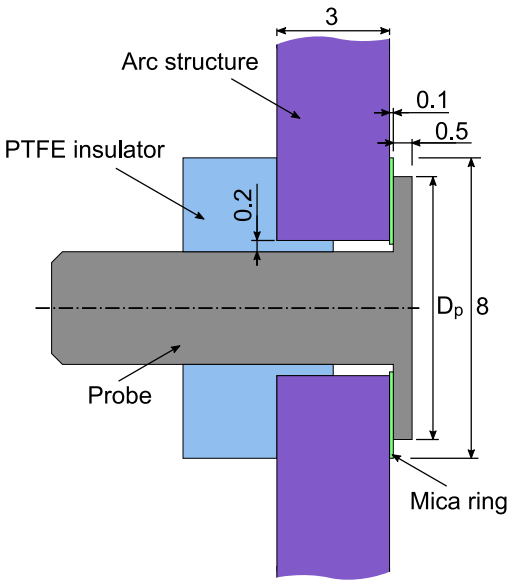

Figure 3.11: Schematic of the assembly of a single probe, all dimensions are given in millimeters (source: [145]).

To determine the actual distribution, a divergence half-angle of 15.5° was assumed based on previous experiments and the expected performance of the thruster. Due to the number of channels in the data acquisition used, the system was designed to use 15 probes, including a probe in the center of the arc. Therefore, $N_T = 8$ is selected (which is the number of probes along only one half of the arc), and $\theta_f \approx 23°$ since no significant signal is expected outside of this zone. The areas of the probes were chosen to balance the signal-to-noise ratio at the acquisition board, ensuring that the current measured by each probe was similar – thus having larger areas in regions where ion current density was expected to be lower and smaller areas where the signal was expected to be stronger. The background plasma sensors do not follow the placement rule described here and are placed at the edges to avoid interference with the beam. Table 3.1 gives the positions of all the sensors and their areas.

Probe construction

The arc has 17 planar probes, which are metallic disks biased to a negative potential so that only the ion saturation current is measured. The probes have a thickness of 0.5 mm and are made of stainless steel. They are positioned on the structure using mica rings with a 0.1 mm thickness for insulation between the probes and the grounded arm. PTFE spacers are used to center the probes on the holding holes correctly. The assembly of a single probe is shown in figure 3.11. The decision to use stainless steel for the probes instead of other materials, such as molybdenum or tungsten, that could offer better characteristics in terms of SEE or sputtering yields, was mainly to ensure an easier manufacturing and prototyping process during the development of the instrument.

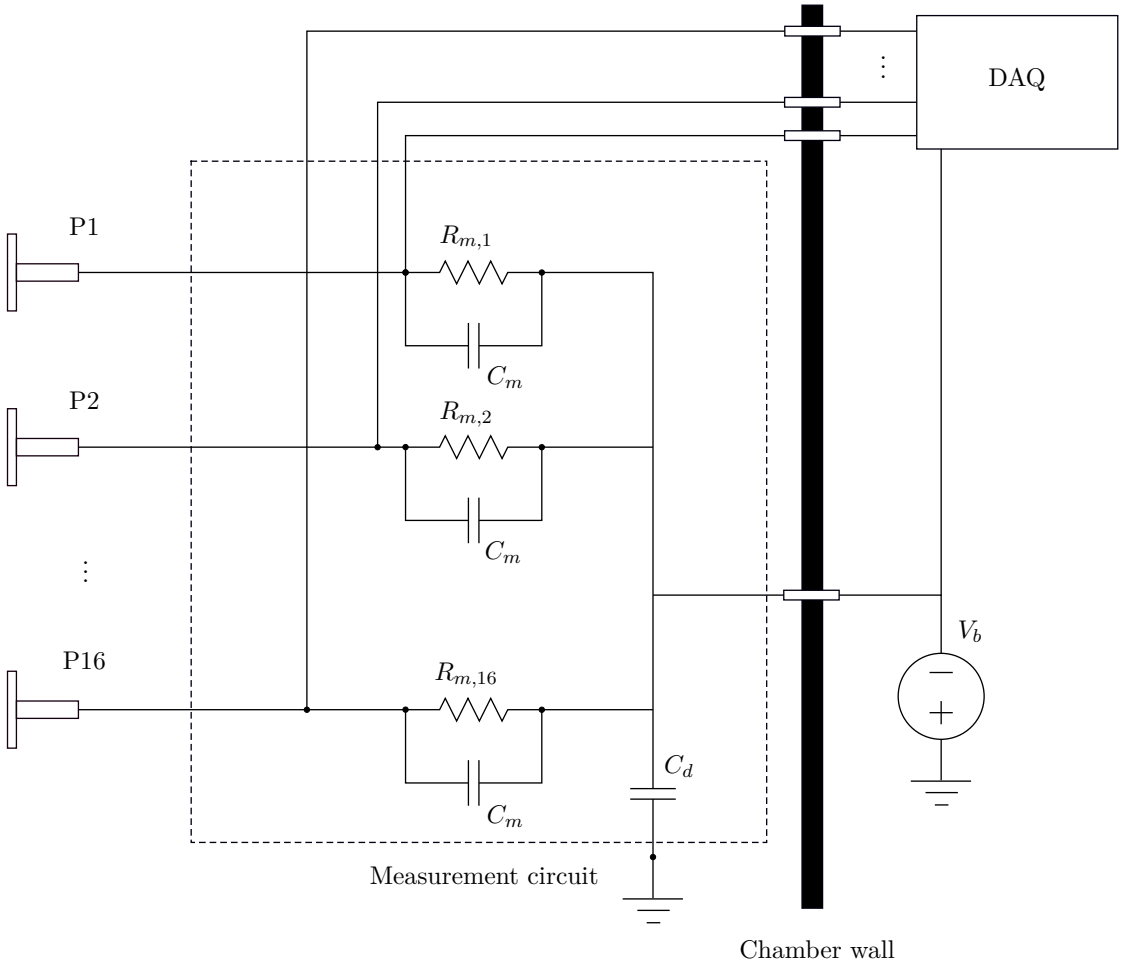

Figure 3.12: Circuit schematic of the probe connection to the measurement circuit.

Electrical design

Each probe was connected to the measurement circuit using 30 AWG silver-plated wires to decrease parasitic resistance. To avoid interference from the plasma on the signals in the wires, they were fixed to the back of the arc and shielded with an adhesive metallic foil which is electrically connected to the vacuum chamber ground.

The connections from the probes to the measurement circuit are shown in figure 3.12. Each probe is connected to a measurement resistor, R_m, and a filtering capacitor, C_m. The values of the measurement resistors are selected such that lower resistances are used for probes where the current is expected to be higher, and higher resistances are used where the current is lower. The values for each probe are given in table 3.1. The capacitor C_m is used to suppress measurement noise and bypass any AC voltage component – it has a value of 10 nF. On the other end, these components are connected to a constant negative bias, V_b, provided by an external power supply.

To reduce the noise level from the power supply, an additional capacitor, C_d, with a value of 2.2 nF, is placed at the measurement circuit and connected between the bias line and the chamber ground.

The measurement lines coming from the LHS terminal of the measurement resistors are connected to a multi-wire cable shielded with a copper braid to avoid electromagnetic interference of the measurement signals. This cable is connected to a 16-channel MCC USB-1608HS data acquisition board (DAQ) for the measurement. Because the measurement reference, in this case, is V_b, the same bias was applied to the measurement ground of the DAQ. This board is capable of simultaneous 16-bit acquisition at speeds up to 250 kS/s.

The stepper motors are powered and controlled by two A4988 driver circuits. These drivers are attached to an Arduino, which in turn is connected to a computer where the control scripts run. The Firmata protocol [149] is used to directly control the stepper motor drivers from a Python script by using the pyFirmata library.

A single dedicated Python script controls the DAQ and the motor movement. This script has a GUI created with the Tkinter library for faster interaction and real-time plotting of the data acquired from the instrument. All data acquired by the DAQ is saved to disk and analyzed by dedicated post-processing scripts.

3.4.2 Measurement calibrations and corrections

The first calibration was the determination of the required bias voltage for the probes to ensure the ion saturation current was obtained. This was done experimentally by measuring the IV curve of a 5 mm planar probe immersed in a xenon plasma plume generated by the NPT30-Xe with a screen voltage of 1 kV and a cathode which is biased to −30 V. The measured curve is shown in figure 3.13. It is possible to see a clear step at the cathode bias voltage, and below that, the current stabilizes, and only the ion saturation current is measured. Between −30 V and −150 V, the measured current slowly drops from 0.17 mA to 0.18 mA, which corresponds to the effect of sheath expansion, as discussed in section 3.3.1. During the experiments done in this work with DC thrusters, it is expected that the conditions will be similar to this calibration test, so it is expected that the electrons will behave similarly. Therefore, a fixed voltage of −48 V was selected as the bias for all probes of the instrument during the experiments.

Due to the resistance of all electric systems, including wires, cables, the measurement circuit, and the DAQ, the signal measured by the instrument exhibits a systematic offset. To correct this, an electrical calibration procedure was conducted, which consisted of connecting resistors with a precisely known value between the surface of each probe and the chamber ground and measuring the voltage drop across the resistor. The current value measured in the calibration resistor and the acquisition board were then compared, and a correction factor was determined for each probe. Two different resistor values were used for each probe to obtain two different calibration points. For the probes that use 100 kΩ measurement resistors, the calibration was done with resistors of 677 kΩ and 4.7 MΩ. For probes using 20 kΩ resistors, the calibration was done for 120 kΩ and 1 MΩ. The two calibration points are then averaged for each probe and used to correct the

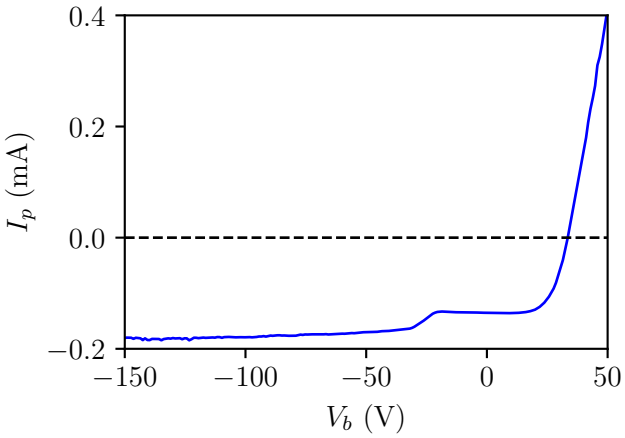

Figure 3.13: Measured IV curve for the determination of the probe bias voltage.

subsequent measurements with the instrument.

As discussed in section 3.3.1, the measurement done with a simple planar probe, with no modifications, suffers from several effects that might make it drift from the actual value. The two most important effects are sheath expansion and ion-induced SEE. In the case of sheath expansion, one straightforward solution would be Sheridan's model [137]; however, this model cannot be applied directly in the present case because of the strong anisotropy caused by the energetic ion beam. A similar strategy to Sheridan is adopted to find a correction for the present case with an ion beam, and the effective current collected by the probe is estimated using a series of PIC simulations.

For this estimation, the open-source PIC code, XOOPIC [150], is used. In this specific problem, it was not possible to use the code developed in the context of this work because a higher degree of flexibility in terms of domain geometry was required, and this implementation was out of the scope of this work[1]. Using XOOPIC, a probe with the same dimensions as the one shown in figure 3.11 was simulated with two different diameters, 4 mm and 7 mm. The plume potential, assumed to be 22 V, is used as the reference, and the probe is set to −48 V. A cylindrical geometry is adopted with a 64×64 cell mesh and spacing of 0.119 mm (total size of 7.5 mm × 7.5 mm). The bottom boundary is used as the cylindrical axis of symmetry, the LHS and RHS boundaries use a fixed potential, and the top boundaries use a zero-electric field condition. A time step of $\Delta t = 5 \times 10^{-11}$ s is used, and the simulation is executed until steady-state. The particles are injected at the LHS boundary, with no drifting electrons with $T_e = 3$ eV, and ions having $T_i = 300$ K and five different drift energies, 0.5 keV, 0.7 keV, 0.9 keV, 1.1 keV and 1.3 keV. The simulations were conducted for three different values of ion

[1] On the other hand, the XOOPIC code could not be used for the simulations done in chapter 2 due to several limitations, namely the impossibility of using time-varying injection currents and of using capacitive boundaries with an external circuit.

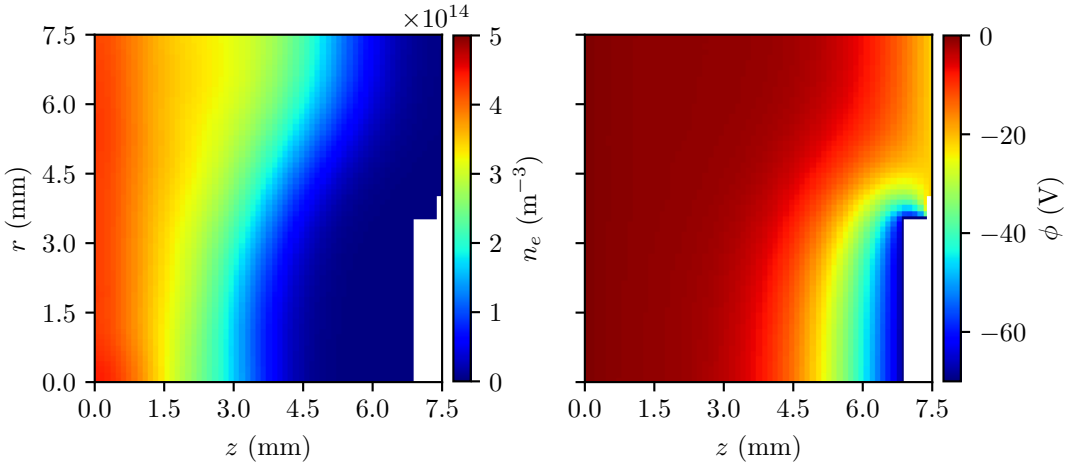

Figure 3.14: Example result of a PIC simulation of the planar probe showing the electron density (left) and the potential (right). This result is for $J_i = 0.2\,\mathrm{mA/cm^2}$, $E_i = 0.9\,\mathrm{keV}$ and $D = 7\,\mathrm{mm}$.

current density J_i, $0.2\,\mathrm{mA/cm^2}$, $0.4\,\mathrm{mA/cm^2}$ and $0.6\,\mathrm{mA/cm^2}$, which is similar to what is expected from the thruster. The magnitude of the electron current injected is calculated to ensure quasi-neutrality and is the same as in equation 2.25. For each simulation case, the particle weight used was calculated as $N_p = 500 J_i$, since, from several tests, this provided a good compromise between computation speed and low statistical noise. Figure 3.14 shows an example of the simulation results showing the electron density, n_e, and the potential, ϕ, for the case where $J_i = 0.2\,\mathrm{mA/cm^2}$, $E_i = 0.9\,\mathrm{keV}$ and $D = 7\,\mathrm{mm}$. As it is possible to see from the figures, a sheath is formed in front of the probe, which varies in size depending on the operating conditions used.

Figure 3.15 show the result of all the simulation cases. The value computed corresponds to $\eta = I_p/I_{\mathrm{ref}} - 1$, where I_p is the current collected by the probe during the simulation during steady-state and I_{ref} is the reference collected current calculated as $I_{\mathrm{ref}} = A J_i$, where $A = \pi D^2/4$ is the area of the probe. As the ions' energy increases, it is possible to observe from the plot that the total collected ion current decreases approaching the ideal case. This can be explained due to the decrease in their transit time across the simulation domain, which decreases the deflection of their trajectory towards the probe. For each ion energy value, it is possible to see a spread in η, which corresponds to the different values of J_i and two trends corresponding to the two different values of D. Each of these trends is fit with a power law curve, which results in

$$\eta_S = 46.506 E_i^{-1.118} \tag{3.14}$$

$$\eta_L = 3.306 E_i^{-0.7037} \tag{3.15}$$

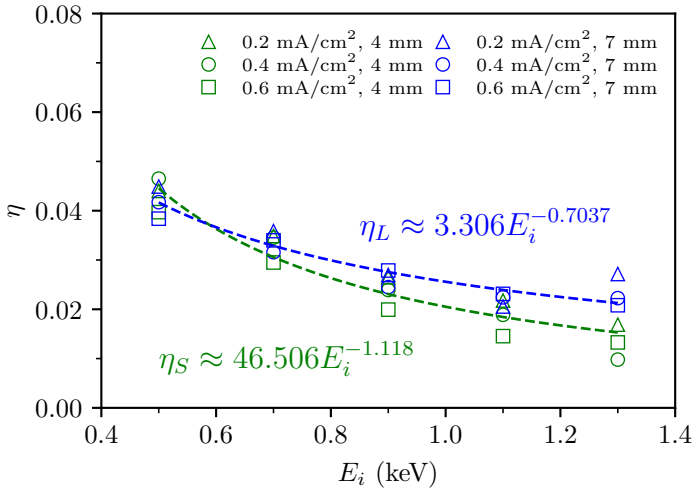

Figure 3.15: Result of all PIC simulations of the planar probes, showing the values of $\eta = I_p/I_{\text{ref}} - 1$ as a function of the injection ion energy, E_i. η_S and η_L are power law fits of the data for probe diameters of 4 mm and 7 mm respectively.

where E_i is the ion energy and, η_S and η_L correspond to the smaller area case ($D = 4\,\text{mm}$) and larger area case ($D = 7\,\text{mm}$) respectively. To apply this data for the correction of the data measured with the planar probes, a correction factor $\eta_p(E_i, A)$ is defined as the linear interpolation between η_S and η_L,

$$\eta_p(E_i, A) = \frac{A - A_S}{A_L - A_S}[\eta_L(E_i) - \eta_S(E_i)] + \eta_S(E_i) \tag{3.16}$$

where A is the area of the probe, and A_S and A_L are the areas of the smaller and larger case respectively. The spread due to the variation of J_i is considered here an uncertainty factor and included in the error of the measured data.

The last factor that needs to be considered is the electron current created by ion-impact SEE. This data is widely available in the literature for several target materials and the most common ion species, such as xenon. However, there is no information available regarding the yield due to the bombardment of iodine ions. Therefore, a series of experiments were done in the context of this work to measure the iodine SEE yields for several common materials typically used in plasma physics and the aerospace industry. These experiments are shown in the next chapter.

Using both the data from the sheath expansion simulations and the available SEE yield data, the corrected ion current measured by a planar probe of the arc can be estimated as

$$J_{i,c} = \frac{k_c J_{i,m}}{1 + \gamma(E_i) + \eta_p(E_i, A)} \tag{3.17}$$

where $J_{i,m} = V_m/R_m A$, A is the frontal area of the probe, V_m is the voltage drop across the measurement resistor, γ is the SEE yield and k_c is the calibration coefficient obtained

for the probe during the procedure described in this section. Equation 3.17 is used to correct all measurements done with this instrument.

3.4.3 Data integration

After measuring the ion current density of the beam and correcting it with the appropriate model, this data can be used to obtain different characteristics of the beam. The first one is simply the two-dimensional profile of the plume that may offer a way to visualize different features in the plume. Beyond this, from this profile, it is possible to estimate both the total ion current emitted by the thruster and the divergence half-angle of the ion beam. To obtain these quantities, the data measured by all probes must be integrated with the appropriate geometric considerations.

Because the instrument arm has a semi-circular shape, the data measured can be better analyzed in a spherical coordinate system. Figure 3.16 shows a schematic of the arrangement of the coordinate system. The origin of the coordinate system is fixed at the center of the exit plane of the thruster, with the x-axis pointing in the direction of thrust, the y-axis pointing upwards, and the z-axis perpendicular to both following the right-hand convention. In this coordinate system, the variable r is the distance from the origin, ϕ is the azimuthal angle, which represents the direction of movement of the probe arm, and θ is the polar angle, representing the position of the sensors. Since the sensors are symmetrically positioned over the instrument's arm, it is convenient to represent their position using the latitude angle, $\Theta = \pi/2 - \theta$. In this way, the central probe is located at $\Theta = 0$.

To estimate the total ion beam current and the divergence half-angle, it is necessary to perform a numerical integration of the measured ion current density $J_i(r, \phi, \theta)$ over the spherical surface shown. Brown *et al.* [151] describes a standard method found in the literature for single-probe experiments, consisting of the integration of the current density in one dimension over half of the azimuthal domain. The authors also show a method to correct for the effect of non-point sources, considering the thruster's actual size. However, in the case of the present work, this approach cannot be used directly since the data must be integrated in two dimensions. Considering that all probes are at a distance R from the origin of the system and that their surfaces are perpendicular to the vector, $\mathbf{r}$, the total ion current can be calculated as

$$I_b = R^2 \int_{-\pi}^{\pi} \int_{0}^{\pi} J_i(r, \phi, \theta) \sin\theta d\theta d\phi \tag{3.18}$$

$$= R^2 \int_{-\pi}^{\pi} \int_{-\pi/2}^{\pi/2} J_i(\phi, \Theta) \cos\Theta d\Theta d\phi \tag{3.19}$$

Equation 3.18 is discretized and evaluated over the data using Simpson's integration rule.

For the estimation of the divergence half-angle, it is necessary to calculate both the total ion current and the axial ion current, I_{ax}, i.e., the current decomposed in the direction of the thrust. As shown in ref. [151], in the case of a single-probe experiment, since the probe crosses the thrust axis, the axial ion current may be obtained simply by

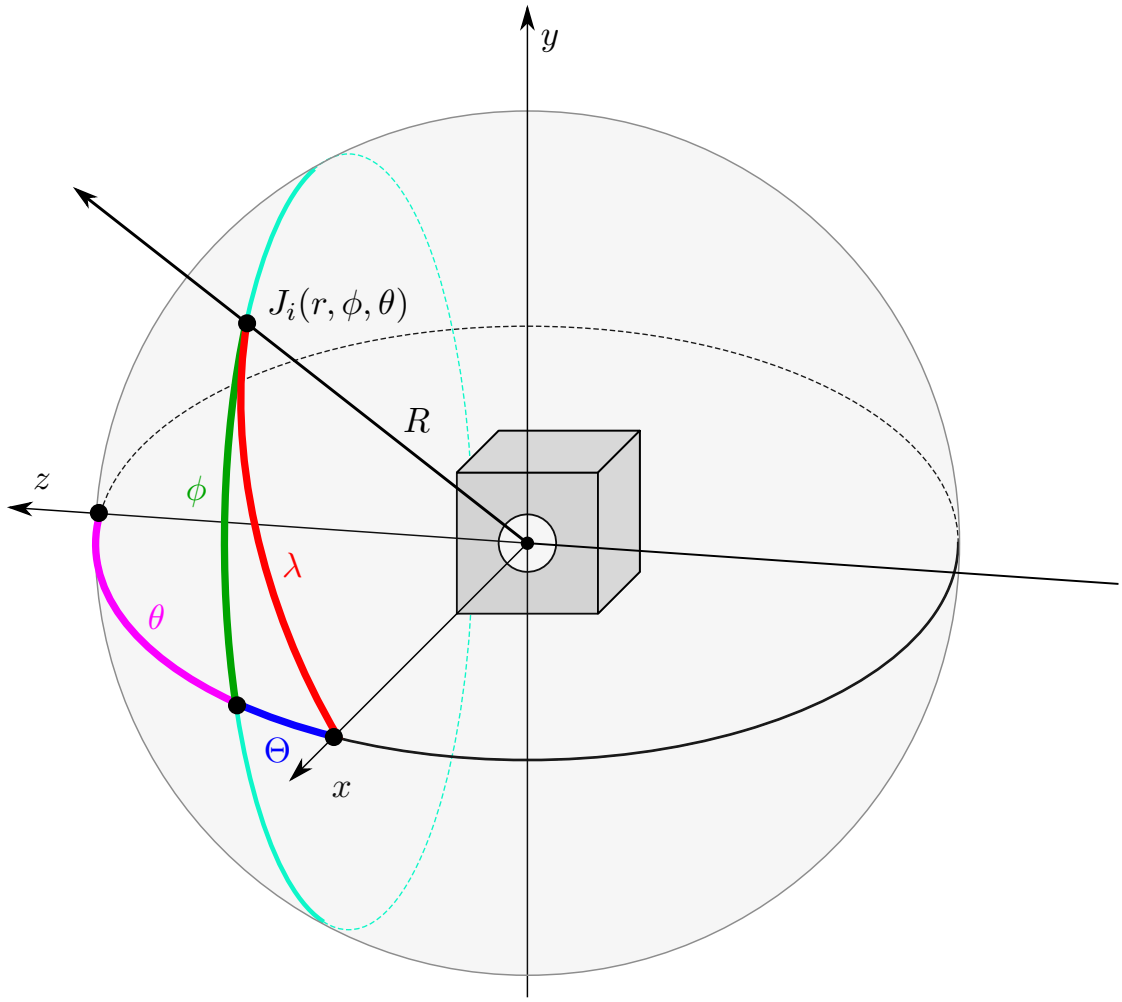

Figure 3.16: Schematic of a spherical coordinate system used for the integration of the data measured by the planar probe array. The x-axis is aligned with the thrust direction, θ and ϕ are the polar and azimuthal angles, respectively, Θ is the latitude angle, and λ is the "great circle" angle.

decomposing the ion current density vector along ϕ. In the 1D case, the axial current is found as $I_{ax} = 2\pi R^2 \int_{-\pi}^{\pi} J_i(\phi) \cos\phi d\phi$, which is the most commonly used formula in the literature. In the 2D case, however, it is necessary to decompose the current density using the angle between the evaluated point and the x-axis. This angle is called here λ and corresponds to the angle formed by the "great circle" distance between the point and the x-axis, which is defined as the shortest path, also called a geodesic, between two points on the surface of a sphere. This path can be found by tracing a circle that intercepts both points, and that has its center coinciding with the sphere's center, and then considering only the path with the shortest length. The angle formed by this distance can be found using the haversine formula, which is written as

$$\lambda = 2\sin^{-1}\sqrt{\sin^2\left(\frac{\Theta_2 - \Theta_1}{2}\right) + \cos\Theta_1 \cos\Theta_2 \sin^2\left(\frac{\phi_2 - \phi_1}{2}\right)} \tag{3.20}$$

where the subscripts 1 and 2 denote the angles for the first and second evaluated points respectively. Considering that point 1 corresponds to the location where the sphere intercepts the x-axis, one has $\Theta_1 = \phi_1 = 0$, making it possible to simplify the formula as

$$\lambda = 2\sin^{-1}\sqrt{\sin^2\frac{\Theta}{2} + \cos\Theta\sin^2\frac{\phi}{2}} \tag{3.21}$$

where the subscripts were dropped since just the position of the point is considered now. Using the half-angle formulae for the sine and cosine, the equation can be further simplified to

$$\lambda = 2\sin^{-1}\sqrt{\frac{1 + \cos\Theta\cos\phi}{2}} \tag{3.22}$$

Using the half-angle formula again for λ, the projection term used for the calculation of the axial current is found as

$$\cos\lambda = \cos\Theta\cos\phi \tag{3.23}$$

It is interesting to note that this expression corresponds simply to the projection of the vector over the two positional angles. The axial current can then be calculated as

$$I_{ax} = R^2 \int_{-\pi}^{\pi}\int_{-\pi/2}^{\pi/2} J_i(\phi,\Theta)\cos\phi\cos^2\Theta d\Theta d\phi \tag{3.24}$$

Then, with equations 3.18 and 3.24, the divergence angle can be obtained as

$$\theta_d = \cos^{-1}\left(\frac{I_{ax}}{I_b}\right) = \cos^{-1}\left(\frac{\int_{-\pi}^{\pi}\int_{-\pi/2}^{\pi/2} J_i(\phi,\Theta)\cos\phi\cos^2\Theta d\Theta d\phi}{\int_{-\pi}^{\pi}\int_{-\pi/2}^{\pi/2} J_i(\phi,\Theta)\cos\Theta d\Theta d\phi}\right) \tag{3.25}$$

CHAPTER 4

SECONDARY ELECTRON EMISSION DUE TO IODINE ION BOMBARDMENT

This chapter describes the first set of experiments of this work, which are done to estimate the secondary electron emission due to the bombardment of iodine ions on several different materials. This is done because there is an important lack of data in the literature regarding the beam and plasma-related properties of iodine and its interaction with surfaces, especially the SEE yields. Apart from being interesting from the point of view of basic physics, this data is also important due to its direct applicability on the correction of plasma diagnostics done in iodine plasmas. It is also expected to be important for theoretical and numerical simulation models. The data collected in this part of the work is used in the following chapter for the adjustment of the planar probe measurements done to characterize the plume of the iodine ion thruster.

4.1 Background

4.1.1 Ion-induced emission

The phenomenon of secondary electron emission (SEE) can be seen, generically, as the emission of electrons due to the interaction of charged particles with the surface of a solid material. At a quantum mechanical level, this interaction modifies the electric potential configuration and provides the required energy for an electron to escape the potential well within the body of the material. Here, the discussion is focused on the emission caused by positive ions since it is the most relevant situation for these experiments. To quantify the amount of electrons emitted, a quantity called the *yield* is used, which is defined as

$$\gamma = \frac{I_{\mathrm{SEE}}}{I_i} \tag{4.1}$$

where I_{SEE} is the current of electrons emitted and I_i is the current of ions reaching the surface of the material. The yield depends on the target material and the ion species and can in principle be estimated from theory, but because of the complexity of this phenomenon, its value is usually obtained from experiments.

Ion-induced secondary electron emissions are mainly caused by two different mechanisms, potential electron emission and kinetic emission [152, 153]. In the potential

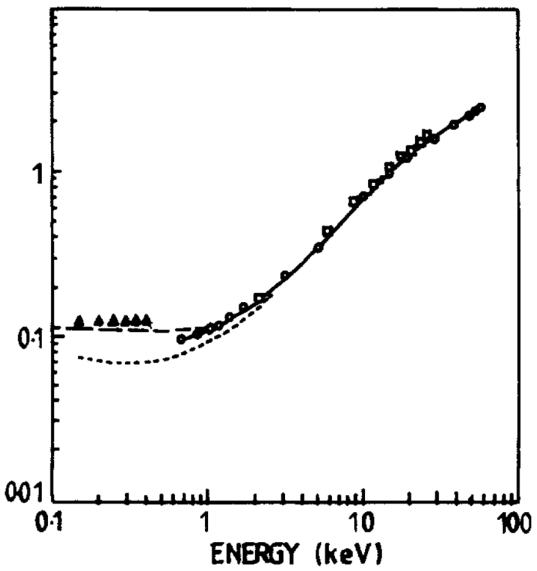

Figure 4.1: Example of experimental SEE yield data for Ar^+ ions bombarding a Mo target (source: [155]).

emission, when the ion reaches the vicinity of the material wall, its potential field configuration induces the transfer of an electron from the solid to the ion, neutralizing it. The transfer occurs either by a process called Auger neutralization or resonance neutralization, which is followed by an Auger de-excitation. In both of these processes, the potential energy of the ion may be transferred to a second electron, which is emitted from the surface if the energy is above a threshold. For metals, this threshold is generally accepted to be $E_{iz} > 2W$, where E_{iz} is the first ionization energy of the ion and W is the work function of the material [153]. A commonly used semi-empirical formula for an approximate estimation of the potential emission is given by [154]

$$\gamma \approx 0.032(0.78E_i - 2W) \tag{4.2}$$

Therefore, the potential emission is favored for noble gases or highly electronegative ions and metals with a low work function. As the first ionization energy for xenon is 12.1 eV, and iodine is 10.45 eV, potential emission will almost always be relevant since the work function for metals are in general lower than 5 eV. The value of the SEE yield relative to potential emission is typically not dependent on the kinetic energy of particles. Therefore, the experimental yield data relative to this mechanism typically shows a constant horizontal trend, especially at low ion energy levels. Figure 4.1 shows an example of experimental SEE yield data measured for Ar^+ ions bombarding a Mo target. It is possible to observe that when the average ion energy is less than roughly 1 keV, the yield behavior is close to what is explained by potential emission, with an almost constant yield with a value of about $\gamma \approx 0.1$–0.15.

On the other hand, kinetic emission is directly related to the transfer of kinetic energy

from the projectile ion to the target's electrons. This happens due to the interaction of time-varying coulomb interactions as the projectile approaches the surface, penetrates, and scatters inside the target's material. This emission is generally divided into three phases: (1) the ion energy transfer as it enters the solid lattice, exciting some of the electrons inside the material; (2) diffusion of the excited electrons towards the surface; and (3) the escape of the electrons from the surface into vacuum. Because there are many possible highly complex mechanisms involved in the production and emission of the electrons, theoretical studies typically model the emission in a semi-empirical manner, assuming that the yield is proportional to the *stopping power*. This power consists of the amount of energy transferred from the ion to the material as it penetrates the surface until it stops, and it is proportional to the velocity of the projectile and other characteristics of the material [156]. Therefore, the main governing parameter in this type of emission is the velocity (or energy-per-mass) of the projectile instead of its energy [154]. Despite existing theoretical models such as the Bethe formula for the estimation of the stopping power, an accurate estimation of its magnitude is a complex problem involving different quantum mechanical mechanisms, and typically is done via simulation. The yield, in this case, has typically a strong relation to the average ion velocity, which can be seen in figure 4.1 for energies above 1 keV, where the kinetic emission starts to be the dominant mechanism and the yield value starts to grow considerably faster. The threshold for kinetic emission is generally accepted to be from 0.6×10^5 m/s to 2×10^5 m/s [153]. Kinetic emission is influenced by a number of characteristics of the beam and the target material, including the surface condition of the target, its crystallographic structure, the reactivity of the beam, and its incidence angle, which can make the emission decrease significantly for angles below 70° [153].

Ion-induced emission has been characterized for several pairs of projectiles and targets – Hasselkamp [154] presents a summary of all the available SEE yield data until 1992. Because of the phenomenon's complexity, typically, these measurements were primarily done with noble gases and clean non-reactive metallic surfaces, such as molybdenum and tungsten, which generally presents a behavior easier to model and is not significantly affected by other phenomena such as sputtering. This way, there is a wide range of available data regarding SEE yields for these cases [155, 157–161]. On the other hand, the data for reactive and molecular ions are scarce and often entirely unavailable for different plasma physics problems. For iodine, as far as the author knows, the SEE yield has been measured just once, in a work by Hird *et al.* [162] for the impact energy range from 40 keV to 115 keV, which is incompatible with space propulsion applications.

4.1.2 Multi-species and molecular ion bombardment

In many plasma and ion beam problems, the bombarding interacting particles do not consist exclusively of monoatomic ions and can have several different ions and neutral species, including atoms and molecules. This happens, for example, in plasma discharges based on polyatomic gases, where a number of reactions may take place, and different ion and neutral species may be formed. In these cases, the characterization of secondary electron emission on surfaces becomes considerably more complex, and the determination

of a single yield value is not possible since its value depends on the exact composition of the plasma and the different energies of the species. Previous works also show that molecular ions do not behave in the same manner as monoatomic ions, and any theoretical approach used for the estimation of atomic yields cannot be directly used in the molecular case. It is found that the molecular yield is typically lower than the sum of the yields of its constituents, but the ratio of both yields may change depending on the energy range; however, the mechanism behind molecular emission is still not well-understood [163]. Emission due to the bombardment of negative ions or neutral species has also been a subject of study [154]. Most of the studies in this context were done for hydrogen and oxygen ions. Different studies found that H^+ presents a slightly higher total yield than and H^0 for energy levels below 5 keV. For energy levels below 8 keV, it was also found that the yield of negative hydrogen and oxygen ions were lower than the positive ions [161].

Several works have been dedicated to estimating and measuring the individual SEE yield values of multi-species plasmas and beams. Hasselkamp [154] provides a detailed review of different works in this domain. Specifically, Mahadevan *et al.* [161] present the yield of ion species present in atmospheric discharges bombarding molybdenum for energies ranging from 0.1 keV to 2 keV. This study is interesting for the present work since, as, in the case of iodine, the most common elements in the atmosphere are stable as a diatomic gas, which may generate similar behavior when in a plasma state. In general, for this energy range, the authors find that diatomic molecular (positive and negative) ions of oxygen, hydrogen, and nitrogen have lower yields than monoatomic ions.

Iodine is a highly reactive element and generally stable as a diatomic gas, I_2. Therefore, when in a plasma discharge, especially in the conditions found in propulsion devices, iodine usually forms multiple species. Apart from the neutral particles (I and I_2), the most common species are I^+, I^{2+} and I_2^+ [70]. In this way, because the exact concentration of each plasma species is typically unknown, the characterization of the emission due to the interaction with an iodine plasma is not straightforward. Therefore, during the study of iodine emission properties, it is also necessary to estimate the incident beam composition so that the influence of each species can be individually verified.

4.1.3 Reactive plasmas and beams

Typically, when studying secondary electron emission, an assumption that is often made is that the target is composed of a single type of material and its surface is clean. This assumption ensures that, at least partially, the measurements are easily repeatable and that the analysis is done just for one projectile-target pair at a time. However, in some cases, this assumption does not hold true due to the continuous modification of the target's surface when in contact with certain species from the plasma. This is especially the case with atoms and molecules with high reactivity, which may deposit themselves on the surface or produce chemical reactions with the target's material. Furthermore, when the energy of the bombarding ions is high enough (typically tens of keV), the surface may also be modified through ion implantation. The products created by these surface processes typically have different emission properties than the target's material and may

also have different electrical characteristics, which can directly affect the interaction between the discharge and the target.

Secondary emission in reactive plasmas was studied, especially in the context of the reactive sputtering process used in the semiconductor industry. Lewis *et al.* [164] show the SEE yield measurement of aluminum and titanium using a mixed ion beam created from an inert and a reactive gas, Ar and N_2. The authors show that as the partial pressure of nitrogen increases, increasing its relative number of ions in the beam, the yield also increases significantly from 0.1 at 0 % of nitrogen, to 0.6 at 100 %. This increase in the yield cannot be explained only by the characteristics of the different ion species, and the authors show that it is linked with the formation of nitrites on the surface of the targets (AlN and TiN), which have much higher yield values than pure metals. A similar experiment was conducted by Corbella *et al.* [165], where the SEE was characterized on aluminum and titanium targets with an argon ion beam and an oxygen gas background. Similar to the previous work, it is shown that the secondary emission for the pure argon beam is considerably lower and closer to theoretical predictions when compared to the case when the oxygen atmosphere is added due to the formation of oxides on the surface of the targets. It is observed as well that the increase in emission is considerably higher for aluminum compared with titanium, which is associated with the higher oxidation rate in the case of the aluminum sample. Depla *et al.* [166] provides an extensive comparative work showing the relative increase or decrease on the SEE yield due to oxidation or nitration for 17 different materials. Generally, metals with higher reactivity, such as aluminum or magnesium, show a more significant change in the yield, while metals with lower reactivity, such as gold or silver, present an almost negligible change. Buschhaus *et al.* [167] study the change of the yield values of copper and nickel targets when oxidized. The authors measure the yield for the bombardment of argon ions and verify an increase of roughly two times in their value when the surface is oxidized. This way, the characterization of emission properties of reactive plasmas is considerably more complex when compared to inert species and requires the consideration of different chemical and surface processes.

Iodine is known for being a highly reactive substance, and its plasma or beam can generate different chemical reactions in the discharge and on the surface of materials [136, 168]. Specifically, when in contact with metals, iodine can generate several types of iodides, that is a kind of halide, and their properties, especially related to electron emission, are not available in the literature. Furthermore, the specific types of reactions and their rates are not easily estimated, making a study of plasma-surface interactions non-trivial. Therefore, because the compound layer is continuously formed and sputtered in almost any reactive beam or plasma, the SEE yield measured represents an effective yield of the target material and the layer. On the other hand, in applications using beams and plasmas based on molecular gases, the most common situation encountered in different applications is indeed the presence of multiple ion species that may collectively change the surface chemistry and modify the effective SEE yield compared with that observed separately with each species. Thus, the present work aims to provide a collective description of the iodine emission since this will be the situation found in ion thruster

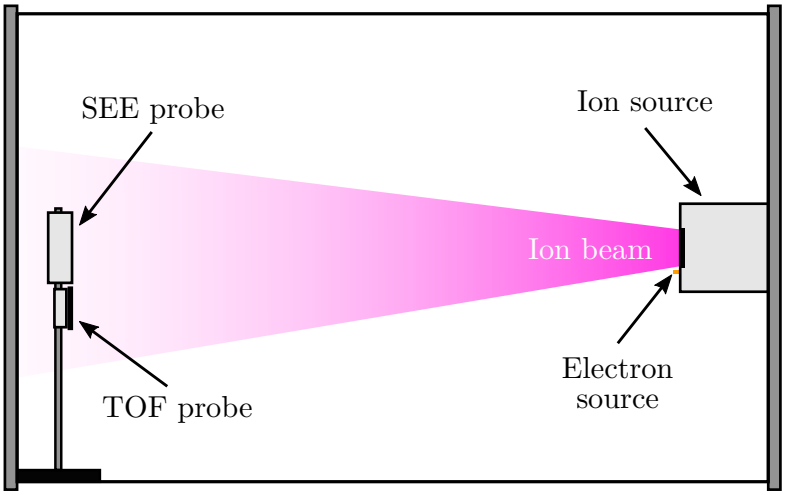

Figure 4.2: Side-view schematic of the SEE experiment (adapted from Ref. [169]).

or material processing applications, and an effort is made to estimate the individual contributions of each species to the measured yield.

4.2 Experimental setup

The experiment performed here aims to estimate mainly two parameters: the SEE yield of iodine ions bombarding a sample; and the relative concentration of each ion species in the beam at the moment of the yield measurement. With this, the objective is to obtain an estimation of the total yield and also estimate the contributions of each species. For the yield measurements, an electrostatic gridded probe was designed, while the beam composition was measured using a time-of-flight (TOF) spectrometry analysis.

A general schematic of the experimental arrangement is seen in figure 4.2. The thruster uses an NPT30-I2 for the generation of the ion beam. The experiment is conducted in the PEGASES vacuum chamber, and the thruster is positioned at the central location of its back flange, while the probes are positioned at the other end, close to its front flange. During electron emission measurements, the screen grid is biased to voltages from 0.5 kV to 1.3 kV relative to ground, which effectively controls the final average kinetic energy of the ions, while the accel grid is kept at -100 V to avoid electron backstreaming from the beam. For the sake of comparison, the SEE yield measurements are also conducted with a xenon ion beam. In this case, an NPT30-Xe is used, with the xenon flow and the power supplied externally. All voltage biases are the same as the iodine cases.

4.2.1 SEE probe

The method used here to measure the ion-induced SEE is similar to what was used in previous experiments [165, 170]. Figure 4.3 shows a section view schematic of the SEE probe used here. In this method, the measurement instrument consists of a metallic grid

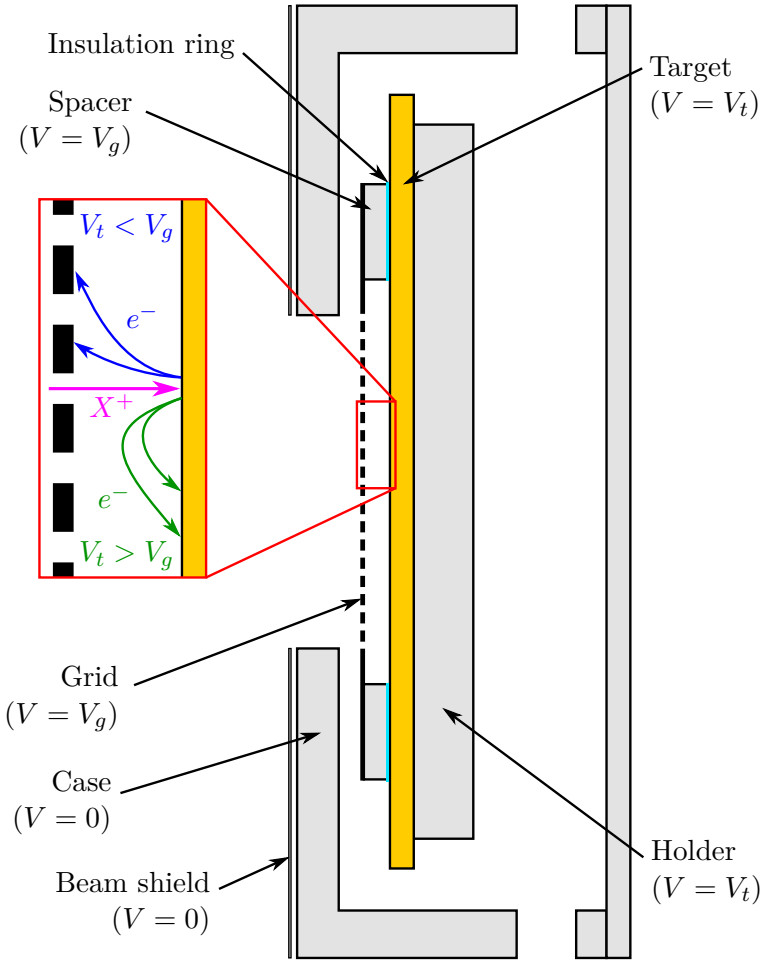

Figure 4.3: Schematic of the section view of the SEE probe. The bias applied to each component is indicated in parenthesis, and V_g is the grid voltage, and V_t is the target voltage. X^+ represents a generic ion and e^- represents a secondary electron (adapted from Ref. [169]).

which is biased to a constant voltage V_g, and a target which is bombarded by the ion beam and is made of the material of interest – the target is biased with a time-varying voltage ramp V_t. Whenever $V_t < V_g$, the secondary electrons emitted at the target are collected by the grid, and the net current passing through the target becomes $I_t(V_t < V_g) \approx I_i + I_{\text{SEE}}$, where I_i is the ion current and I_{SEE} is the current due to the secondary electrons. When $V_t > V_g$, the secondary electrons are reflected back to the target, and their current is not measured anymore. The target current in this case is simply $I_t(V_t > V_g) \approx I_i$. In this way, using the current collected at these two points, the secondary electron current may be estimated as

$$I_{\text{SEE}} \approx I_t(V_t - \Delta V) - I_t(V_t + \Delta V) \tag{4.3}$$

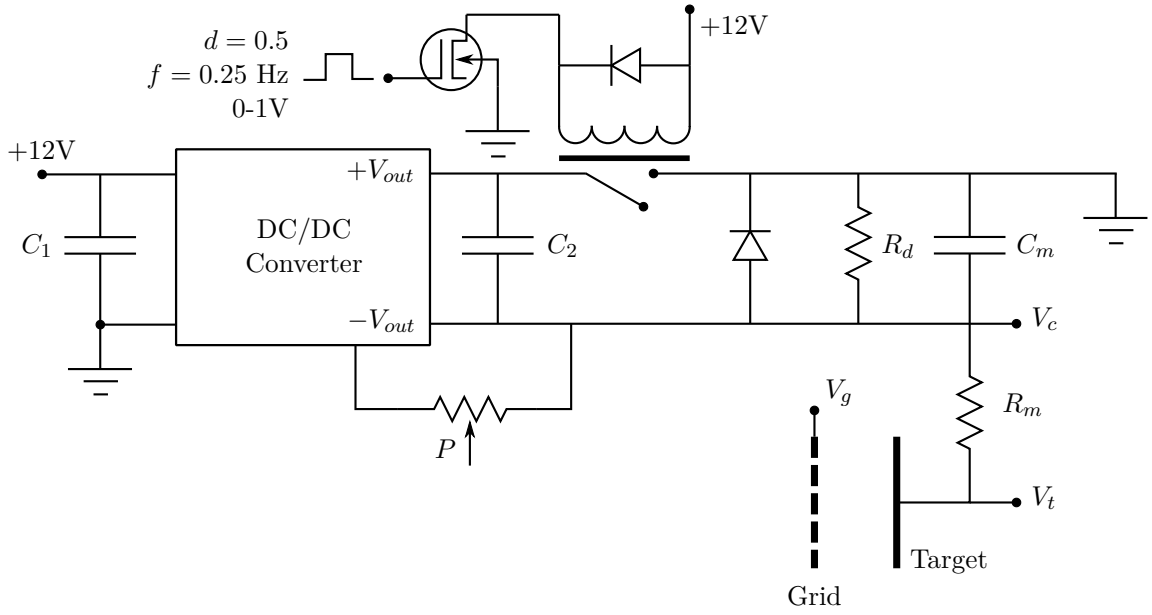

Figure 4.4: Schematic of the measurement circuit of the SEE probe. V_t and V_c are the target voltage and the capacitor voltage respectively. The measurement capacitor, C_m, has a value of 4.7 µF, and the measurement resistor, R_m, a value of 1 kΩ. The discharge resistor has a value of 2 MΩ. C_1 and C_2 have a value of 4.7 µF.

To ensure that the majority of the emitted electrons are completely reflected or repelled towards the grid, it is necessary to have $\Delta V > \langle E_e^{\mathrm{SEE}} \rangle$, where $\langle E_e^{\mathrm{SEE}} \rangle$ is the average kinetic energy of the emitted electrons. From previous works [171], the average energy of electrons is expected to be of the order of $\langle E_e^{\mathrm{SEE}} \rangle \sim 3\,\mathrm{eV}$.

The construction details of the SEE probe can also be seen in figure 4.3. The probe's outer case is made of aluminum and has a cylindrical shape with a diameter of 8 cm and a width of 2.8 cm. The front face of the probe has a circular aperture with a diameter of 2.8 cm through which the ion beam can enter. A grid, made of molybdenum, is placed below the casing aperture with a 2 cm vacuum gap. An aluminum spacer ring with a thickness of 2 mm, followed by a 0.2 mm thick mica insulating ring, are placed between the grid and the target to ensure their proper spacing. The material sample is a square of 5 cm × 5 cm, which is placed between the mica ring and an aluminum holder that clamps the target in place. A circular shield is placed in front of the probe covering the aluminum surface (which would otherwise be directly facing the ion beam) to reduce sputtering and avoid arcing due to the possible formation of iodides on the outer casing. The shield is made from molybdenum due to its lower reactivity to iodine [136, 172], and its higher resistance to sputtering compared with aluminum.

To estimate the SEE yield of the sample, the target's IV curve is measured, resulting in a step-like curve centered around the grid voltage. This is performed by an external measurement circuit, shown in figure 4.4, that applies a voltage ramp on the target

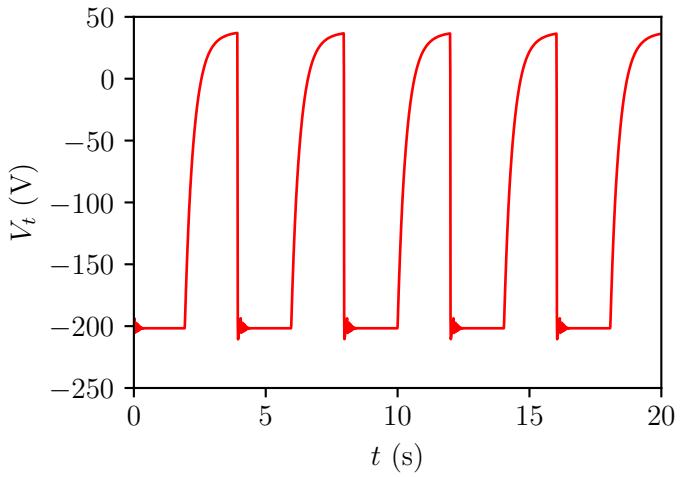

Figure 4.5: Example of the temporal variation of the target voltage, V_m, relative to ground.

holder and which measures the current passing through the measurement resistor, R_m, ($I_m = (V_c - V_t)/R_m$) with value of 1 kΩ, using a MCC DT9824 data acquisition board connected to a computer. A capacitor generates the voltage ramp applied to the target, C_m, which is initially charged to approximately −200 V and discharged gradually by the ion current passing through the target and a 2 MΩ discharge resistor, R_d, that is connected in parallel to the measurement capacitor. This discharge resistor also guarantees that the capacitor discharges even though there is no ion current present at a given moment. It is important to note that the shape and limits of the ramp might slightly change due to the intensity of the ion current; however, since the discharge current passing through R_d is considerably larger than the ion current, the measurements are not affected. The capacitor is charged by an isolated DC/DC converter that converts the 12 V input voltage to −200 V. The exact value of the converter output voltage can be controlled by a potentiometer, P. Between the converter and the measurement capacitor, there is a relay that either connects or disconnects them. When the relay is closed, the capacitor is charged, and when it is open, it can be discharged by the ion current. The relay is controlled by a 555 timer that operates at 0.25 Hz and with a 50 % duty cycle. This timer is connected to a transistor that connects the relay circuit to ground or lets it float. Two capacitors, C_1 and C_2, are used to decrease the noise on the input and output signals of the converter. Finally, two diodes are used to avoid damaging the relay and the converter by undesired currents. The complete voltage ramp goes roughly from −200 V to 5 V in 2 s, which corresponds to approximately 200 recorded points per scan. Figure 4.5 shows a measurement of the probe voltage, V_t, relative to ground. It is possible to see that, as expected, the period of the charge and discharge cycle is 4 s and because of the duty cycle used, the voltage increase only starts at half of the cycle. It is also possible to see a short period of signal ringing at the beginning of each cycle. However, this does not

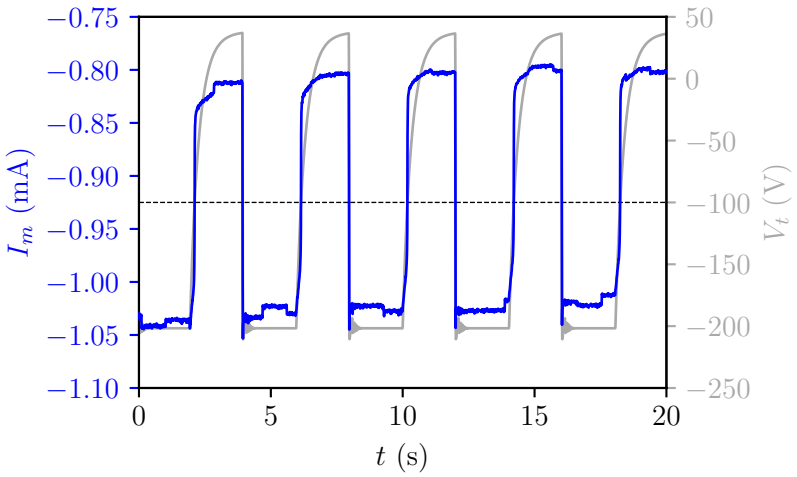

Figure 4.6: Example measurement of the temporal evolution of the current with an aluminum target bombarded by a 0.7 keV beam (blue). The target voltage, V_t, is also shown for sake of clarity (gray). The dashed line marks the grid voltage, $V_g = -100\,\mathrm{V}$.

affect the measurement since the IV curve is extracted only for the points between the beginning and the end of the voltage ramp.

The probe is placed within a quasi-neutral ion beam produced by the thruster during the experiments. To mitigate the effect of the incidence angle of the ions, the probe is axially aligned with the source, favoring ions with velocity vectors perpendicular to the target surface. Electrons in the beam are emitted from a thermionic neutralizer located near the exit of the ion source. This neutralizer is connected to the vacuum chamber ground, thus ensuring that the beam electrons cannot enter the SEE probe and be collected by the target, which would give rise to an additional undesired electron current. The probe's grid voltage V_g is kept at $-100\,\mathrm{V}$ during all measurements to stop these electrons. This negative grid bias also prevents the collection of any possible I^- ions that may be generated within the plume during operation.

Figure 4.6 shows an example of the current measured at the measurement resistor, R_m, for an aluminum sample and a 0.7 keV beam, corresponding to the same example as depicted in figure 4.5. It is possible to see that the average current value is negative since the current is an ion current, and it varies between roughly $-0.8\,\mathrm{mA}$ to $-1.05\,\mathrm{mA}$. The gray curve reproduces again the target voltage so that the influence of the voltage on the measured current is more clear, and the dashed line shows the grid voltage V_g. Whenever $V_t = -200\,\mathrm{V}$, and thus $V_t < V_g$, the measured current has the highest magnitude since the emitted electron current contributes to the net target current. As the probe voltage starts to increase, the current magnitude decreases until it reaches its minimum roughly 1 s after the beginning of the ramp. It is also possible to observe a slight drift on the average current value, which corresponds to the natural drift of the thruster during operation. Figure 4.7 shows the plot of the measured current versus the probe voltage for

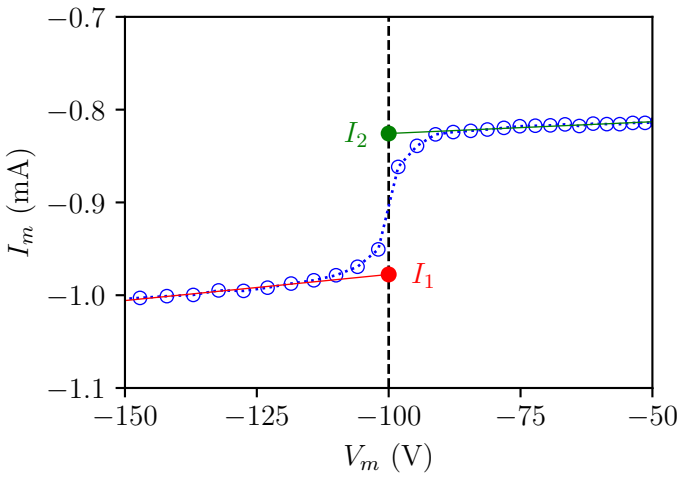

Figure 4.7: Example IV curve measured with an aluminum target bombarded by a 0.7 keV beam. The vertical dashed line show the grid voltage V_g and the red and green lines show fits to the right and left part of the voltage step.

one of the cycles. The vertical dashed line shows the grid voltage value, V_g. As expected, it is possible to see that there is a clear step around V_g, representing the contribution of the SEE current. It can also be seen that on both sides of the step, the current is not entirely "flat" but presents a slope, which ideally should not be present. Mainly two effects can explain this phenomenon: a leakage current corresponding to a connection of a few megaohms to the chamber ground; and (2) the penetration of the target potential through the grid, which may cause the plasma sheath to expand and slightly increase the collection area of slow ions. To compensate for these effects, instead of taking a fixed voltage step (ΔV) for the estimation of the yield, a linear fit is performed on both sides of the current step as shown in figure 4.7. The current values used to calculate the SEE yield, I_1 and I_2, are determined by the value of the linear fits calculated at the voltage V_g. The value of the yield is estimated from the IV curve as

$$\gamma \approx \frac{I_1 - I_2}{I_2} \tag{4.4}$$

Depending on the magnitude of the ion current used and the material properties, the signal measured by the SEE probe can be quite weak, with current step sizes as low as a few micro-amps, making the signal-to-noise ratio become relatively low. Therefore, to estimate the value of a SEE yield data point, several voltage ramp cycles are recorded for the same operational point (fixed ion current, acceleration voltage, and target material). The post-processing procedure to estimate the yield from the recorded cycles consists of (1) detecting the starting and ending times of each voltage ramp by using a peak detection algorithm; (2) storing the IV curve for each individual cycle; (3) making the linear fits of each IV curve as shown in figure 4.7; (4) estimating the yield for each

cycle using equation 4.4; and (5) estimating the final yield as an average of the yield of each cycle, $\gamma \approx \frac{1}{N}\sum_i \gamma_i$. The error bars for each yield data point are assumed to be the standard deviation of the cycle yields, γ_i. The estimation of each yield point used between 20 to 30 individual IV curve measurements.

As discussed, both diatomic and monoatomic iodine is strongly reactive with an extensive range of materials, including some of the targets used here [136]. Because of this, it is expected that the beam and background neutral gas reacts with the surface of the samples to form a thin layer of iodide compounds, which may have very different SEE yield coefficients when compared with a clean surface. On the other hand, during the measurements, the samples are constantly cleaned by the bombardment of high-energy ions, which partially removes these reaction products. The balance between surface reactions and ion cleaning should yield a constant thickness layer at steady state. In similar experiments done by Corbella *et al.* [165], the authors conclude that the reactions producing the oxide layer happen only in the first atomic monolayers of the sample producing an oxidized layer with a thickness of the order of 5 nm. Due to technical limitations and the fact that it is beyond the scope of the work to study all iodine reactions taking place on the surface of the samples, only measurements of the effective SEE yields of the possibly partially iodized samples are reported. Nevertheless, it is expected that, on real applications of iodine beams and plasmas, the surface of the materials will also react with the iodine in similar ways to the present experiments and form as well the compounds experienced here. Therefore, the measurements done in this experiment are in fact more representative of real applications than a hypothetical case where the yield could be measured for a clean surface.

4.2.2 Time-of-flight spectrometry

As described in the previous sections, the beam generated by the ion thruster using iodine contains multiple ion species, mainly I^+, I_2^+ and I^{2+} [70, 76]. Each of these ion species may have different emission properties when they impact a given material. Thus, to correctly estimate the SEE yield of the ion beam, it was also necessary to characterize its composition. This composition is estimated using a time-of-flight (TOF) spectrometry technique [173]. This technique consists of determining the composition of a monoenergetic group of particles based on the time they take to travel a given distance. The travel time is approximately given by

$$t = L\sqrt{\frac{m}{2qE}} \tag{4.5}$$

where L is the travel length, m is the particle's mass, q is its charge, and E is its energy. If a bunched group of particles is emitted where each ion species has a different charge-to-mass ratio but the same energy, as time evolves, the species groups start to drift apart, and they reach their final destination at different times. If a detector is placed at the end of the travel length and the length is long enough, the groups are detected separately, which enables the estimation of the relative composition of the group.

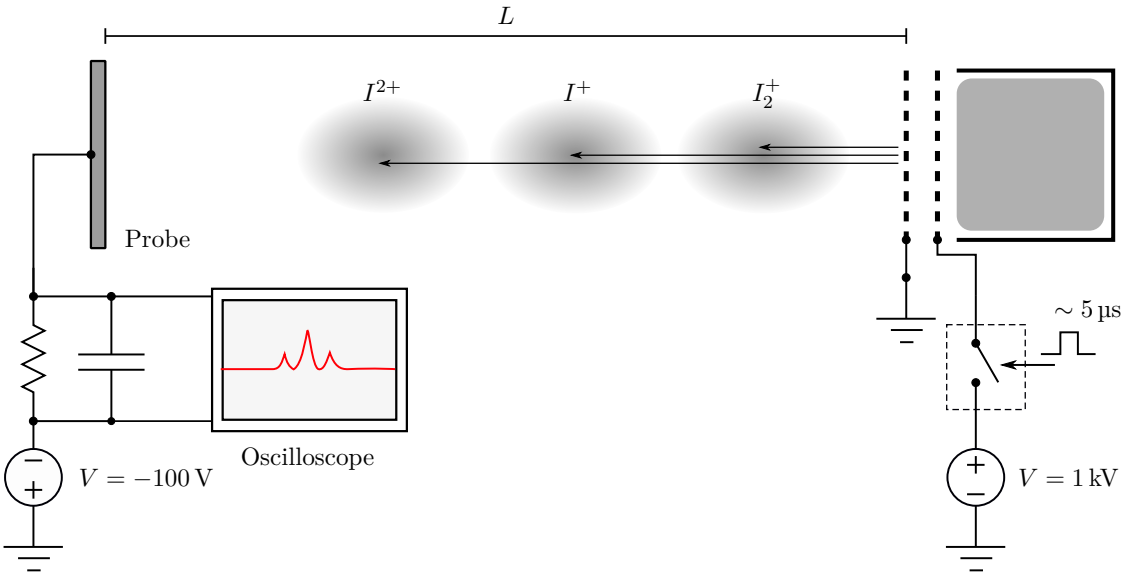

Figure 4.8: Schematic of the experimental setup used for the TOF measurements.

Figure 4.8 shows the schematic of the experimental setup used for the TOF measurements during this work. The ion current detection is done using a circular probe with a diameter of 7 cm, made of molybdenum, and placed at 54 cm from the thruster's accel grid. For these measurements, the thruster's accel grid is always kept at ground potential, while the screen grid is connected to a high-voltage switch controlled by a digital trigger. This switch is kept open when idle, and the screen grid remains connected to ground. At the moment of the measurement, a rectangular pulse of approximately 4.5 µs, produced by a wave generator, is applied to the switch, connecting the screen grid to a 1 kV bias that is generated by a high-voltage power supply. This generates a high-voltage pulse on the screen grid, accelerating a group of approximately monoenergetic ions towards the TOF probe. In this configuration, the travel times for I^{2+}, I^{+} and I_2^{+} are expected to be roughly 9.7 µs, 13.8 µs, and 19.5 µs respectively. The probe is connected to a measurement resistor in series with a low-value filtering capacitor used to reduce the high-frequency noise of the signal. The time constant for the complete circuit is estimated to be of the order of 1 µs, therefore it is expected that the signal is measurable by the system. To decrease the collection of electrons produced at the neutralizer and any possible negative ions, the probe is biased to −100 V by a constant-voltage power supply. A digital oscilloscope is used to measure the voltage signal at the resistor, which is generally composed of distinct current peaks corresponding to the different species. The automatic high-speed trigger oscilloscope is used to synchronize the measurement and emission timings. The neutralizer is kept on and connected to ground during all experiments.

Figure 4.9 shows an example of a measurement performed with the TOF apparatus. The red curve shows the acceleration voltage pulse applied to the screen grid of the source, while the blue curve is the current collected by the probe. Each current peak

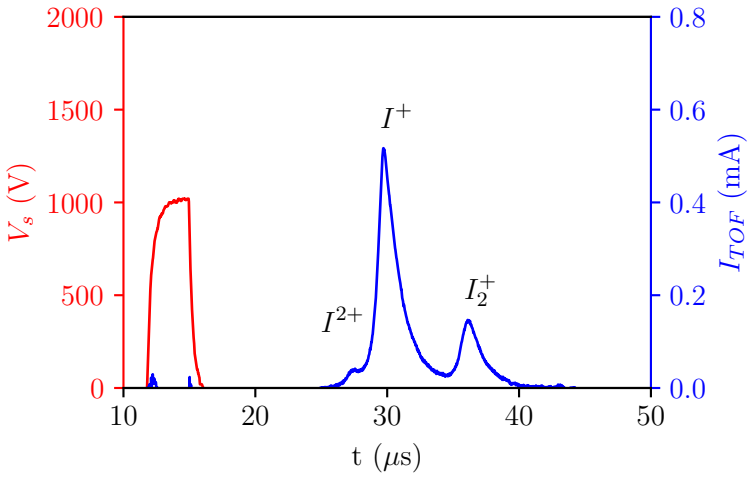

Figure 4.9: Example TOF measurement showing the current collected by the TOF probe (blue) and pulse applied to the screen grid (red).

corresponds to a different species, and it is possible to estimate their relative concentration by calculating the integral value of each peak. Because of limitations on the physical length of the drift region and the distortion and width of the pulse, the individual peaks are not clearly separated but have a certain degree of overlap between them, and the travel time for each species differs from the ideal case. However, these distortions do not significantly impact the measurements since the principal quantity of interest is the relative magnitude of the integral of each peak, which is done computationally. The peaks are fitted using an exponentially modified Gaussian function, which has a general form given by

$$f(t; A, \mu, \sigma, \gamma) = \frac{A\gamma}{2} \exp[\gamma(\mu - t + \gamma\sigma^2/2)] \operatorname{erfc}\Big(\frac{\mu + \gamma\sigma^2 - t}{\sqrt{2}\sigma}\Big) \tag{4.6}$$

where $\operatorname{erfc}(t) = 1 - \operatorname{erf}(t)$. The curve fits are done using the open-source LMFIT library. This functional form was selected for the fits since it presented the best shape match and the lowest error. After each peak is detected and fitted, the integral, Q_i, of each curve is calculated and the relative concentration of a given species j may be determined as

$$\bar{Q}_j = \frac{Q_j}{q_j \sum_i \frac{Q_i}{q_i}} \tag{4.7}$$

where q_i is the charge of the species i. The relative concentration $\bar{Q}_j$ gives an estimation of the ratio of particles of each species to the ion beam current.

The TOF measurements provide a methodology to assess the concentration of particles in the beam and inside the ICP discharge since it is assumed that the relative concentrations do not change significantly in the plume. During the SEE experiments,

Table 4.1: Materials used as target samples in the electron emission experiment.

Material	Manufacturer	Composition
Molybdenum (Mo)	Goodfellow	Mo > 99.9%
Tungsten (W)	Goodfellow	W > 99.9%
Aluminum (Al)	Goodfellow	Al > 99.0%
Titanium (Ti)	Goodfellow	Ti > 99.6%
Copper (Cu)	Goodfellow	Cu > 99.9%
Carbon-carbon (CC)	Goodfellow	Unspecified
Steel	Precision Brand	AISI 1008

the mass flow rate is kept constant, so the only operational parameter that can affect the composition is the ICP RF power. In this way, to estimate the yield with different beam compositions, the TOF measurement is performed for different ion beam currents at the moment of the SEE measurement.

4.3 Results

4.3.1 Target materials and procedure

The main goal of the experiments is to measure the SEE yield of different targets while computing the relative ion species composition of the beam bombarding the sample. The SEE yield is measured for targets of the following materials: Mo, W, Al, Ti, Cu, carbon-carbon, and steel. These materials were selected due to their presence in propulsion and other space applications. The material manufacturers and their purity are summarized in table 4.1, and all samples are polycrystalline. Before installing the SEE probe, each sample went through the same cleaning procedure to mitigate undesired effects due to other possible deposited materials. Each sample is cleaned superficially and placed for 15 minutes inside an ultrasonic bath with ethanol. After this, and immediately before the measurements, the sample is exposed to the iodine ion beam for 20 minutes at 1 keV to further clean the surface of the target, as typically done for SEE yield measurements [155], and induce any surface chemical reactions (which would be present in any realistic iodine plasma application) that might take place during the bombardment to avoid transient processes during the measurements.

As shown in previous works [70, 76], in the low ICP RF power range, the production of I_2^+ is favored, while I^{2+} is almost nonexistent. This happens because the I_2 molecules are not dissociated due to the low power while being nonetheless directly ionizable. In the mid-power range, the production of I_2^+ decreases, and the dominant population is I^+, with some I^{2+} appearing. In the high power end, I_2^+ decreases considerably, and the production of I^{2+} is favored. In the power range of the NPT30-I2, it was seen that the population of I^{2+} ions is quite small. For all TOF experiments, the I^{2+} peak is almost imperceptible, with a low signal-to-noise ratio – after fitting and integration, their contribution for all cases is less than 1 % of the particles, which decreases even further

due to a $\frac{1}{2}$ factor due to its charge number. Therefore, in the experiments here, the contribution of I^{2+} is not accounted for.

To verify the impact of each ion species on the emitted current, the SEE yield measurement for each material is divided into two phases. In the first phase, the thruster is operated in a low-power mode, called mode A, that produces an ion beam current of roughly 6.5 mA and beam composition where the proportion of I^+ and I_2^+ is similar with a ratio of approximately 50:50; while for the second phase, the source is operated in a high-power mode, denoted mode B, which generates an ion beam current of approximately 12.6 mA, with a discharge dominated by I^+ with a ratio of approximately 75:25. With the TOF probe, the composition of the beam is assessed before each phase of the SEE measurement.

For each mode, the SEE yield is measured for different ion energies, between 0.6 keV and 1.4 keV with steps of 50 V. The average kinetic energy of ions that impact the target can be approximated by $\langle E_i \rangle \approx V_p + V_s - \langle V_c \rangle$, where V_p is the ICP plasma potential, V_s is the screen grid voltage, and $\langle V_c \rangle$ is the average voltage of the SEE probe collector close to moment of the current step used for the measurement. Because $V_p \ll V_s$ and $\langle V_c \rangle \approx -100\text{V}$, the ion bombarding energy is estimated as $\langle E_i \rangle \approx V_s + 100\text{V}$. Approximately 20 voltage ramps in the target are executed and measured for every energy step. The emission yield is then estimated for every individual IV curve using the curve fitting method described above. Lastly, the set of measured yields for each energy step is averaged, which provides a mean SEE yield curve as a function of beam energy.

4.3.2 Xenon SEE measurements

The first part of the SEE measurements was done for a xenon ion beam. This was done primarily to verify the measurement methodology and compare the results with past data available in the literature. As known [14], the dominant species in xenon ion beams for typical low-power RF thrusters is Xe^+, and doubly charged ions, Xe^{2+}, represent a considerably smaller fraction of the total particle population. Therefore, past SEE measurements do not typically study the impact of different ion beam compositions. Furthermore, xenon ions are not reactive, so, in contrast with iodine, the only possible surface modification, in this case, are ion sputtering, adsorption, or implantation; the energy range used here does not favor implantation, and the other effects are not expected to occur in a significant rate.

Figure 4.10 shows the measurement of the SEE yield for xenon ion bombardment on a molybdenum target. The measurements are compared with the data provided by Hagstrum [158], Magnuson and Carlston [159], and Ferron *et al.* [155]. It is important to note that the data sets present an important spread between them, with values varying roughly two times for a given energy. This happens mainly because, at this energy, the yield value is less than 3 % of the impinging ion current; therefore, the signal measured in this case is weak and can be sensitive to different factors in the experiment. Nevertheless, in general, it is possible to see that the yield values measured in the present experiment have a relatively good agreement with all data sets from the literature. Furthermore,

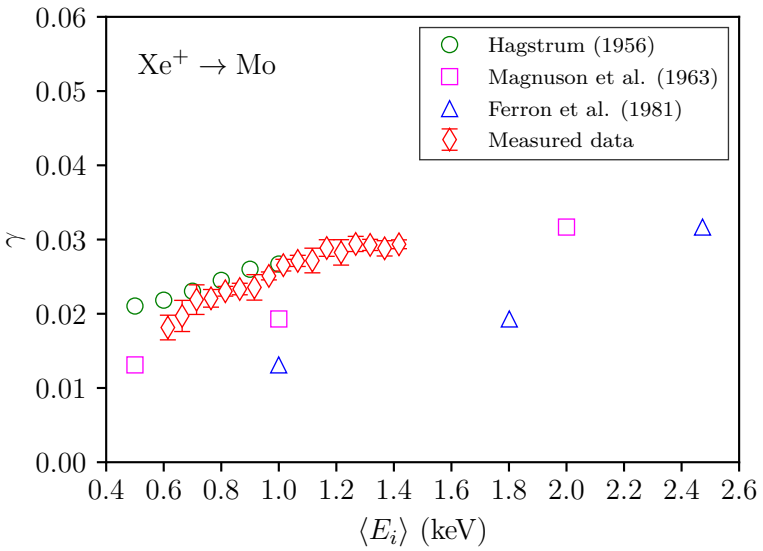

Figure 4.10: Measurement of the SEE yield for a xenon ion beam on a molybdenum target. The plot shows the comparison of the measured data with the yield values from Hagstrum [158], Magnuson and Carlston [159], and Ferron *et al.* [155].

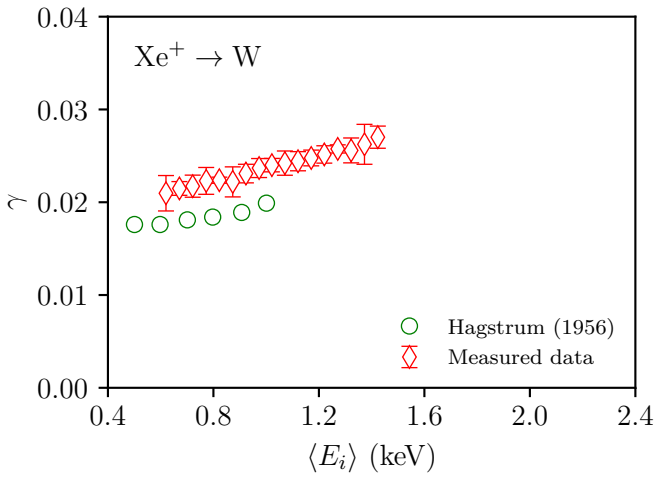

Figure 4.11: Measurement of the SEE yield for a xenon ion beam on a tungsten target. The plot shows the comparison of the measured data with the yield values from Hagstrum [158].

all the sets of data, including the measurements done here, present a similar slope in relation to the energy level, which is a piece of evidence that, despite the offset, all the measurements are characterizing the same phenomenon.

Table 4.2: Relative concentration of I^+ and I_2^+ ions in the beam, measured with the TOF probe before each SEE measurement.

	Mode A		Mode B	
Target	I^+	I_2^+	I^+	I_2^+
Mo	0.567	0.433	0.760	0.240
W	0.515	0.485	0.754	0.246
Al	0.495	0.505	0.739	0.261
Ti	0.531	0.469	0.740	0.260
Cu	0.572	0.428	0.761	0.239
CC	0.544	0.456	0.767	0.233
Steel	0.556	0.444	0.751	0.249

Figure 4.11 shows the xenon measurements of the SEE yield with the tungsten target. The measurements are compared only with the data measured by Hagstrum [158] since SEE yield data are scarce for this specific pair. It is possible to see a discrepancy of roughly 8 % between both data sets. However, as seen in the case of molybdenum, this difference is not significant and is expected due to different experimental conditions. Here, the data sets present similar slopes, which again indicates that the measurements are consistent. The complete tabulated yield data for xenon is presented in appendix A.

4.3.3 Iodine SEE measurements

Table 4.2 shows the results of the TOF measurements during the SEE experiments. The table presents the relative concentration of I^+ and I_2^+ for every target material and each operational mode. It is possible to see that, as expected, the modes show close values of the stipulated ratio, with minor variations in the order of a few percent. The complete tabulated yield data for iodine is presented in appendix A.

Figure 4.12 show the results for the yield measurements with iodine and the molybdenum and tungsten targets. It is possible to see that when compared to the xenon case with the same materials (figures 4.10 and 4.11), the yield value is roughly two times lower on average, with both modes. For non-reactive materials, it is expected that the SEE yield for iodine is lower since its ionization energy is lower than xenon. Furthermore, it is possible to see that the relative uncertainty is higher, showing a more important spread in the data due to the lower current signal. Comparing mode A and mode B, in general, it is also possible to see that the latter has slightly lower uncertainty values, which happens because this mode uses a higher ion current, which increases the magnitude of the measured signal. In the case of tungsten, the data collected for each mode show very similar behavior, with no noticeable difference between them. On the other hand, the data for molybdenum shows a slightly higher yield for mode A, possibly indicating a higher yield from I_2^+. Despite the increase in the yield value with energy on both materials, this increase is quite small, and this profile is more compatible with the potential emission mechanism, similar to what is seen in figure 4.1 for energies below

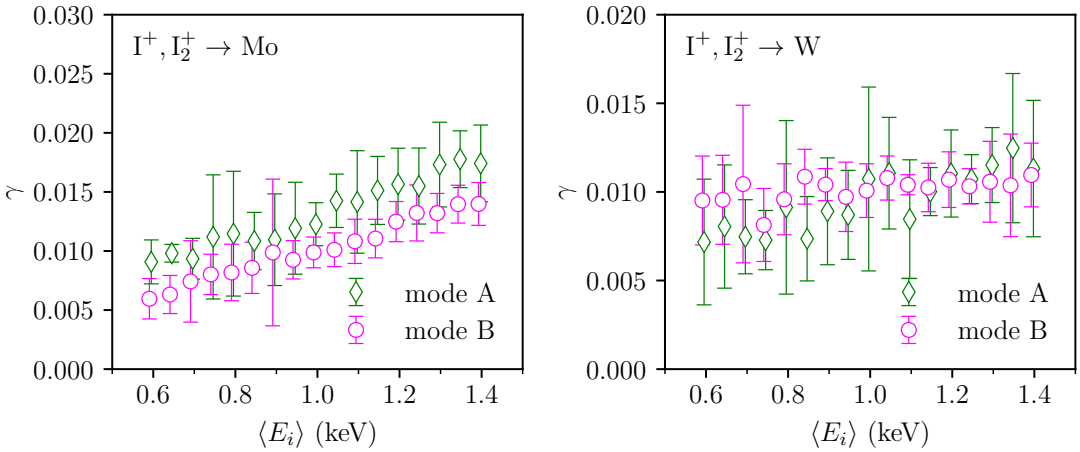

Figure 4.12: Measurement of the iodine SEE yield for the molybdenum (left) and tungsten (right) targets.

1 keV.

Figure 4.13 shows the SEE yield measurements for the titanium and aluminum targets. In contrast with the previous cases, here, the yield magnitude for both materials increases significantly, reaching 0.08 for titanium and 0.4 for aluminum, which is the highest yield value recorded on all the experiments done in this work. The steeper linear increase in the yield value suggests that the secondary electrons are generated in these cases mainly through kinetic emission. As before, the uncertainty is considerably smaller for mode B, where the magnitude of the ion current is higher. Alonso *et al.* [174] shows the SEE yield of different ions species bombarding a clean aluminum target. For krypton, the yield goes from zero to roughly 0.1 at 2 keV, and for xenon, it goes from zero to roughly 0.05 also at 2 keV. The higher emission for aluminum and iodine, in this case, may be associated with reaction products formed on the surface of the samples. As shown by Depla *et al.* [166], between all metals that the authors studied, the SEE yield of aluminum is one of the most affected by the formation of chemical products when exposed to either nitrogen or oxygen with an increase of roughly 20 %. This reactivity is not directly analogous to the case with the exposure to iodine; however, it is reasonable to expect that the formation of iodides, such as AlI or Al_3I, is favored when using aluminum, and that the products' yield increases significantly the final current reading. In the case of titanium, it is possible to see that the yield is lower. Apart from its SEE yield value which may be smaller than aluminum, its reactivity is also lower, which may not favor the formation of products on the surface.

Figure 4.14 shows the iodine SEE yield measurements for targets made of copper and steel. The yield values for copper present quite high values, being comparable to the aluminum case. It is possible to compare the measurements qualitatively to the data collected by Buschhaus *et al.* [167]. For argon bombarding a copper surface, the authors show that for 1 keV ions, the yield is roughly 0.08 for a clean surface and about 0.2 for

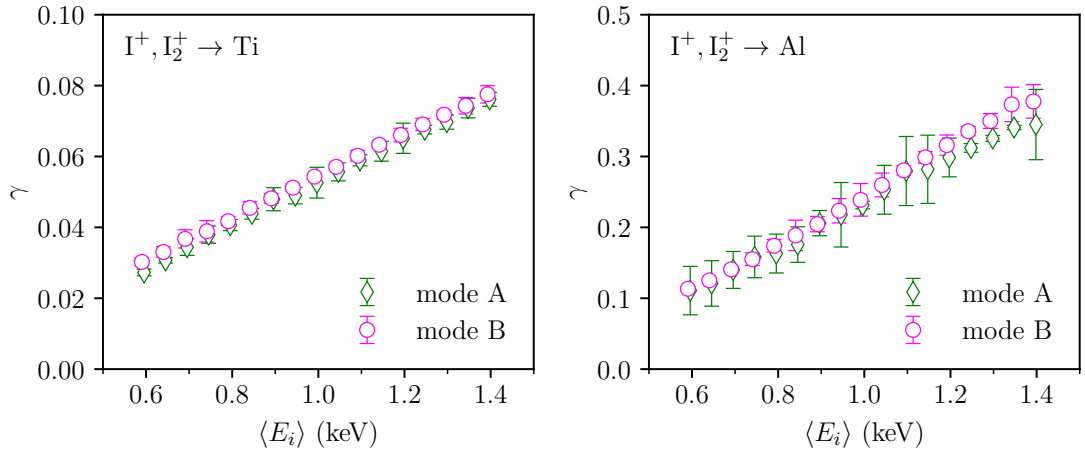

Figure 4.13: Measurement of the iodine SEE yield for the titanium (left) and aluminum (right) targets.

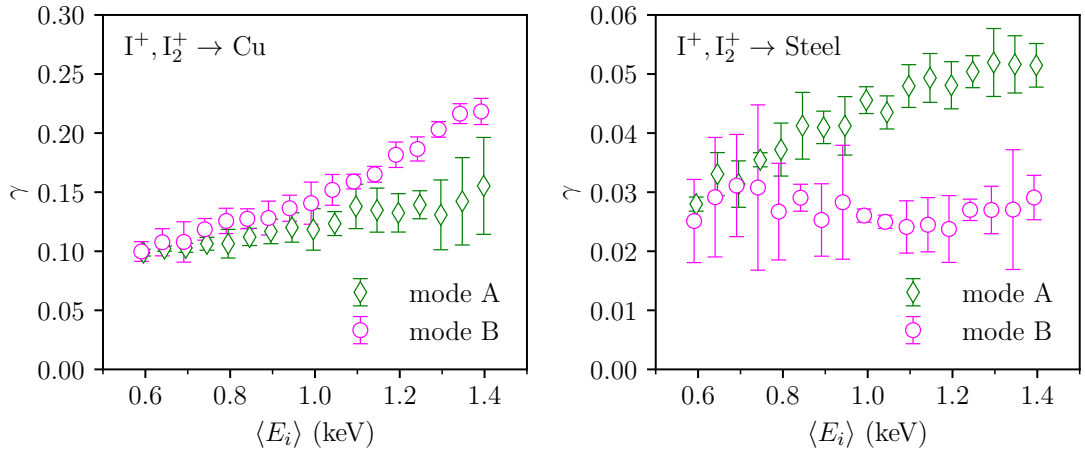

Figure 4.14: Measurement of the iodine SEE yield for the copper (left) and steel (right) targets.

an oxidized surface, which is similar to what is seen in the present case for copper. It is interesting to note that both of these materials displayed a unique behavior compared to the other targets, where the yield for each mode displays very distinct trends, with considerably lower values in mode A for copper and lower values for mode B in steel. These results were partially confirmed with repeated measurements with different times of initial exposure to the beam before each measurement cycle, indicating that this behavior was not due to chemical transient processes. This behavior is still not well understood; however, because both copper and steel are very reactive to iodine [136], this behavior is expected to be a direct consequence of the formation of compounds such as CuI and FeI_2

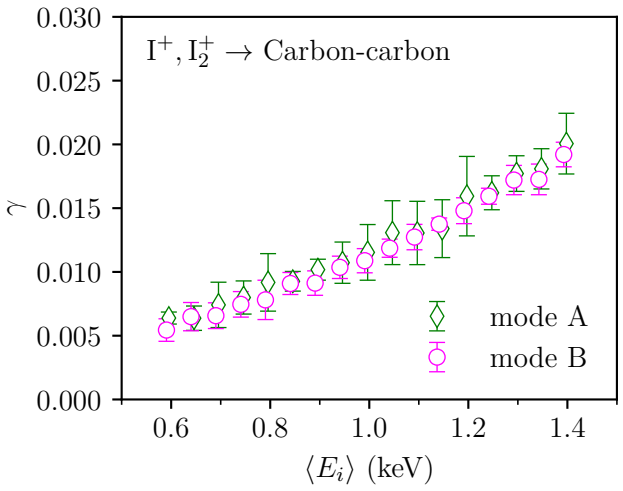

Figure 4.15: Measurement of the iodine SEE yield for the carbon-carbon target.

on the surface of the samples. The steel sample is the only sample in this study that is not a "pure" material since it is made of an AISI 1008 alloy, which has about 1 % of its mass composed of materials other than iron, namely manganese, carbon, and sulfur among others. Despite representing a small fraction of the sample mass, these components may have a significant impact on the yield having different emission properties or participating in creating other chemical products. These components and products can also create more complex emission behavior, as seen in the measured data, which may be linked to surface irregularities and the superposition of different emission curves.

Figure 4.15 shows the SEE yield measurements for a carbon-carbon target. This is the only non-metallic material that was tested, and it was selected due to its typical applications in the aerospace industry, especially for space propulsion. It is possible to see that its yield value in the energy range used is quite small and comparable with the emission yield of tungsten and molybdenum. In contrast with these other two targets, in the carbon-carbon case, the yield grows in a linear fashion, presenting a relatively low uncertainty level, which may be related to a smaller number of reactions taking place on its surface. Furthermore, the measurements do not present any differences in both modes.

Using the total SEE yield obtained for mode A and B, and the relative composition of the beam given in table 4.2, it is possible to estimate the individual SEE yields of each ion species assuming that the effective measured value is a linear superposition of the emission of each species. In this way, the total yield can be decomposed as $\gamma = \bar{Q}_{I^+}\gamma_{I^+} + \bar{Q}_{I_2^+}\gamma_{I_2^+}$, where Q_{I^+} and $\bar{Q}_{I_2^+}$ give the relative composition of each species. For both modes, the

individual yields, γ_{I^+} and $\gamma_{I_2^+}$, can be estimated by solving

$$\begin{bmatrix} \gamma^A \\ \gamma^B \end{bmatrix} = \begin{bmatrix} \bar{Q}^A_{I^+} & \bar{Q}^B_{I_2^+} \\ \bar{Q}^A_{I^+} & \bar{Q}^B_{I_2^+} \end{bmatrix} \begin{bmatrix} \gamma_{I^+} \\ \gamma_{I_2^+} \end{bmatrix} \tag{4.8}$$

where the superscripts A and B indicate that the variable is related to mode A or B, respectively. It is important to note that this assumption does not capture the effect of a change in surface chemistry caused by each species which may be important and lead to a different functional relationship depending on the beam composition. In this way, this estimation is done primarily as a first-order approach to verify the influences of each species but does not represent a high-fidelity result. The equation 4.8 is solved for every pair of points, γ^A and γ^B, for a given value of average ion energy. However, because the experimental points display a considerable dispersion, if the system of equations 4.8 is directly solved, some values of γ_{I^+} and $\gamma_{I_2^+}$ may be calculated as negative. To avoid this, a non-negative least squares method is used. This method consists of a mathematical optimization algorithm to estimate the solution of a linear system while imposing the constraint that the solution is non-negative. The SciPy optimization toolset is used for this calculation.

Figure 4.16 shows the estimation of the individual SEE yields for all target materials. It is possible to see that the estimations for the copper and steel targets display a non-physical behavior, with the yield of I_2^+ going to zero as the energy increases. This non-physical behavior is related to the complex surface chemical behavior observed in the total yield measurements for these materials, which probably violates the linear assumption made here that allows a direct superposition. Therefore, these estimations are considered unusable here and are mentioned just for the sake of completion. The estimations for the other targets display very similar behavior to the total yield. In general, it is expected that the yield value for I^+ is higher than for I_2^+ since the latter has a lower ionization potential, which impacts the potential emission and lowers the absolute speed, which impacts the kinetic emission. This behavior is observed for W, Ti, and Al targets. The Mo and carbon-carbon targets present a slightly higher value of I_2^+ yield. However, it is important to note that both of these materials present a very high uncertainty level due to the low SEE signal, with yield values lower than 3 %. Therefore, it is unclear if this behavior is physical or due to the low signal-to-noise ratio of these specific experiments.

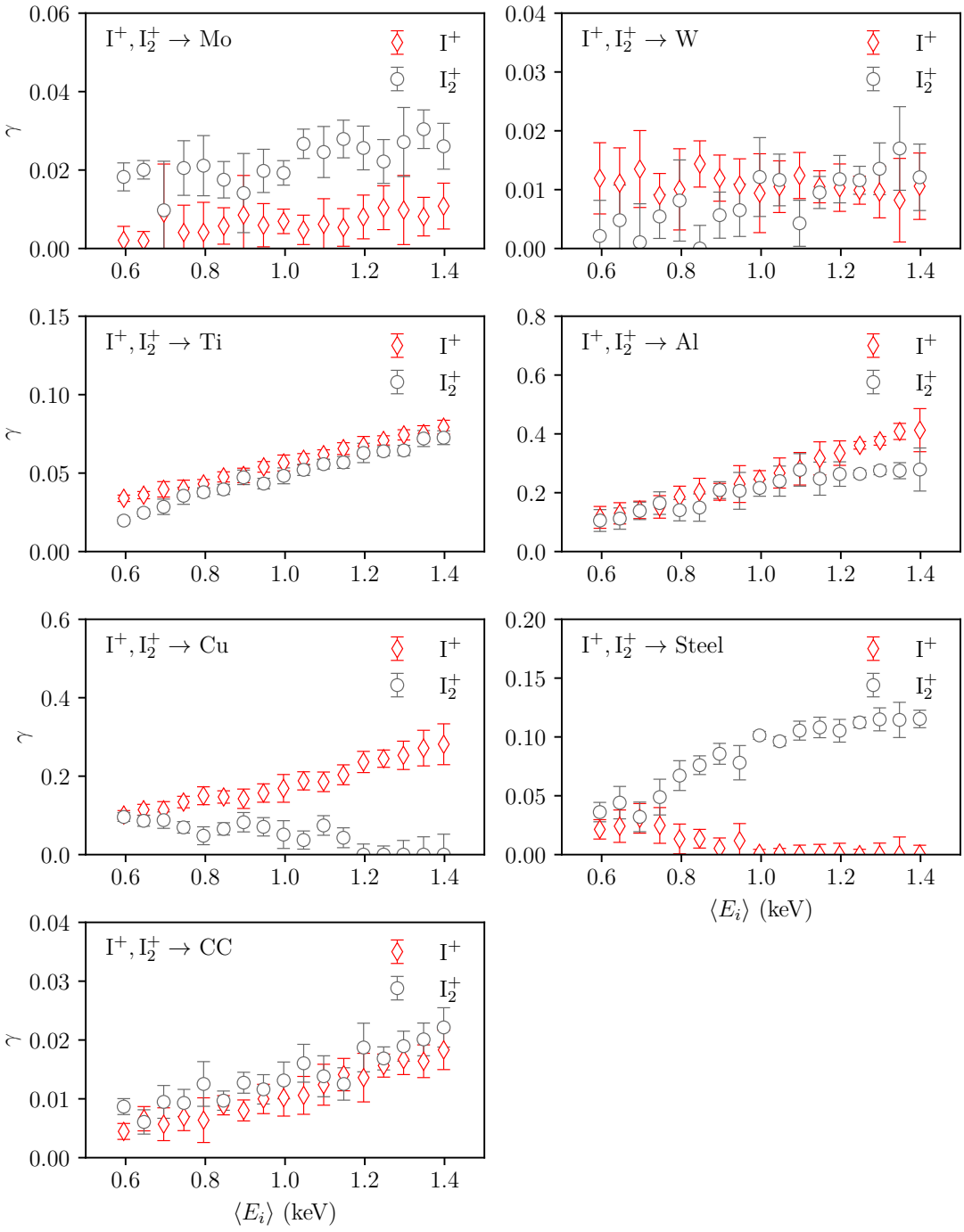

Figure 4.16: Estimated individual SEE yield for all target materials for each ion species as a function of mean ion bombarding energy. The data are estimated using the relative composition measured with the TOF apparatus detailed in table 4.2.

CHAPTER 5

CHARACTERIZATION OF DC ION THRUSTER USING IODINE AND XENON

This chapter presents the results of an investigation on the plume and performance of an ion thruster working with xenon and iodine. In the first part, the main characteristics of the plume are presented and compared, showing the results of the plasma diagnostics discussed in chapter 3. The next part shows an investigation of the ion beam profile and divergence using the automated planar probe array developed in this work. The SEE yield data measured in chapter 4 are used to correct the planar probe measurements done here. Next, the system performance is studied while using iodine, and the key differences to xenon operation are highlighted. In the last part, a brief comparison is made between the data measured on the ground and during the thruster test in space.

5.1 Results

5.1.1 Plume characterization

The main objective of these experiments was to study the characteristics of the plume generated by an ion thruster when using xenon and when using iodine. With this, the aim is to identify the main differences between both cases and how the usage of iodine impacts the thruster's performance. For the experiments, the NPT30-Xe and the NPT30-I2 are both operated in the PEGASES vacuum chamber and axially positioned inside the chamber when tested. When using xenon, the thruster is fed with gas externally.

The first results shown are the measurements of the plume plasma potential for both cases. The emissive probe is positioned close to the edge of the ion beam, with the hairpin loop perpendicular to the thrust axis. The tip of the probe is positioned axially, 35 cm away from the grid exit plane and 15 cm away from the beam axis. A constant current of 3.1 A was applied to the wire, generated by an external circuit powered by a 4-cell lithium battery. The current through the probe kept its surface temperature at approximately 3100 K. Here, the thrusters are operated at three different values of screen grid voltage, 0.5 kV, 0.9 kV and 1.3 kV, and three different values of ICP RF power, 8 W, 10 W and 13 W, which directly corresponds to different total ion beam currents. The figures 5.1 and 5.2 show the results of the measurements for xenon. Since the emissive

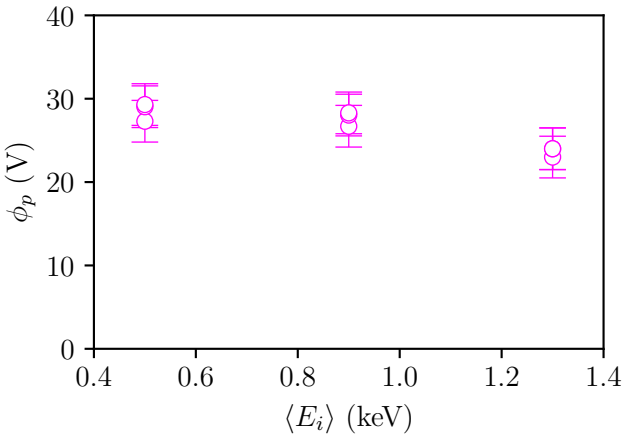

Figure 5.1: Measurement of the plume potential, ϕ_p, as a function of the average ion energy, $\langle E_i \rangle$, with the emissive probe for xenon.

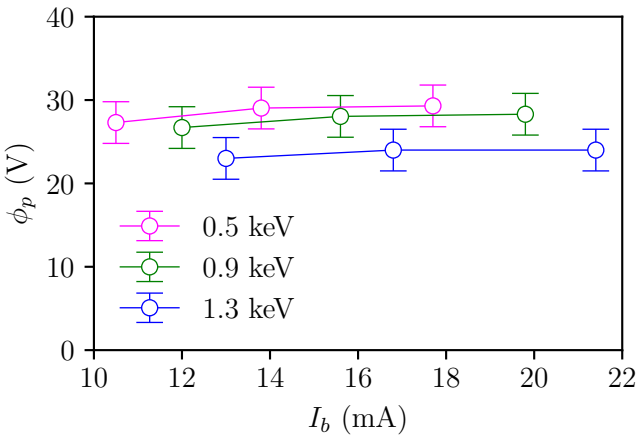

Figure 5.2: Measurement of the plume potential, ϕ_p, as a function of the total ion current, I_b, with the emissive probe for xenon.

probe was used in floating potential configuration, the uncertainty in the plasma potential can be approximated by the magnitude of the electron temperature, which is assumed to be roughly 2 eV. However, during the experiments, it was observed that the measured voltage had an important random noise component, with fluctuations of approximately 5 eV peak-to-peak. As recommended by Sheehan *et al.* [140], this voltage fluctuation may be a better measure of the uncertainty, and, since it is larger than the electron temperature, the error bars were taken to be half of this observed variation. In figure 5.1, the plume potential data is displayed as a function of total ion beam current, set by the

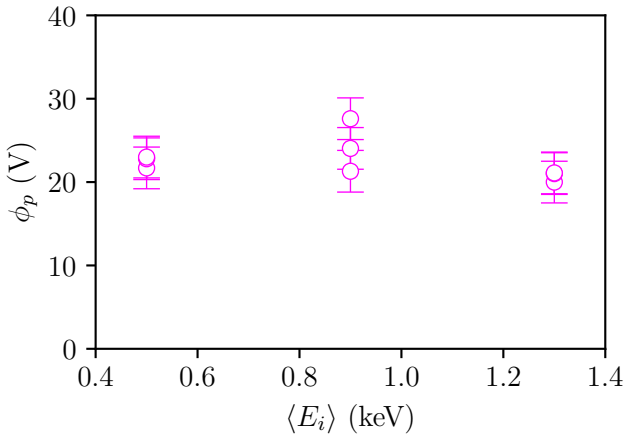

Figure 5.3: Measurement of the plume potential, ϕ_p, as a function of the average ion energy, $\langle E_i \rangle$, with the emissive probe for iodine.

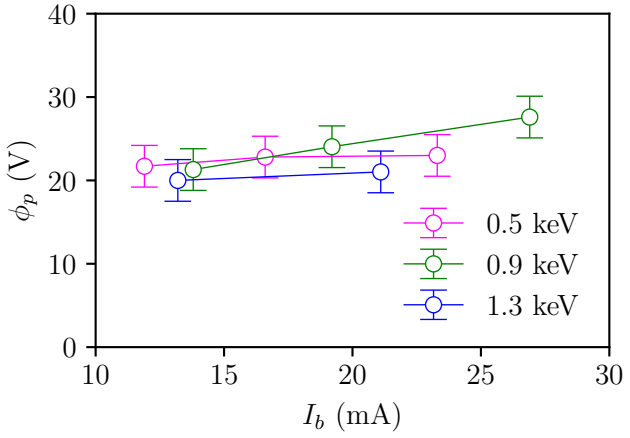

Figure 5.4: Measurement of the plume potential, ϕ_p, as a function of the total ion current, I_b, with the emissive probe for iodine.

voltage of the screen grid. It is possible to see that for all cases the the plume potential stays between 24 V and 27 V, which is similar to previous data from the literature [175].

As the ion energy increases, it is possible to see that the potential presents a slightly decreasing trend. This effect is most probably related to a distortion on the emissive probe sheath due to the ion beam energy and the change in the ion beam divergence, which may affect the measurement conditions. Furthermore, the increase in the ion beam energy also increases the slow ion population, affecting the plume potential. Figure 5.2 shows the plume potential as a function of the total ion beam current, corresponding

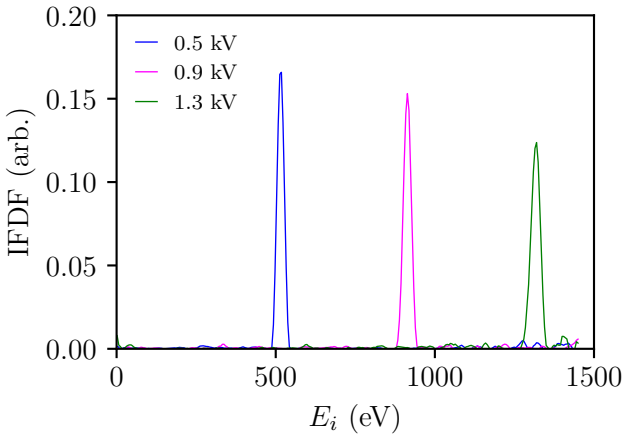

Figure 5.5: Measurement of the normalized ion flux distribution function (IFDF) for xenon.

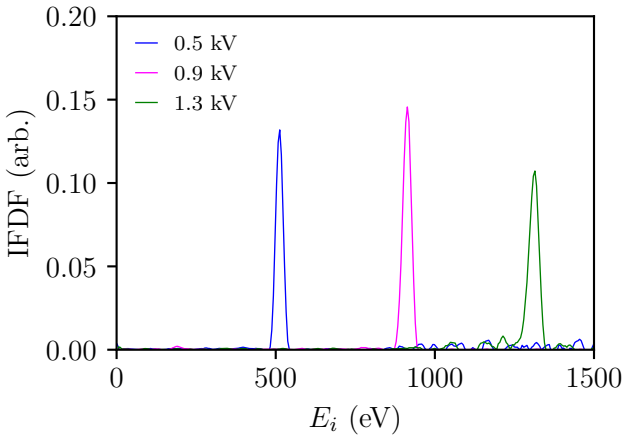

Figure 5.6: Measurement of the normalized ion flux distribution function (IFDF) for iodine.

to the three RF power cases. It is possible to see that for a given ion energy value, the value of the plume potential remains roughly constant as the ion current changes.

Figures 5.3 and 5.4 show the results of the measurements of the plasma potential for iodine. The first thing to note is that, in this specific experiment, the thruster became unstable in the operational point corresponding to 1.3 kV and 8 W, therefore no point was recorded for these parameters. Figure 5.3 shows the dependence of the plume potential on the acceleration voltage. In contrast to the xenon case, the plume potential in this case has a more flat behavior. Furthermore, the plume potential is in general lower,

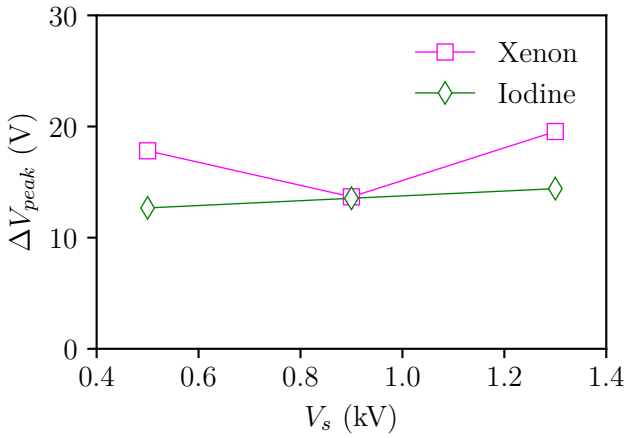

Figure 5.7: Voltage difference between the distribution peak value and the screen grid voltage.

spanning from approximately 19 V to 27 V. This is most likely due to differences in the ionization threshold and the several chemical processes in the iodine discharge, which can remove energy from the system. The figure 5.4 shows the dependence of the potential on the ion beam current for the different values of ion energy. In contrast to the xenon case, the data displays less uniform trends, which is probably due to the collisional processes and the many species involved in the discharge. For both the xenon and the iodine cases, the low measured plasma potential, is strong evidence that the plume is being correctly neutralized by the electron source.

Figures 5.5 and 5.6 show the measurements of the normalized ion flux distribution function done with the Impedans Semion RFEA for xenon and iodine, respectively. The measurements were done for three different values of screen grid voltage, 0.5 kV, 0.8 kV and 1.3 kV. Following the configuration recommended by the manufacturer, during these experiments, the first grid of the RFEA was kept at ground potential, ensuring that the ion beam at the entrance of the probe had an average kinetic energy close to E_i. The first grid can also be left floating, which is commonly done to reduce perturbation of the probe on the surrounding plasma, especially in cases where the plasma potential is high. In the present case, however, the plume plasma potential is relatively low (within the range of 15 to 35 V) and is similar to that expected for a floating sheath (which is typically of the order of $5T_e$, with T_e the electron temperature). Since the ion energy measured by an RFEA is increased due to ion acceleration through the sheath in front of the probe, a slight energy offset always develops regardless of whether the first grid is grounded or floating. The ion energy measured with both methods should be the same with an appropriate offset correction. Since the nominal ion beam energy is much greater than the plume plasma potential, this offset is minimal, and grounding or floating the first grid has no significant impact on the measured ion distributions discussed here. On

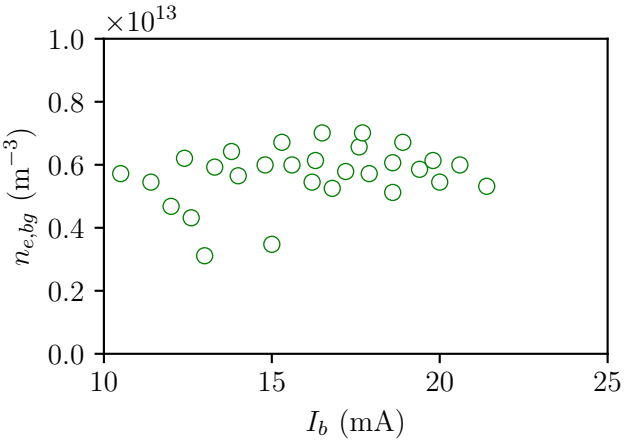

Figure 5.8: Measurement of the background plasma density measured with a dipole probe for xenon.

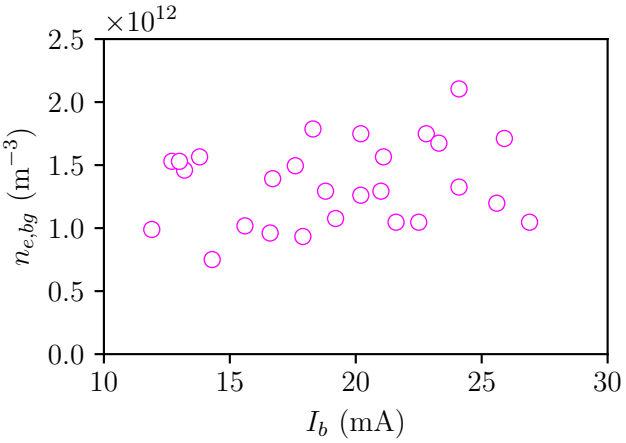

Figure 5.9: Measurement of the background plasma density measured with a dipole probe for iodine.

both plots, it is possible to observe peaks close to the location of the bias applied to the screen grid, showing that the ions are indeed mostly monoenergetic and with an energy approximately equal to the acceleration voltage. The offset of the peaks relative to the applied voltage to the screen grid, $\Delta V_{peak} = V_{peak} - V_s$, is shown in figure 5.7 for all cases. It is possible to see that this difference ranges from 12 V to 20 V and is slightly higher for xenon. This offset is due to the plasma sheath in front of the probe and the additional energy acquired by the ions in the ICP through the sheath in front of the screen grid. It is possible to observe that the offset increases with the bias voltage and is also slightly

higher for xenon. This corroborates the observation of the higher plume potential in the case of xenon, which suggests that electron temperature in the iodine case may be lower due to the different collisional processes taking place in the discharge. This lower temperature electron temperature is also observed in the analytical work developed by Grondein *et al.* [70]. It is also important to note that in figures 5.5 and 5.6 it was not possible to distinguish any peak close to the origin, which would correspond to the slow ion population in the plume. The slow ion population is expected to exist, however due to the distance of the probe to the thruster's exit and the low signal-to-noise ratio, the peak cannot be distinguished.

Figures 5.8 and 5.9 show measurements of the background plasma density with the matched dipole probe as a function of the ion beam current. The probe tip was positioned 40 cm away from the thruster exit and 20 cm away from the beam axis. It is possible to see that for both xenon and iodine, the background density displays a roughly constant behavior as the ion beam current increases. On average, the density in the xenon case is approximately higher by a factor of four. This may happen for different reasons, first, iodine also shows a higher mass utilization efficiency, thus exhausting less neutral gas for a given ion current, which in turn decreases the neutral density in the plume and the production of slow ions due to ion-neutral collisions. Furthermore, the different value of ion beam divergence also changes the distance between the beam edge and the probe, increasing the density in the case of xenon. The lower divergence in the case of iodine can also be related to the higher mass utilization efficiency which decreases the chance of collisions between ions and neutral particles, and hence decreasing diffusion of the beam radially.

5.1.2 Ion beam divergence

In this section, the results of the study of the beam with the automated probe array presented in section 3.4 are presented. The measurements with the instrument are done for five different values of screen grid bias, 0.5 kV, 0.7 kV, 0.9 kV, 1.1 kV and 1.3 kV, and six different values of RF power, 8 W, 9 W, 10 W, 11 W, 12 W and 13 W, which generates a total ion beam current in the range of 10 mA to 26 mA. For xenon, all 30 operational points are recorded, however, for iodine, the thruster becomes unstable for a few limit cases, and only 27 points are studied. Firstly, two-dimensional ion beam profiles are shown for both xenon and iodine, and following this, the total ion current and the beam divergence is estimated from these profiles.

Figures 5.10 and 5.11 show the two-dimensional profiles of the ion beam for xenon and iodine respectively. The profiles show the intensity of the ion current density in A/m^2 and are shown in order of increasing perveance, $I_b/V_s^{3/2}$, with the value of the divergence and the perveance displayed at each of the profiles. Each obtained data set consists of an approximately 800 by 16 data array having a much higher angular resolution in the direction of movement of the probe arm. It is possible to observe that the profiles, both for xenon and iodine, display a symmetric pattern close to a two-dimensional gaussian curve, as expected. As the perveance increases, one can note that the divergence angle

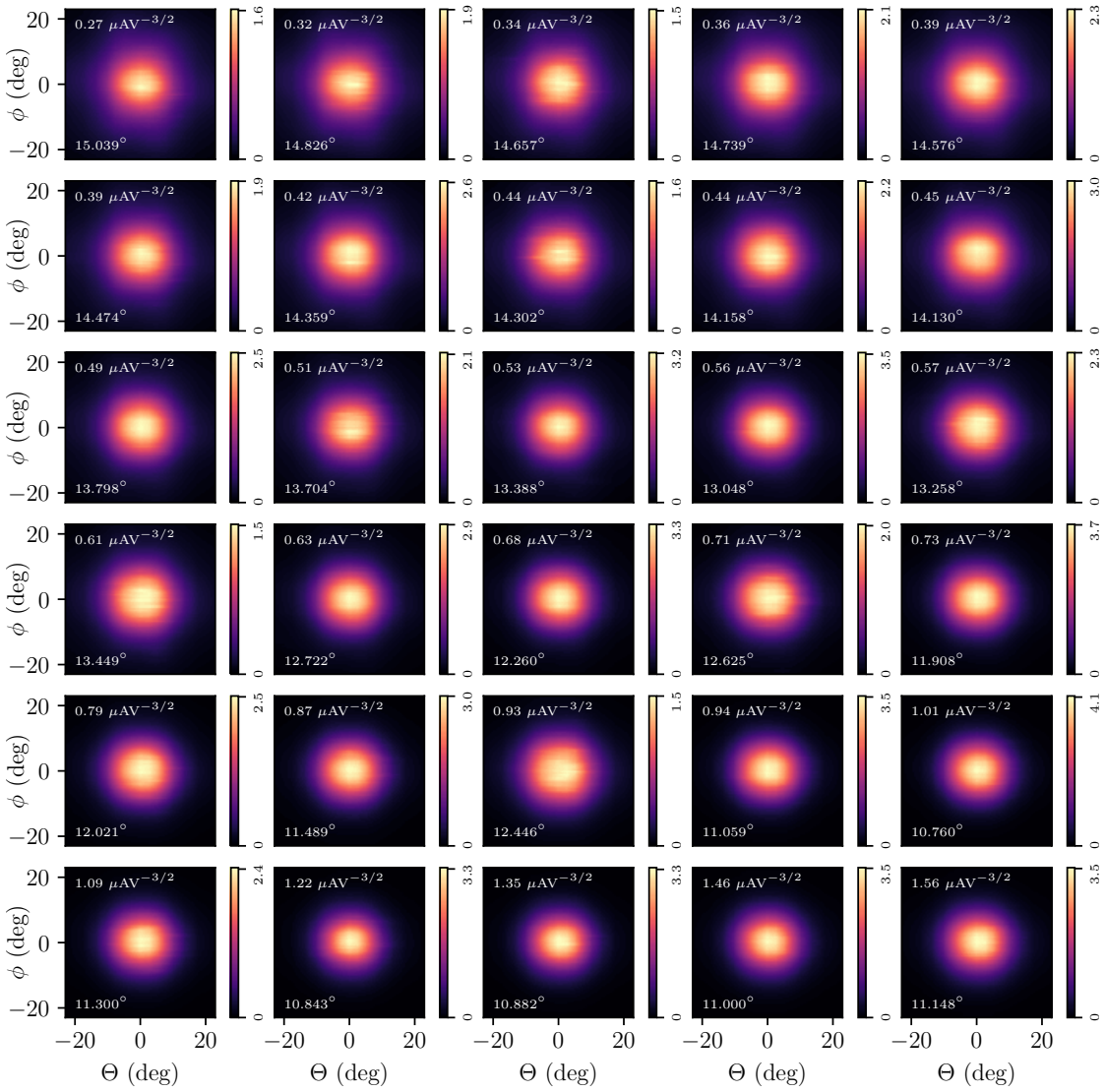

Figure 5.10: Ion beam profile measured with the planar probe array for xenon. The magnitude in the plots represent the ion current density given in A/m^2. Each plot show the corresponding value of the perveance, $I_b/V_s^{3/2}$, and the calculated divergence.

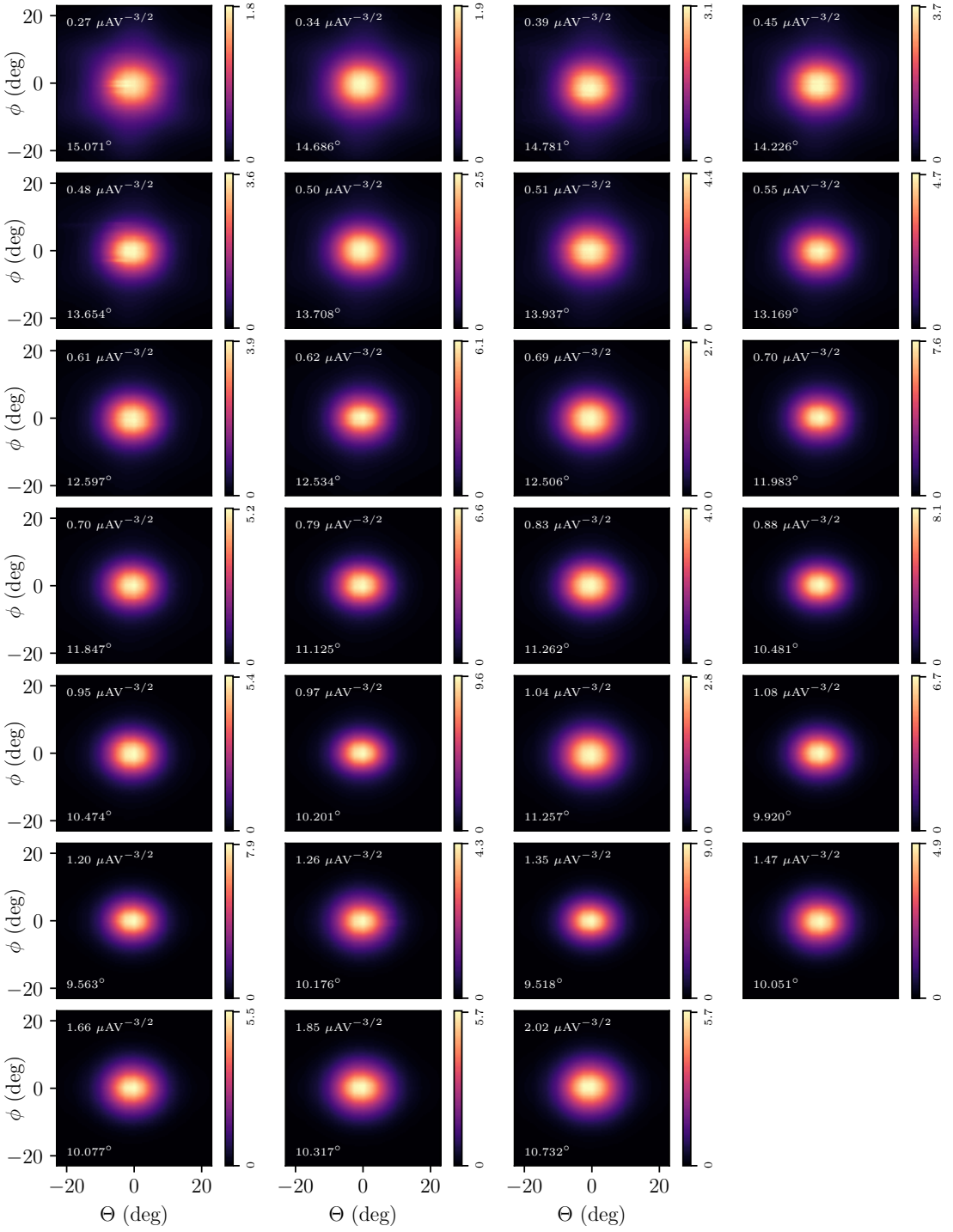

Figure 5.11: Ion beam profile measured with the planar probe array for iodine. The magnitude in the plots represent the ion current density given in A/m^2. Each plot show the corresponding value of the perveance, $I_b/V_s^{3/2}$, and the calculated divergence.

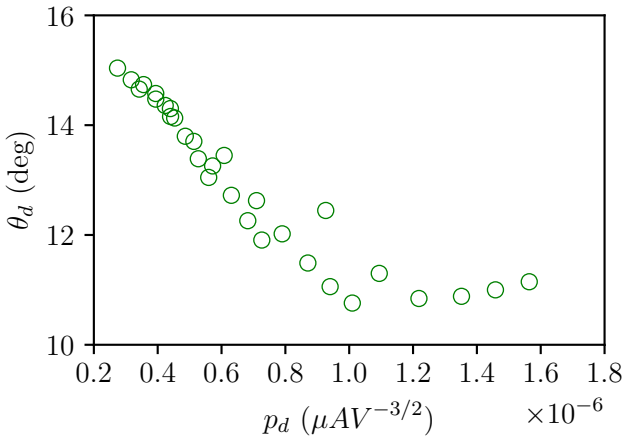

Figure 5.12: Estimation of the divergence half angle, θ_d, for the xenon ion beam as a function of the perveance, $p_d = I_b/V_s^{3/2}$.

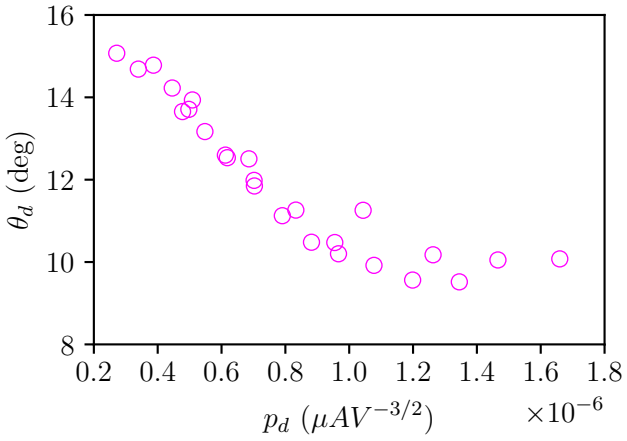

Figure 5.13: Estimation of the divergence half angle, θ_d, for the iodine ion beam as a function of the perveance, $p_d = I_b/V_s^{3/2}$.

decreases until a minimum point. For xenon, the minimum is found at roughly $1\,\mu A/V^{3/2}$ and is 10.7°, while for iodine it occurs at $1.35\,\mu A/V^{3/2}$ and is 9.5°. In the profiles with the lowest perveance values, where the divergence is the highest, it is possible to see that the beam presents a faint hexagonal shape on its outer edges. This happens because the orifices of the thruster's grids are arranged with a hexagonal pattern, generating a beam with a similar shape. Nevertheless, the beam region with the highest intensity does not reproduce this geometrical pattern, showing a symmetrical profile.

Figure 5.12 and 5.13 shows the value of the beam divergence as a function of the

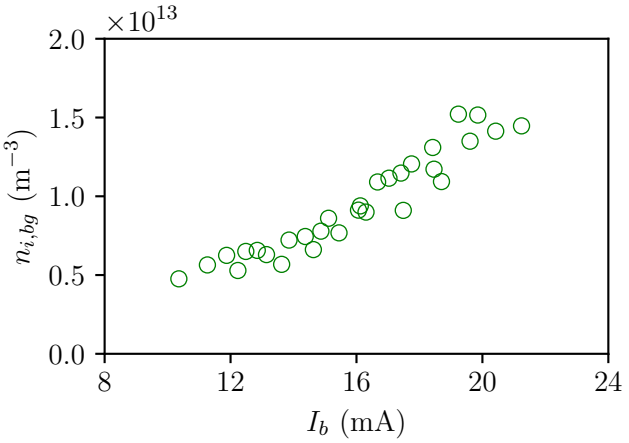

Figure 5.14: Plasma density estimated by the measurements of the background planar probe as a function of the total ion current for xenon.

perveance for xenon and iodine respectively. For both propellants, the data follows a very similar profile seen in other works from the literature as shown in figure 1.5. Furthermore, it is possible to observe that the data for xenon and iodine present very similar patterns between them, demonstrating that the thruster works similarly with both propellants. For $p_d < 0.6 \times 10^{-6}\,\mu\text{A/V}^{-3/2}$, the divergence values for both cases present very similar values. However, as the perveance grows, the divergence for iodine starts to be slightly lower, by roughly 10 %. It is also possible to observe in the work by Aston *et al.* [48] for example, that the ion beam divergence varies with different propellants, which agrees with the present case. The lower divergence can also be related to the lower electron temperature, which can cause a slower downstream expansion of the plume.

Figures 5.14 and 5.15 show the estimation of the background plasma density during the measurements with the probe array using the two background planar probes described previously. The estimation in this case is done as $n_{i,g} \approx J_i/eu_B$, and $T_e \approx 2\,\text{eV}$. Despite this estimation not being very precise, since the information of the electron temperature is not precise, it is possible to observe that the estimation has the same order of magnitude as the measurements from the dipole probe, shown in figures 5.8 and 5.9. It is also possible to observe that, as in the case of the dipole probe measurements, the background plasma density for iodine is considerably lower than in the xenon case, which partially confirms that this phenomenon indeed takes place, and it is not just an artifact. In contrast to the dipole measurements however, the density, in this case, increases in a linear fashion as the ion beam current grows. This is mainly due to the different measurement methods since in the dipole probe case, the position is different, and also the measurement is less intrusive, while the background planar probe is biased to $-48\,\text{V}$, which can cause a considerable sheath expansion and attract low-energy background ions.

A comparison of the ion beam current measured at the screen grid and estimated by

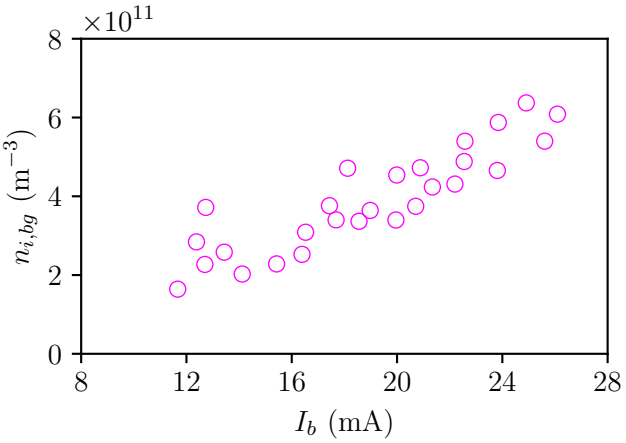

Figure 5.15: Plasma density estimated by the measurements of the background planar probe as a function of the total ion current for iodine.

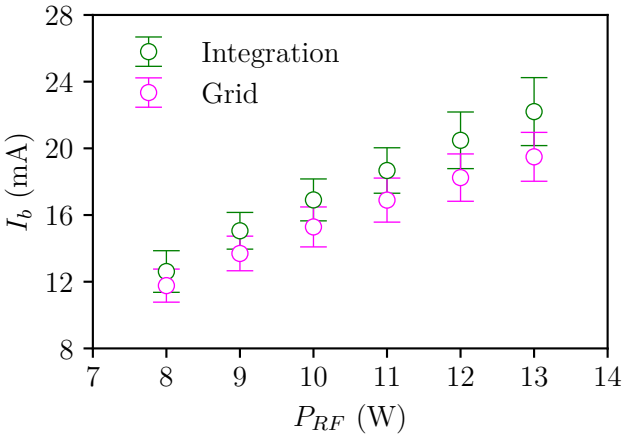

Figure 5.16: Comparison of the total ion beam current measured at the screen grid and estimated by integration of the scanned profile, for xenon.

integration of the two-dimensional profiles are shown in figures 5.16 and 5.17. Each point represents an average of five measurements for different values of screen grid voltage and the same RF power. The error bars represent the standard deviation of these points. It is possible to see that, for iodine, the estimated and the directly measured currents show excellent agreement, suggesting that the method used here is adequate. The comparison of the currents for xenon shows a systematic difference between both data sets, with the integrated data being higher by a factor of roughly $\frac{I_{b,i}}{I_{b,s}} \approx 1.11$, where $I_{b,i}$ is the current estimated by integration and $I_{b,s}$ is the current measured at the screen grid. This

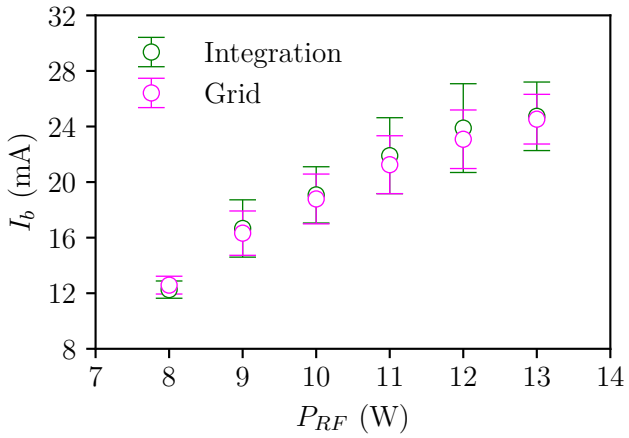

Figure 5.17: Comparison of the total ion beam current measured at the screen grid and estimated by integration of the scanned profile, for iodine.

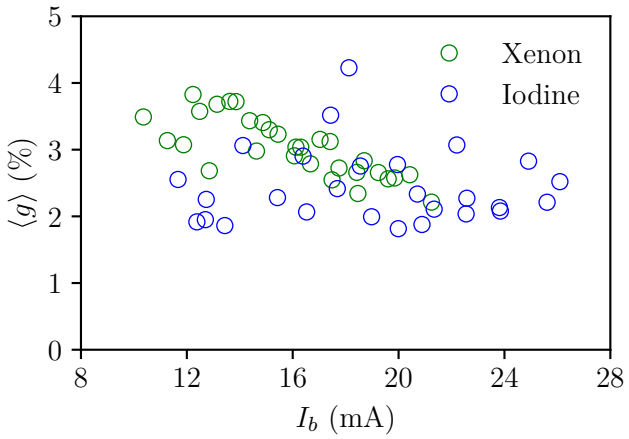

Figure 5.18: Average gaussian noise per channel generated in the measured signals for different ion beam currents.

difference can have different origins, such as the modification of the probe surface by reactions with iodine or the additional production of slow ions downstream of the plume. Since this is the case for all measurements with xenon, this difference is assumed to be a correction factor and is applied to the data.

To evaluate the quality of the measurements with the probe array, figure 5.18 shows the average random noise per channel. The noise level g_n for each channel n was estimated by calculating a smoothed data curve $j_{sn}(\phi)$ by the application of a Savitzky-Golay filter using $\Delta j_n(\phi) = (j_n(\phi) - j_{sn}(\phi))/j_n(\phi)$, where j_n is the raw data measured by each

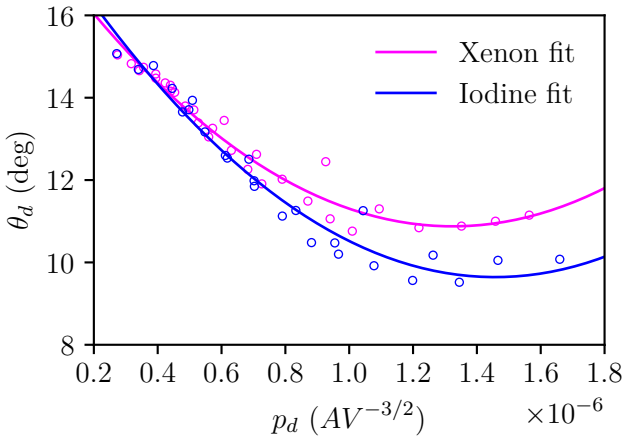

Figure 5.19: Curve fit of the iodine divergence data.

channel. The noise was then estimated by $g_n = 2s(\Delta j_n(\phi))$, where s is a function that returns the standard deviation of a set of points. The average noise per channel was then calculated as $\langle g \rangle = \frac{1}{N} \sum_{n=0}^{N} g_n$, where N is the number of probes. It is possible to observe in the resulting figure that the overall average noise level has a slightly decreasing trend as the total ion current increases, which is expected as the signal-to-noise ratio increases. Furthermore, the noise stays below about 5% of the measured signal for all of the different operational points, suggesting that the random noise generated by the source and the instrument does not significantly affect the probe array measurements.

5.1.3 Thruster performance

The main objective of this section is to study the behavior of the thruster's performance when using iodine and compare it with the utilization of xenon. In the first part of the section, the estimation of the thrust correction is presented, including the divergence and the beam composition factors. Next, the electric measurements are shown, and different performance parameters are estimated, such as thrust and specific impulse. Then the results of the direct thrust measurements, made with a thrust balance, are presented for the iodine case and used to validate the thrust estimation method.

To better estimate the thrust generated by the propulsion system, it is necessary to have a reasonable computation of the ion beam divergence half-angle at any given operational point. The divergence data computed from the measurements done with the planar probe array, and shown in figures 5.13 and 5.12 are used. To estimate the divergence at any point, the data is fitted with quadratic functions. The fit results are given by

$$\theta_{d,Xe}(p_d) \approx 4.087 \times 10^{12} p_d^2 - 1.082 \times 10^7 p_d + 18.039 \tag{5.1}$$

$$\theta_{d,I_2}(p_d) \approx 4.194 \times 10^{12} p_d^2 - 1.222 \times 10^7 p_d + 18.547 \tag{5.2}$$

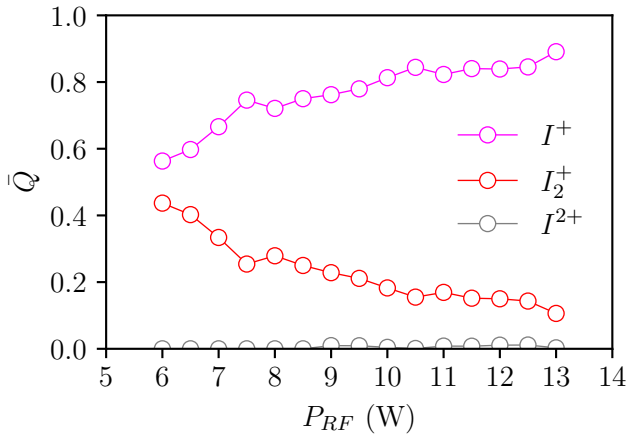

Figure 5.20: Iodine ion beam composition measured with the time-of-flight apparatus as a function of the RF power.

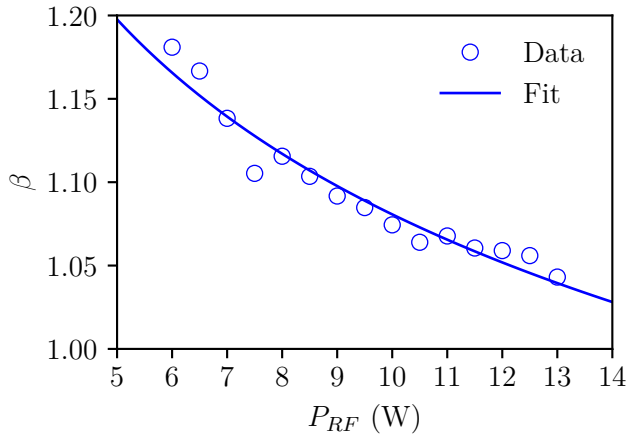

Figure 5.21: Beam composition thrust correction factor for iodine, showing the experimental data and the curve fit.

where $p_d = I_b/V_s^{3/2}$. The curves are shown in figure 5.19 and their R^2 coefficient are 0.960 and 0.953 respectively.. It is important to notice that the curve fits have acceptable precision only for the perveance range of the experimental data, therefore this is where the fits are applied when used for correcting the thrust estimation.

The second correction that is needed to improve the thrust estimation is to account for the different ion species in the beam as calculated in equation 1.50. To estimate this correction factor, the time-of-flight apparatus described in chapter 4 is used to measure the beam composition at several thruster operational points. Figure 5.20

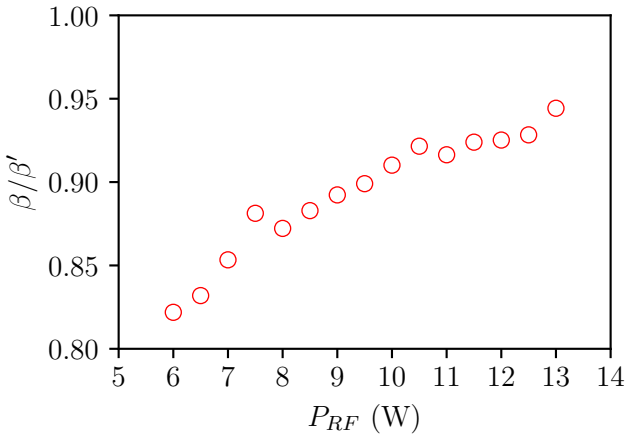

Figure 5.22: Beam composition specific impulse correction factor for iodine.

shows measurements of the beam composition for different values of the ICP RF power, P_{RF}. During the experiments, it was observed that, for the operational range of the thruster, the composition does not vary significantly when the mass flow rate changes and mainly depends on the RF power used. Therefore the measurements were done using an intermediate fixed value of mass flow rate, 0.06 mg/s, and an RF power varying from 6 W to 13 W. It is possible to observe that, at the low RF power limit, the beam is composed of approximately equal amounts of I^+ and I_2^+ ions (56 % and 44 %) and no I^{2+}. As the power increases, the fraction of I_2^+ continuously decreases as iodine dissociation is more favored. At the high power limit, 13 W, the beam is composed of 89 % of I^+, 10 % of I_2^+ and roughly 1 % of I^{2+}. This composition profile is very similar to that measured by Dietz *et al.* [76], with experiments with an ion thruster using iodine, and what is predicted by Grondein *et al.* [70] in their analytical model. Using the measured data and equation 1.50, the beam composition correction factor can be calculated. The calculated correction factors are shown in figure 5.21. It is interesting to note that, in contrast to typical correction factors for doubly charged xenon ions found in the literature [14], the factor for iodine is typically higher than one due to the more massive I_2^+ ions. In this way, the thrust generated by the system when using iodine for a given value of ion beam current and acceleration voltage will be higher than when using xenon. This aspect offers an advantage, especially for low-power propulsion systems that typically have a low performance, since the average mass of ions will be increased by higher production of I_2^+, improving the thrust generated. To apply the correction factor to any operational modes, the data is fitted with a power-law shown in the figure. The resulting curve fit is given by

$$\beta(P_{RF}) \approx 1.5202 P_{RF}^{-0.1482} \tag{5.3}$$

The R^2 coefficient for the fit is 0.945.

It is also possible to evaluate the impact of the different beam compositions on the

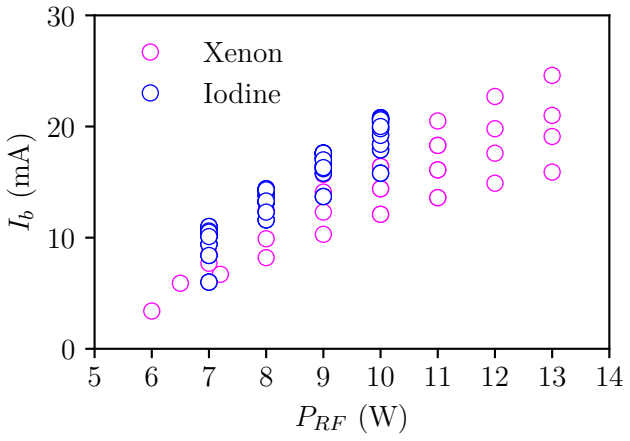

Figure 5.23: Ion beam current as a function of the RF power.

specific impulse of the thruster. Using equation 1.51, one can calculate the ratio β/β', which computes the change of the I_{sp} in relation to its value if the beam was composed only of I^+. Figure 5.22 shows the resulting calculation. It can be seen that the specific impulse decreases as the RF power decreases and the ratio of I_2^+ ions increases, varying between 0.94 and 0.82, which is expected since the average velocity of ions decreases as $\sim 1/\sqrt{m_i}$. In this way, despite producing a higher thrust than xenon, the final specific impulse in low-power devices will typically be lower.

To study the performance of the system, 120 operational points were recorded, consisting of 4 values of RF power (7 W, 8 W, 9 W and 10 W), 10 values of mass flow rate (37.7 µg s^{-1}, 44.5 µg s^{-1}, 51.4 µg s^{-1}, 58.2 µg s^{-1}, 65.1 µg s^{-1}, 71.9 µg s^{-1}, 78.8 µg s^{-1}, 85.6 µg s^{-1}, 92.5 µg s^{-1} and 99.3 µg s^{-1}), and 3 values of screen grid voltage (0.7 kV, 1.0 kV and 1.3 kV). During all measurements, the accel grid is kept at −70 V. The recorded quantities during the operation are the total power consumed by the system and the screen grid and accel grid currents. In the case of xenon, 32 operational points are used representing its full operational range, consisting of 4 values of RF power (6 W to 13 W), 4 values of mass flow rate (58.9 µg s^{-1}, 68.8 µg s^{-1}, 78.6 µg s^{-1} and 98.3 µg s^{-1}), and 2 values of screen grid voltage (1.0 kV and 1.3 kV). The raw data used in this part was measured by both the author and the ThrustMe team in collaboration.

Figure 5.23 shows an overview of all the operational points, showing the ion beam current, which is assumed to be equivalent to the screen grid current, as a function of the ICP RF power for both xenon and iodine. It is possible to observe that in general the ion beam increases with the RF power used, varying from about 5.5 mA to 22 mA for iodine, and from 2.5 mA to 24 mA for xenon. The spread of points at each RF power value corresponds to the variation of both mass flow rate and screen grid voltage for each operational point. This shows that the most important dependence of the ion beam current is on the RF power, which is expected. It can be seen that although the xenon

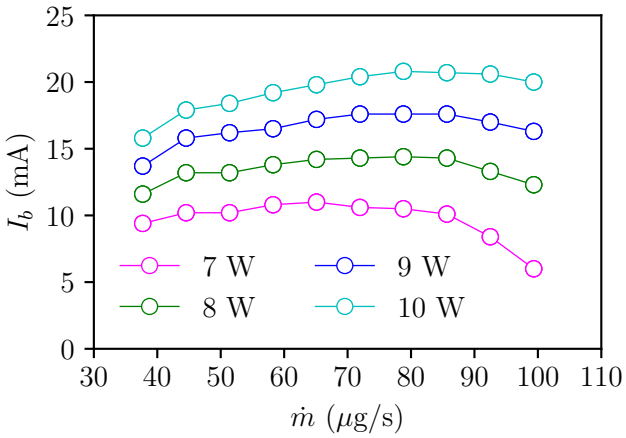

Figure 5.24: Ion beam current as a function of the mass flow rate for different RF powers for iodine.

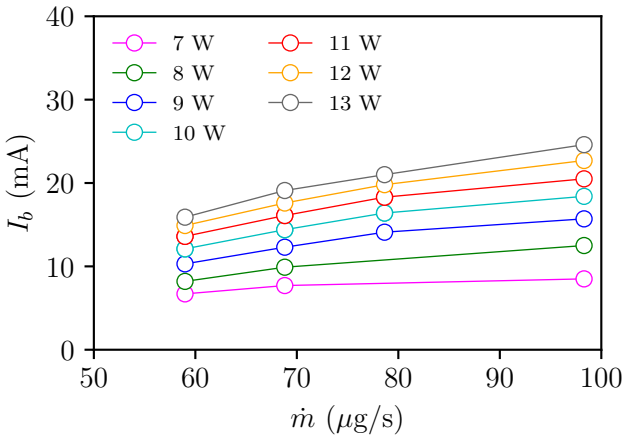

Figure 5.25: Ion beam current as a function of the mass flow rate for different RF powers for xenon.

thruster has been tested for a broader range of RF power values, the ion beam produced by the iodine thruster is on average higher than in the xenon case for the RF power values where they are compared. In the simulation work done by Grondein *et al.* [70], it is also observed that the ion current production becomes higher at low mass flow rates when compared to xenon after an RF power threshold, which is consistent with what is observed here.

Figure 5.24 shows the ion beam current as a function of the mass flow rate for the different values of RF power. It is possible to observe that, for a fixed value of RF power,

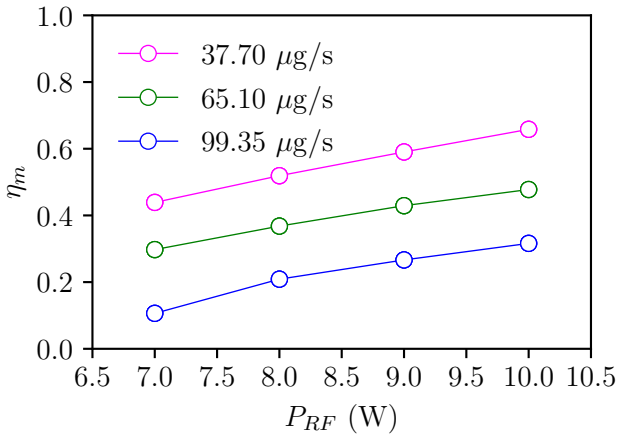

Figure 5.26: Mass utilization efficiency for different values of mass flow rate for the thruster as a function of the RF power for iodine.

the ion beam current follows a trend that initially increases until a maximum value and then decreases. This is due to the change in electron temperature as the neutral gas pressure increases which changes the configuration of chemical reactions taking place inside the plasma and can increase the energy loss in inelastic collisional processes; this effect is typically observed in ICP discharges [4]. Therefore, it is interesting to note that an optimal mass flow rate value produces the maximum possible ion beam current at each value of RF power. Figure 5.25 shows a similar plot for the xenon case. It is possible to see that, in contrast with the iodine case, the ion beam current continuously grows as the mass flow is increased for all RF power values. Comparing both plots, it is possible to see a similarity between the xenon plot and the iodine plot for the mass flow rate range below the optimal mass flow rate. This may indicate that the xenon ICP discharge operates below the optimal point and requires a higher mass flow rate to achieve its optimal condition.

Using the measured ion beam current, it is possible to estimate the mass utilization efficiency of the thruster, η_m, given in 1.52. The beam composition correction factor, β', is given in this case by $\beta' = \bar{Q}_I + 2\bar{Q}_{I_2^+} + \bar{Q}_{I^{2+}}/2$, and is interpolated from the collected experimental data. Figure 5.26 shows the mass utilization efficiency as a function of the RF power for three different values of mass flow rate. The mass utilization efficiency varies between approximately 0.1 and 0.67. It is possible to observe that, for a fixed value of mass flow rate, the mass utilization efficiency increases with the RF power in a linear fashion. This is expected since the plasma density, and thus the ion beam current, increases with the power injected into the ICP plasma [42, 70]. On the other hand, as the mass flow rate increases, the mass utilization efficiency decreases since the gas pressure increases without increasing the power, which decreases the ratio of ions to neutrals leaving the thruster. This can also be seen in figure 5.27 which plots η_m as

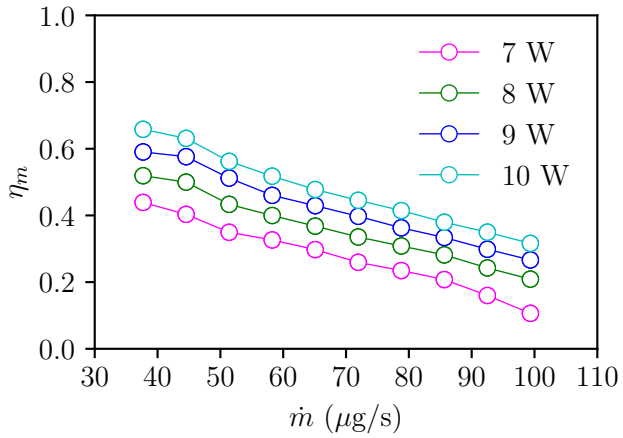

Figure 5.27: Mass utilization efficiency for different values of RF power for the thruster as a function of the mass flow rate for iodine.

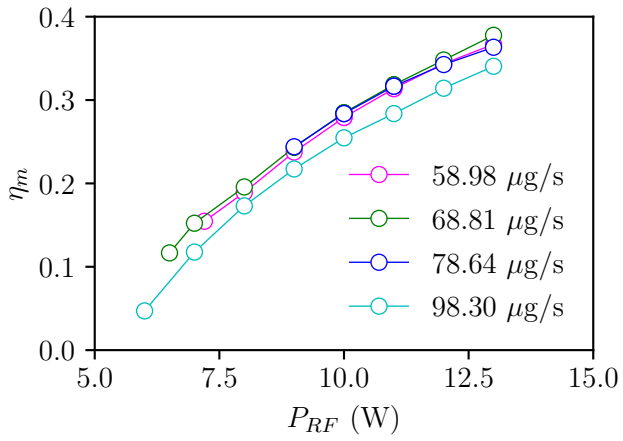

Figure 5.28: Mass utilization efficiency for different values of mass flow rate for the thruster as a function of the RF power for xenon.

a function of the mass flow rate for different values of the RF power. It is possible to see that for a fixed RF power value, the mass utilization efficiency decreases in a linear fashion as the mass flow rate increases. In general, it is possible to observe that, in this case, it is always more advantageous operating the thruster with the lowest possible mass flow rate for a given RF power. Figure 5.28 shows the mass utilization efficiency for xenon. In contrast with the iodine case, the xenon operation overall shows a lower mass utilization efficiency, ranging from 0.05 to 0.39. It is possible to see, as in the case of iodine, that the efficiency decreases when the mass flow rate is increased; however, this

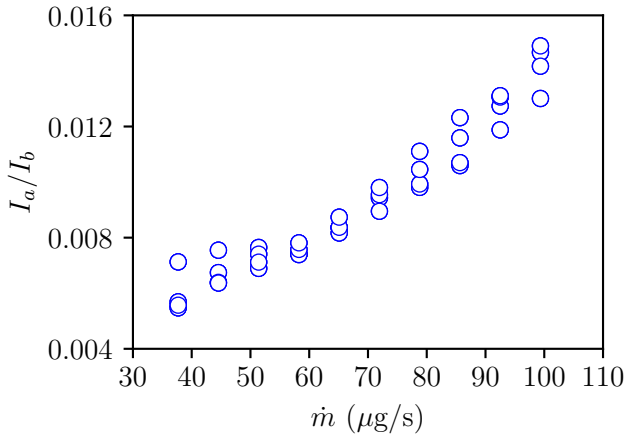

Figure 5.29: Ratio of accel-to-screen grid current as a function of mass flow rate for iodine.

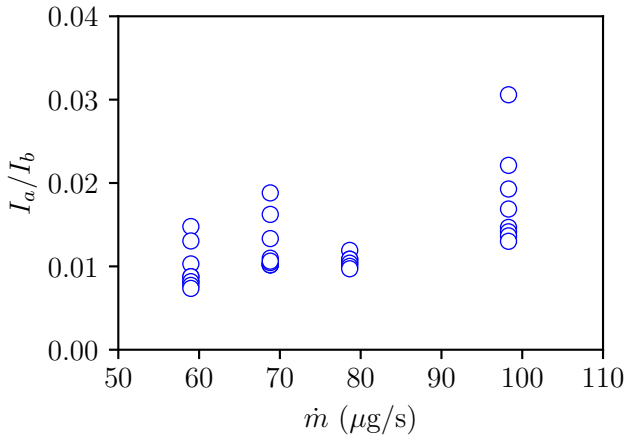

Figure 5.30: Ratio of accel-to-screen grid current as a function of mass flow rate for xenon.

variation for xenon is considerably lower, which may be due to a higher RF coupling efficiency at higher mass flow rate and the higher ion beam current production due to lower power losses caused by a lower electron temperature at this condition. The higher mass utilization efficiency of iodine might be explained by lower power losses within the discharge, such as lower total collisional energy losses (particularly of inelastic processes such as excitation, lower ionization potential and different cross section profiles).

Another critical aspect of the performance characterization is to verify the magnitude of the accel grid current over the different modes. This current is mainly connected with

the backstreaming of slow ions formed in the plume due to high-energy ions that collide with neutrals, and energetic ions from the beam which may intercept the accel grid due to poor focusing. It is observed that the main dependence of the accel grid current is on the iodine gas mass flow rate. Figure 5.29 shows a plot of the ratio of the accel grid current to the screen grid current, I_a/I_b, as a function of the mass flow rate, for iodine. The accel grid current ratio, in this case, displays a clear correlation with mass flow rate, which is expected since downstream ionization and charge exchange increases with neutral density, and the density inside the grid-gap also increases, which can lead to collisions and deflect beam ions towards the accel grid. On the other hand, the accel grid current does not present any correlation with both the screen grid voltage, V_s, or the beam perveance, p_d. This may indicate that the accel grid current is primarily caused by backstreaming slow ions produced in the plume rather than direct impingement of beam ions, which is expected. This is also evidence that the thruster is operating within the optimal perveance range, since no important dependence on the acceleration voltage is observed, showing a plateau behavior as expected from the literature [14]. It is important to note that the slow ion production may be artificially enhanced due to the limited pumping speed capability of the vacuum system, causing the neutral background density to be higher than in space. To estimate the slow ion production in a more realistic situation, it is necessary to perform the experiments in a vacuum facility with a higher pumping speed, or in space. The measurements for the xenon case display a different behavior as shown in figure 5.30. In this case, the accel-to-screen grid current goes up to roughly 0.03, which is two times higher than in the iodine case. The data points also display a more important spread at each value of mass flow rate, which indicates that the accel grid current is more sensitive to the other beam parameters such as its divergence. The higher accel grid current in this case can be explained by the lower mass utilization efficiency of xenon for a given mass flow rate which suggests a higher neutral gas density in the plume. This higher gas density increases the production of slow ions which increases the ion backstreaming current.

Using the collected data and the correction factors obtained from the divergence and the composition estimations, it is possible to estimate the thrust, T, using equation 1.48 and the specific impulse, $I_{sp} = T/g_0\dot{m}$, of the thruster, permitting a visualization of the complete picture of the system's performance. Figure 5.31 shows the value of the specific impulse for each operational point as a function of the estimated thrust. The color of each point shows the total power consumed, and the lines of constant mass flow rate are represented by the dashed lines connecting the points. The value of the mass flow rate increase for lines closer to the x-axis, and the lines of the limit mass flow rate points are indicated with the arrows. The estimated thrust ranges from 0.28 mN to 1.27 mN, and the specific impulse from 290 s to 2610 s. It is possible to observe that the total power consumed by the system increases when following a given line of constant mass flow rate. This is expected since the total power is roughly proportional to the jet power, $P_T \sim P_j = \frac{1}{2}\dot{m}u_e^2$, thus $I_{sp} \sim \sqrt{P_T/\dot{m}}$. In this way, as shown in the figure, to obtain the maximum possible specific impulse of the thruster, it is necessary to maximize the system's total power while minimizing the mass flow rate used. This behavior is the

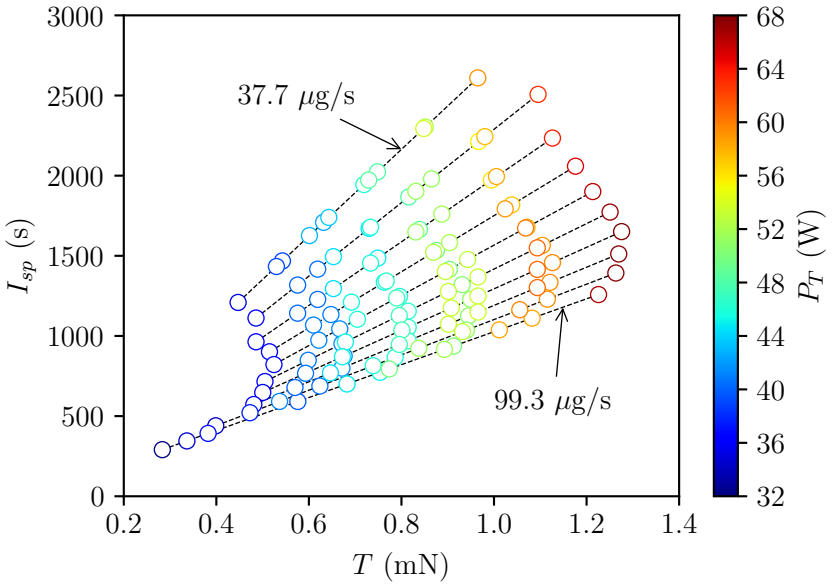

Figure 5.31: Complete performance map of the thruster using iodine showing thrust, T, versus specific impulse, I_{sp}. The color depicts the total power, P_T, while the the dashed lines show lines of constant mass flow rate, $\dot{m}$.

same behavior as observed in the mass utilization efficiency, where it is necessary to operate with the maximum possible RF power for a given mass flow rate to maximize η_m, which is expected since the $I_{sp} \propto \eta_m$. Another interesting characteristic is that it is possible to observe trends of constant total power in the upward direction of the plot. For $T > 0.5\,\text{mN}$, each of these total power trends have very similar values of thrust, suggesting that the total power depends mostly on the pair of values of specific impulse and thrust, but not on the mass flow rate. As the thrust, and thus the ion beam current, is fixed while increasing the mass flow rate, the mass utilization decreases, hence decreasing the I_{sp} while keeping a similar power consumption, since $P_T \sim I_b V_s$.

Figure 5.32 shows the performance map for the xenon thruster. It is first possible to see that the thruster, in this case, reaches a considerably narrower operational range when compared to iodine, with its specific impulse ranging from approximately 180 s to 1600 s. This happens because the thruster when using xenon is only stable for mass flow rate values above approximately $58\,\mu\text{g}\,\text{s}^{-1}$, which limits how high the specific impulse of the thruster can get. This limitation may be related to several complex collisional processes that aid the ICP discharge to be sustained at lower mass flow rates in the iodine case compared to xenon. Nevertheless, the total power and thrust level generated by the thruster is very similar to the iodine case, ranging from roughly 0.2 mN to 1.3 mN.

To confirm the quality of the thrust estimation used here and verify that the correction factors were indeed required, a direct thrust measurement of the system was performed

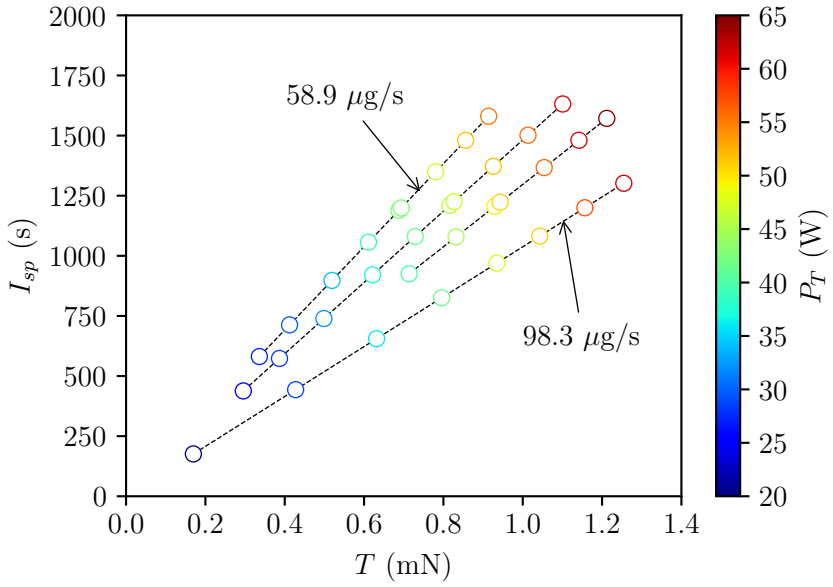

Figure 5.32: Complete performance map of the thruster using xenon showing thrust, T, versus specific impulse, I_{sp}. The colormap depicts the total power, P_T, while the dashed lines show curves of constant mass flow rate, $\dot{m}$.

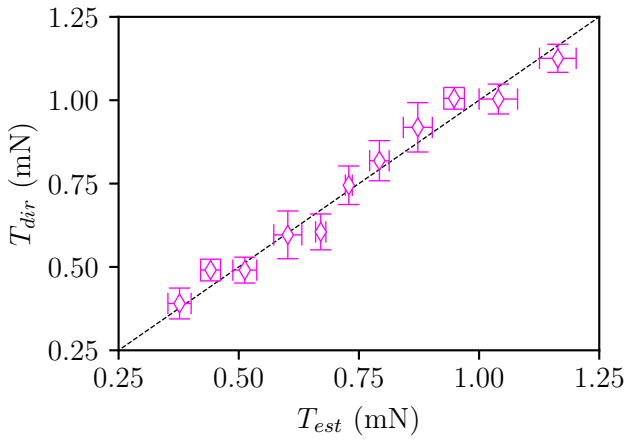

Figure 5.33: Comparison of thrust obtained through direct measurement, T_{dir}, and obtained through estimation, T_{est}.

using a thrust balance. The thrust balance consists of a device used to measure the force produced by the thruster. This system was developed by ThrustMe and it consists of a single pendulum balance that uses a high-precision S256 load cell that produces an

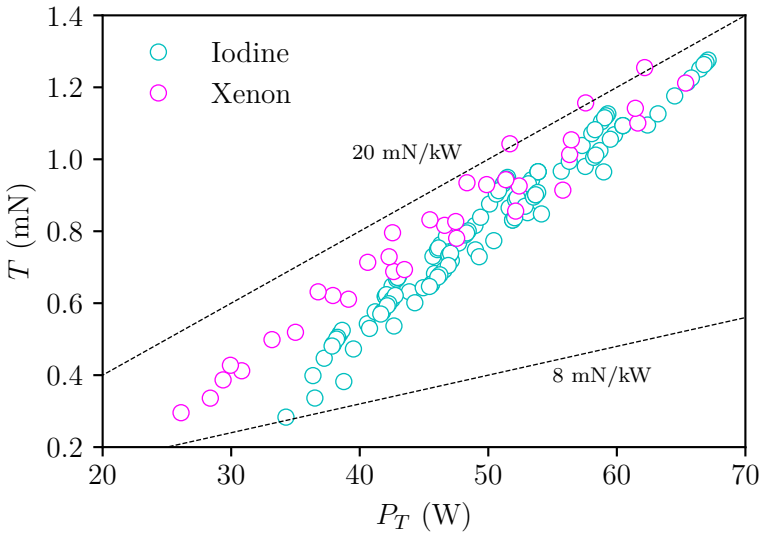

Figure 5.34: Thrust as a function of total power. The dashed lines show two lines of constant thrust-to-power ratio at 8 and 20 mN/kW.

analogue voltage output with sensitivity of 1 mV/V to read the force produced by the thruster. The balance is constructed in such a way that the thrust vector and the load cell are not aligned which effectively amplifies the force signal, making the balance have a precision of 30 µN and a maximum load of 100 mN. A more detailed description of the thrust balance can be found in ref. [176]. The measurements with the thrust balance were done for a fixed value of screen grid voltage at 1 kV, and 11 different points of RF power varying from 6 W to 13 W. Figure 5.33 shows the results of the measurement comparing the estimated thrust, T_{est}, and the thrust directly measured, T_{dir}; the dashed line show where the points should be ideally located. It is possible to see that the points are in close proximity of the ideal line, which is good evidence that the thrust estimation method used here is reliable.

An important performance parameter of a thruster is its thrust-to-power ratio, which effectively determines the thrust generated for given input power. Figure 5.34 shows a plot of the estimated thrust as a function of the total power of the iodine and xenon thrusters. It is worth noting that the total power, P_T, used in this analysis corresponds to the power consumed by the complete propulsion system, including the power losses in the power processing unit (PPU), and other subsystems (including the electron-emitting cathode). In this way, the data shown here gives an overall performance estimation for the system, instead of focusing on just the thruster itself. This contrasts with other works studying propulsion systems in the literature that typically do not consider the power losses in subsystems as the PPU. The dashed lines show two constant thrust-to-power ratio lines that envelop the data set. In this way, the thrust-to-power ratio of the thruster ranges from 8 mN/kW to 20 mN/kW. It is possible to see that, independently of the acceleration

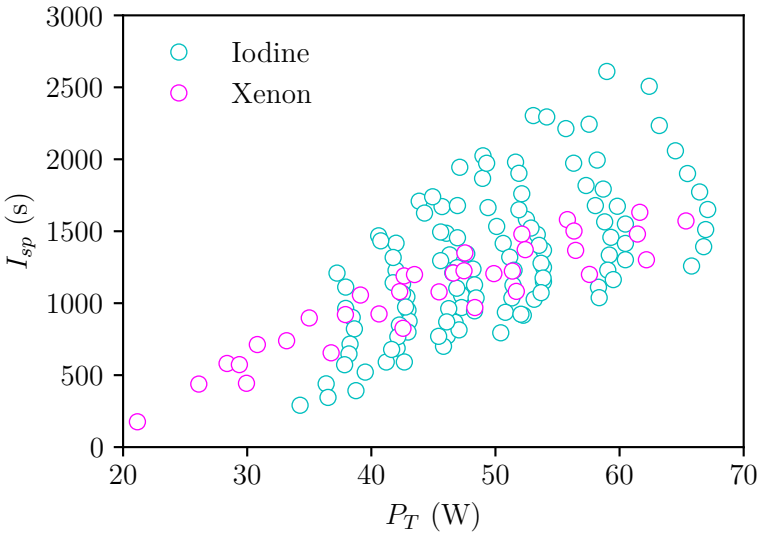

Figure 5.35: Specific impulse as a function of total power for xenon and iodine.

voltage or mass flow rate, the iodine and xenon data show a linearly increasing trend, intercepting the two dashed limes close to 55 W. In the lower power range, the iodine thruster shows a lower thrust-to-power ratio, which is also seen in the modelling by [70]. Because of its linear trend, the iodine data can be trivially fit by a line curve, giving $T(P_T) = 2.759 \times 10^{-5} P_T - 5.629 \times 10^{-4}$, which can be used as an approximate model of the thruster behavior to be used for high-level planning. Dividing this curve fit by P_T, it is possible to see that if one extrapolated this curve to higher powers, the thrust-to-power ratio would approach 27 mN/kW in the limit. This thrust-to-power ratio could be theoretically achieved at 95 W, and would lead to a thruster efficiency of roughly 37 % for a mass utilization efficiency of 0.5 and an ion beam current of 30 mA. Figure 5.35 shows the plot of the specific impulse as a function of the total power. It can be seen that xenon displays a more linear behavior with a lower spread and a more direct dependency on the total power. Iodine, on the other hand, shows a much larger variation. One of the main reasons for this behavior is that in the iodine case the thruster can operate with lower mass flow rates. In this plot, similarly to figures 5.31 and 5.32, as the specific impulse is increased the mass flow rate decreases since $I_{sp} \sim \sqrt{P_T/\dot{m}}$.

Another way to evaluate the performance of the thruster is to evaluate the thrust-to-power ratio as a function of the specific impulse, as shown in figure 5.36. The dashed lines in the figure show the lines of constant beam-to-total power ratio calculated from $T/P_T = 2P_b/P_T g_0 I_{sp}$. The ratio P_b/P_T gives information on how much of the power input is converted to actual beam power. It is possible to see that the iodine thruster can achieve a much higher power ratio compared to xenon. This higher value is again a consequence of the capability of the thruster of operating with lower mass flow rates and because at a given RF power, a higher ion current is generated in the case of iodine due

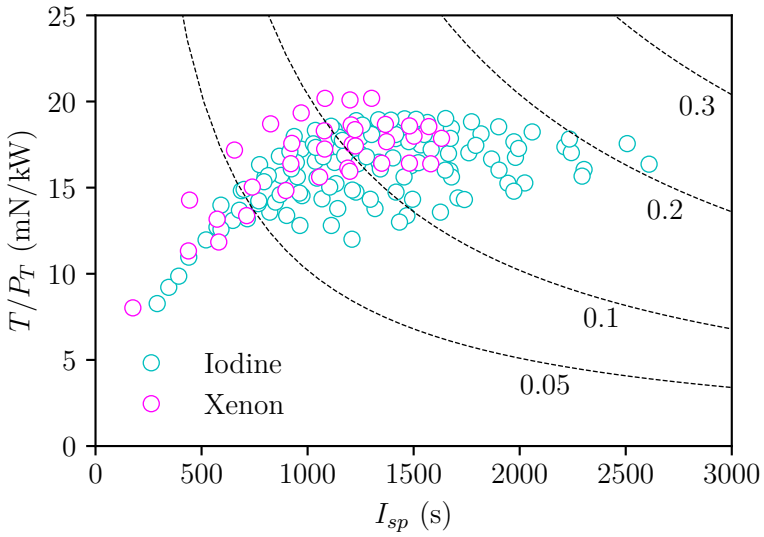

Figure 5.36: Thrust-to-power ratio, T/P_T, as a function of the specific impulse for xenon and iodine. The dashed lines show the theoretical lines of constant beam-to-total power ratio, P_b/P_T.

to lower power losses in the ICP discharge when compared to xenon.

5.2 In-orbit testing

The NPT30-I2 was launched onboard the Beihangkongshi-1 mission on November 2020, and started operation in space from December 2020. In this section, the results obtained from the in-orbit operation are presented and then compared with the laboratory measurements to verify that the measurements done on the ground are a good representation of the actual thruster operation. The second part presents an overview of the maneuvers performed in orbit. The data used in this section was obtained by the ThrustMe team during the operation of the mission and is processed and analyzed here to provide a complete picture of the operation of an iodine ion thruster.

5.2.1 Operational characteristics

To compare the system's operation on the ground and in space, one of the firings of the system during the mission is analyzed. This maneuver consisted of a 90 min operation with the screen grid voltage set to 1 kV and fixed ion beam current at 16 mA. To verify that the behavior is equivalent, the thruster was tested on the ground with the same operational conditions during a similar amount of time.

Figure 5.37 shows the results of the measurements on both tests. In the first row, the total ion beam current measurement is displayed. It is possible to see that despite a

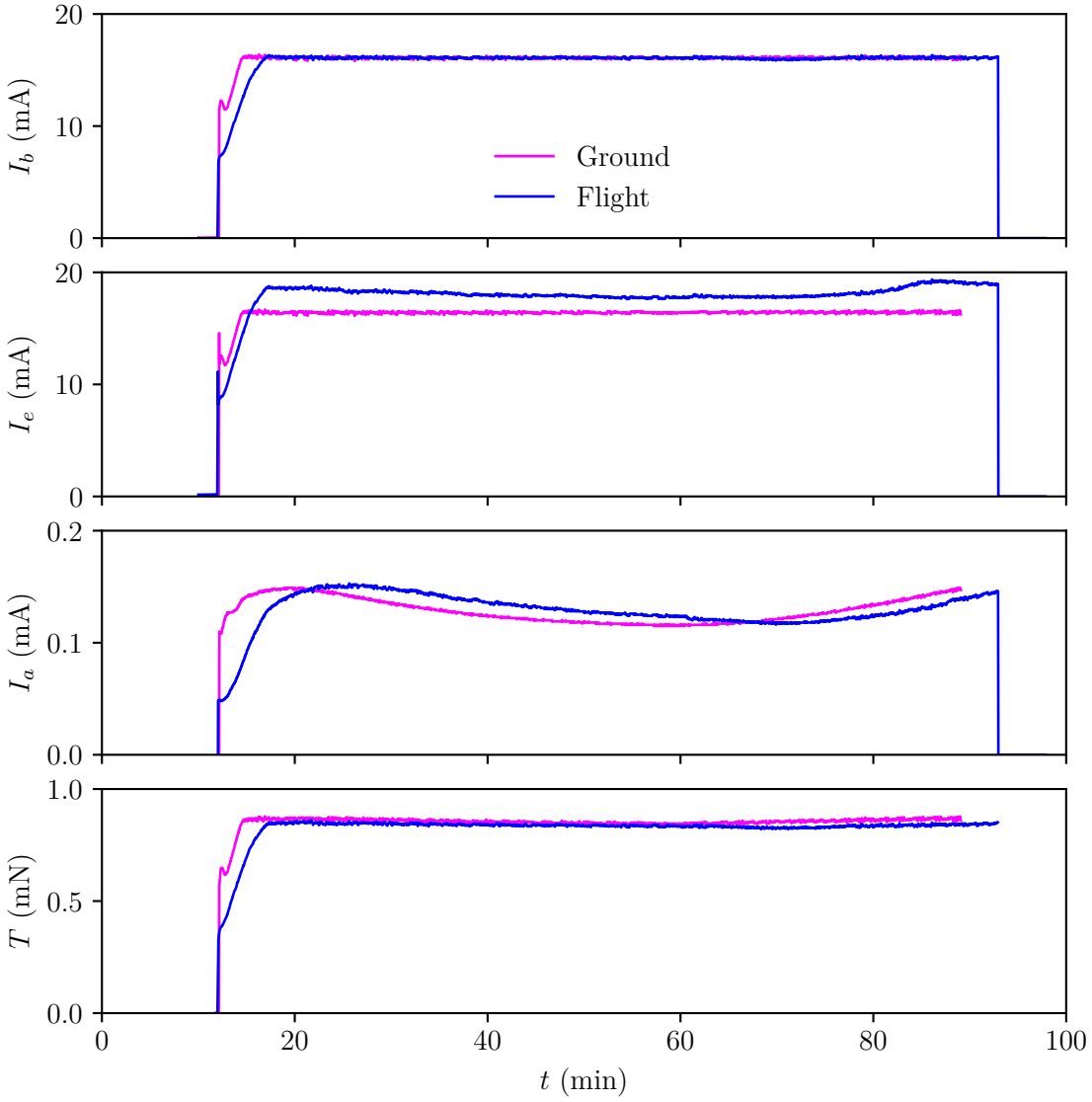

Figure 5.37: Comparison of the thruster currents measured on the ground and during the in-orbit operation.

disparate behavior during the initial startup transient, the ion beam current during the whole operation remains effectively coincident. This shows that both systems behave in similar manner and that the thruster in space can effectively generate and accelerate an ion beam under similar operational conditions. The non-coincident behavior in the startup transient can be attributed mainly to the significantly different thermal conditions between the ground and flight measurements. In the second row, the electron current emitted by the neutralizer is shown. It is possible to see that, in the case of the ground experiment, the current emitted by the electron source coincides with the total ion beam current, which is the expected behavior to maintain good plume neutralization and maintain current-free operation. However, in the case of the flight experiment, it is possible to see that the emitted current is slightly higher than the ion current. This difference varies by roughly 2 mA to 3 mA during operation. This can be explained by the fact that the thruster and the spacecraft are electrically floating. Therefore, the population of slow ions created in the plume or other charged particles present in the space environment can be collected by the body of the spacecraft, charging it to a given potential. In this way, to keep the spacecraft and the thruster close to neutrality the electron source must emit a higher current than what is seen in the ground experiment, where the thruster is connected to the laboratory ground. In this context, the slow drift of the emitted current can be related to the change in the space environment as the satellite moves along its orbital trajectory. The third row shows the value of the accel grid current during operation. It is possible to see that the current is almost two orders of magnitude lower than the ion beam current and slowly drifts during the operation both in the ground and in the space experiments. This drift is associated with temperature transients of the system during the firing that may slightly affect the mass flow rate injected into the plasma chamber and change the temperature of the neutral gas, affecting the production of slow ions in the plume. This also explains the fact that the curves show a phase shift, which may be related to different thermal conditions in both environments. In the last row, the thrust estimation is shown for both tests. The thrust here is estimated using the method described in the last section, considering the correction factors determined experimentally. The thrust in both cases is approximately 0.85 mN at steady-state. As time evolves, one can see that the estimated thrust of both cases shows a slight difference, with the value in the flight case slightly lower than in the ground case by a few percent. This difference may be related to the different thermal conditions, which may create slightly different discharge conditions and mass flow rates, nevertheless, this difference is quite small and does not impact the operation.

In general, the results from the ground experiments and flight tests show good agreement, not only in the case of the firing analyzed here but also on other operational points summarized in the next section. This serves as good evidence that, apart from electrical and thermal conditions that are complex to replicate, the operational conditions in the vacuum systems used in the present work mimic the conditions found in orbit with acceptable fidelity.

Table 5.1: List of maneuvers up until 28 February 2021. Δa is the change in the semi-major axis (adapted from Ref. [135]).

Firing slot	Date	Operation mode	Startup time (min)	Δa_{GMAT} (m)	Δa_{GPS} (m)
1A	29/12/2020	FS	9.2	299 (P)	334 (P)
1B	02/01/2021	N1	13.2	373 (P)	368 (P)
2A	13/01/2021	N1	11.2	272 (R)	322 (R)
2B	14/01/2021	N1	17.2	265 (P)	411 (P)
2C	17/01/2021	N1	11.5	427 (R)	408 (R)
2D	21/01/2021	N1	14.2	303 (R)	310 (R)
2E	25/01/2021	N1	12.1	200 (R)	248 (R)
2F	28/01/2021	N1	11.8	262 (R)	265 (R)
2G	30/01/2021	N1	11.5	-	-
2H	09/02/2021	N1	12.2	212 (R)	232 (R)
2I	20/02/2021	N1	11.6	232 (R)	227 (R)

5.2.2 Orbital maneuvers

The Beihangkongshi-1 satellite consists of a 12U CubeSat with a total mass of approximately 20 kg which was launched into a sun-synchronous orbit with an altitude of 480 km on 6 November 2020 on board a Long March 6 rocket. The satellite started operating the propulsion system from December 2020 and up until 28 February 2021 the system performed a total of 11 firings. A summary of the maneuvers is shown in table 5.1, where the code FS represents the fail-safe mode, and N1 is the nominal firing mode. The firings 1A and 1B consisted of operations to check the system's overall health after launch. Then, the subsequent firings (from 2A to 2I) were nominal, consisting of 80 to 90-minute maneuvers, including a 10-20 minute startup time to initialize the system and heat up the iodine propellant. These maneuvers generated a change in the orbital semi-major axis, Δa, between 200 and 400 m. The table shows the estimation of the altitude change using two different methods, a simulation using the GMAT software and the data from the Space Surveillance Network (SSN) operated by the US Space Command. It is possible to see that the estimations done with both methods agree quite well. During the nominal firings, the system was set to generate 0.8 mN of thrust and consumed a total power of 55 W on average.

Figure 5.38 shows the change in the semi-major axis of the satellite over the period of time, where the arrows show the initial time of each maneuver. The figure shows the estimation of the altitude using four different methods: the GMAT simulation based on the predicted planned maneuver profile; the onboard GPS data; the SSN data available online; and an analytical prediction based on simplified orbital dynamics theory. As shown in the figure, all prediction methods show excellent agreement, which also confirms that the thruster is indeed producing the thrust estimated by the current measurements in the last section. It is possible to observe that the semi-major axis continuously decreases as time evolves, resulting from the atmospheric drag present at low orbits. Nevertheless, it is shown that the operation of the thruster can compensate for this atmospheric drag, raising the satellite's orbit back to its original state. As shown, all the maneuvers except

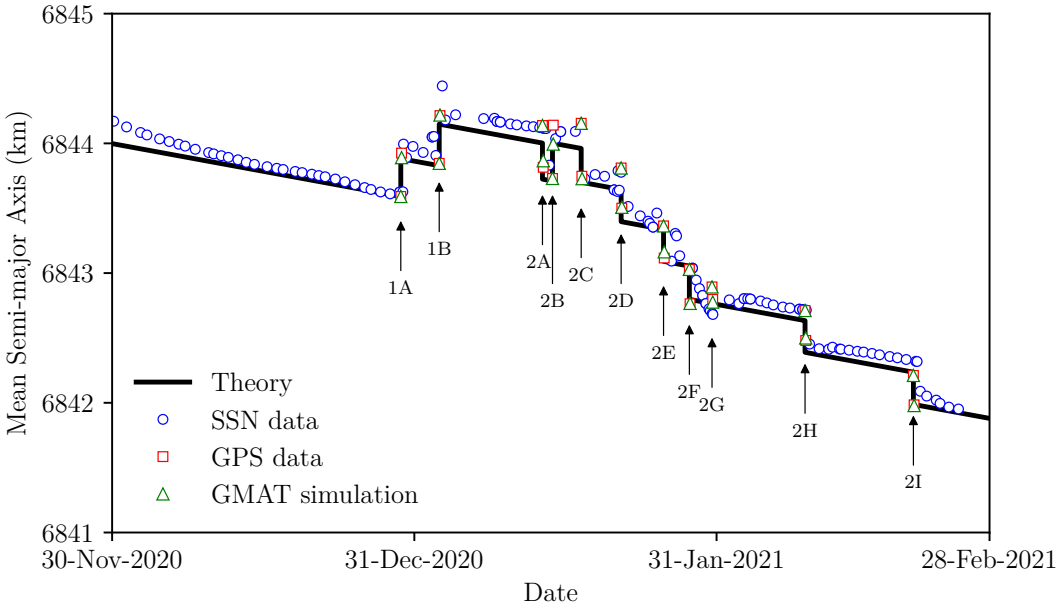

Figure 5.38: Mean semi-major axis of the Beihangkongshi-1 satellite for each of the maneuvers. The data is obtained from the Space Surveillance Network (SSN), GPS data, and compared with the prediction from numerical simulations and theory (adapted from Ref. [135]).

for 1A, 1B, and 2B were in the retrograde direction, decreasing the satellite's orbital altitude.

CHAPTER 6

CHARACTERIZATION OF ION THRUSTER USING RF GRID BIASING

This chapter presents the results of the experiments with the ion thruster using RF grid biasing. In the first part of the chapter, a review of the results from previous experimental works available in the literature is presented, giving an initial background to the experimental investigation done in the context of this work. In the second part, the details of the experiments are presented, showing measurements of different parameters focusing mainly on the operational differences when using two distinct acceleration frequencies. The experiments here are compared to both previous data and the predictions done by the simulation performed in chapter 2.

6.1 Previous experiments

The coincident acceleration of ions and electrons through a grid system using RF biasing was first proposed by Dudin and Rafalskyi [177] based on asymmetric CCP discharges that form self-bias voltages and accelerate particles towards one of the electrodes. In their system, an ICP discharge was used to produce an argon plasma, an electrode is placed within ICP discharge, and a single grid is used to accelerate the particles. A high-voltage RF bias is applied between these two electrodes, forming a high-voltage sheath capable of accelerating both ions and electrons through the orifices of the grid. The authors tested this concept using the same frequency, of 13.56 MHz, for both the plasma generation and the acceleration, and with an amplitude of acceleration voltage from 0 to 200 V. The authors measured the ion energy distribution function with a gridded energy analyzer, demonstrating that ions were successfully accelerated, and showed that the beam is correctly neutralized. However, the source could not be operated at higher voltage amplitudes than 300 V, and because the source uses only one grid, the ion beam is not focused, generating sputtering erosion of the grid and electrodes, making the concept unfeasible for propulsion applications.

Based on the single-grid design, Rafalskyi and Aanesland [62] more recently proposed the utilization of the RF biasing technique on a GIT-like architecture, as described in chapters 1 and 2. In their work, the authors use a rectangular thruster with two grids and a planar coil to generate an ICP discharge based on argon. A single RF generator

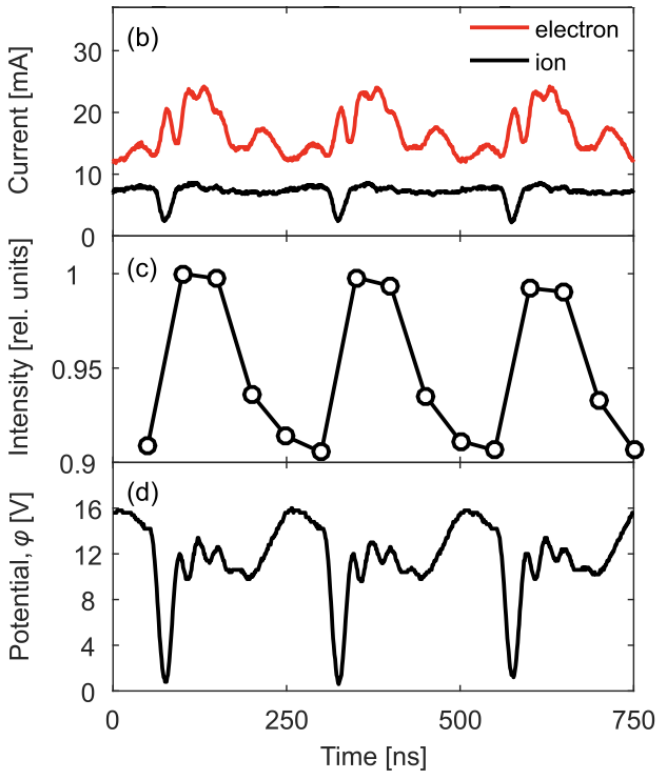

Figure 6.1: Measurement of ion and electron flux (b), emission intensity (c) and plume potential (d) during RF acceleration (source: [67]).

powers both the ICP and the acceleration grids at a frequency of 4 MHz. The amplitude of the RF acceleration signal is varied between 0 and 350 V, and, for reference, the thruster is also operated with DC grid biasing for acceleration voltages in the same range. In the studied range, the authors successfully demonstrated the formation of a DC self-bias, which increases linearly with the amplitude of the RF signal, as $V_{sb} \approx 0.78 V_{RF}$. Comparing the current extraction in the DC and RF cases, the authors show that in both cases, the magnitude is similar for a given DC bias voltage, however around 30 % higher in the RF case. For both the DC and RF case, the plasma potential measured in the plume varied roughly from 10 V to 20 V.

The RF biasing was also studied by Rafalskyi and Aanesland [65] using the same device in similar conditions, but this time focusing on characterizing the anisotropy of the ion and electron beam and the spatial variation of plasma potential across the plume. Using an RFEA oriented either perpendicular or parallel to the beam, the authors measured the electron energy distribution in these two directions. Their measurements show that, in the RF case, the electrons were considerably more energetic in the axial direction presenting an important anisotropic component, which is consistent with the modeling done by Lafleur and Rafalskyi [66]. The plume potential was measured using a movable emissive probe, which was displaced in the radial direction of the plume. Their

data show very similar values of plume potential between the DC and RF cases, with a peak at about 25 V on the axis of the beam. Lastly, measurements of the flux of electrons were done in the parallel and perpendicular directions of the beam. The data shows that in the RF case there is a much higher flux anisotropy when compared to the typical DC case, with a considerably higher flux of electrons in the axial direction than in the radial direction.

The work by Dedrick *et al.* [67] focuses on time-resolved measurements of plume properties during RF biasing. The authors use the same thruster from refs. [62, 65], operating under similar conditions, and use a phase-resolved optical emission spectroscopy apparatus to study the propagation of electrons through the plume during the acceleration process. The spectroscopic study shows a clear appearance of a pulsed electron beam in the RF case with energy higher than 13 eV. The authors also measure the time-resolved ion and electron flux with a planar probe, and the plume potential. The measurements are displayed in figure 6.1 and show similar behavior with what was seen in the simulations done in chapter 2. As in the simulations, it is possible to see that the electron current does not present a single peak in phase with the injection, but rather several higher frequency oscillations. Furthermore, it can also be seen that the oscillation profile of the plume potential over time shows a very similar shape to the time variation of the axial potential shown in figure 2.22, especially at the farthest sheath location, which mimics better the situation found in the experiments.

Lastly, Rafalskyi and Aanesland [64] present a preliminary study of a thruster prototype similar to an NPT30, which uses xenon for the first time while using the RF grid biasing technique. The authors demonstrate the direct measurement of thrust produced with the RF acceleration.

Theoretical works and discussions have also been published on the relation of the performance with different operational parameters and the limitations of the concept. In the work by Lafleur *et al.* [68], through a numerical and analytical approach, the authors confirm the existence of a frequency threshold for correct operation of the system. Lafleur [178] performs an theoretical study of the space-charge limitation of the current extracted in RF biased electrodes with a DC self-bias. The author shows that the frequency and the initial particle velocity have a very important impact on maximum current extracted by the system serving as further support for the selection of adequate parameters for operation. It is shown that, when the particle transit time is much longer than the applied RF period, the current limit approaches the value of a DC system, and, as the frequency decreases, the current transmission is significantly decreased down to a case where the voltage across the electrodes have no influence anymore on efficient, focused, particle extraction. Finally, Fu and Ding [179] presents a discussion on the main problems and limitations of thrusters using RF grid biasing, connected mainly with the power loss due to electron backstreaming acceleration, and incompatibility of the frequency ranges used for acceleration and plasma production which may lead to the need for further RF generation equipment on a future flight device.

6.2 Results

As described in chapter 3, the RF biasing experiments were done using a prototype based on a modified NPT30 using xenon and connected to an external RF power supply. The main objective of the experiment was to study the thruster working at a high-frequency regime, above the frequency threshold determined by equation 1.65, which is different from past experiments. The primary frequency used is 17.6 MHz, and the thruster is also operated with a low-frequency mode, at 8.3 MHz, for comparison. The study focuses on verifying the plume and performance characteristics as the acceleration signal amplitude is changed. During all measurements, the thruster was operated with a fixed xenon mass flow rate of 0.15 mg/s. The mass flow rate used had to be considerably higher in this case because the modifications on the structure and circuit of the thruster decreased the RF power deposition in the plasma making it less stable and requiring a higher mass flow rate to operate at a similar operational point to the DC version. During all experiments, the thruster is operated constantly at 11 W of RF power, which generates between 8 mA and 11 mA of total ion beam current depending on the acceleration voltage. The ion beam current was estimated using a planar probe on a few operational points and compared to the values obtained during the DC experiments.

To generate the high-voltage signal on the grids, it was necessary to impedance matching the RF generator and the acceleration grids by selecting a proper tuning inductor for the operational frequencies selected. As in a typical RF circuit, impedance matching is required to maximize the power transfer from the RF power source to the load, which in this case is the grid set, and minimize the reflected power to the source. The matching is done by approaching as closely as possible the real part of the impedance of the load (resistance) to that of the source, while approaching the imaginary part of the impedance (reactance) to that of the source but with an opposite sign so that they effectively cancel out. In the matching circuit topology used here, similar to a "pi matching network", the value of the inductor is used to control the final impedance of the circuit and do the proper matching. A VNA was used to read the RF response of the signal and select the inductor that approaches the resonance peak of the circuit closer to the required range. The inductance of the tuning coil used for the high-frequency mode is 0.9 µH and the low-frequency mode, 4 µH. Figures 6.2 and 6.3 show the impedance response of the circuit using the coils measured with the VNA. It is possible to see that the peak of each curve has a slight offset from the nominal frequency at each mode, which is indicated by the vertical dashed lines; however, it is worth mentioning that when the RF amplifier is connected to the thruster, the impedance of the system changes. To verify the resonance frequency at the moment of operation, a frequency sweep is done with the amplifier while measuring the amplitude of the generated wave.

To test the effective formation of the self-bias at the grids, the screen grid was excited with an RF signal in bursts of approximately 1.5 ms, with a period of 100 ms. This enabled the test of the thruster without the risk of overheating the system due to thermal dissipation at the matching circuit and the grids. Figure 6.4 shows the value of the screen grid voltage during one of these bursts, where the applied voltage amplitude is roughly

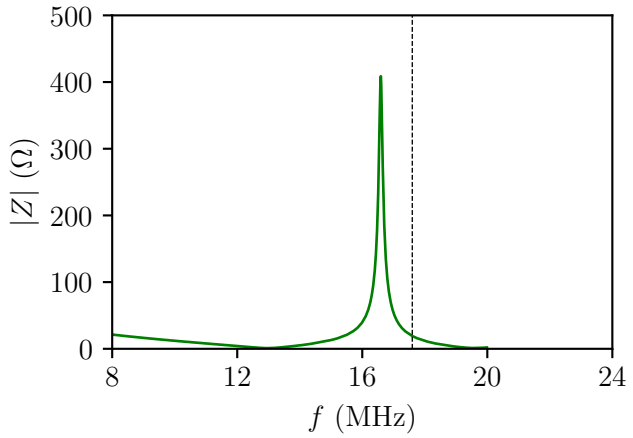

Figure 6.2: RF response of the circuit using the high-frequency coil. The vertical dashed line indicates the resonance frequency during the experiments, $f = 17.6\,\mathrm{MHz}$.

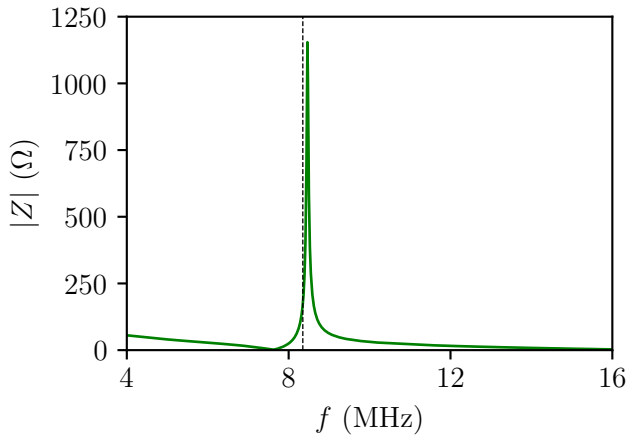

Figure 6.3: RF response of the circuit using the low-frequency coil. The vertical dashed line indicates the resonance frequency during the experiments, $f = 8.3\,\mathrm{MHz}$.

438 V. It is possible to see that when the signal starts, the screen grid voltage starts its oscillation around zero, which is expected since the bias capacitor is not charged. As time evolves and the capacitor is charged, the average value of the oscillation increases until it reaches steady-state. In this case, steady-state is achieved in roughly 0.25 ms. When the RF signal is turned off, the screen voltage gradually decreases back from the self-bias voltage to zero. The dashed line shows the average value of the voltage during steady-state, which corresponds to the self-bias voltage that effectively accelerates the ions. The empirical approximation, $V_{sb} \approx 0.78 V_{RF}$, used to estimate the self-bias voltage

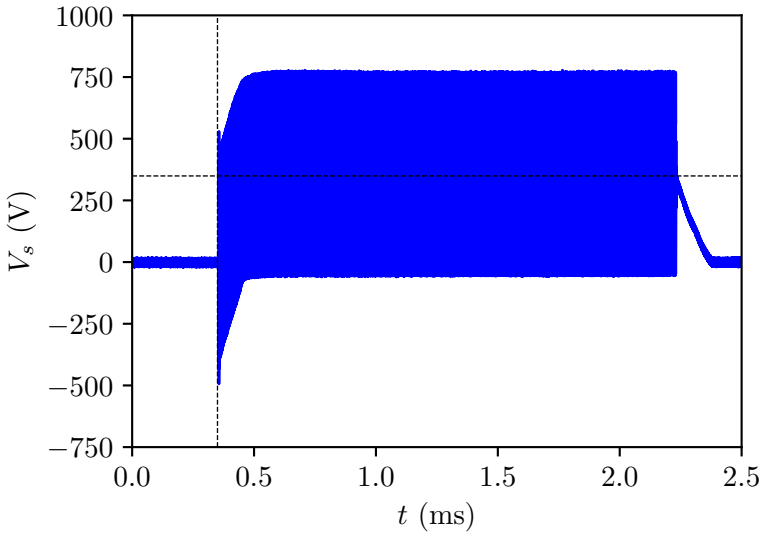

Figure 6.4: Screen grid voltage as a function of the time during the formation of the self-bias. The horizontal dashed line shows the average voltage at steady-state. The vertical dashed line shows the time instant where the screen grid signal is switched on.

[65] gives $V_{sb} \approx 341.25\,\text{V}$ which is quite close to the average voltage calculated from the data, 349.14 V, showing that the self-bias is well-formed and the behavior is close to what was seen in previous works. It is important to note that the empirical approximation used is typically what is found in very asymmetrical CCPs, and it does not necessarily agree with what is estimated by equation 1.64, which gives $V_{sb} \approx V_{RF}$. This happens because the theoretical model only considers current flowing between the two electrodes, however, in an actual system, part of the RF current may flow through several components including the ICP plasma and the ceramic discharge chamber towards the antenna and other grounded surfaces, which makes the system behave more like an asymmetric CCP. The simulations done by Lafleur *et al.* [68] confirm the theoretical prediction of $V_{sb} \approx V_{RF}$, however this happens because in their model (as in the theory) does not account for RF currents flowing through the ICP plasma and to surrounding conductors. The burst mode used here is adequate for verifying the system, however this method cannot be used to study the plume since there can be several transient processes during its formation and propagation within the chamber that may take up to a few seconds. Therefore, for all the following measurements done here, a continuous acceleration mode was used to allow the proper formation of the plume within the chamber.

Figure 6.5 shows the detail of the screen grid voltage oscillation during steady-state. The figure shows the oscillation for the two frequencies used and similar voltage amplitude values. It is possible to see that the voltage oscillates with an offset from zero, corresponding to the self-bias voltage. At the lower point, the oscillations cross the zero line and become negative, which is the point when electrons escape the ICP plasma and

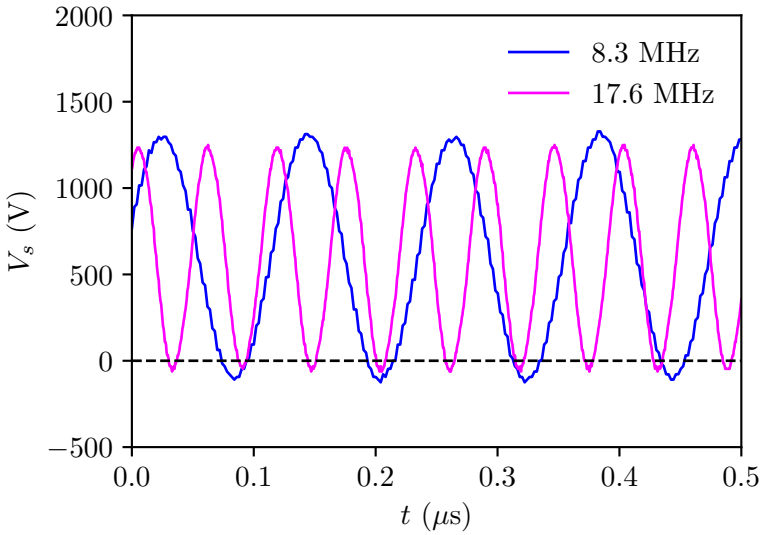

Figure 6.5: Screen grid voltage as a function of time during steady-state for the two different frequencies used.

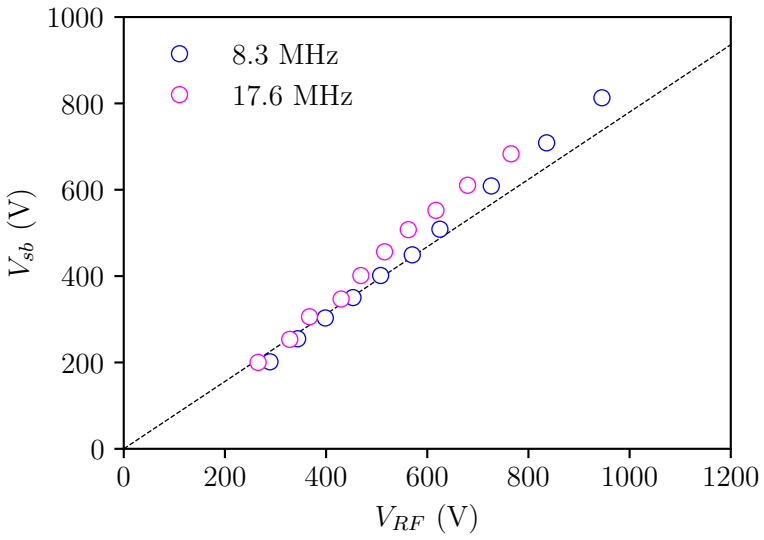

Figure 6.6: Self-bias voltage as a function of the RF voltage amplitude. The dashed line shows the function $V_{sb} = 0.78 V_{RF}$.

are injected into the plume. An interesting aspect is that, as predicted by theory, the formation of the self-bias in the experiments is not significantly affected by the frequency of the voltage waveform applied to the grids, depending primarily on the amplitude of

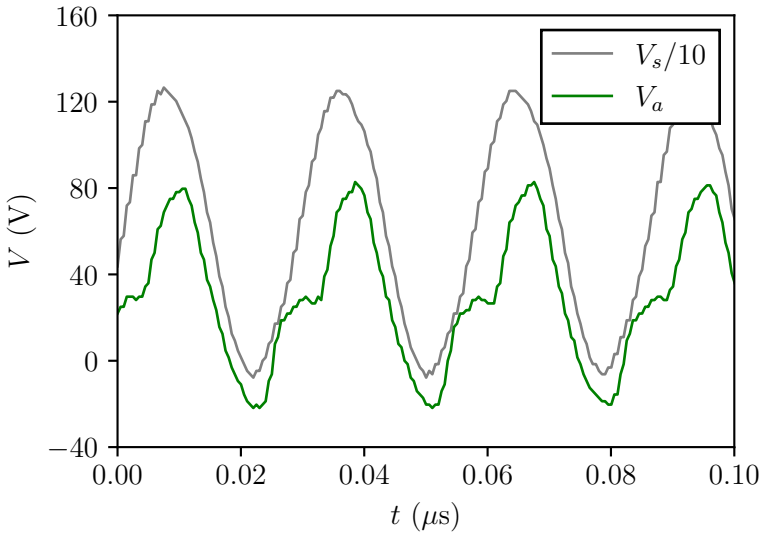

Figure 6.7: Oscillation of the accel grid, V_a, and screen grid, V_s, voltages as a function of time in the high-frequency mode.

the RF signal used. This can be seen in figure 6.6 which shows the measurement of the self-bias voltage as a function of the RF voltage amplitude at the screen grid. The dashed line shows the relation $V_{sb} = 0.78V_{RF}$. As shown, the data for both frequencies increases proportionally with the RF voltage amplitude, closely following the dashed line. After a certain amplitude, the self-bias starts to deviate above the dashed line slightly. This difference is not significant and might be related to the specific experimental condition used here, including the different capacitive connections in the cables and mechanical structure. The voltage amplitude used in the experiments varied between 200 V and roughly 1000 V, and was limited mainly because of excessive power consumption and instabilities in the discharge. Furthermore, not all data points could be recorded because of these instabilities.

As explained in chapter 3, in the present experiments, the thruster's accel grid is connected to ground through a capacitor, thus becoming electrically floating. Figure 6.7 shows the oscillation of its voltage during the RF cycle, in the high-frequency mode and for $V_{RF} \approx 600$ V, showing as well the voltage at the screen grid for reference. It is possible to observe that the oscillation follows the oscillation of the screen grid with the same phase and varies, at this operational point, between -20 and 80 V, with an average value of 28 V. Figure 6.8 shows the oscillation of the accel grid voltage in the low-frequency mode, also for $V_{RF} \approx 600$ V. In contrast to the high-frequency mode, here the average value is negative with a value of -19.89 V, oscillating roughly between -9 V and -34 V. In this case, the profile of the oscillation is less well-formed, however, it is possible to see similar behavior in the two modes, with the curve following the trend of the screen grid voltage and presenting higher frequency features that are most probably

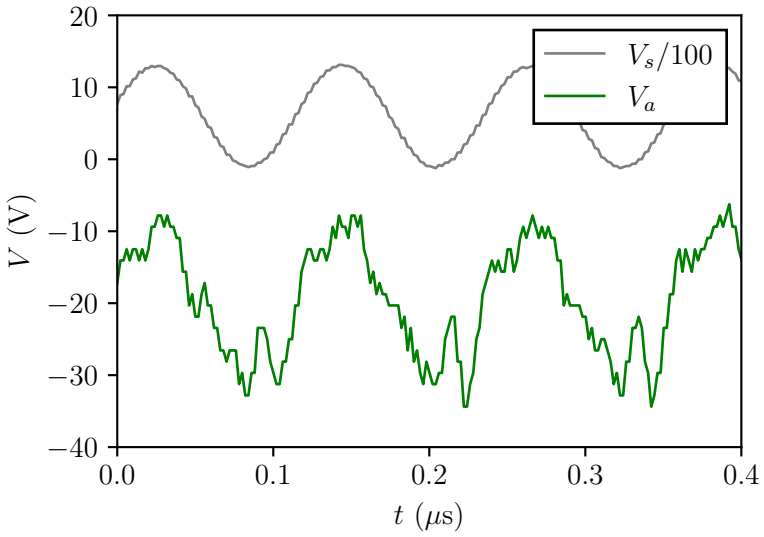

Figure 6.8: Oscillation of the accel grid, V_a, and screen grid, V_s, voltages as a function of time in the low-frequency mode.

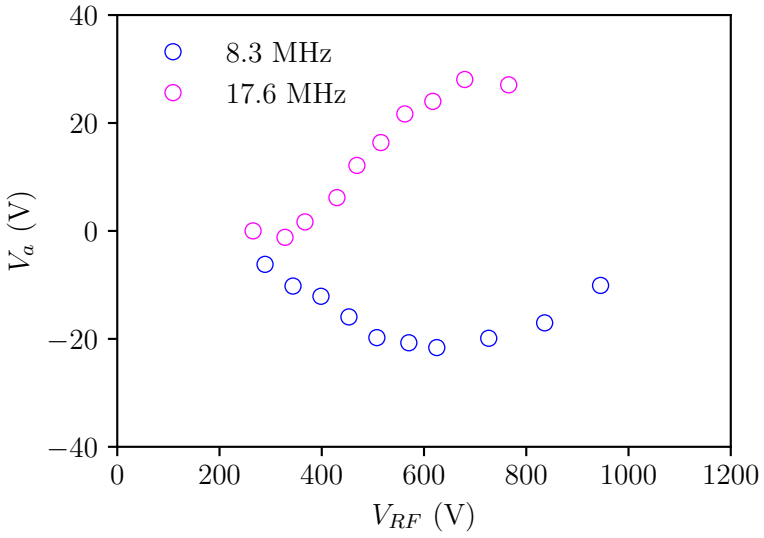

Figure 6.9: Average accel grid voltage as a function of the RF voltage amplitude for the two acceleration frequencies used.

related to the dynamics of the particles during acceleration. The general trend of the average accel grid voltage as a function of the RF signal amplitude for both frequency modes can be seen in figure 6.9. In the high-frequency mode, the average accel grid

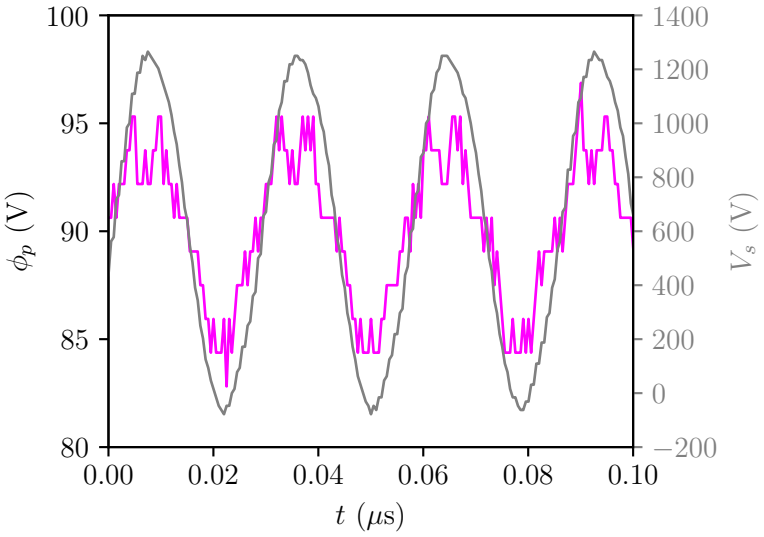

Figure 6.10: Measurement of the time-resolved plume potential with the emissive probe in the high-frequency mode.

voltage presents an increasing trend going from 0 V up to roughly 30 V. On the other hand, in the low-frequency mode, the average voltage varies roughly between −6 V and −20 V showing a minimum point close to $V_{RF} \approx 600$ V. The change in polarity of the accel grid voltage between both modes can be related to the simulation study performed in chapter 2. In figure 2.24 it is shown that the average boundary potential decreases as the frequency is increased. If one considered instead that the boundary is the electrical reference, being grounded, and left the accel grid floating, the average voltage of the potential of the accel grid, in this case, would decrease and go to negative values as the frequency decreases and go to positive values as the frequency increases, which is what is observed in the experiments. Therefore, this change in the voltage can be caused by a change in the average charge accumulated during a cycle that changes to guarantee equal currents to the grid on average.

The plasma plume potential was measured using an emissive probe placed at 4 cm from the exit plane of the thruster and 5 cm from the beam centerline. The probe is operated in the floating mode, and a lithium-ion battery provides its heating current to avoid degradation of the signal due to RF current going through an external power supply. The measurement of the plume potential, ϕ_p, as a function of time in the high-frequency is shown in figure 6.10. It is possible to see that the potential follows a similar trend to the screen grid voltage varying from 85 V to 95 V, with an average value of 89 V. The high value of the plume potential was also observed in the plume simulations performed in chapter 2. This is most probably caused by the high-energy electron population in the plume, which obtains energy during their pulsed injection. Figure 6.11 shows the measurement of the plume potential for the low-frequency mode. The potential in this

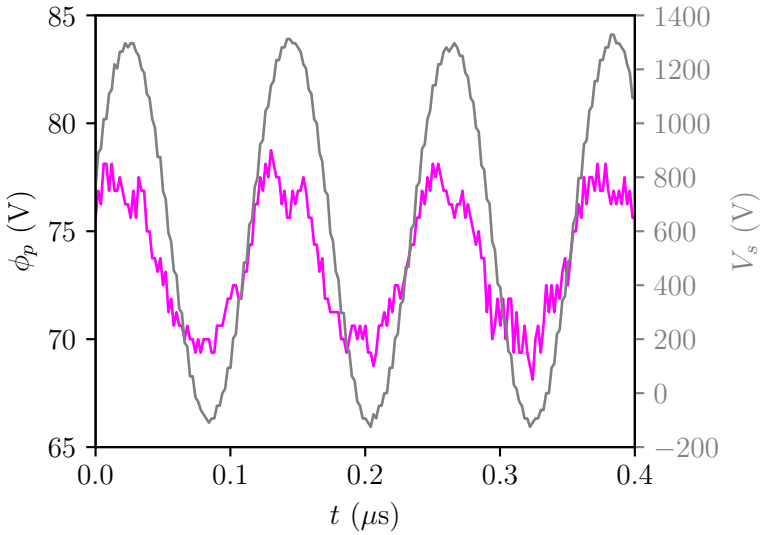

Figure 6.11: Measurement of the time-resolved plume potential with the emissive probe in the low-frequency mode.

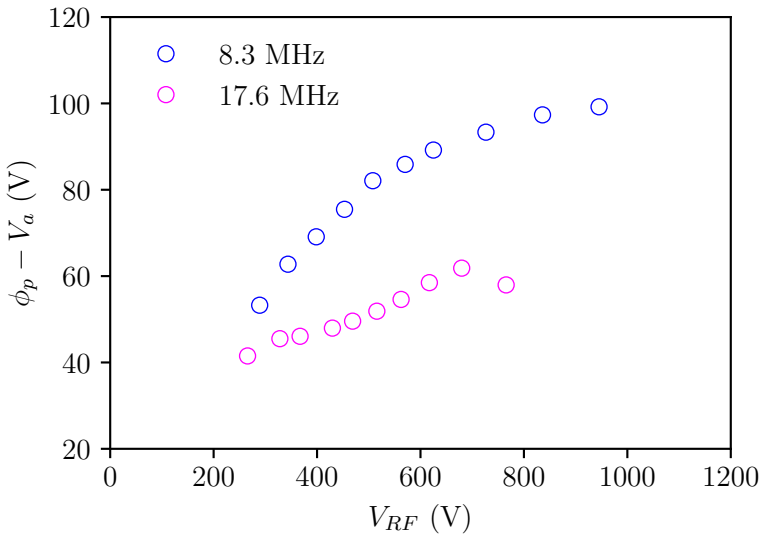

Figure 6.12: Average plume potential, ϕ_p, in relation to the accel grid voltage for both modes.

case varies between roughly 70 V and 77 V, with an average value of 73 V. To be able to compare the plasma potential with the plume simulation results, it is necessary again to change the electrical reference of the system, subtracting the value of the accel grid

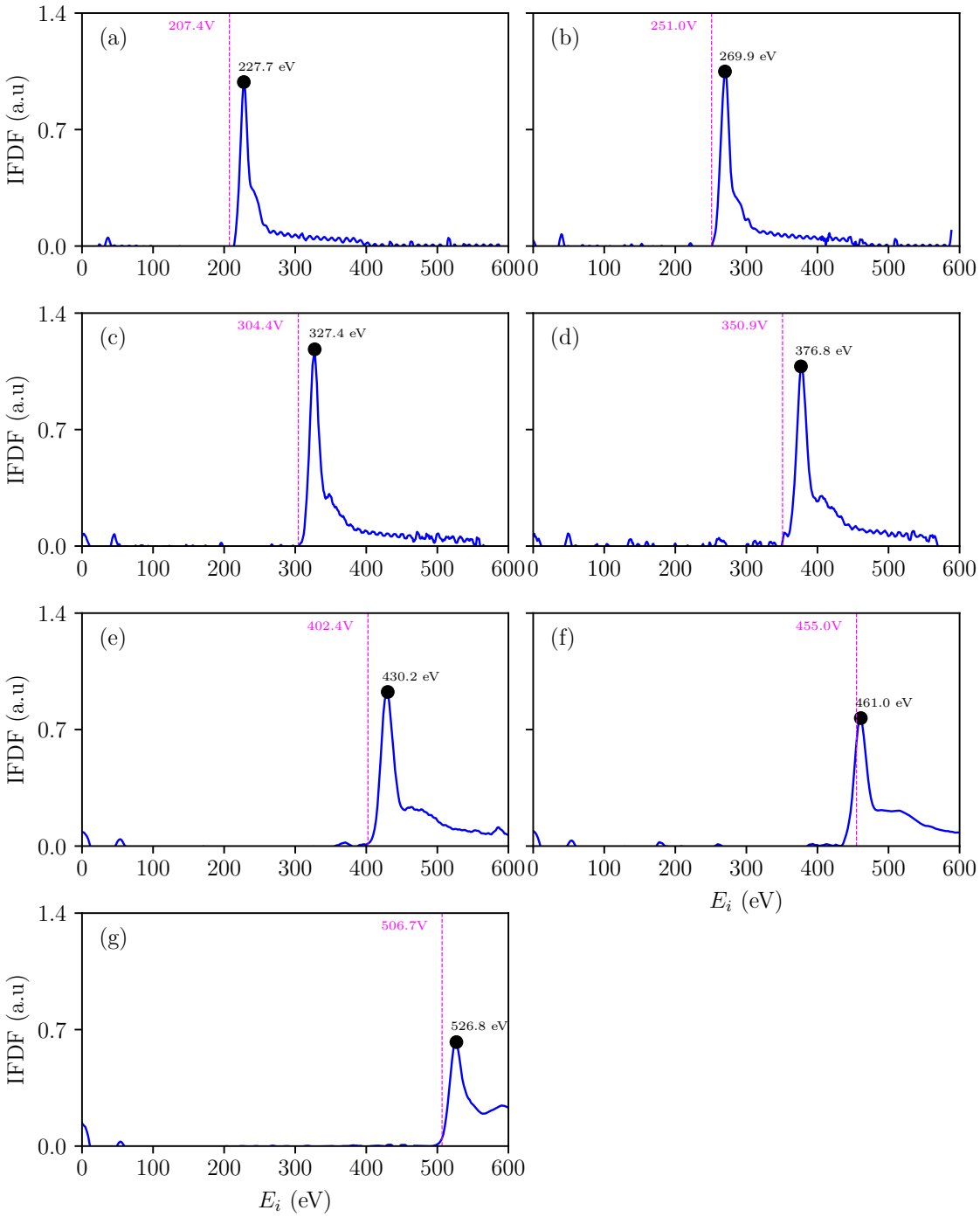

Figure 6.13: Measurement of the ion flux distribution function in the high-frequency mode.

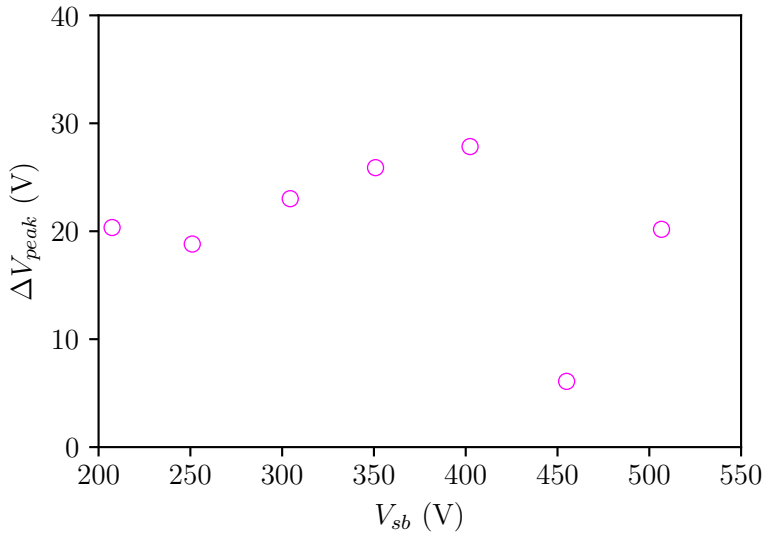

Figure 6.14: Difference between peak and self-bias voltage of the RFEA measurements.

voltage from the measured potential. Figure 6.12 shows the value of the average plume potential with respect to the accel grid. It is possible to observe that the plume potential in both modes increases as the amplitude of the RF signal increases. In the low-frequency case, the potential varies from roughly 50 V up to 100 V, while in the high-frequency mode, it varies from about 40 V to 60 V. This difference in the plume potential can also be observed in the simulation results, with a decreasing trend of the potential as the frequency increases shown in figure 2.24. Besides the more elevated electron temperature, the higher plume potential in the low-frequency case may also suggest a worse plume neutralization. The exact cause of this decrease in the neutralization quality is complex, however it may be connected to the higher period of positive charge accumulation during the RF cycle due to a longer interval between electron pulses. In this way, this higher charging time can increase the value of the average plasma plume potential.

To verify acceleration of ions through the grids, the energy of the ion beam was measured in the high-frequency mode using an RFEA for seven values of V_{RF}. To decrease the influence of the RF component of the signal, the RFEA signal was measured 64 times and averaged for each of the cases. Figure 6.13 show the results of the measurements, where the dashed line shows the value of the self-bias voltage at that given operational point, and the dot shows the value of the peak of the distribution. One can see that all measurements indeed show a sharp peak close to the value of the self-bias voltage, suggesting that the acceleration of ions is occurring as expected. The more pronounced tail on the RHS of the peak is most likely related to the fact that although the average ion acceleration voltage is $V_{sb} = 0.78 V_{RF}$, the maximum voltage of the acceleration waveform is as high as $V_{sb} + V_{RF}$. Thus, one may expect some higher energy ions depending on when in the RF cycle they enter the grids. This high-energy tail can also be seen in grid

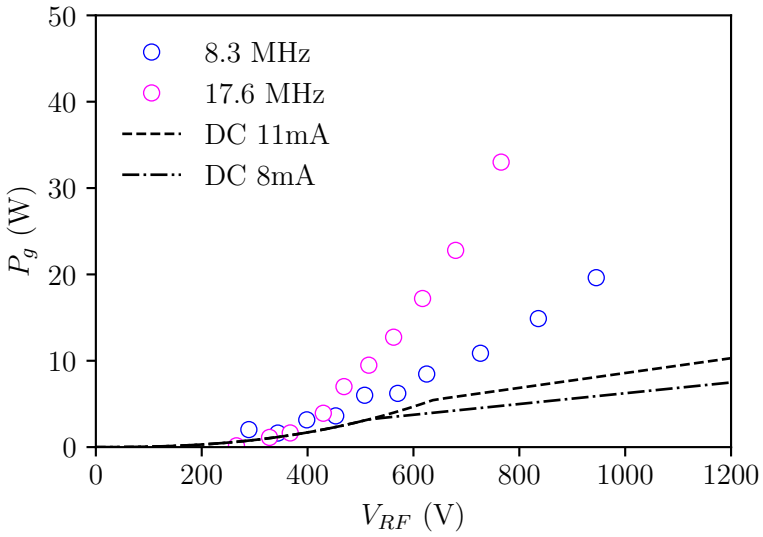

Figure 6.15: RF acceleration power as a function of the RF wave amplitude. The dashed lines show the power consumed by a DC thruster, $P = I_b V_s$, to accelerate a beam of 8 mA and 11 mA.

RF biasing simulations of ref. [68] for frequencies roughly from 10 MHz to 20 MHz. In the context of this phase-dependent acceleration, the maximum expected ion energy is roughly $\sim 2V_{RF}$. In an analogous way to the DC case, shown in figure 5.7, it is also possible to see that in all cases, the peak of the distribution stays slightly above the self-bias voltage. This can be a consequence of the average ICP plasma potential and further acceleration by the sheath of the RFEA. The voltage difference, $\Delta V_{peak} = V_{peak} - V_{sb}$, is shown in figure 6.14. For almost all operational points, the difference stays roughly between 18 V and 28 V, apart from an outlier point that shows a difference of approximately 5 V. Even with very different dynamics, the voltage difference is similar to what was found in the DC case, suggesting that this effect might be indeed more connected to the ICP discharge rather than the plume physics. This agrees with what is expected from a typical ICP with an electron temperature of 4-5 eV, which would generate a sheath in front of the screen grid with a magnitude of the order of $\Delta\phi_f \approx 5T_e \approx 20$ V.

Another important aspect of these experiments is to estimate the performance of the RF acceleration process and the prototype so that it can be compared to previous experiments and the simulations. This is done here by measuring the RF power consumed by the amplifier during each test. The forward and reflected RF power were read from a meter on the amplifier itself and subtracted to obtain the net absorbed power. Figure 6.15 shows the acceleration power as a function of the RF wave amplitude for both frequency modes. It is important to note, however, that the matching circuit dissipates a non-negligible amount of power during operation. This power loss, which is not of interest to the current experiments since they are very sensitive to the specific circuit

design used, may be mitigated with proper optimization, and therefore does not provide direct information on the physics of the RF acceleration. Therefore, the power values shown in the plot were obtained by subtracting off the power consumption measured during operation with no plasma at the same V_{RF} values. As one can observe, the acceleration power measured goes up to 32 W for the high-frequency mode and 21 W in the low-frequency mode. Between 200 and 400 V, it is possible to see that the power approaches zero in both modes, which is most probably an effect of the higher uncertainty of the power measurement in lower power ranges, of the order of 2 W to 5 W for the RF amplifier used. It is possible to see that the power consumption increases monotonically as the amplitude and the self-bias voltage increase, which is expected, since the power required to generate an ion beam with a given current is roughly proportional to the average acceleration energy. To study the performance of the system in comparison with a typical DC ion thruster, it is possible to compare its power consumption with the power required to produce a similar ion beam current with DC acceleration. The beam power in a DC system is given roughly by $P_b = I_b V_s$. However, because of the space-charge current limitation expressed by equation 1.34, this equation is only valid as long as

$$V_s > \left(\frac{I_b}{\frac{4}{9}\varepsilon_0 \frac{A_i}{L_{\text{eff}}^2} \sqrt{\frac{2e}{m_i}}} \right)^{2/3} \tag{6.1}$$

where the accel grid voltage is assumed to be zero and A_i is the exit area of ions. Therefore, the DC beam power is assumed to be $P_b \approx I_b V_s$ when the condition 6.1 is satisfied, and given by $P_{b,CL} \approx I_{b,CL} V_s$ otherwise, where $I_{b,CL}$ is the space charge limited current at the voltage V_s. Using equation 1.34, the power at the space-charge limited regime is given by

$$P_{b,CL} \approx \frac{4}{9}\varepsilon_0 \frac{A_i}{L_{\text{eff}}^2} \sqrt{\frac{2e}{m_i}} V_s^{5/2} \tag{6.2}$$

Using this piecewise approximation, and assuming that $V_s \approx V_{sb}$, the power of the DC beam is plotted in figure 6.15 for two different values of ion beam current, 8 mA and 11 mA, which represent lower and upper bounds for this experiment as determined previously. The resulting DC power curves, in general, follow an increasing monotonic behavior, and close to a voltage roughly between 500-600 V, the power consumption changes its regime, and the curve profile moves from a polynomial to a linear function as expected. It is possible to observe that despite presenting a considerably lower value when compared to the RF power measured, the behavior, especially at the space-charge limited regime, presents very similar trends. The rapid decrease of the beam power due to the limitation of the emitted ion beam current can be one of the explanations on why the measured RF power decreases to very low values at low acceleration amplitudes. This provides evidence that the space charge limitation works similarly to a typical DC thruster and is consistent with the general behavior predicted by theoretical works [178]. The considerably higher power loss in the RF case is interesting and expected to mainly be connected to the electron backstreaming current and other losses, such the capacitive coupling of the ICP discharge to the structure and antenna of the device.

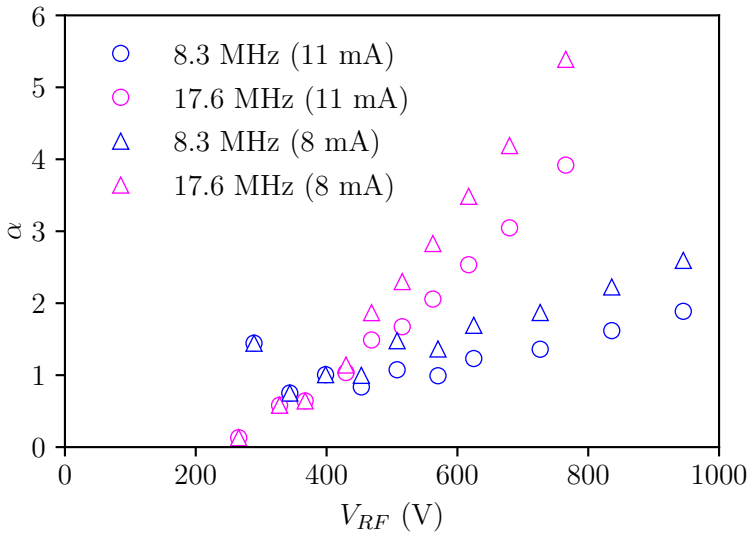

Figure 6.16: Estimation of the electron-to-ion current ratio, α, considering a 8 mA and 11 mA ion beam current.

The electron dynamics during the RF grid biasing acceleration is a complex process. As discussed by Fu and Ding [179], one of the most significant issues of the RF grid biasing technique is that besides the outwards electron pulse, backstreaming electrons that arrive at the grid at a specific moment in the RF cycle might also be accelerated by the high-voltage signal but in the backward direction, which can generate substantial power losses. This, in fact, can be one of the main components for the high power losses when compared to the DC thruster as observed in figure 6.15 – on the other hand, it is important to note that DC thrusters must provide extra power to the neutralizer, which is not accounted here. There is clear evidence of this high-voltage backstreaming current in previously detailed grid simulations [66, 68], and also in the plume simulations done in the context of this work as shown in figure 2.19. As in the plume model developed in chapter 2, it is expected that, if an average electron current $\langle I_e \rangle = \alpha I_b$ is injected into the plume, there must be a current $\langle I_{e,b} \rangle \approx (\alpha - 1) I_b$ that flows back to the thruster in order to maintain the current-free condition. This is seen in the simulation results of the average current flowing to the boundaries in the steady-state, shown in figure 2.17. Electrons flowing back to the thruster generally enter the grid orifices due to the higher local potential and are accelerated by the screen grid voltage back into the ICP source. Because of the high mobility of electrons and their very short transit time between the grids, they are not influenced by the oscillation of the acceleration voltage but, in fact, will roughly feel a constant electric field between the grids. As the voltage is constantly oscillating, it is expected that, on average, the backstreaming electrons will experience a backward acceleration voltage of approximately V_{sb}. In this way, one can expect that the

average power consumed by the backstreaming electron current is given by

$$P_{b,e} \approx \langle I_{e,b} \rangle V_{sb} \approx (\alpha - 1) I_b V_{sb} \tag{6.3}$$

Thus, the total power consumed by the acceleration system, accounting for the ion beam power and the backstreaming electron power loss, can be estimated as

$$P_b \approx (\alpha - 1) I_b V_{sb} + I_b V_{sb} = \alpha I_b V_{sb} \tag{6.4}$$

Comparing equation 6.4 to the DC beam power (and assuming that the RF space-charge limited current is similar), it is possible to see that in this approximation their ratio gives an estimation of the magnitude of the injected electron current, $\alpha \approx P_b / P_{b,DC}$. Using this formulation, the ratio is estimated and shown in 6.16. The calculation used the RF experimental data and considered the two ion beam current limits of 8 mA and 11 mA so that the estimation is done for the complete operational range. As one can see, apart from an outlier point, the major part of the α values varies roughly between 1 and 5.5 for the high-frequency mode and 1 and 2.5 in the low-frequency one. This represents some of the first experimental estimations of the actual electron-to-ion current ratio extracted during the operation of an RF-biased device. However, in contrast to the numerical plume model of chapter 2, α is not a controllable parameter in the experiments and is self-consistently adjusted by the operational conditions in order to maintain a quasi-neutral plume. It is interesting to note that the range of values is very similar to what was observed in previous grid simulations [66], where the authors estimated the electron-to-ion current to be of the order of 2.5, and is also close to the values selected for the plume simulations done here. The higher values observed here, especially in the high-frequency mode, might be related to an overestimation due to additional power loss mechanisms not connected to electron backstreaming that were not considered for this first approximation. As observed previously in simulation and theoretical discussions, for the neutralization to happen properly in the RF case, the thruster necessarily has to eject an average electron current which is considerably higher in magnitude compared to the ion current. An electron current equivalent to the ion current flows away with the ion beam and the electron surplus is reflected back to the source. It is worth noting that this is also the case when using an external electron source, such as a hot filament, where the emitted current must be considerably higher than the ion beam current as shown by equation 2.25. In the DC case, for $T_e \approx 5\,\text{eV}$ and $E_i \approx 1\,\text{keV}$, the current ratio would be roughly $\alpha \approx 9.6$. The power loss in this case is avoided by using a negatively biased accel grid voltage which reflects electrons and prevents them from entering the grids, which is not the case in the RF acceleration device. Furthermore, it is also important to note that the operational points that present $\alpha \lesssim 1$ do not necessarily represent a realistic estimation of the actual electron current magnitude since the precision of measurements decreases at low powers. These estimations serve as strong confirmation that the electron dynamics predicted by the theoretical and numerical models successfully reproduce what is seen in actual devices, which is an important step forward in understanding the physics and operation of these RF biased sources.

Two important points are demonstrated through the RF acceleration experiments done in the context of this work. The first is that the thruster using RF grid biasing was successfully operated using the highest values of frequency and self-bias voltage to date, which is considerably closer to realistic parameters of interest than previous works. The measurements of the accel grid voltage and the plume potential show that, in this operational range, the system can generate a well-neutralized plume without significant instabilities. The determination of the IFDF also gave clear evidence that the ions were successfully accelerated to the predicted energy, close to V_{sb}. The second important point is that the data showed a clear correlation between experiment and the theoretical and numerical predictions. The high-voltage plume potential values measured here, roughly 40 V to 100 V, are similar to what is seen in previous grid simulations and also to the plume simulations done in chapter 2, which may be a piece of evidence that the average electron energy has a much higher value than the DC case as predicted by theory and simulations. This higher plume potential is also necessary for the operation of the RF biased source, because the plume potential needs to be high enough to trap some electrons within the plume to ensure charge compensation, and prevent complete backstreaming of all electrons through the grids back into the ICP source. It was also verified that the average plume potential is considerably higher in the low-frequency mode when compared to the high-frequency case. This confirms the observations done in chapter 2, where it was seen that an increase in frequency in general decreases both electron energy and the plasma plume potential. The electron-to-ion current ratio estimated from the experiments also showed similar values to what was self-consistently determined in previous grid simulations and close to the values used in the plume simulations in this work. The nominal simulation case for the plume study considered $\alpha = 3$, which is similar to the average value measured in the experiments, showing that the numerical model can replicate the physics of the thruster using similar parameters to the actual device. This information is an important factor for possible future theoretical and numerical efforts to determine the self-consistent value of α.

CHAPTER 7

CONCLUSION

The need for miniaturized and efficient space propulsion devices has been increasing in the last decade with the advent of small satellites for complex missions. In this context, plasma-based propulsion, especially ion thrusters, has been gaining more interest due to its capability to enable different orbital maneuvers and significantly increase the lifetime of missions while using a relatively low amount of propellant. Nevertheless, ion thrusters still have technical drawbacks that may hinder a more widespread adoption, especially on low-cost missions. One of the main drawbacks is the traditional usage of xenon as a propellant, a considerably expensive gas that requires high-pressure apparatus for its storage and flow control. This creates engineering challenges, requires a more expensive mechanical design, and typically drives up the launch cost of a mission due to the presence of high-risk elements in the spacecraft. Another of these drawbacks is the need for an external electron source to neutralize the ion beam. The systems typically employed are hollow cathodes or thermionic filaments. The first is typically expensive and susceptible to atmospheric poisoning, requiring special handling, while the latter typically have a short lifetime, limiting the duration of the mission.

In this context, two technological innovations appeared in the last few years to mitigate these bottlenecks. The first is the adoption of iodine as a propellant. Iodine offers several advantages over xenon, namely a lower cost and the fact that it can be stored as a solid at room temperature requiring no high-pressure equipment and allowing a less voluminous design due to its considerably higher density. The second is a technique to co-extract electrons from the inner plasma discharge using a particular RF grid biasing that allows the ions to be accelerated continuously while ejecting electrons in pulses into the plume. In this way, because the grid system extracts enough electrons to neutralize the plume, no external neutralization system is required. However, despite being already proven as feasible, the impact and behavior of the system while using these techniques are still not completely understood. In particular, the plume behavior when using these technologies can have significant differences from a typical plasma plume, possibly impacting its operation or causing unexpected interactions with the surrounding environment and the spacecraft. Therefore, to investigate these unknown points, in this work, the main objective was to study the characteristics of the plume generated by a miniaturized ion thruster when using these technologies and to verify the impact that it might have on

the performance of the system. In the context of iodine, the study is conducted primarily with an experimental approach, while in the RF biasing case, the investigation is divided between a numerical and an experimental part.

In the first chapter, the introduction of the work was presented, highlighting necessary background theory and contextualization. The chapter started by presenting the basic plasma physics used during the text. Then a review of the electric propulsion technology used today was shown, including the basic modeling of a gridded ion thruster, the RF grid biasing technique theory, and lastly, a review of the application of iodine in electric propulsion. In the last part of the chapter, the physics of the plasma plume was presented, showing the fundamental modeling and characteristics of typical plasma plumes generated by ion thrusters.

The second chapter presented the numerical investigation of the plasma plume using RF biasing. This work was published as a peer-reviewed article (Ref. [112]). A new 2D electrostatic particle-in-cell simulation code was developed for this study to enable the utilization of the injection and boundary condition models required to study the RF biasing plume. The code was developed in C++, parallelized using MPI, and successfully tested with the self-consistent benchmarks proposed by Turner *et al.* [121]. In an RF grid biasing situation, the electrons are injected in pulses. Therefore, a new time-dependent electron injection model was derived from the previously available analytical modeling to study this technique. The resulting formulation mimics the injection of periodic electron pulses with an approximate shape of a gaussian function, with a magnitude that depends on a controlled parameter $\alpha = \langle I_e \rangle / I_i$ and width depending on the ratio V_{RF}/T_e. Despite not being fully self-consistent and thus not perfectly realistic, this model works as a first approximation to study the pulsed electron injection allowing one to verify the most significant influences of its parameters on the expansion of the plume. Future work may include the further development of this model considering the space charge distribution within the grids, penetration of the potential fields within the accel grid holes, and the calculation of the electron energy during the pulse.

One of the major difficulties in simulating a plasma plume expansion is the definition of appropriate outer boundary conditions to spatially truncate its expansion within the simulation domain. In this work, a capacitive boundary condition was used in the simulation of a plume expansion for the first time. In this model, the boundary is modeled as a Dirichlet boundary condition which has its potential defined by an external capacitive circuit. This circuit is simultaneously solved with the charge distribution in the domain using the superposition of Poisson's equation. The simultaneous solution, in contrast to an iterative circuit solution which is often used, plays an important role in the present simulation due to the rapid current and potential oscillations taking place in the expansion of the RF plume. Notably, the capacitive condition provides a self-consistent method to maintain the current-free condition in steady-state without adding artificial parameters, which was something not possible with the traditionally used boundary conditions. When compared to a practical scenario, the electrical topology where the thruster is grounded and the surroundings are connected to a capacitor may represent two different cases. The first one is the case where the thruster is floating inside a grounded

vacuum chamber, where the reference is chosen as the thruster, which is often seen in actual experiments. In the second scenario, the thruster is electrically floating in space and possesses a self-capacitance relative to infinity. Based on the original derivation presented by Vahedi and DiPeso [122] where the domain was assumed to be uniform, a more generalized derivation of the simultaneous solution of the capacitive boundary was presented here considering a non-uniform rectangular grid, which may be useful for future work that may want to use this approach. To improve the simulation fidelity and include effects such as slow ion backstreaming, ion-neutral and electron-neutral collisions were considered using the MCC algorithm and cross sections available from experimental databases. The neutral flow field used for the collisions was simulated using a collisionless particle pusher that was implemented using the moving algorithm from the PIC code. The correctness of the collision algorithm was also verified using the numerical benchmark.

The simulation study was divided into two parts; in the first a DC and an RF case were simulated and compared. The results show clear and important differences between the expansion in both cases. The plume presents a considerably higher divergence and average plasma potential in the RF case. These effects are associated with a higher electron temperature in the RF plume caused by the initial electron energy at the moment of injection, which is much higher than in the DC case, and due to secondary acceleration mechanisms due to the charge accumulation and dynamics in the plume. These effects were also observed in comparing the electron velocity distribution function, which shows much hotter and anisotropic electrons in the RF case. This electron anisotropy was also observed in past experiments [65], which serves as evidence that the model is reproducing the correct physical phenomena. Because of the higher electron temperature and oscillatory dynamics of the plume, the boundary capacitor in the RF case assumes a value with a much higher magnitude on average, suggesting that the thruster in a floating configuration might present much higher potential values when compared to the DC case, which was also expected from theory. The behavior of the ion and electron current entering and leaving the domain also presented an interesting behavior compared to experiments. A strong electron backstreaming current was observed following the injection pulse, which was caused primarily by the formation of a virtual cathode just in front of the thruster. A similar phenomenon was also seen in previous self-consistent simulations of the grids when using RF biasing, which suggests again the reproduction of similar physics. An interesting point is that here the physics of the grids is not simulated, and the electron reflection was caused only by space-charge accumulation, while in previous self-consistent simulations this reflection may be connected by other secondary effects connected with the electron and ion dynamics in that specific configuration. This might suggest that the electron backstreaming may not be influenced so much by a specific grid configuration but can also be present as a phenomenon strongly connected with the dynamics in the plume. Another intriguing effect observed was secondary electron oscillations in the plume, which leads to an outgoing electron current with different harmonics and a higher frequency than the pulse frequency. The shape of the electron current collected at the outer boundary shows very close similarity to experimental

measurements done by Dedrick *et al.* [67]. This partially confirms that this behavior is not exclusively found in these experiments but might be intrinsic to this type of plume. This is also interesting because, intuitively, one might expect that the electron current flowing in the plume would follow a pulsed behavior with a strong peak in phase with the injected pulse. However, it seems that secondary damping and interference effects in the plume play an important role in reducing the electron energy and smoothing its initially coherent propagation. Because of the rapid variation of the plume potential, it was also observed that the displacement current has a significant impact on the capacitor average charge value and magnitude of its oscillation. This is important because it indicates that any future effort to model the plume expansion or acceleration processes cannot neglect the influence of the displacement current component.

In the second part of the simulation study, a parametric investigation of the RF expansion was conducted, varying the pulse frequency, pulse magnitude, and boundary capacitance. It was observed first that there is clearly a minimum pulse magnitude in order to properly neutralize the plume, which is approximately around 2.5 times the magnitude of the ion current. This was also the approximate magnitude observed in previous self-consistent grid simulations, indicating that this is the required current magnitude to neutralize the plume. For pulse magnitudes lower than this value, the plume potential became considerably high until the ion beam eventually starts to stall, increasing the divergence significantly and reflecting back the high-energy ions. The plume potential and the divergence also strongly dependent on the pulse frequency, corroborating previous predictions. The plume parameters showed no important dependence on the boundary capacitance, which shows that this technique does not add important artifacts to the simulation. Therefore, overall, the RF plume simulations provided an interesting complement to the previous grid simulations since they considerably expanded the simulated domain and shed light on several important phenomena in the downstream region of the plume, which are essential for developing a flight prototype.

In the third chapter, the experimental apparatus of the DC and RF experiments was presented. All experiments were conducted at ThrustMe facilities in two different vacuum chambers. For experiments of the DC case, two different thrusters were used, the NPT30-Xe for xenon and NPT30-I2 for iodine. In the RF case, a modified prototype of the NPT30-Xe is used. This chapter also describes the development of a new automated probe array used to characterize the plume of the DC thruster. The development and application of this new instrument were published as a peer-reviewed article (Ref. [145]). The instrument consists of a semi-circular metallic arm that holds a set of planar probes and is moved by a pair of stepper motors. Using a digital control system, the equipment can generate two-dimensional maps of the ion current density, enabling one to estimate the divergence of the plume. This instrument was used in the next chapter to measure the divergence of the plume in the xenon and iodine cases, which is interesting to verify the differences between both cases and to aid in the correction of the thruster performance models.

The fourth chapter presents the experiments done to measure the secondary electron emission yield due to iodine ion bombardment. The measurements of these yields were

necessary due to a lack of SEE data on iodine plasmas and beams, which often makes, for example, the calculation of corrections due to SEE not straightforward. In the context of this work, this need became evident as with the development of the planar probe array described in chapter 3, which uses metallic probes to measure the ion beam current density, and their measurement needs to be corrected for the emission of secondary electrons which would otherwise appear as an additional positive current contribution. This chapter presented some of the first measurements of SEE yield due to iodine bombardment, which may be of interest for many future works on iodine plasmas. The data was also published as a peer-reviewed article (Ref. [169]). A dedicated probe was designed to measure the SEE yield, which allows a direct replacement of the target material. Because the beam produced by the iodine ion thruster is composed of different ion species, I^+, I_2^+ and I^{2+}, it was also necessary to measure the approximate composition of the beam. This was done using a time-of-flight spectrometry apparatus. For comparison, the yield of xenon on molybdenum and tungsten was measured and compared to previous results from the literature, showing good agreement. The yield for iodine was measured for seven different targets. Due to the strong reactivity of iodine on some of the materials and the possible formation of different iodides on their surface, it is possible to observe that the measured yield presents a higher uncertainty and non-linear behavior that are not expected from typical SEE experiments. Using the beam composition data measured with the TOF instrument, the SEE data for each species was estimated. However, because of the reactivity, the decomposition did not present satisfactory estimations on some of the materials. Nevertheless, in this case, an important point is that in most iodine plasma and beam applications, it is reasonable to expect that these surface chemical reactions will also occur. Therefore, the effective SEE yield of the material plus the surface compounds may, in fact, offer a better estimation of the secondary current emitted than the yield for a clean material.

In the fifth chapter, experiments for the characterization of the plume and performance of the DC thruster using both iodine and xenon were presented. The experiments done in this context, together with the results of the orbital tests of the NPT30-I2 thruster, were also published in a peer-reviewed article (Ref. [135]). When studying the plume, several differences were noticed between xenon and iodine. Iodine presented, in general, a slightly lower plume potential when compared to xenon and a lower ion beam divergence which can be associated with a lower electron temperature in the plume. Furthermore, a considerably lower ion backstreaming current was measured in the iodine case, indicating that the production of slow ions due to charge exchange or ionization is less favored than in the xenon case. This can be attributed to the complex collisional process in the iodine case, which may decrease this production, and also because a higher mass utilization efficiency was measured in the case of iodine, which decreases the neutral gas pressure in the plume for a given operational point. In general, it was observed that the thruster presented a better performance when using iodine when compared to xenon. It was verified that, when using iodine, the thruster could stably operate with much lower mass flow rate levels. This helps in the increase of the mass utilization efficiency and allows the specific impulse of the thruster to increase up to roughly 2600 s, in contrast

with the xenon thruster, which achieved only 1600 s. On the other hand, the iodine thruster showed a slightly lower thrust-to-power ratio than the xenon thruster, especially at lower power levels. The iodine thruster was tested in space for the first time onboard the Beihangkongshi-1 satellite, and the results show very similar behavior to the data collected in the laboratory. In general, the performance of the thruster with iodine shows very promising results both in the laboratory and in the flight experiments, and it gives reasonable evidence that it can be used as a feasible alternative to xenon without major drawbacks; not only in ion thrusters but also on other types of plasma-based thrusters.

The results of the experiments with the thruster using RF grid biasing were shown in the last chapter. The thruster was operated using two different frequencies, a high-frequency and low-frequency mode. The experiments demonstrated that the thruster was successfully operated and could correctly produce a well-neutralized ion beam with energy close to the measured self-bias voltage as expected. The thruster was operated with a self-bias voltage up to roughly 800 V and a high-frequency mode at 17.6 MHz, which represent both the highest frequency and acceleration voltage that an ion thruster using RF grid biasing has been tested with to date. These conditions are much closer than previous works to what is expected for an actual propulsion system, which can serve as an important information source for comparing theoretical and numerical models and for the design of future thrusters. The experiments have shown that, when operating the thruster at these conditions, the plume stays within an acceptable range of plume potential, demonstrating that the pulsed neutralization process happens correctly even for a relatively high-energy beam. During the experiments, the accel grid of the thruster was kept floating, which is analogous to the floating boundary condition of the simulations done in chapter 2. It was observed that the average voltage of the grid when operating at the high-frequency mode obtained a positive potential on average, while in the low-frequency, it obtained a negative value. Assuming the accel grid as the electrical reference replicates the same behavior as seen in the numerical parametric plume study. This serves as further evidence that the simulation correctly reproduces the physical behavior of the thruster and also shows that this is a behavior that might be intrinsic to the thruster as expected from theoretical models. The plume potential presents as well a similar behavior to the simulation with potentials much higher than in the DC case, showing that indeed the electron temperature in the RF case is considerably higher and a decreasing behavior of the potential as the frequency is increased. The higher electron temperature may be a drawback of this type of thruster since it may increase its divergence, increase the production of slow downstream ions due to ionization, and enhance power losses. Therefore, an essential point for future work may be optimizing the system and identifying methods to decrease the electron temperature in the plume. The power consumed by the acceleration process was also estimated by measuring the power consumed by the RF amplifier used. The measured power is considerably higher than the DC case for similar conditions. This is expected to be mainly related to the acceleration of backstreaming electrons to high voltages, which is a significant power loss mechanism and is not present in the DC case. On the other hand, the DC thruster requires additional power for the neutralizing system, which is not considered here. The enhanced power loss

observed during the experiments might also be related to the prototype's specific design, which can cause secondary electrical effects such as capacitive coupling to the thruster structure. This coupling might induce behaviors that resemble a capacitively coupled plasma (CCP) having RF currents flowing to the components such as the ICP antenna other grounded surfaces. In a future work, a relevant point for the understanding and optimization of the system is the analysis of the plasma power consumption trends using the theoretical framework available on capacitive discharges [18]. It is important to note that when electrons are accelerated backward towards the upstream ICP discharge, this power is not reused and is effectively lost – as they enter the ICP, the electrons do not contribute significantly to the ionization rate since their transit time is very short and their collisional mean free path very large, and so they directly impact the wall of the plasma chamber generating additional heat. This high-energy electron beam entering the ICP might also create secondary effects such as the emission of secondary electrons at the wall and elevate the plasma sheath potential. Because power consumption is a critical factor in the performance of propulsion systems, these mechanisms stand out as a significant point for future work and improvement. The optimization of the circuit can be maybe more straightforward; however, the losses due to the electron acceleration may need intensive work for further understanding of its physics, requiring further research. Nevertheless, it is important to note that, despite the high power consumption, the experiments effectively demonstrated that the thruster could operate close to the required operating range while maintaining acceptable performance characteristics in terms of ion acceleration and neutralization, which is an essential step in the development of this technology and was not available previously. Furthermore, the experiments also gave for the first time solid evidence that the theoretical and numerical formulations used to model the thruster can correctly predict the behavior of the acceleration process and the plume expansion. This is also a significant step in developing this technique since it confirms the current understanding of the physics of the thruster and gives confidence for further expansion of the current theoretical formulation.

In general, this work provided evidence that both the iodine and the RF grid biasing technologies might offer a feasible alternative for current ion thruster technologies and shed light on different processes taking place in the plume expansion in both cases. In the iodine propellant case, this work serves to optimize flight thrusters further and helps to consider its application in other thruster concepts. On the other hand, the RF grid biasing technique is still not as mature, and this work helps to understand more basic phenomena occurring in the plume to aid in more complex modeling of its behavior in future studies.

APPENDIX A

SEE YIELD TABLES

Table A.1: SEE yield data for xenon on the molybdenum and tungsten targets.

V_s (kV)	γ_{Mo}	γ_W
0.50	0.0181 ± 0.0017	0.0210 ± 0.0019
0.55	0.0197 ± 0.0021	0.0215 ± 0.0007
0.60	0.0219 ± 0.0020	0.0217 ± 0.0012
0.65	0.0221 ± 0.0012	0.0223 ± 0.0014
0.70	0.0230 ± 0.0007	0.0224 ± 0.0003
0.75	0.0233 ± 0.0008	0.0222 ± 0.0016
0.80	0.0236 ± 0.0017	0.0231 ± 0.0010
0.85	0.0251 ± 0.0005	0.0237 ± 0.0010
0.90	0.0265 ± 0.0008	0.0240 ± 0.0007
0.95	0.0271 ± 0.0008	0.0242 ± 0.0013
1.00	0.0272 ± 0.0017	0.0244 ± 0.0010
1.05	0.0289 ± 0.0011	0.0248 ± 0.0008
1.10	0.0283 ± 0.0017	0.0252 ± 0.0009
1.15	0.0294 ± 0.0010	0.0257 ± 0.0004
1.20	0.0293 ± 0.0008	0.0256 ± 0.0013
1.25	0.0288 ± 0.0010	0.0262 ± 0.0022
1.30	0.0294 ± 0.0006	0.0270 ± 0.0012

Table A.2: SEE yield data for iodine on the molybdenum target.

V_s (kV)	γ_A	γ_B	γ_{I^+}	$\gamma_{I_2^+}$
0.50	0.0091 ± 0.0019	0.0060 ± 0.0017	0.0021 ± 0.0036	0.0183 ± 0.0036
0.55	0.0098 ± 0.0007	0.0063 ± 0.0016	0.0020 ± 0.0024	0.0201 ± 0.0024
0.60	0.0093 ± 0.0017	0.0092 ± 0.0108	0.0090 ± 0.0125	0.0097 ± 0.0125
0.65	0.0112 ± 0.0053	0.0080 ± 0.0017	0.0041 ± 0.0070	0.0205 ± 0.0070
0.70	0.0115 ± 0.0053	0.0082 ± 0.0024	0.0041 ± 0.0077	0.0211 ± 0.0077
0.75	0.0108 ± 0.0024	0.0086 ± 0.0022	0.0057 ± 0.0046	0.0175 ± 0.0046
0.80	0.0110 ± 0.0039	0.0099 ± 0.0062	0.0085 ± 0.0101	0.0141 ± 0.0101
0.85	0.0119 ± 0.0039	0.0093 ± 0.0016	0.0059 ± 0.0055	0.0198 ± 0.0055
0.90	0.0123 ± 0.0018	0.0099 ± 0.0013	0.0069 ± 0.0031	0.0193 ± 0.0031
0.95	0.0142 ± 0.0023	0.0100 ± 0.0015	0.0047 ± 0.0037	0.0267 ± 0.0037
1.00	0.0142 ± 0.0043	0.0106 ± 0.0022	0.0062 ± 0.0065	0.0246 ± 0.0065
1.05	0.0151 ± 0.0029	0.0108 ± 0.0019	0.0054 ± 0.0048	0.0279 ± 0.0048
1.10	0.0157 ± 0.0030	0.0123 ± 0.0025	0.0080 ± 0.0056	0.0256 ± 0.0056
1.15	0.0155 ± 0.0032	0.0132 ± 0.0024	0.0104 ± 0.0056	0.0222 ± 0.0056
1.20	0.0173 ± 0.0036	0.0140 ± 0.0052	0.0098 ± 0.0088	0.0271 ± 0.0088
1.25	0.0178 ± 0.0024	0.0135 ± 0.0025	0.0081 ± 0.0049	0.0304 ± 0.0049
1.30	0.0174 ± 0.0032	0.0145 ± 0.0026	0.0108 ± 0.0058	0.0261 ± 0.0058

Table A.3: SEE yield data for iodine on the tungsten target.

V_s (kV)	γ_A	γ_B	γ_{I^+}	$\gamma_{I_2^+}$
0.50	0.0072 ± 0.0035	0.0095 ± 0.0025	0.0119 ± 0.0061	0.0021 ± 0.0061
0.55	0.0080 ± 0.0035	0.0096 ± 0.0025	0.0111 ± 0.0060	0.0048 ± 0.0060
0.60	0.0075 ± 0.0021	0.0104 ± 0.0044	0.0135 ± 0.0065	0.0011 ± 0.0065
0.65	0.0073 ± 0.0017	0.0081 ± 0.0021	0.0090 ± 0.0037	0.0054 ± 0.0037
0.70	0.0091 ± 0.0049	0.0096 ± 0.0020	0.0101 ± 0.0069	0.0082 ± 0.0069
0.75	0.0074 ± 0.0024	0.0109 ± 0.0015	0.0144 ± 0.0039	0.0000 ± 0.0039
0.80	0.0089 ± 0.0030	0.0104 ± 0.0009	0.0120 ± 0.0039	0.0057 ± 0.0039
0.85	0.0087 ± 0.0025	0.0097 ± 0.0020	0.0108 ± 0.0045	0.0065 ± 0.0045
0.90	0.0107 ± 0.0052	0.0101 ± 0.0015	0.0094 ± 0.0067	0.0121 ± 0.0067
0.95	0.0111 ± 0.0031	0.0108 ± 0.0012	0.0105 ± 0.0044	0.0116 ± 0.0044
1.00	0.0085 ± 0.0033	0.0104 ± 0.0006	0.0124 ± 0.0039	0.0043 ± 0.0039
1.05	0.0100 ± 0.0014	0.0103 ± 0.0014	0.0105 ± 0.0027	0.0095 ± 0.0027
1.10	0.0110 ± 0.0025	0.0107 ± 0.0016	0.0103 ± 0.0040	0.0118 ± 0.0040
1.15	0.0107 ± 0.0014	0.0103 ± 0.0010	0.0099 ± 0.0024	0.0116 ± 0.0024
1.20	0.0115 ± 0.0021	0.0106 ± 0.0023	0.0096 ± 0.0044	0.0135 ± 0.0044
1.25	0.0125 ± 0.0042	0.0104 ± 0.0029	0.0082 ± 0.0071	0.0170 ± 0.0071
1.30	0.0113 ± 0.0038	0.0110 ± 0.0018	0.0106 ± 0.0056	0.0121 ± 0.0056

Table A.4: SEE yield data for iodine on the titanium target.

V_s (kV)	γ_A	γ_B	γ_{I^+}	$\gamma_{I_2^+}$
0.50	0.0273 ± 0.0009	0.0302 ± 0.0011	0.0339 ± 0.0020	0.0197 ± 0.0020
0.55	0.0307 ± 0.0008	0.0330 ± 0.0015	0.0360 ± 0.0023	0.0247 ± 0.0023
0.60	0.0344 ± 0.0023	0.0368 ± 0.0026	0.0396 ± 0.0049	0.0285 ± 0.0049
0.65	0.0379 ± 0.0024	0.0389 ± 0.0030	0.0401 ± 0.0054	0.0355 ± 0.0054
0.70	0.0406 ± 0.0016	0.0417 ± 0.0012	0.0431 ± 0.0028	0.0378 ± 0.0028
0.75	0.0438 ± 0.0015	0.0455 ± 0.0017	0.0476 ± 0.0032	0.0396 ± 0.0032
0.80	0.0479 ± 0.0033	0.0482 ± 0.0014	0.0485 ± 0.0046	0.0473 ± 0.0046
0.85	0.0490 ± 0.0023	0.0512 ± 0.0010	0.0540 ± 0.0034	0.0433 ± 0.0034
0.90	0.0526 ± 0.0043	0.0543 ± 0.0007	0.0565 ± 0.0051	0.0482 ± 0.0051
0.95	0.0557 ± 0.0025	0.0571 ± 0.0011	0.0588 ± 0.0036	0.0521 ± 0.0036
1.00	0.0589 ± 0.0016	0.0602 ± 0.0015	0.0618 ± 0.0031	0.0557 ± 0.0031
1.05	0.0615 ± 0.0028	0.0633 ± 0.0010	0.0656 ± 0.0038	0.0568 ± 0.0038
1.10	0.0651 ± 0.0043	0.0661 ± 0.0019	0.0672 ± 0.0062	0.0628 ± 0.0062
1.15	0.0676 ± 0.0012	0.0690 ± 0.0017	0.0708 ± 0.0029	0.0639 ± 0.0029
1.20	0.0697 ± 0.0020	0.0718 ± 0.0013	0.0744 ± 0.0033	0.0644 ± 0.0033
1.25	0.0737 ± 0.0028	0.0743 ± 0.0023	0.0751 ± 0.0051	0.0720 ± 0.0051
1.30	0.0761 ± 0.0020	0.0775 ± 0.0024	0.0793 ± 0.0044	0.0726 ± 0.0044

Table A.5: SEE yield data for iodine on the aluminum target.

V_s (kV)	γ_A	γ_B	γ_{I^+}	$\gamma_{I_2^+}$
0.50	0.1108 ± 0.0342	0.1134 ± 0.0029	0.1162 ± 0.0371	0.1055 ± 0.0371
0.55	0.1209 ± 0.0321	0.1252 ± 0.0040	0.1299 ± 0.0361	0.1120 ± 0.0361
0.60	0.1399 ± 0.0260	0.1408 ± 0.0035	0.1416 ± 0.0296	0.1383 ± 0.0296
0.65	0.1583 ± 0.0293	0.1551 ± 0.0089	0.1517 ± 0.0383	0.1647 ± 0.0383
0.70	0.1631 ± 0.0274	0.1741 ± 0.0089	0.1859 ± 0.0363	0.1407 ± 0.0363
0.75	0.1757 ± 0.0251	0.1887 ± 0.0214	0.2025 ± 0.0465	0.1495 ± 0.0465
0.80	0.2060 ± 0.0178	0.2046 ± 0.0108	0.2031 ± 0.0286	0.2088 ± 0.0286
0.85	0.2178 ± 0.0455	0.2234 ± 0.0171	0.2294 ± 0.0626	0.2063 ± 0.0626
0.90	0.2313 ± 0.0052	0.2388 ± 0.0230	0.2468 ± 0.0282	0.2162 ± 0.0282
0.95	0.2530 ± 0.0345	0.2598 ± 0.0167	0.2670 ± 0.0512	0.2394 ± 0.0512
1.00	0.2795 ± 0.0487	0.2804 ± 0.0066	0.2814 ± 0.0553	0.2776 ± 0.0553
1.05	0.2819 ± 0.0481	0.2987 ± 0.0081	0.3167 ± 0.0562	0.2478 ± 0.0562
1.10	0.2986 ± 0.0274	0.3160 ± 0.0142	0.3346 ± 0.0416	0.2634 ± 0.0416
1.15	0.3121 ± 0.0061	0.3357 ± 0.0066	0.3610 ± 0.0127	0.2641 ± 0.0127
1.20	0.3255 ± 0.0042	0.3501 ± 0.0105	0.3763 ± 0.0146	0.2757 ± 0.0146
1.25	0.3409 ± 0.0030	0.3735 ± 0.0243	0.4083 ± 0.0273	0.2748 ± 0.0273
1.30	0.3450 ± 0.0496	0.3777 ± 0.0237	0.4126 ± 0.0732	0.2789 ± 0.0732

Table A.6: SEE yield data for iodine on the copper target.

V_s (kV)	γ_A	γ_B	γ_{I^+}	$\gamma_{I_2^+}$
0.50	0.0988 ± 0.0029	0.0998 ± 0.0083	0.1010 ± 0.0112	0.0959 ± 0.0112
0.55	0.1023 ± 0.0022	0.1076 ± 0.0115	0.1143 ± 0.0138	0.0861 ± 0.0138
0.60	0.1029 ± 0.0038	0.1079 ± 0.0171	0.1141 ± 0.0209	0.0879 ± 0.0209
0.65	0.1063 ± 0.0055	0.1185 ± 0.0092	0.1340 ± 0.0146	0.0694 ± 0.0146
0.70	0.1064 ± 0.0121	0.1257 ± 0.0107	0.1500 ± 0.0228	0.0481 ± 0.0228
0.75	0.1121 ± 0.0073	0.1275 ± 0.0084	0.1469 ± 0.0157	0.0655 ± 0.0157
0.80	0.1168 ± 0.0104	0.1281 ± 0.0143	0.1424 ± 0.0247	0.0826 ± 0.0247
0.85	0.1201 ± 0.0124	0.1364 ± 0.0110	0.1570 ± 0.0234	0.0709 ± 0.0234
0.90	0.1184 ± 0.0175	0.1407 ± 0.0178	0.1688 ± 0.0354	0.0511 ± 0.0354
0.95	0.1234 ± 0.0101	0.1520 ± 0.0130	0.1880 ± 0.0232	0.0371 ± 0.0232
1.00	0.1380 ± 0.0188	0.1590 ± 0.0062	0.1856 ± 0.0250	0.0743 ± 0.0250
1.05	0.1348 ± 0.0186	0.1651 ± 0.0067	0.2035 ± 0.0253	0.0430 ± 0.0253
1.10	0.1325 ± 0.0162	0.1817 ± 0.0108	0.2362 ± 0.0270	0.0000 ± 0.0270
1.15	0.1394 ± 0.0118	0.1866 ± 0.0102	0.2446 ± 0.0220	0.0000 ± 0.0220
1.20	0.1308 ± 0.0295	0.2031 ± 0.0066	0.2531 ± 0.0361	0.0000 ± 0.0361
1.25	0.1423 ± 0.0370	0.2165 ± 0.0084	0.2716 ± 0.0454	0.0000 ± 0.0454
1.30	0.1553 ± 0.0410	0.2183 ± 0.0111	0.2814 ± 0.0521	0.0000 ± 0.0521

Table A.7: SEE yield data for iodine on the steel target.

V_s (kV)	γ_A	γ_B	γ_{I^+}	$\gamma_{I_2^+}$
0.50	0.0280 ± 0.0012	0.0251 ± 0.0070	0.0215 ± 0.0082	0.0361 ± 0.0082
0.55	0.0330 ± 0.0037	0.0292 ± 0.0101	0.0242 ± 0.0138	0.0442 ± 0.0138
0.60	0.0314 ± 0.0039	0.0311 ± 0.0087	0.0308 ± 0.0126	0.0321 ± 0.0126
0.65	0.0355 ± 0.0012	0.0308 ± 0.0140	0.0248 ± 0.0152	0.0489 ± 0.0152
0.70	0.0372 ± 0.0045	0.0267 ± 0.0082	0.0133 ± 0.0127	0.0671 ± 0.0127
0.75	0.0412 ± 0.0056	0.0291 ± 0.0023	0.0135 ± 0.0079	0.0760 ± 0.0079
0.80	0.0410 ± 0.0027	0.0253 ± 0.0061	0.0053 ± 0.0089	0.0857 ± 0.0089
0.85	0.0412 ± 0.0049	0.0283 ± 0.0096	0.0118 ± 0.0146	0.0781 ± 0.0146
0.90	0.0456 ± 0.0023	0.0260 ± 0.0011	0.0011 ± 0.0034	0.1013 ± 0.0034
0.95	0.0435 ± 0.0028	0.0250 ± 0.0011	0.0013 ± 0.0039	0.0963 ± 0.0039
1.00	0.0480 ± 0.0036	0.0241 ± 0.0044	0.0000 ± 0.0080	0.1054 ± 0.0080
1.05	0.0493 ± 0.0041	0.0245 ± 0.0046	0.0000 ± 0.0087	0.1081 ± 0.0087
1.10	0.0481 ± 0.0040	0.0238 ± 0.0057	0.0000 ± 0.0096	0.1053 ± 0.0096
1.15	0.0504 ± 0.0027	0.0270 ± 0.0018	0.0000 ± 0.0045	0.1123 ± 0.0045
1.20	0.0520 ± 0.0058	0.0270 ± 0.0040	0.0000 ± 0.0098	0.1149 ± 0.0098
1.25	0.0516 ± 0.0048	0.0271 ± 0.0101	0.0000 ± 0.0150	0.1145 ± 0.0150
1.30	0.0515 ± 0.0037	0.0291 ± 0.0038	0.0005 ± 0.0075	0.1153 ± 0.0075

Table A.8: SEE yield data for iodine on the carbon-carbon target.

V_s (kV)	γ_A	γ_B	γ_{I^+}	$\gamma_{I_2^+}$
0.50	0.0064 ± 0.0005	0.0054 ± 0.0009	0.0045 ± 0.0014	0.0087 ± 0.0014
0.55	0.0064 ± 0.0010	0.0065 ± 0.0011	0.0066 ± 0.0021	0.0061 ± 0.0021
0.60	0.0074 ± 0.0018	0.0066 ± 0.0010	0.0057 ± 0.0028	0.0095 ± 0.0028
0.65	0.0080 ± 0.0013	0.0075 ± 0.0010	0.0069 ± 0.0023	0.0093 ± 0.0023
0.70	0.0092 ± 0.0023	0.0078 ± 0.0015	0.0064 ± 0.0038	0.0125 ± 0.0038
0.75	0.0093 ± 0.0008	0.0091 ± 0.0009	0.0089 ± 0.0016	0.0097 ± 0.0016
0.80	0.0102 ± 0.0008	0.0091 ± 0.0010	0.0080 ± 0.0018	0.0127 ± 0.0018
0.85	0.0107 ± 0.0016	0.0104 ± 0.0009	0.0100 ± 0.0025	0.0116 ± 0.0025
0.90	0.0115 ± 0.0022	0.0109 ± 0.0009	0.0102 ± 0.0031	0.0131 ± 0.0031
0.95	0.0131 ± 0.0025	0.0119 ± 0.0007	0.0106 ± 0.0032	0.0160 ± 0.0032
1.00	0.0131 ± 0.0025	0.0127 ± 0.0010	0.0124 ± 0.0035	0.0138 ± 0.0035
1.05	0.0134 ± 0.0023	0.0137 ± 0.0005	0.0141 ± 0.0028	0.0125 ± 0.0028
1.10	0.0159 ± 0.0031	0.0148 ± 0.0010	0.0136 ± 0.0041	0.0187 ± 0.0041
1.15	0.0162 ± 0.0013	0.0159 ± 0.0006	0.0157 ± 0.0020	0.0169 ± 0.0020
1.20	0.0177 ± 0.0014	0.0172 ± 0.0011	0.0167 ± 0.0025	0.0190 ± 0.0025
1.25	0.0181 ± 0.0016	0.0173 ± 0.0012	0.0164 ± 0.0028	0.0201 ± 0.0028
1.30	0.0201 ± 0.0024	0.0192 ± 0.0010	0.0183 ± 0.0033	0.0221 ± 0.0033

APPENDIX B

LIST OF PUBLICATIONS

Below is a list of peer-reviewed articles that were published during the course of this thesis:

L. Habl, D. Rafalskyi, and T. Lafleur, "Ion beam diagnostic for the assessment of miniaturized electric propulsion systems," *Review of Scientific Instruments*, vol. 91, no. 9, p. 093 501, Sep. 2020

L Habl, T Lafleur, D Rafalskyi, and P Chabert, "Plasma plume expansion with pulsed electron neutralization," *Plasma Sources Science and Technology*, vol. 30, no. 4, p. 045 014, Apr. 1, 2021

L. Habl, D. Rafalskyi, and T. Lafleur, "Secondary electron emission due to multi-species iodine ion bombardment of different target materials," *Journal of Applied Physics*, vol. 129, no. 15, p. 153 302, Apr. 2021

D. Rafalskyi, J. M. Martínez, L. Habl, E. Z. Rossi, P. Proynov, A. Boré, T. Baret, A. Poyet, T. Lafleur, S. Dudin, and A. Aanesland, "In-orbit demonstration of an iodine electric propulsion system," *Nature*, vol. 599, no. 7885, pp. 411–415, Nov. 2021

BIBLIOGRAPHY

[1] F. F. Chen, *Introduction to Plasma Physics and Controlled Fusion*. New York, NY: Springer Science & Business Media, 2015.

[2] J. A. Bittencourt, *Fundamentals of Plasma Physics*. Springer New York, 2004.

[3] O. D. Cortázar and A. Megía-Macías, "Bimodal ion energy distribution functions in a hydrogen magnetized plasma," *Plasma Sources Science and Technology*, vol. 28, no. 2, p. 025 010, 2019.

[4] M. A. Lieberman and A. J. Lichtenberg, *Principles of Plasma Discharges and Materials Processing*. Hoboken, NJ, USA: John Wiley & Sons, Inc., Apr. 2005.

[5] M. Kallenrode, *Space Physics: An Introduction to Plasmas and Particles in the Heliosphere and Magnetospheres* (Advanced Texts in Physics). Springer Berlin Heidelberg, 2013.

[6] E. R. Williams, S. G. Geotis, and A. Bhattacharya, "A radar study of the plasma and geometry of lightning," *Journal of Atmospheric Sciences*, vol. 46, no. 9, pp. 1173–1185, 1989.

[7] R. Schunk and A. Nagy, "Ionospheres of the terrestrial planets," *Reviews of Geophysics*, vol. 18, no. 4, pp. 813–852, 1980.

[8] A. J. Hundhausen, "Composition and dynamics of the solar wind plasma," *Reviews of Geophysics*, vol. 8, no. 4, p. 729, 1970.

[9] B. T. Draine, *Physics of the interstellar and intergalactic medium*. Princeton University Press, 2010, vol. 19.

[10] W. M. Stacey, *Fusion Plasma Physics*. Wiley, Aug. 2005.

[11] Z. M. Liu, S. Cui, Z. Luo, C. Zhang, Z. Wang, and Y. Zhang, "Plasma arc welding: Process variants and its recent developments of sensing, controlling and modeling," *Journal of Manufacturing Processes*, vol. 23, pp. 315–327, Aug. 2016.

[12] J. Shohet, "Plasma-aided manufacturing," *IEEE Transactions on Plasma Science*, vol. 19, no. 5, pp. 725–733, 1991.

[13] M. Martinez-Sanchez and J. E. Pollard, "Spacecraft electric propulsion-an overview," *Journal of propulsion and power*, vol. 14, no. 5, pp. 688–699, 1998.

[14] D. M. Goebel and I. Katz, *Fundamentals of Electric Propulsion: Ion and Hall Thrusters* (JPL Space Science and Technology Series 1). Hoboken, N.J: Wiley, 2008.

[15] Z. Donko, P. Hartmann, and G. J. Kalman, *Strongly coupled plasma liquids*, 2007.

[16] G. Colonna, "Boltzmann and Vlasov equations in plasma physics," in *Plasma Modeling*, ser. 2053-2563, IOP Publishing, 2016, 1–1 to 1–23.

[17] U. S. Inan and M. Gołkowski, *Principles of Plasma Physics for Engineers and Scientists*. Cambridge ; New York: Cambridge University Press, 2011.

[18] P. Chabert and N. Braithwaite, *Physics of Radio-Frequency Plasmas*. 2011.

[19] M. Benilov, "The child–langmuir law and analytical theory of collisionless to collision-dominated sheaths," *Plasma Sources Science and Technology*, vol. 18, no. 1, p. 014 005, 2008.

[20] "Plasma data exchange project (LXCat)." (2022), [Online]. Available: `https://lxcat.net/`.

[21] S. Gong and M. Macdonald, "Review on solar sail technology," *Astrodynamics*, vol. 3, no. 2, pp. 93–125, 2019.

[22] Y. A. Rezunkov, *High Power Laser Propulsion*. Springer International Publishing, 2021.

[23] J. D. Clark, *Ignition!* Rutgers University Press, 2018.

[24] G. Sutton and O. Biblarz, *Rocket Propulsion Elements* (A Wiley Interscience publication). Wiley, 2001.

[25] W. Von Braun and F. Ordway, *History of Rocketry & Space Travel*. Crowell, 1975.

[26] D. H. DeVorkin and M. J. Neufeld, "Space artifact or nazi weapon? displaying the smithsonian's v-2 missile, 1976-2011," *Endeavour*, 2011.

[27] E. Y. Choueiri, "A critical history of electric propulsion: The first 50 years (1906-1956)," *Journal of Propulsion and Power*, vol. 20, no. 2, pp. 193–203, Mar. 2004.

[28] J. S. Sovey, V. K. Rawlin, and M. J. Patterson, "Ion propulsion development projects in u.s.: Space electric rocket test i to deep space 1," *Journal of Propulsion and Power*, vol. 17, no. 3, pp. 517–526, May 2001.

[29] D. Lev, R. M. Myers, K. M. Lemmer, J. Kolbeck, H. Koizumi, and K. Polzin, "The technological and commercial expansion of electric propulsion," *Acta Astronautica*, vol. 159, pp. 213–227, Jun. 2019.

[30] "Starlink statistics (Jonathan McDowell's Space Report)." (2022), [Online]. Available: `https://planet4589.org/space/stats/star/starstats.html`.

[31] J. Ashkenazy, G Appelbaum, T Ram-Cohen, A Warshavsky, I Tidhar, and L Rabinovich, "Venμs technological payload - the israeli hall effect thruster electric propulsion system," in *47th Israel Annual Conf. on Aerospace Sciences, Tel-Aviv & Haifa, Israel*, Feb. 2007.

[32] H. Kuninaka, K. Nishiyama, I. Funaki, T. Yamada, Y. Shimizu, and J. Kawaguchi, "Powered flight of electron cyclotron resonance ion engines on hayabusa explorer," *Journal of Propulsion and Power*, vol. 23, no. 3, pp. 544–551, May 2007.

[33] H. Bassner, R. Killinger, M. Marx, R. Kukies, M. Aguirre, C. Edwards, and H.-P. Harmann, "Ion propulsion for drag compensation of GOCE," in *36th Joint Propulsion Conference and Exhibit*, American Institute of Aeronautics and Astronautics, Jul. 2000.

[34] E. Stuhlinger, *Ion propulsion for space flight*. McGraw-Hill New York, 1964.

[35] H. R. Kaufman, *An ion rocket with an electron-bombardment ion source*. National Aeronautics and Space Administration, 1961.

[36] H. R. Kaufman, "Origin of the electron-bombardment ion thruster," *Journal of Spacecraft and Rockets*, vol. 18, no. 4, pp. 289–292, Jul. 1981.

[37] H. Kuninaka and S. Satori, "Development and demonstration of a cathodeless electron cyclotron resonance ion thruster," *Journal of Propulsion and Power*, vol. 14, no. 6, pp. 1022–1026, Nov. 1998.

[38] H. W. LOEB, "Recent work on radio frequency ion thrusters," *Journal of Spacecraft and Rockets*, vol. 8, no. 5, pp. 494–500, May 1971.

[39] M. G. Marcucci and J. E. Polk, "NSTAR xenon ion thruster on deep space 1: Ground and flight tests (invited)," *Review of Scientific Instruments*, vol. 71, no. 3, pp. 1389–1400, Mar. 2000.

[40] J. R. Brophy, C. E. Garner, and S. C. Mikes, "Dawn ion propulsion system: Initial checkout after launch," *Journal of Propulsion and Power*, vol. 25, no. 6, pp. 1189–1202, Nov. 2009.

[41] K. Nishiyama, S. Hosoda, R. Tsukizaki, and H. Kuninaka, "In-flight operation of the hayabusa2 ion engine system on its way to rendezvous with asteroid 162173 ryugu," *Acta Astronautica*, vol. 166, pp. 69–77, Jan. 2020.

[42] P. Chabert, J. A. Monreal, J. Bredin, L. Popelier, and A. Aanesland, "Global model of a gridded-ion thruster powered by a radiofrequency inductive coil," *Physics of Plasmas*, vol. 19, no. 7, p. 073 512, Jul. 2012.

[43] H. Kuninaka and P. Molina-Morales, "Spacecraft charging due to lack of neutralization on ion thrusters," *Acta Astronautica*, vol. 55, no. 1, pp. 27–38, Jul. 2004.

[44] A. Wheelock, D. L. Cooke, and N. A. Gatsonis, "Investigation of ion beam neutralization processes with 2d and 3d pic simulations," *Computer physics communications*, vol. 164, no. 1-3, pp. 336–343, 2004.

[45] R. I. S. Roy, D. E. Hastings, and N. A. Gastonis, "Ion-thruster plume modeling for backflow contamination," *Journal of Spacecraft and Rockets*, vol. 33, no. 4, pp. 525–534, Jul. 1996.

[46] F. Elliott, J. Foster, and M. Patterson, "An overview of the high power electric propulsion (HiPEP) project," in *40th Joint Propulsion Conference and Exhibit*, American Institute of Aeronautics and Astronautics, Jun. 2004.

[47] J. E. Polk, D. M. Goebel, J. S. Snyder, A. C. Schneider, L. K. Johnson, and A. Sengupta, "A high power ion thruster for deep space missions," *Review of Scientific Instruments*, vol. 83, no. 7, p. 073 306, Jul. 2012.

[48] G. Aston, H. R. Kaufman, and P. J. Wilbur, "Ion beam divergence characteristics of two-grid accelerator systems," *AIAA Journal*, vol. 16, no. 5, pp. 516–524, May 1978.

[49] R. Bond and P. Latham, "Ion thruster extraction grid design and erosion modelling using computer simulation," in *31st Joint Propulsion Conference and Exhibit*, 1995, p. 2923.

[50] R. Wirz, D. Goebel, C. Marrese, and J. Mueller, "Development of cathode technologies for a miniature ion thruster," in *39th Joint Propulsion Conference and Exhibit*, American Institute of Aeronautics and Astronautics, Jun. 2003.

[51] D. R. Lev, I. G. Mikellides, D. Pedrini, D. M. Goebel, B. A. Jorns, and M. S. McDonald, "Recent progress in research and development of hollow cathodes for electric propulsion," *Reviews of Modern Plasma Physics*, vol. 3, no. 1, Jun. 2019.

[52] A. Gurciullo, "Electric propulsion technologies for enabling the use of molecular propellants.," Ph.D. dissertation, University of Surrey, 2020.

[53] M. Guarnieri, "The age of vacuum tubes: Early devices and the rise of radio communications [historical]," *IEEE Industrial Electronics Magazine*, vol. 6, no. 1, pp. 41–43, 2012.

[54] A. Sengupta, J. Brophy, and K. Goodfellow, "Status of the extended life test of the deep space 1 flight spare ion engine after 30, 000 hours of operation," in *39th AIAA/ASME/SAE/ASEE Joint Propulsion Conference and Exhibit*, American Institute of Aeronautics and Astronautics, Jun. 2003.

[55] Y. Takao, K. Hiramoto, Y. Nakagawa, Y. Kasagi, H. Koizumi, and K. Komurasaki, "Electron extraction mechanisms of a micro-ecr neutralizer," *Japanese Journal of Applied Physics*, vol. 55, no. 7S2, p. 07LD09, 2016.

[56] K. D. Diamant, "Microwave cathode for air breathing electric propulsion," in *31st International Electric Propulsion Conference, University of Michigan, Ann Arbor, Michigan, USA*, 2009.

[57] V. Godyak, Y. Raitses, and N. J. Fisch, "Rf plasma cathode-neutralizer for space applications," in *30th International Electric Propulsion Conference, Florence, Italy*, 2007.

[58] W. Ohmichi and H. Kuninaka, "Performance degradation of a spacecraft electron cyclotron resonance neutralizer and its mitigation," *Journal of Propulsion and Power*, vol. 30, no. 5, pp. 1368–1372, Sep. 2014.

[59] D Rafalskyi and A Aanesland, "Brief review on plasma propulsion with neutralizer-free systems," *Plasma Sources Science and Technology*, vol. 25, no. 4, p. 043 001, 2016.

[60] D. Koda, H. Kuninaka, and R. Tsukizaki, "Characteristics of ion–ion thruster generating continuously positive and negative ion beams," *Journal of Propulsion and Power*, vol. 35, no. 3, pp. 565–571, May 2019.

[61] D. Rafalskyi, L. Popelier, and A. Aanesland, "Experimental validation of the dual positive and negative ion beam acceleration in the plasma propulsion with electronegative gases thruster," *Journal of Applied Physics*, vol. 115, no. 5, p. 053 301, Feb. 2014.

[62] D Rafalskyi and A Aanesland, "Coincident ion acceleration and electron extraction for space propulsion using the self-bias formed on a set of RF biased grids bounding a plasma source," *Journal of Physics D: Applied Physics*, vol. 47, no. 49, p. 495 203, Nov. 2014.

[63] D. Rafalskyi and A. Aanesland, "Neutralizer-free gridded ion thruster," in *50th AIAA/ASME/SAE/ASEE Joint Propulsion Conference*, Cleveland, OH: American Institute of Aeronautics and Astronautics, Jul. 2014.

[64] D. Rafalskyi and A. Aanesland, "A Neutralizer-Free Gridded Ion Thruster Embedded Into A 1U Cubesat Module," in *35th International Electric Propulsion Conference*, 2017.

[65] D. Rafalskyi and A. Aanesland, "Plasma acceleration using a radio frequency self-bias effect," *Physics of Plasmas*, vol. 22, no. 6, p. 063 502, Jun. 2015.

[66] T Lafleur and D Rafalskyi, "Radio-frequency biasing of ion acceleration grids," *Plasma Sources Science and Technology*, vol. 27, no. 12, p. 125 004, Dec. 2018.

[67] J. Dedrick, A. R. Gibson, D. Rafalskyi, and A. Aanesland, "Transient propagation dynamics of flowing plasmas accelerated by radio-frequency electric fields," *Physics of Plasmas*, vol. 24, no. 5, p. 050 703, May 2017.

[68] T. Lafleur, D. Rafalskyi, and A. Aanesland, "Radio-frequency biasing of ion thruster grids," in *36th International Electric Propulsion Conference*, 2019.

[69] N. Fazio, S. Gabriel, and I. O. Golosnoy, "Alternative propellants for gridded ion engines," in *Space Propulsion 2018 (14/05/18 - 18/05/18)*, 2018, p. 00 102.

[70] P. Grondein, T. Lafleur, P. Chabert, and A. Aanesland, "Global model of an iodine gridded plasma thruster," *Physics of Plasmas*, vol. 23, no. 3, p. 033 514, Mar. 2016.

[71] T. A. Collard, J. P. Sheehan, and A. D. Gallimore, "Pressurized xenon propellant management system for the cubesat ambipolar thruster," in *34th International Electric Propulsion Conference*, 2015.

[72] J. Wertz and W. Larson, *Space Mission Analysis and Design* (Space Technology Library). Springer Netherlands, 1999.

[73] P. Linstrom and W. Mallard, *NIST Chemistry WebBook, NIST Standard Reference Database 69*, en. National Institute of Standards and Technology, 2022.

[74] D. A. Herman and K. G. Unfried, "Xenon acquisition strategies for high-power electric propulsion nasa missions," NASA, Tech. Rep. NTRS-20150023080, 2015.

[75] F. Marmuse, "Iodine plasmas : experimental and numerical studies. Application to electric propulsion," Theses, Sorbonne Université, Jul. 2020.

[76] P. Dietz, W. Gärtner, Q. Koch, P. E. Köhler, Y. Teng, P. R. Schreiner, K. Holste, and P. J. Klar, "Molecular propellants for ion thrusters," *Plasma Sources Science and Technology*, vol. 28, no. 8, p. 084 001, 2019.

[77] R. Lucken, F. Marmuse, A. Tavant, A. Bourdon, and P. Chabert, "Global model of a magnetized ion thruster with xenon and iodine," in *36th International Electric Propulsion Conference*, 2019.

[78] R. Lucken, "Theory and simulation of low-pressure plasma transport phenomena : Application to the PEGASES Thruster," Theses, Université Paris Saclay (COmUE), Sep. 2019.

[79] U. Samir, K. H. Wright, and N. H. Stone, "The expansion of a plasma into a vacuum: Basic phenomena and processes and applications to space plasma physics," *Reviews of Geophysics*, vol. 21, no. 7, p. 1631, 1983.

[80] I. G. Brown, *The physics and technology of ion sources*. John Wiley & Sons, 2004.

[81] M Capitelli, A Casavola, G Colonna, and A De Giacomo, "Laser-induced plasma expansion: Theoretical and experimental aspects," *Spectrochimica Acta Part B: Atomic Spectroscopy*, vol. 59, no. 3, pp. 271–289, 2004.

[82] S. B. Punjabi, N. K. Joshi, H. A. Mangalvedekar, B. K. Lande, A. K. Das, and D. C. Kothari, "A comprehensive study of different gases in inductively coupled plasma torch operating at one atmosphere," *Physics of Plasmas*, vol. 19, no. 1, p. 012 108, Jan. 2012.

[83] J. F. Kolb, A.-A. H. Mohamed, R. O. Price, R. J. Swanson, A. Bowman, R. Chiavarini, M Stacey, and K. Schoenbach, "Cold atmospheric pressure air plasma jet for medical applications," *Applied Physics Letters*, vol. 92, no. 24, p. 241 501, 2008.

[84] F. Cichocki, M. Merino, E. Ahedo, M. Smirnova, A. Mingo, and M. Dobkevicius, "Electric Propulsion Subsystem Optimization for "Ion Beam Shepherd" Missions," *Journal of Propulsion and Power*, vol. 33, no. 2, pp. 370–378, Mar. 2017.

[85] H. Daido, M. Nishiuchi, and A. S. Pirozhkov, "Review of laser-driven ion sources and their applications," *Reports on Progress in Physics*, vol. 75, no. 5, p. 056 401, May 2012.

[86] J. E. Crow, P. L. Auer, and J. E. Allen, "The expansion of a plasma into a vacuum," *Journal of Plasma Physics*, vol. 14, no. 1, pp. 65–76, Aug. 1975.

[87] A. V. Arefiev and B. N. Breizman, "Collisionless plasma expansion into vacuum: Two new twists on an old problem," *Physics of Plasmas*, vol. 16, no. 5, p. 055 707, May 2009.

[88] J. E. Allen and M. Perego, "On the ion front of a plasma expanding into a vacuum," *Physics of Plasmas*, vol. 21, no. 3, p. 034 504, Mar. 2014.

[89] C Sack and H Schamel, "Evolution of a plasma expanding into vacuum," *Plasma Physics and Controlled Fusion*, vol. 27, no. 7, pp. 717–749, Jul. 1985.

[90] C Charles, "Plasmas for spacecraft propulsion," *Journal of Physics D: Applied Physics*, vol. 42, no. 16, p. 163 001, Aug. 2009.

[91] Y. Hu, J. Wang, and Q. Sun, "Geometrically self-similar ion acceleration in collisionless plasma beam expansion," *Plasma Sources Science and Technology*, vol. 29, no. 12, p. 125 004, 2020.

[92] C. Charles, R. W. Boswell, A. Bouchoule, C. Laure, and P. Ranson, "Plasma diffusion from a low pressure radio frequency source," *Journal of Vacuum Science & Technology A: Vacuum, Surfaces, and Films*, vol. 9, no. 3, pp. 661–663, May 1991.

[93] M. Merino, J. Mauriño, and E. Ahedo, "Kinetic electron model for plasma thruster plumes," *Plasma Sources Science and Technology*, vol. 27, no. 3, p. 035 013, Mar. 2018.

[94] T Lafleur, F Cannat, J Jarrige, P. Q. Elias, and D Packan, "Electron dynamics and ion acceleration in expanding-plasma thrusters," *Plasma Sources Science and Technology*, vol. 24, no. 6, p. 065 013, 2015.

[95] M. Merino and E. Ahedo, "Influence of electron and ion thermodynamics on the magnetic nozzle plasma expansion," *IEEE Transactions on Plasma Science*, vol. 43, no. 1, pp. 244–251, Jan. 2015.

[96] T. Kojima, T. Morita, and N. Yamamoto, "Analysis of plasma detachment in the magnetic thrust chamber using full particle-in-cell simulation," *High Energy Density Physics*, vol. 36, p. 100 814, 2020.

[97] M. Merino and E. Ahedo, "Plasma detachment in a propulsive magnetic nozzle via ion demagnetization," *Plasma Sources Science and Technology*, vol. 23, no. 3, p. 032 001, 2014.

[98] A. Korsun, E. Tverdokhlebova, and F. Gabdullin, "Mathematical model of hypersonic plasma flows expanding in vacuum," *Computer Physics Communications*, vol. 164, no. 1-3, pp. 434–441, Dec. 2004.

[99] Y. Hu and J. Wang, "Expansion of a collisionless hypersonic plasma plume into a vacuum," *Physical Review E*, vol. 98, no. 2, p. 023 204, Aug. 2018.

[100] J. Wang and Y. Hu, "On the limitations of hybrid particle-in-cell for ion thruster plume simulations," *Physics of Plasmas*, vol. 26, no. 10, p. 103 502, Oct. 2019.

[101] P. Mora, "Plasma expansion into a vacuum," *Phys. Rev. Lett.*, vol. 90, p. 185 002, 18 2003.

[102] J. Wang and D. E. Hastings, "Ionospheric plasma flow over large high-voltage space platforms. II: The formation and structure of plasma wake," *Physics of Fluids B: Plasma Physics*, vol. 4, no. 6, pp. 1615–1629, Jun. 1992.

[103] Y. Hu and J. Wang, "Fully kinetic simulations of collisionless, mesothermal plasma emission: Macroscopic plume structure and microscopic electron characteristics," *Physics of Plasmas*, vol. 24, no. 3, p. 033 510, Mar. 2017.

[104] D. Parks and I. Katz, "A preliminary model of ion beam neutralization," in *14th International Electric Propulsion Conference*, Princeton,NJ,U.S.A.: American Institute of Aeronautics and Astronautics, Oct. 1979.

[105] P. Mora, "Collisionless expansion of a Gaussian plasma into a vacuum," *Physics of Plasmas*, vol. 12, no. 11, p. 112 102, Nov. 2005.

[106] M. Merino, F. Cichocki, and E. Ahedo, "A collisionless plasma thruster plume expansion model," *Plasma Sources Science and Technology*, vol. 24, no. 3, p. 035 006, Apr. 2015.

[107] M Merino, E Ahedo, C Bombardelli, H Urrutxua, and J Peláez, "Hypersonic Plasma Plume Expansion in Space," in *32nd International Electric Propulsion Conference*, 2011.

[108] A Domínguez-Vázquez, F Cichocki, M Merino, P Fajardo, and E Ahedo, "Axisymmetric plasma plume characterization with 2D and 3D particle codes," *Plasma Sources Science and Technology*, vol. 27, no. 10, p. 104 009, Oct. 2018.

[109] J. Peralez-Díaz, F. Cichocki, M. Merino, and E. Ahedo, "Formation and neutralization of electric charge and current of an ion thruster plume," *Plasma Sources Science and Technology*, vol. 30, no. 10, p. 105 023, 2021.

[110] J. S. Miller, S. H. Pullins, D. J. Levandier, Y.-h. Chiu, and R. A. Dressler, "Xenon charge exchange cross sections for electrostatic thruster models," *Journal of Applied Physics*, vol. 91, no. 3, pp. 984–991, 2002.

[111] I. H. Hutchinson, *Principles of Plasma Diagnostics*. Cambridge University Press, Jul. 2002.

[112] L Habl, T Lafleur, D Rafalskyi, and P Chabert, "Plasma plume expansion with pulsed electron neutralization," *Plasma Sources Science and Technology*, vol. 30, no. 4, p. 045 014, Apr. 1, 2021.

[113] M. Li, M. Merino, E. Ahedo, and H. Tang, "On electron boundary conditions in PIC plasma thruster plume simulations," *Plasma Sources Science and Technology*, vol. 28, no. 3, p. 034 004, Mar. 2019.

[114] R. W. Hockney and J. W. Eastwood, *Computer Simulation Using Particles*, Special student ed. Bristol [England] ; Philadelphia: A. Hilger, 1988.

[115] C. K. Birdsall and A. B. Langdon, *Plasma Physics via Computer Simulation*. New York: McGraw-Hill, 1985.

[116] J. H. Ferziger and M. Perić, *Computational Methods for Fluid Dynamics*, 3rd, rev. ed. Berlin ; New York: Springer, 2002.

[117] L. Brieda, *Plasma Simulations by Example*. CRC Press, 2019.

[118] D. J. Hardy, D. I. Okunbor, and R. D. Skeel, "Symplectic variable step size integration for n-body problems," *Applied Numerical Mathematics*, vol. 29, no. 1, pp. 19–30, 1999.

[119] K. Cartwright, J. Verboncoeur, and C. Birdsall, "Loading and injection of maxwellian distributions in particle simulations," *Journal of Computational Physics*, vol. 162, no. 2, pp. 483–513, Aug. 2000.

[120] V. Vahedi and M. Surendra, "A Monte Carlo collision model for the particle-in-cell method: Applications to argon and oxygen discharges," *Computer Physics Communications*, vol. 87, no. 1-2, pp. 179–198, May 1995.

[121] M. M. Turner, A. Derzsi, Z. Donkó, D. Eremin, S. J. Kelly, T. Lafleur, and T. Mussenbrock, "Simulation benchmarks for low-pressure plasmas: Capacitive discharges," *Physics of Plasmas*, vol. 20, no. 1, p. 013 507, Jan. 2013.

[122] V. Vahedi and G. DiPeso, "Simultaneous Potential and Circuit Solution for Two-Dimensional Bounded Plasma Simulation Codes," *Journal of Computational Physics*, vol. 131, no. 1, pp. 149–163, Feb. 1997.

[123] S. Biagi, *Biagi-v7.1 (Magboltz version 7.1)*, `www.lxcat.net/Biagi-v7.1`, 2020.

[124] W. L. Morgan, *Morgan (Kinema Research Software)*, `www.lxcat.net/Morgan`, 2020.

[125] A. V. Phelps, *Phelps database*, `http://jilawww.colorado.edu/~avp/`, 2020.

[126] G. A. Bird, *The DSMC method*. U.S: CreateSpace, 2013.

[127] S.-A. Dragly, M. H. Mobarhan, M. E. Lepperød, S. Tennøe, M. Fyhn, T. Hafting, and A. Malthe-Sørenssen, "Experimental directory structure (exdir): An alternative to HDF5 without introducing a new file format," *Frontiers in Neuroinformatics*, vol. 12, Apr. 2018.

[128] "Numpy NPY format." (2022), [Online]. Available: `https://numpy.org/devdocs/reference/generated/numpy.lib.format.html`.

[129] R. L. Graham, T. S. Woodall, and J. M. Squyres, "Open mpi: A flexible high performance mpi," in *Parallel Processing and Applied Mathematics*, R. Wyrzykowski, J. Dongarra, N. Meyer, and J. Waśniewski, Eds., Berlin, Heidelberg: Springer Berlin Heidelberg, 2006, pp. 228–239.

[130] R. D. Falgout, J. E. Jones, and U. M. Yang, "The design and implementation of hypre, a library of parallel high performance preconditioners," in *Numerical Solution of Partial Differential Equations on Parallel Computers*, A. M. Bruaset and A. Tveito, Eds., Berlin, Heidelberg: Springer Berlin Heidelberg, 2006, pp. 267–294.

[131] S Wilczek, J Trieschmann, J Schulze, E Schuengel, R. P. Brinkmann, A Derzsi, I Korolov, Z Donkó, and T Mussenbrock, "The effect of the driving frequency on the confinement of beam electrons and plasma density in low-pressure capacitive discharges," *Plasma Sources Science and Technology*, vol. 24, no. 2, p. 024 002, 2015.

[132] H.-C. Wu, T. Tajima, D. Habs, A. W. Chao, and J. Meyer-ter Vehn, "Collective deceleration: Toward a compact beam dump," *Phys. Rev. ST Accel. Beams*, vol. 13, p. 101 303, 10 2010.

[133] "Cubesat design specification," Cal Poly, Tech. Rep. CP-CDS-R14, 2020.

[134] J Martinez Martinez, D Rafalskyi, P Cordesse, L Habl, P Barbier, S Carpentier, Y Fendler, and E Guilbaud, "Optimization of the ignition delay of a xenon miniaturized gridded ion thruster," in *72nd International Astronautical Congress, Dubai, UEA*, 2021.

[135] D. Rafalskyi, J. M. Martínez, L. Habl, E. Z. Rossi, P. Proynov, A. Boré, T. Baret, A. Poyet, T. Lafleur, S. Dudin, and A. Aanesland, "In-orbit demonstration of an iodine electric propulsion system," *Nature*, vol. 599, no. 7885, pp. 411–415, Nov. 2021.

[136] J. M. Martínez and D. Rafalskyi, "Design and development of iodine flow control systems for miniaturized propulsion systems," *CEAS Space Journal*, vol. 14, no. 1, pp. 91–107, Aug. 2021.

[137] T. E. Sheridan, "How big is a small langmuir probe?" *Physics of Plasmas*, vol. 7, no. 7, pp. 3084–3088, Jul. 2000.

[138] D. L. Brown, M. L. Walker, J. Szabo, W. Huang, and J. E. Foster, "Recommended practice for use of faraday probes in electric propulsion testing," *Journal of Propulsion and Power*, vol. 33, no. 3, pp. 582–613, 2017.

[139] V Hugonnaud, S. Mazouffre, and D Krejci, "Faraday cup sizing for electric propulsion ion beam study: Case of a field-emission-electric propulsion thruster," *Review of Scientific Instruments*, vol. 92, no. 8, p. 084 502, 2021.

[140] J. P. Sheehan, Y. Raitses, N. Hershkowitz, and M. McDonald, "Recommended practice for use of emissive probes in electric propulsion testing," *Journal of Propulsion and Power*, vol. 33, no. 3, pp. 614–637, May 2017.

[141] M. Y. Ye and S. Takamura, "Effect of space-charge limited emission on measurements of plasma potential using emissive probes," *Physics of Plasmas*, vol. 7, no. 8, pp. 3457–3463, Aug. 2000.

[142] J. P. Sheehan and N Hershkowitz, "Emissive probes," *Plasma Sources Science and Technology*, vol. 20, no. 6, p. 063 001, 2011.

[143] D. Rafalskyi and A. Aanesland, "Matched dipole probe for magnetized low electron density laboratory plasma diagnostics," *Physics of Plasmas*, vol. 22, no. 7, p. 073 504, Jul. 2015.

[144] K. Balmain, "The impedance of a short dipole antenna in a magnetoplasma," *IEEE Transactions on Antennas and Propagation*, vol. 12, no. 5, pp. 605–617, Sep. 1964.

[145] L. Habl, D. Rafalskyi, and T. Lafleur, "Ion beam diagnostic for the assessment of miniaturized electric propulsion systems," *Review of Scientific Instruments*, vol. 91, no. 9, p. 093 501, Sep. 2020.

[146] A. Neumann, "Update on diagnostics for DLR's electric propulsion test facility," *Procedia Engineering*, vol. 185, pp. 47–52, 2017.

[147] G. F. Benavides, J. Mackey, D. Ahern, and R. Thomas, "Diagnostic for verifying the thrust vector requirement of the AEPS hall-effect thruster and comparison to the NEXT-c thrust vector diagnostic," in *2018 Joint Propulsion Conference*, American Institute of Aeronautics and Astronautics, Jul. 2018.

[148] R Theunissen and P Gjelstrup, "Adaptive sampling in higher dimensions for point-wise experimental measurement techniques," *Measurement Science and Technology*, vol. 29, no. 8, p. 085 007, Jul. 2018.

[149] H.-C. Steiner, "Firmata: Towards making microcontrollers act like extensions of the computer.," in *NIME*, Citeseer, 2009, pp. 125–130.

[150] J. Verboncoeur, A. Langdon, and N. Gladd, "An object-oriented electromagnetic PIC code," *Computer Physics Communications*, vol. 87, no. 1-2, pp. 199–211, May 1995.

[151] D. L. Brown, M. L. R. Walker, J. Szabo, W. Huang, and J. E. Foster, "Recommended practice for use of faraday probes in electric propulsion testing," *Journal of Propulsion and Power*, vol. 33, no. 3, pp. 582–613, May 2017.

[152] R. A. Baragiola and P. Riccardi, "Electron Emission from Surfaces Induced by Slow Ions and Atoms," in *Reactive Sputter Deposition*, ser. Springer Series in Materials Science, D. Depla and S. Mahieu, Eds., ed. by R. Hull, R. M. Osgood, J. Parisi, and H. Warlimont, vol. 109, Berlin, Heidelberg: Springer Berlin Heidelberg, 2008, pp. 43–60.

[153] S. Y. Lai, A. Brown, J. C. Vickerman, and D. Briggs, "The relationship between electron and ion induced secondary electron imaging: A review with new experimental observations," *Surface and Interface Analysis*, vol. 8, no. 3, pp. 93–111, Jun. 1986.

[154] D. Hasselkamp, "Kinetic electron emission from solid surfaces under ion bombardment," in *Particle Induced Electron Emission II*, Springer Berlin Heidelberg, 1992, pp. 1–95.

[155] J Ferron, E. V. Alonso, R. A. Baragiola, and A Oliva-Florio, "Electron emission from molybdenum under ion bombardment," *Journal of Physics D: Applied Physics*, vol. 14, no. 9, pp. 1707–1720, 1981.

[156] J. M. Magnusson, A. L. Collins, and R. E. Wirz, "Polyatomic ion-induced electron emission (IIEE) in electrospray thrusters," *Aerospace*, vol. 7, no. 11, p. 153, Oct. 2020.

[157] H. D. Hagstrum, "Auger Ejection of Electrons from Tungsten by Noble Gas Ions," *Physical Review*, vol. 96, no. 2, pp. 325–335, Oct. 15, 1954.

[158] H. D. Hagstrum, "Auger Ejection of Electrons from Molybdenum by Noble Gas Ions," *Physical Review*, vol. 104, no. 3, pp. 672–683, Nov. 1, 1956.

[159] G. D. Magnuson and C. E. Carlston, "Electron Ejection from Metals due to 1- to 10-keV Noble Gas Ion Bombardment. I. Polycrystalline Materials," *Physical Review*, vol. 129, no. 6, pp. 2403–2408, Mar. 15, 1963.

[160] P. Mahadevan, J. K. Layton, and D. B. Medved, "Secondary Electron Emission from Clean Surface of Molybdenum Due to Low-Energy Noble Gas Ions," *Physical Review*, vol. 129, no. 1, pp. 79–83, Jan. 1, 1963.

[161] P. Mahadevan, G. D. Magnuson, J. K. Layton, and C. E. Carlston, "Secondary-Electron Emission from Molybdenum Due to Positive and Negative Ions of Atmospheric Gases," *Physical Review*, vol. 140, A1407–A1412, 4A Nov. 15, 1965.

[162] B. Hird, C. Pepin, and G. Kelly, "Charge dependence of secondary electron emission coefficients," *Journal of Applied Physics*, vol. 56, no. 11, pp. 3304–3307, Dec. 1984.

[163] R. A. Baragiola, "Principles and mechanisms of ion induced electron emission," *Nuclear Instruments and Methods in Physics Research Section B: Beam Interactions with Materials and Atoms*, vol. 78, no. 1-4, pp. 223–238, May 1993.

[164] M. A. Lewis, D. A. Glocker, and J. Jorne, "Measurements of secondary electron emission in reactive sputtering of aluminum and titanium nitride," *Journal of Vacuum Science & Technology A: Vacuum, Surfaces, and Films*, vol. 7, no. 3, pp. 1019–1024, May 1989.

[165] C. Corbella, A. Marcak, T. de los Arcos, and A. von Keudell, "Revising secondary electron yields of ion-sputtered metal oxides," *Journal of Physics D: Applied Physics*, vol. 49, no. 16, 16LT01, Apr. 27, 2016.

[166] D Depla, X. Y. Li, S Mahieu, and R De Gryse, "Determination of the effective electron emission yields of compound materials," *Journal of Physics D: Applied Physics*, vol. 41, no. 20, p. 202 003, Oct. 21, 2008.

[167] R. Buschhaus, M. Prenzel, and A. von Keudell, "Ion-induced secondary electron emission of oxidized nickel and copper studied in beam experiments," *Plasma Sources Science and Technology*, Jan. 2022.

[168] J. M. Martinez, D. Rafalskyi, and A. Aanesland, "Development and testing of the npt30-i2 iodine ion thruster," in *36th International electric propulsion conference*, 2019.

[169] L. Habl, D. Rafalskyi, and T. Lafleur, "Secondary electron emission due to multi-species iodine ion bombardment of different target materials," *Journal of Applied Physics*, vol. 129, no. 15, p. 153 302, Apr. 2021.

[170] A. Marcak, C. Corbella, T. de los Arcos, and A. von Keudell, "Note: Ion-induced secondary electron emission from oxidized metal surfaces measured in a particle beam reactor," *Review of Scientific Instruments*, vol. 86, no. 10, p. 106 102, Oct. 2015.

[171] Y. Yamauchi and R. Shimizu, "Secondary Electron Emission from Aluminum by Argon and Oxygen Ion Bombardment below 3 keV," *Japanese Journal of Applied Physics*, vol. 22, no. Part 2, No. 4, pp. L227–L229, Apr. 1983.

[172] K. A. Polzin, S. R. Peeples, J. F. Seixal, S. L. Mauro, B. L. Lewis, G. A. Jerman, D. H. Calvert, J. Dankanich, H. Kamhawi, T. A. Hickman, J. Szabok, B. Pote, and L. Lee, "Propulsion system development for the iodine satellite (iSAT) demonstration mission," in *34th International Electric Propulsion Conference*, 2017.

[173] V. Gushenets, A. Nikolaev, E. Oks, L. Vintizenko, G. Y. Yushkov, A Oztarhan, and I. Brown, "Simple and inexpensive time-of-flight charge-to-mass analyzer for ion beam source characterization," *Review of scientific instruments*, vol. 77, no. 6, p. 063 301, 2006.

[174] E. V. Alonso, R. A. Baragiola, J. Ferrón, M. M. Jakas, and A. Oliva-Florio, "Z_1 Dependence of ion-induced electron emission from aluminum," *Physical Review B*, vol. 22, no. 1, pp. 80–87, Jul. 1980.

[175] J. Polansky, J. Wang, and N. Ding, "Experimental investigation on plasma plume potential," *IEEE Transactions on Plasma Science*, vol. 41, no. 12, pp. 3438–3447, 2013.

[176] E Zorzoli Rossi, D Rafalskyi, S Dudin, and J Martínez Martínez, "Direct thrust measurements of an iodine cold gas propulsion system," in *7th Space Propulsion Conference, Estoril, Portugal*, 2021.

[177] S. V. Dudin and D. V. Rafalskyi, "On the simultaneous extraction of positive ions and electrons from single-grid ICP source," *EPL (Europhysics Letters)*, vol. 88, no. 5, p. 55 002, Dec. 1, 2009.

[178] T. Lafleur, "Space-charge induced particle reflection between hybrid AC/DC biased electrodes," *Plasma Sources Science and Technology*, vol. 30, no. 5, p. 055 018, May 2021.

[179] S. H. Fu and Z. F. Ding, "Comment on 'Coincident ion acceleration and electron extraction for space propulsion using the self-bias formed on a set of RF biased grids bounding a plasma source'," *Journal of Physics D: Applied Physics*, vol. 54, no. 30, p. 308 001, Jul. 2021.

ECOLE
DOCTORALE

Titre : Étude des phénomènes de panache des propulseurs ioniques à grille, polarisés en courant continu et en radiofréquence.

Mots clés : panache de plasma, expansion de plasma, radiofréquence, iode, propulseur ionique à grille

Résumé : Ces dernières années, deux technologies prometteuses sont apparues pour améliorer les performances et diminuer le coût des propulseurs ioniques, la polarisation RF des grilles d'accélération et l'utilisation de l'iode comme combustible. Ces techniques peuvent représenter une étape technologique importante ; cependant, lors de l'utilisation de l'une ou l'autre de ces techniques, les processus physiques dans la génération du plasma et surtout sur le panache de plasma en aval sont complexes, ce qui a des implications importantes sur les performances du dispositif. L'objectif principal de ce travail était d'élucider la physique du panache de plasma lors de l'utilisation de ces technologies par une approche numérique et expérimentale.
Un modèle numérique dédié du panache a été développé pour étudier la polarisation de la grille RF, ce qui a permis de déterminer le comportement de plusieurs phénomènes et d'étendre les travaux numériques précédents. Un prototype utilisant la polarisation de la grille RF a également été étudié expérimentalement. Il a été exploité aux valeurs les plus élevées d'énergie d'accélération et de fréquence à ce jour, démontrant qu'il peut générer un panache bien neutralisé avec des performances acceptables et fournir les données disponibles pour ce type de propulseur. Les expériences ont également montré un excellent accord avec les prédictions numériques et théoriques, ce qui a confirmé à la fois la justesse du modèle développé ici, et les travaux précédents étant une avancée importante vers le développement d'un prototype de vol.
Pour l'iode, les caractéristiques du panache et les performances du propulseur sont mesurées et comparées au cas du xénon, montrant des caractéristiques uniques et, dans plusieurs cas, meilleures. Un nouvel instrument automatisé pour déterminer le profil du faisceau d'ions est développé, et pour améliorer la qualité des expériences et augmenter la base de connaissances sur les plasmas d'iode, le rendement d'émission des électrons secondaires des ions d'iode a été mesuré pour la première fois. Pendant les travaux, le propulseur testé a été lancé sur une mission spatiale, ce qui a permis de comparer les résultats au sol et en vol avec un excellent accord.

Title : Investigation of DC and RF biased gridded ion thruster plume phenomena

Keywords : plasma plume, plasma expansion, radio-frequency, iodine, gridded ion thruster

Abstract : In recent years, two promising technologies emerged to improve the performance and decrease the cost of ion thrusters; RF biasing of ion acceleration grids and the use of iodine as a propellant. These techniques may represent a significant technological step forward; however, when using either of them, the physical processes in the plasma generation and especially on the downstream plasma plume are intricate, having significant implications on the device's performance. The main goal of this work was to elucidate the physics of the plasma plume when using these technologies through a numerical and experimental approach.
A dedicated numerical model of the plume was developed to study RF grid biasing, which allowed a determination of the behavior of several phenomena and the expansion of previous numerical work. A prototype using RF grid biasing was also investigated experimentally, which was operated at the highest values of acceleration energy and frequency to date, demonstrating that it can generate a well-neutralized plume with acceptable performance and provide initial benchmark data available for this type of thruster. The experiments also showed an excellent agreement with the numerical and theoretical predictions, which confirmed both the correctness of the model developed here, and previous works, and being an important advancement towards developing a flight prototype.
For iodine, the characteristics of the plume and the thruster performance were measured and compared to xenon, showing unique and, in several cases, better characteristics. A new automated instrument to determine the ion beam profile was developed, and to improve the quality of experiments and increase the knowledge base on iodine plasmas, the secondary electron emission yield of iodine ions was measured for the first time. During this work, the thruster tested was launched onboard a space mission, which permitted a comparison of ground and flight results with excellent agreement obtained.

Institut Polytechnique de Paris
91120 Palaiseau, France